Cape Peninsula
University of Technology

The critical process conditions for controlled growth of iron oxide nanoparticles synthesized using continuous hydrothermal synthesis.

by

Brett Craig Kriedemann

Thesis Submitted in Fulfilment of the Requirements for the Degree

Master of Technology: Chemical Engineering

in the Faculty of Engineering

at the Cape Peninsula University of Technology

Supervisor: Prof V.G Fester

Cape Town Campus

October 2014

Declaration

I, Brett Craig Kriedemann, declare that the contents of this dissertation/thesis represent my own unaided work, and that the dissertation/thesis has not previously been submitted for academic examination towards any qualification. Furthermore, it represents my own opinions and not necessarily those of the Cape Peninsula University of Technology.

20th of March 2015

Signed **Date**

"Nano-scale science and engineering most likely will produce the strategic technology breakthroughs of tomorrow. Our ability to work at a molecular level, atom by atom, to create something new, something we can manufacture from the 'bottom up,' opens huge vistas for many of us."

- David Swain, Senior VP of engineering and technology, Boeing

Abstract

Iron oxide nanoparticles have recently become attractive for use in gas sensing, as catalysts and have also shown promise in other fields, such as biomedicine, for targeted drug delivery and cancer treatment. Despite these growing applications, the ability to produce iron oxide and one dimensional (1D) iron oxide nanoparticles on an industrial scale has proven to be a challenge. The continuous hydrothermal synthesis, (CHS), method has been proposed as the most promising method, yet the effect of the operating parameters on particle characteristics are still widely contested in the literature. One such parameter, temperature, is still widely contested on its effect on APS.

To address this issue, a CHS pilot plant was constructed and commissioned. The inability to isolate certain parameters in CHS is a common shortcoming. Parameters such as temperature and flow rate are prime examples, as changing the temperature has several effects on the system resulting in a change in reaction rate, a change in density and a change in the reactor residence time while the flow rate is closely linked to the residence time and mixing conditions.

A 3-level Box-Behnken factorial design method was used to statistically analyze the correlations and interactions between operating parameters (temperature, concentration and flow rate) in CHS and evaluate their resulting effect on particle characteristics, with focus on morphology.

All particles were characterized by X-ray diffraction (XRD) and high resolution transmission electron microscopy (HRTEM). Reactions in the presence of solvents or surfactants proved incapable of modifying particle morphology, although significant particle size reduction revealed that they were actively involved in particle growth and may be used as a further tool for controlling particle characteristics. The concentration was found to have the greatest effect on particle characteristics including a slight alteration of particle shape and a massive influence on the average particle size. The interactions between operating parameters were significant, especially in the case of temperature and concentration. The temperature and concentration were found to interact revealing three different trends on APS, offering a solution to conflicting reports in the literature. The temperature was also observed to interact favourably with the flow rate, presenting a method of increasing the PY and RC, with little change in APS and PSD. This knowledge will prove invaluable for the design of future experiments in CHS.

Acknowledgments

I wish to thank:

- God, for granting me with the wisdom required to complete my research.
- Professor Fester, for her encouragement, advice and faith in me. I am grateful for her giving me the opportunity to pursue this research under her supervision.
- Mahabubur Rahman Chowdhury, for his advice and mentorship.
- Honeil Meyo, for his aid in laboratory work
- Alwyn Bester, for his aid in the construction of the CHS pilot plant and his Engineering insight.
- Richard Du Toit, for his advice and aid in the construction in the CHS pilot plant.
- Tommy, for his aid in the construction of the CHS pilot plant.
- Mohamed Jaffer (UCT), for assisting with HR TEM characterisation.
- Nicholas Laidler (UCT), for assisting with XRD characterisation.
- Unitemp, Teledyne Isco and Air Liquide - for their excellent and professional and service.
- All staff and colleagues at the Flow Process and Rheology centre, for allowing me to be part of the unit, for the use of their facilities and always making me feel welcome.

In Loving memory of Hendrick "Tommy" Joseph Thomas

1964 to 2014

The financial assistance of the National Research Foundation towards this research is acknowledged. Opinions expressed in this thesis and the conclusions arrived at, are those of the author, and are not necessarily to be attributed to the National Research Foundation.

Dedication

To my dearest and loving parents

Geoff and Renae Kriedemann

For their love, support and guidance, and financial contribution throughout my studies

To my older brother and his wife

Ryan and Kim Kriedemann

For their support and encouragement

To my loving girlfriend

Jessica Hobden

For her love, patience and sacrifice over the course of my research

In Family life, love is the oil that eases friction, the cement that binds us together, and the music that brings harmony.

-Friedrich Nietzche

Table of Contents

List of Figures

List of Tables

Glossary - Terms and Concepts

Nanoparticles: Any ultrafine particles between 1 and 100 nm in size.

One Dimensional (1D) nanoparticles: Nanoparticles where the dimensions of their cross section is in the nanometer range, whilst their length may range up to a few micrometers, such as nanorods/wires.

Crystal Structure: A repeating arrangement of like atoms, which creates a uniform, repeating structure.

Anisotropic: Materials that exhibit properties with different values when measured along axes in different directions.

Hydrothermal synthesis: The precipitation of inorganic materials in an aqueous solution at temperatures above boiling point and pressure which exceed the surrounding atmospheric conditions.

Supercritical water: Water above its critical temperature and pressure of 373°C and 22.1MPa, which displays characteristics of both its liquid and gaseous phases.

Nucleation site: The locations at which seed crystals begin to develop.

Ostwald Ripening: Ostwald ripening is a particle growth mechanism, which can be described as a diffusion or reaction rate-limited growth of particles at the expense of smaller ones.

Oriented Attachment: Oriented attachment is a particle growth mechanism, where particles with common crystallographic orientations directly combine to form larger particles.

Polymer: A large molecule or macromolecule, composed of many subunits known as monomers.

Surfactant: An amphiphilic molecule with a head and a tail which has hydrophobic and hydrophilic properties. They are commonly used to lower surface tension between two liquids.

Solvent: A liquid which dissolves a solid, liquid or gaseous solute, resulting in a solution.

List of Abbreviations

STM - Scanning tunnelling microscope

AFM - Atomic force microscope

1D - one dimensional

CHS - Continuous hydrothermal synthesis

TEM - transmission electron microscope

XRD - X-ray diffraction

APS - average particle size

RC - relative crystallinity

PY - product yield

CV - coefficient of variation

PSD - particle size distribution

T_c - critical temperature

P_c - critical pressure

LAI - light adsorption imaging

CFD - computational fluid dynamics

SR - saturation ratio

OD - outer diameter

ID - inner diameter

RPM - revolutions per minute

HLB - hydrophile-lipophile balance

List of symbols

Symbol	Description	Unit
C	concentration	mol/dm^3
C_{eq}	equilibrium concentration	mol/dm^3
d	diameter	m
D_{LS}	lattice spacing	-
D_e	effective diffusion coefficient	cm^2/s
D_o	initial particle size	nm
D(t)	particle size at time t	nm
E	energy of the emission line	-
g	gravitational constant	$m.s^{-2}$
G	Gibbs free energy	kj/mol
Gr	Grashoff number	dimensionless
K_{OA}	growth rate constant	$min^{-1/3}$
K_{OR}	growth rate constant	min^{-1}
L_a	anion	-
M	molarity	mol/dm^3
M_c	metal cation	-
n	number of reflected wavelengths	-
P	pressure	Pa
Q	volumetric flow rate	$m^3.s^{-1}$
R	universal gas constant	J/mol.K
Re	Reynolds number	dimensionless
S	metal oxide solubility at reaction conditions	mol/kg
S_o	metal oxide solubility at ambient conditions	mol/kg
t	time	seconds
T	temperature	°C
v	fluid velocity	$m.s^{-1}$
V	volume	m^3
Z	atomic number	-
α	chemical activity	-
α_o	initial chemical activity	-
ε	Dielectric constant	dimensionless
ρ	density	kg/m^3
τ	residence time	seconds
δ	characteristic dimension	m
μ_d	dynamic viscosity	$kg.m^{-1}.s^{-1}$
μ_k	Kinematic viscosity	$m^2.s^{-1}$
λ	X-ray wavelength	-
θ	angle of diffraction	°
σ	supersaturation	-

Chapter 1 – Introduction

1.1 Introduction

History has reported the use of ultrafine particles which dates back hundreds of years (Ramsden 2011). There is even evidence to suggest that 400 year old Damascus swords with advanced metallurgical features were recently found to contain carbon nanotubes embedded in their blades (Ramsden 2011). However the field of nanoscience only became prominent in the late 20th century, with reference often made to Richard Feynman's lecture at California Institute of Technology in 1959 entitled "There's plenty of room at the bottom." Feynman envisaged machines constructing smaller machines, which would continue until precise manipulation of the atomic realm was reached (Schiller 2010).

In current times, a fundamental aspect of nanotechnology research is the development of reliable synthesis protocols for nano structured materials over a range of chemical compositions, shapes and sizes (Mandal & Muller 2008). As the physical and chemical properties of nanoscale materials are strongly dependent on their size, size distribution, structures and dimensions, it is essential to maintain control over particle characteristics (Zhu et al. 2011). As a consequence, the effects and potential applications of uniquely shaped nanomaterials have been studied. Structures such as nanocubes, nanorods/wires, nanotubes, nanoflakes, urchin-like, flower-like, nanopropellers and nanodisks has been reported by various groups (Yang et al. 2006; Mandal & Muller 2008; Jiang et al. 2010; Zhu et al. 2011). Non-spherical nanoparticles have also become attractive due to their anisotropic behavior (Jiang et al. 2010).

Nanowires, nanotubes, and nanorods of iron oxides represent a class of one dimensional (1D) nano structured materials, in which carrier motion is restricted in two directions, so that they are expected essentially to improve photochemical, photophysical, and electron-transport properties (Zhu et al. 2011). A number of synthesis methods have been developed for generating 1D iron oxide nanostructures. These methods include vapour–solid reaction, vapour–liquid–solid growth technique, metalorganic chemical vapour deposition technique, sol–gel process, hard porous templates, the gamma-irradiation method (Mandal & Muller 2008) and batch hydrothermal synthesis (Wang & Yao 2010). However, it is still a challenge to develop a general synthesis strategy to prepare 1D iron oxide nanostructures on a large scale and at low cost (Wang et al. 2008). Teja and Koh (2009) reviewed numerous synthesis strategies for three different types of iron oxide nanoparticles, and proposed that continuous hydrothermal synthesis (CHS) is most promising for process control, particle characteristics control and plant scalability. Although high quality particles with a narrow size distribution have been produced via the CHS method, Xu (2006) stressed that the effects of operating

parameters are not well understood, often citing conflicting reports in the literature. One of these uncertain parameters in CHS is the effect of temperature on particle size, where Hao and Teja (2003) reported that temperature has no evident effect on the size of iron oxide nanoparticles, while Xu and Teja (2008) identified that particle size increased with increasing temperature. On the contrary, it was shown by Hakuta et al. (1998) that ceria particles decreased in size along with an increase in temperature.

Numerous authors have studied the effects of isolated operating parameters in CHS, such as concentration (Hao & Teja 2003; Kawai-Nakamura et al. 2008; Xu & Teja 2008), reaction temperature (Xu 2006; Liang et al. 2010), pressure (Noguchi et al. 2008), residence time (Hao & Teja 2003; Xu & Teja 2008; Sue et al. 2011) and pH (Cote & Teja 2002). Yet Cote et al. (2003) identified that operating parameters in CHS are rather complex and difficult to isolate. One such example is that of temperature. When the temperature increases, it changes the fluid density and viscosity and hence the reaction rate and residence time. The resulting affect is a change in particle growth, mixing characteristics and reaction time. As the evaluation of parameters through isolation appears to be feeble, a new technique was required. A more appealing approach was identified by Aimable et al. (2008). They used a factorial design to study the effect of operating parameters on the particle characteristics of $BaZrO_3$ powders, which used a set of statistical experiments to analyze the system as a whole. The factorial design was deemed successful, highlighting the temperature and NaOH concentration as having the largest influence on APS. However, the interactions between parameters were not reported.

Although the dependence of particle characteristics on the variation of operating parameters in CHS has been reported by several authors, a systematic study has yet to be performed to determine the critical process parameters and their interactions required for controlled growth of iron oxide nanoparticles.

1.2) Objectives of this research

- To construct and commission a fully functional CHS pilot plant for the synthesis of iron oxide nanoparticles.
- To evaluate the effect of operating parameters and their interactions through a factorial trial analysis in order to identify the critical conditions for particle characteristic and morphology control.

1.3) Significance of this research

As highlighted above, the effects of operating parameters are clearly not well understood. The difficulty and often inherent inability to isolate certain parameters is also problematic, and it is therefore hypothesised that parameter interactions may be responsible for conflicting reports in the literature. By identifying and analysing these parameter interactions, it may shed light on the results reported from existing studies. Further, by understanding these interactions, the critical process parameters may be identified and utilized for greater control over particle characteristics.

1.4) Delineation

Although potential applications were considered, no testing was conducted. The CHS pilot plant remained unchanged between experimental runs, and no physical modifications were evaluated. All chemicals were used as received, and no further purification was carried out.

1.5) Thesis structure

Chapter 1 served as an introduction to the study and introduced the various research questions, highlighted the objectives and discussed the significance of this study. This was followed by a detailed and relevant literature review in Chapter 2. Chapter 3 consists of two separate sections, the first part encompassed the design, construction and commissioning of the CHS pilot plant, with the second section focusing on the experimental work conducted. In chapter 4, the results from the factorial trial were discussed and the effect of operating parameters were evaluated on the resulting average particle size (APS) and particle size distribution (PSD). This was continued in chapter 5, with the evaluation of the product yield (PY) and the relative crystallinity (RC). In chapter 6, attempts at particle morphology control were highlighted which included the use different solvents and surface modifiers. Chapter 7 showcased a summary of all the findings, conclusions and recommendations for further research.

Chapter 2 – Literature Review

2.1 Introduction

This chapter presents a review of the literature on iron oxide, including the characteristics, properties and some general synthesis strategies including continuous and batch methods. The focus, however, is on the continuous hydrothermal synthesis (CHS) of iron oxide nanomaterials using supercritical water as a reactant medium. Various design aspects have also been identified and summarized, such as the numerous mixer orientations and designs. The theoretical reaction and growth mechanisms have also been reviewed, while the effects of operating parameters within CHS reported by other authors have been examined. Conventional morphology control strategies of 1D nanoparticles have also been assessed .

2.2) Nanotechnology

2.2.1) General description and definition of nanotechnology

The word 'nano' originates from the Greek word 'nanos', which means "midget" or "dwarf" (Johnson 2006). The term 'nano' is used as a prefix, which literally means one billionth. One nanometer is therefore one billionth of a meter and is abbreviated as 1 nm. To get a perspective on the nanoscale, a human hair measures 50,000 nm across, a bacteria cell measures a few hundred nanometers, while a hydrogen atom measures only 0.1 nm - the naked eye is only capable of seeing 10,000 nm across (Ratner & Ratner 2002). Nanotechnology involves manipulating the qualities and structures of materials on the nanoscale, and may therefore be defined as the study of matter in which at least two dimensions are within the range of 1 to 100 nm (Sepeur 2008). This definition may be further broadened to accommodate objects which contain one dimension under 100 nm and another under one micrometer (1 μm), allowing ultrathin layers with lateral sub micron structures sizes to be included as nanostructures (Kohler & Fritzsche 2004).

2.2.2) Unique properties at the nanoscale

At the nanoscale, particles tend to behave unexpectedly, differing physically, chemically, and biologically when compared to their macro scale counterparts (Averick 2007). At the nanoscale, a material's size and mass is so small, that gravity is no longer the primary force. Therefore other forces such as electromagnetic forces become more prominent, giving rise to unique properties at the nanoscale (California Nanoscale Institute 2002). It was stressed by Varadan et al. (2010), that intrinsic properties of materials that are normally size independent (such as conductivity), do not remain size independent at the nanoscale, which can be correlated to three main factors:

- The small length scales directly influences the structures of energy bands, which indirectly leads to changes in a materials atomic structure. This so called "quantum confinement" changes the total energy of a system.
- Size reduction may change the chemical reactivity of a system, which is a function of the structure and occupation of the outermost energy levels. Physical properties such as electrical, thermal, optical and magnetic are also dependent on the arrangement of the outermost energy levels and can change as the size decreases. In an isolated nanoparticle, a large portion of the total number of atoms will be present either at or near the free surface.
- Mechanical strength, which is dependent on electronic structure, may also be affected by size reduction. Finally, owing to the change of electron energy levels, properties of materials at the nanoscale may exhibit quantized behaviour, as opposed to continuous behaviour.

2.3 Iron Oxides

2.3.1) Introduction to oxides of iron

Iron oxides are common compounds which are found throughout nature and can be readily synthesized in a laboratory (Cornell & Schertmann 2003). All iron oxides and oxide hydroxides play a fundamental role in pure, environmental and industrial chemistry; in soil sciences, in geology, in mineralogy, in biology and medicine to name a few (Schwertmann & Cornell 2000). There are 17 known types of iron oxides which are displayed in Table 2.1 (Cornell & Schertmann 2003).

Table 2. 1- The 17 known oxides of iron adapted from Cornell and Schertmann (2003)

Oxide-hydroxides and hydroxides	**Oxides**
Goethite FeOOH α-FeOOH	Hematite α-Fe_2O_3
Lepidocrocite FeOOH γ-FeOOH	Magnetite Fe_3O_4
Akaganeite β-FeOOH	Maghemite γ-Fe_2O_3
Shertmannite $Fe_{16}O_{16}(OH)_y(SO_4)_z \cdot n\ H_2O$	β- Fe_2O_3
δ-FeOOH	ε- Fe_2O_3
Feroxyhyte δ'-FeOOH	Wustite FeO
High pressure FeOOH	
Ferrihydrite $Fe_5HO_8 \cdot 4\ H_2O$	
Bernalite $Fe(OH)_3$	
$Fe(OH)_2$	
Green Rusts $Fe_x^{III}Fe_y^{II}(OH)_{3X+2Y-Z}(A^{--})_Z$;$A^{--}$= Cl^{--};$\frac{1}{2}SO_4^{2-}$	

The most important iron oxides are hematite (α-Fe_2O_3), magnetite (Fe_3O_4) and maghemite (γ-Fe_2O_3) which have been discussed in greater detail below.

2.3.2 Hematite (α-Fe_2O_3)

Hematite is the oldest of the known iron oxides and is widely found in rocks and soils. It is also commonly referred to as ferric oxide, iron sesquioxide, red ochre, specularite, specular iron ore, kidney ore, or martite. Hematite ranges in colour from blood-red if finely divided, to black or grey if coarsely crystalline. It is very stable under ambient conditions, and is often the end product when other iron oxides undergo transformation (Teja & Koh 2009). Hematite also exhibits antiferromagnetic behaviour (Grau-Crespo et al. 2010). The crystal structure of hematite (Figure 2.1) has been described as closely packed planes of oxygen anions and iron cations in octahedral interstitial sites where the oxygen ions are in a hexagonal closely-packed arrangement and the Fe^{3+} ions occupy the octahedral sites (Teja & Koh 2009). Hematite crystals are commonly found to form rhombohedral, platy and/or rounded shapes, and it has been found that these three morphologies tend to predominate successively as the temperature decreases while under hydrothermal conditions (Cornell & Schertmann 2003). The crystal structure of hematite has a less directional effect on crystal habit when compared to goethite, allowing for the shape to be readily modified. Thus a variety of morphologies have been synthesized (Cornell & Schertmann 2003). Hematite is favourable in many applications due to its low cost, high resistance to corrosion (Zhu et al. 2011) and non toxicity (Mandal & Muller 2008), leading to applications in magnetic materials, gas sensors, catalysts, drug delivery, and biomedical therapies (Wang et al. 2008).

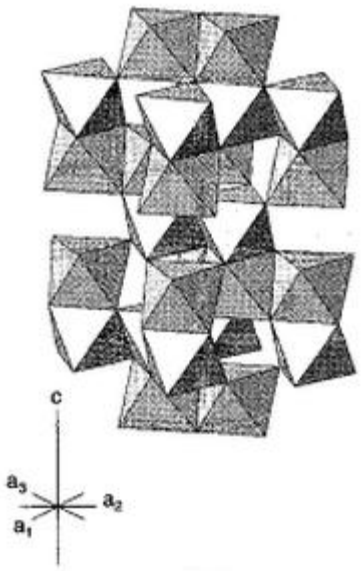

Figure 2. 1- Crystal structure of hematite (α-Fe_2O_3) as illustrated from Schertmann & Cornell (2000)

2.3.3) Magnetite (Fe_3O_4)

Magnetite minerals range in colour from reddish-black to brownish-black, are optically opaque, and exhibit a metallic to sub metallic lustre (Virtual Museum Soils 2005). Magnetite may also be referred to as black iron oxide, magnetic iron ore, loadstone, ferrous ferrite or Hercules stone and is ferromagnetic, displaying the strongest magnetism of any transitional metal oxide (Teja & Koh 2009). Magnetite differs from most iron oxides as it contains iron in its divalent and trivalent state (Cornell & Schertmann 2003). The oxygen ions are bound in a closely packed cubic arrangement, and magnetite has an inverse spinel structure with Fe^{3+} ions distributed randomly between octahedral and tetrahedral sites while Fe^{2+} ions occupy octahedral sites (Teja & Koh 2009; Grau-Crespo et al. 2010).

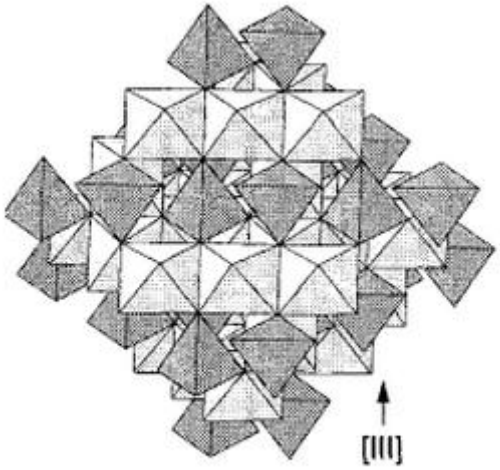

Figure 2. 2 - Crystal structure of magnetite (Fe_3O_4) as illustrated from Schertmann & Cornell (2000)

2.3.4) Maghemite (γ-Fe_2O_3)

Maghemite occurs naturally in soils as the product of weathering and breakdown of magnetite, and is also a product formed when other iron oxides undergo heating (Teja & Koh 2009). It is optically opaque, yet transparent in thin fragments and its colour ranges from brown, bluish back; brown to yellow in transmitted light (Mineral Data Publishing 2001). Maghemite is the second most stable polymorph of iron oxide and is ferrimagnetic with a net magnetic moment (Grau-Crespo et al. 2010). Maghemite is metastable when compared to the likes of hematite, and has been known to almost always adopt the morphology of the precursor iron oxide or iron compound from which it was formed (Mineral Data Publishing 2001; Cornell & Schertmann 2003). The oxygen ions of maghemite are bound in a closely packed cubic arrangement, and it has a spinel structure similar to that of

magnetite (Figure 2.2), although it has vacancies in the cation sublattice and all the iron cations are in the trivalent state (Teja & Koh 2009; Grau-Crespo et al. 2010). Two thirds of the sites are filled with regularly arranged Fe^{3+} ions, where two filled sites are followed by a vacant one (Teja & Koh 2009).

Table 2. 2- Physical and magnetic properties of iron oxides adapted from Cornell and Schertmann (2003)

Property	Oxide		
	Hematite	**Magnetite**	**Maghemite**
Molecular formula	Hematite α-Fe_2O_3	Magnetite Fe_3O_4	Maghemite γ-Fe_2O_3
Density (g/cm)	5.26	5.18	4.87
Melting point	1350	1583-1597	N/A
Hardness	6.5	5.5	5
Type of magnetism	Weakly ferromagnetic/ antiferromagnetic	Ferromagnetic	Ferrimagnetic
Curie temperature (K)	956	850	820-986
Ms at 300 K	0.3	92-100	60-80
Standard free energy of formation (kJ/mol)	-742.7	-1012.6	-711.1
Crystallographic system	Rhombohedral, Hexagonal	Cubic	Cubic or tetrahedral
Structural type	Corundum	Inverse spinel	Defect spinel
Space group	R3c (hexagonal)	Fd3m	P4332 (Cubic), P4(1)2(1)2 (tetragonal)

2.4) Synthesis routes for producing nanoparticles

Iron oxide nanoparticles have been synthesized through numerous procedures which is owed to their varied applications in research and industry. However, these techniques can be split into two major categories: Physical production methods and wet chemical synthesis methods (Gunn 2008).

The physical production methods encompasses gas phase production (aerosol preparation, laser pyrolysis and plasma-prepared nanoparticles) and gas phase deposition methods. Although the above gas phase methods allow for fabrication of high quality particles, the yields are usually low and the potential upscale of equipment for industrial manufacture would prove challenging (Gunn 2008;

Teja & Koh 2009). Wet chemical synthesis methods include micro emulsion systems, co-precipitation, sol-gel and solvothermal/hydrothermal synthesis. Liquid phase methods tend to be inexpensive and offer higher product yield, as well as ease of surface treatment. The wet phase systems are also found to be more tunable, offering control over size, shape, surface character, and composition of the particles via the tuning of the nucleation and growth processes (Gunn 2008; Teja & Koh 2009). As high quality particles are sought after in this research, only wet synthesis techniques which offer good control over particle characteristics and the potential for upscale will be explored.

2.4.1) Micro emulsion synthesis

A certain combination of water, oil and surfactants can produce seemingly clear and homogeneous solutions which are commonly known as emulsions. The oil in this case is a simple long chain hydrocarbon and the surfactants are molecules which exhibit a hydrophobic head and lipophilic tail (Cushing et al. 2004). Water in oil emulsions can be thought of as extremely small water containing reactors, hence the water has a large interfacial area and particle flocculation and growth are limited to some extent. The term macro and micro can be used to describe the volume of water dispersed in oil. Micro emulsions have low water volume and are transparent and stable for long periods of time, while macro emulsions have higher water volumes, are opaque, and are only stable when often or continuously stirred (Phillips et al. 2003). The reaction occurs when two water droplets containing reactants collide and mix with one another. The small droplet size, hence reaction environment, leads to a small particle size with a narrow size distribution (Chaudhry 2008).

2.4.2) Co-precipitation synthesis

The co-precipitation method involves the addition of a source of ions in solution (Fe^{2+} or Fe^{3+} for iron oxides) in the presence of a base under an inert atmosphere or at elevated temperatures, allowing the particles to precipitate from solution (Kumar 2009). Therefore co-precipitation refers to the simultaneous occurrence of nucleation, growth, coarsening, and/or agglomeration of particles from solution (Chaudhry 2008). The products obtained through precipitation are relatively insoluble species formed under an environment of high supersaturation. The supersaturated conditions required for precipitation are normally the result of chemical reactions. The above conditions allow for nucleation to be the primary step of the precipitation and for promoting the growth of large numbers of small particles. Secondary processes, which includes Ostwald ripening and agglomeration, will drastically affect the particle size, morphology and properties (Cushing et al. 2004).

2.4.3) Sol-gel synthesis

The sol-gel process is a chemical approach to produce high purity materials in the form of powders, thin film coatings, fibres and bulk structures, with the concept of the process being to turn a homogeneous solution of precursors and reactants into an infinite-molecular-weight oxide polymer through a combination of chemical reactions (Edelstein & Cammarata 1996; Nolan 2010). The sol-gel processing involves the hydrolysis and condensation of alkoxide based precursors (e.g. tetraethyl orthosilicate) and poses several advantages over other synthesis techniques such as high purity, homogeneity, stoichiometric control, ease of adding dopants and the ability to produce thin coatings or porous powders (Chaudhry 2008; Nolan 2010).

For simplicity the sol-gel process can be described through several distinctive steps (Cushing et al. 2004). The first step (1) involves the formation of a stable alkoxide metal precursor (the sol). Secondly (2), gelation occurs resulting in the formation of a gel. This is a result of an oxide or alcohol-bridged network being formed through a polycondensation or polyesterfication reaction which rapidly increases the viscosity of the solution. The third step (3), involves the ageing of the gel, where the polycondensation reaction occurs until the gel transforms into a solid mass which can take up to several days. The fourth (4) and fifth (5) steps include the drying and dehydration respectively. Water and other volatile liquids are removed during drying, and surface bound M-OH groups are removed during the dehydration process, which is done through calcining at temperatures of up to 800°C. The sixth (6) and final step is the densification and decomposition of the gels at temperatures greater than 800°C, allowing the gel network to collapse. However, this step is commonly reserved for dense ceramics or glasses (Cushing et al. 2004).

2.4.4) Solvothermal/Hydrothermal synthesis

In a sealed vessel or container, it is possible to heat up solvents well above their boiling points by an increase in autogenous pressures as a result of heating. When chemical reactions occur under such conditions it is referred to as "solvothermal processing", yet in the case of only water being used as a solvent the term "hydrothermal processing" is used (Cushing et al. 2004). Hydrothermal synthesis has been described by Xu (2006) as the precipitation of inorganic materials in an aqueous solution at temperatures above boiling point and at pressures which exceed the surrounding atmospheric conditions. Unlike the sol-gel and coprecipitation synthesis routes, hydrothermal synthesis requires substantially higher reaction temperatures although its advantage is that the products are usually crystalline and post annealing treatments such as calcination are not required (Cushing et al. 2004). Hydrothermal synthesis has also gained interest by researchers due to it being environmentally

benign as no organics and post treatment is required, making it an appealing synthesis route (Sue et al. 2004). It has therefore been widely investigated for a wide variety of nanomaterials, specifically metal oxides which includes iron oxides such as hematite (Xu 2006). Numerous authors have reported the fabrication of high quality iron oxide particles through batch hydrothermal processing, such as rhombohedral shaped particles being produced by Srivastava et al. (2010) using no template or organic surfactants. Hematite nanorods were reported by Zeng et al. (2007) using no solvents or surfactants, although a 2 hour calcination step was required to transform the akaganeite into its hematite form whilst maintaining its rod-like morphology or structure. Similar findings were reported by Guo et al. (2011), prior to calcination the addition of 3,3 thiodipropionic acid was required for growth control of akaganeite nanorods, thus leading to hematite nanorods.

Traditional batch hydrothermal synthesis is generally carried out in a sealed vessel reactor at temperatures between 373-473K. The solution was slowly heated and allowed to react or age over several hours or days (Arai et al. 2002; Adshciri et al. 2005). In the formation of metal oxides it is believed that two reactions occur; initially the hydrolysis of the metal salt followed by a dehydration step. Hydrothermal synthesis offers good control over size, shape, crystallinity and composition when compared to other common synthesis routes. Despite the disadvantage of slow reaction rates, hydrothermal synthesis is still one of the most extensively used approaches for the fabrication of high quality nanomaterials with controlled particle characteristics (Xu 2006).

Hydrothermal synthesis can however also be carried out in a continuous flow system, which differs from batch synthesis. Recent advances and studies have shown that through using supercritical water as a reactant medium, much higher reaction rates can be achieved with residence times under one minute (Hakuta et al. 2003). This form of synthesis is known as continuous hydrothermal synthesis (CHS) and it is somewhat possible to control particle characteristics through varying and controlling critical process conditions (Xu 2006).

2.4.5) Synthesis route comparison and overview

Table 2.3 below provides a comparison and an overview of the most common synthesis routes for producing high quality, functional nanomaterials with specific particle characteristics.

Table 2. 3- Synthesis process comparison adapted form Xu (2006)

	Sol-gel	Coprecipitation	Hydrothermal
Cost	High	Moderate	Moderate
Composition control	Excellent	Good	Good-Excellent
Morphology control	Moderate	Moderate	Good
Purity (%)	>99.99%	>99.5%	>99.5%
Calcination step	Yes	Yes	No
Milling step	Yes	Yes	No

Teja and Koh (2009) stated that substantial progress has been made in the synthesis techniques used for the preparation of monodisperse nanoparticles, concluding that many offer good control over particle shape, size, size distribution and crystal structure. After reviewing several methods, including emulsion synthesis, sol-gel synthesis and high pressure hydrothermal synthesis, the researchers hypothesised that the continuous hydrothermal synthesis method probably offered the most promise for process control and scalability. The lack of solvents and the high reaction rates make this approach appealing, although its shortcomings are potentially the difficulty in surface treating of particles and plant safety due to the requirement of high pressures (Teja & Koh 2009).

2.5) Continuous hydrothermal synthesis (CHS)

2.5.1) The CHS origin

In recent times, continuous hydrothermal synthesis (CHS) using supercritical water has been recognized as an effective method of producing functional metal oxide particles in an environmentally benign manner when compared with other methods (Shin et al. 2009; Kawasaki et al. 2010). This process has gathered widespread attention and research as worldwide demand for sub-micron metal oxide particles has increased due to their use in applications such as catalysis, electronics and biomedical devices (Xu & Teja 2008).

Despite batch hydrothermal synthesis research dating back to the mid 19th century, the CHS method was developed in the early 1990's by Japanese researchers working in the Arai group at Tohoku university (Suchanek & Riman 2006; Chaudhry 2008). Since then, a handful of research groups around the world have modified and improved the original CHS system and ultimately have expanded on the wide range of materials which can be synthesized through this process (Chaudhry 2008). However, before the CHS system can be reviewed, the basic principles and properties of supercritical water need to be well understood.

2.5.2) Properties of supercritical water

A supercritical fluid can be defined as the state of a compound, mixture or element which is above its critical temperature (T_c) or critical pressure (P_c) but is below the pressure required to condense it into a solid (Jessop & Leitner 1999). Water is the second most commonly used supercritical fluid, only preceded by carbon dioxide. It also has numerous applications, such as in green solvents which can replace volatile organic solvents, as a supercritical anti-solvent which can aid in the re-crystallization of polymers and explosives and in the formation of fine particles from solution (Hakuta et al. 2003; Xu 2006; Fang 2010). As water exceeds its critical temperature and pressure of 374°C and 218 atm, it is said to be in the supercritical domain, as depicted in Figure 2.3 (Cansell et al. 2003). Under these conditions, a supercritical fluid such as water is neither a liquid nor a gas, but can posses properties of both phases (Weng et al. 2011). Therefore supercritical fluids exhibit physicochemical properties such as density, viscosity and diffusivity, which are intermediate between those of liquids and gases and are continuously adjustable through small variations of temperature and pressure (Cansell et al. 2003). Interfaces of supercritical fluids and solid surfaces also lack surface tension (Cushing et al. 2004). Various properties of water under different conditions have been compared in Table 2.4 (Xu 2006).

Table 2. 4- Comparative properties of water under different conditions i.e. at variations of temperature and pressure adapted from Xu (2006)

Fluid		Ambient water	SCW	Superheated steam
Typical conditions	T (°C)	25	450	450
	P (atm)	1	272.1	13.6
Dielectric constant		78	1.8	1
Density (kg/m^{-3})		0.998	0.128	0.00419
Solubility (O_2 solubility mg/l)		8	∝	∝
Viscosity (cp)		0.890	0.0298	2.65 x 10^{-5}
Effective diffusion coefficient, De (cm^2/s)		7.74 x 10^{-6}	7.67 x 10^{-4}	1.79 x 10^{-3}

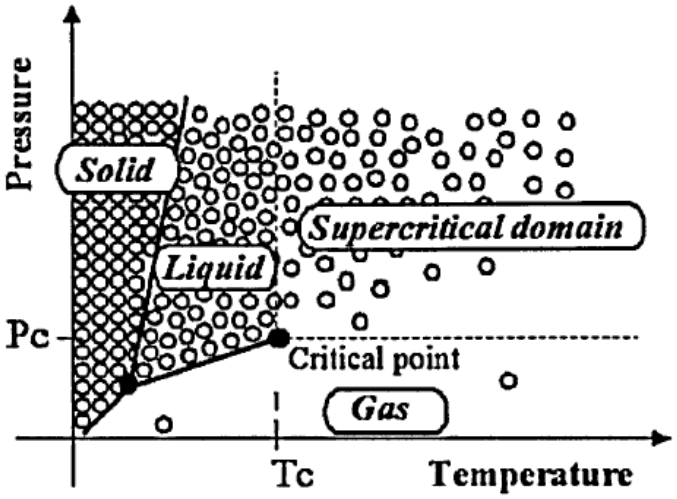

Figure 2. 3 - Schematic representation of microscopic behaviour of a pure fluid in the P-T plane phase diagram illustrated from Cansell et al. (2003)

Water therefore has two degrees of freedom, its temperature and pressure, which can be adjusted to fine tune its physicochemical properties (Marcus 2012). The fundamental properties of supercritical water relating to this study are depicted in Figures 2.4, 2.5 and 2.6.

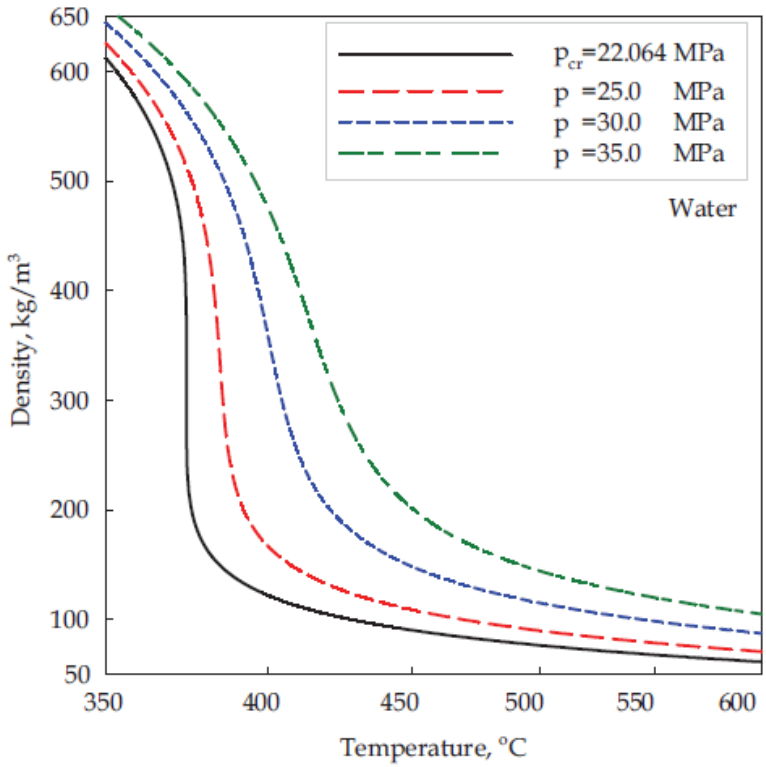

Figure 2. 4 - Properties of supercritical water: Density versus Temperature at different pressures illustrated from Pioro & Mokry (2011)

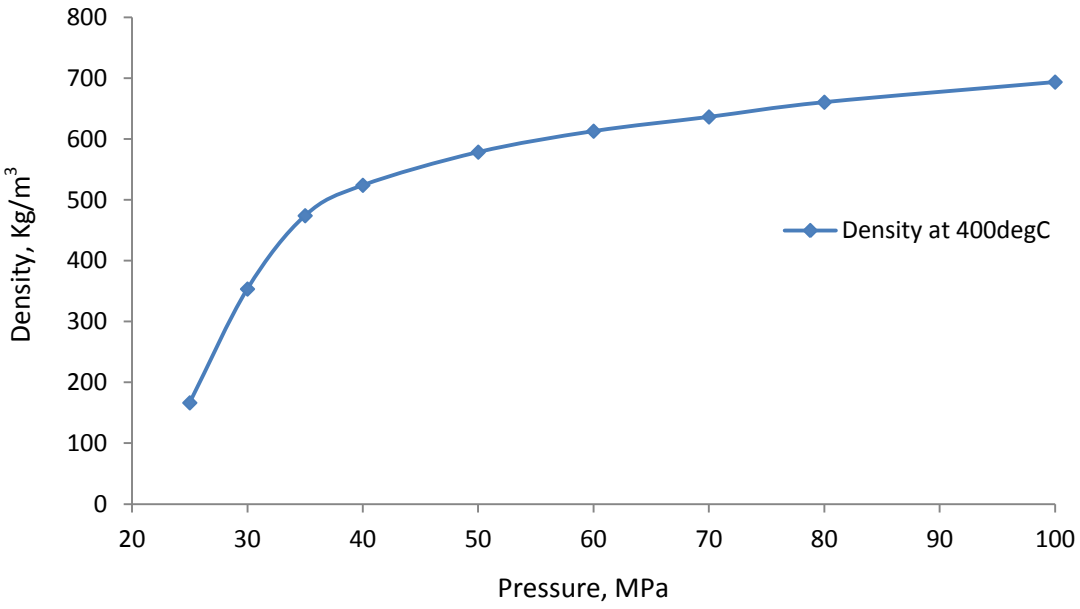

Figure 2. 5 - Properties of supercritical water at 400°C: Density versus Pressure plotted using data from Marcus (2012)

The dielectric constant of water is one of the most important physical parameters which rules the dissolution of organic and inorganic substances in water (Yoshii et al. 2001). The behaviour of the dielectric constant, ε, is responsible for the solvent power and the ionic dissociation of salts (Xu 2006). Water has a high dielectric constant of 78 at 25°C and at ambient pressure, and can dissolve many inorganic salts. The dielectric constant of water decreases along with a decrease in water density, or an increase in temperature at constant pressure. For example, at 440°C and 25-35MPa its dielectric constant ranges between 1.45 - 3.15 (Chaudhry 2008; Morimoto et al. 2012). Water may be a good solvent for organic species, however it is a poor solvent for low dielectric substances such as hydrocarbons (Xu 2006). However as the temperature of water increases the polarity and density decrease, and water starts to take on many properties of organic solvents above 200°C. For example, at 300°C water has similar solvent properties to those of acetone, which can be attributed to a reduction of hydrogen bonding of water at higher temperatures (Lancaster 2002).

At supercritical conditions (as depicted in Figure 2.3), the dielectric constant of water drops drastically as does its ability to dissolve and ionize electrolytes (Xu 2006). Therefore, in supercritical water inorganic salts become insoluble and precipitate out (Chaudhry 2008). In the case of heavy metals, however, hydrated metal ions become hydrolysed and proceed to precipitate as crystalline metal oxides through dehydration at a high temperature. This is the principle mechanism of metal oxide formation by hydrothermal synthesis (Hakuta et al. 2003). Reaction equations for the rapid hydrolysis and dehydration steps were proposed by Lester et al. (2006), where M_c represents the metal cation and L_a represents the anion.

$$\text{Hydrolysis : } M_c L_{a\,x} + xOH^- \rightarrow M_c (OH)_x + x L_a^- \qquad \text{(Equation 2.1)}$$

$$\text{Dehydration: } M_c (OH)x \rightarrow M_c O_{x/2} + 1/2xH_20 \qquad \text{(Equation 2.2)}$$

Thus, the key to the synthesis of nanoparticles at this point is to maximise the degree of supersaturation, which inturn increases the nucleation rate leading to the precipitation of smaller nanoparticles (Chaudhry 2008).

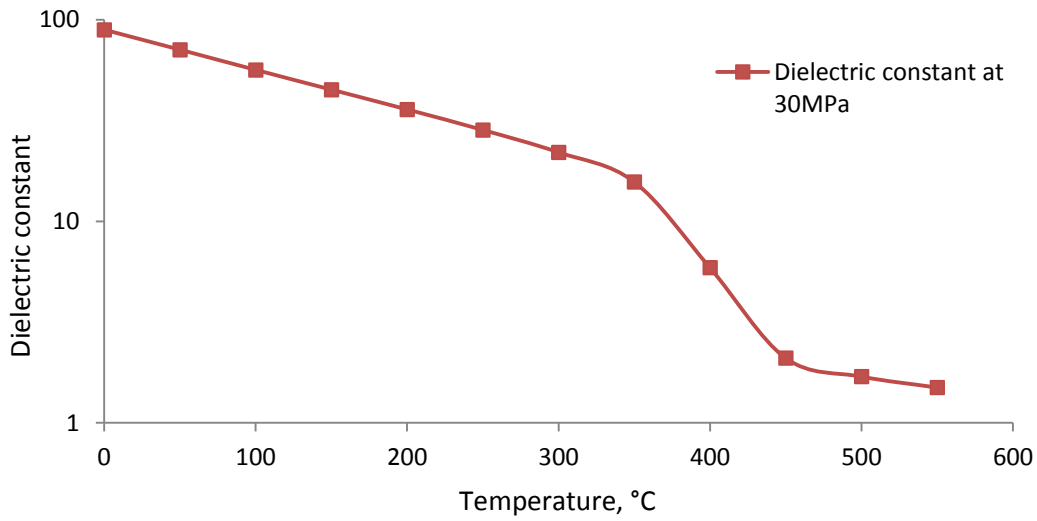

Figure 2. 6 - Dielectric constant of supercritical water at a constant pressure of 30MPa: Effect of temperature adapted from Brunner (2014)

2.5.3) CHS previous designs and engineering considerations

Initial CHS design considerations are mostly dependent on the chemistry and the reaction mechanism of the desired nanomaterial which is to be synthesized. This will determine the number of pumps and feed streams required for a system. For example, Xu (2006) produced iron oxide nanoparticles using ferric nitrate as the only precursor, reacting it with supercritical water. Although more complex nanomaterials, such as the $LiCoO_2$ produced by Shin et al. (2009) required the use of two separate precursor streams, namely a LiOH solution and a $Co(NO_3)_2$ solution. Other complex nanomaterials also required the addition of a strong base, such as sodium hydroxide (NaOH), which was required to produce $CoFeO_4$. When a mixture of iron nitrate and cobalt nitrate were reacted in flow synthesis, only α-Fe_2O_3 precipitated from solution. The base was therefore required to suppress the higher charge trivalent cation (Fe^{3+}) from precipitating at low temperatures before the lower charge divalent cation (Co^{2+}). The strong base was able to shift the equilibrium of both metal cations towards the formation of hydroxides, allowing them to precipitate simultaneously and form $CoFeO_4$ (Cote et al. 2003).

A typical CHS pilot plant consists of two or more high pressure pumps, a water heater, a reactor or crystallizer, a cooling unit and a back pressure regulator followed by a collection vessel as depicted in Figure 2.7.

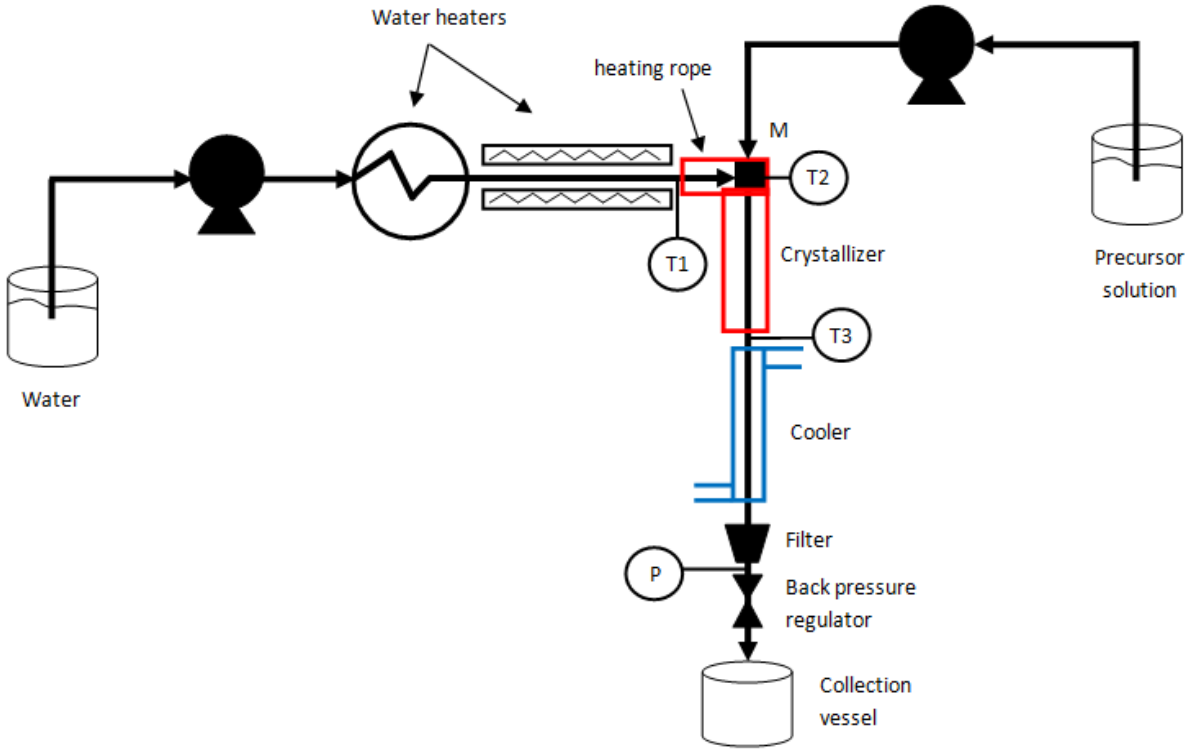

Figure 2. 7 - Schematic diagram of the typical apparatus used in the CHS process adapted from Xu (2006)

The design of water heaters and post reactor cooling systems differ from author to author, although they are generally designed according to the plant parameters such as the required temperature and flow rate range. The method of how the water is heated prior to mixing is far less important than the actual temperature of the water itself, and does not generally effect the particle characteristics. Hakuta et al. (2003) discussed the parameters which directly influence particle characteristics and identified that reaction temperature, pressure, concentration, chemistry of raw materials, type of salt, reactor (mixer) design and the pre-treatment of starting solution had an effect. It is clear from the above list of parameters that the key engineering and design challenge is the reactor (mixer) design, as all other parameters such as temperature and pressure can be controlled or manipulated.

2.5.3.1) Reactor/mixer design considerations

As mentioned earlier, the reactor or mixer is where the supercritical water comes into contact with a metal salt solution, furthermore the metal salts are insoluble in supercritical water and precipitate out in solution in the form of nanocrystals (Chaudhry 2008). It was stated by Sierra-Palleres et al. (2011) that the proper design of mixing devices in the supercritical synthesis of nanoparticles is a key parameter to obtain particles characterized by small size and narrow particle size distributions. The simplest and most commonly used mixer is a T-shaped mixer, and its use has been reported by many

authors (Adschiri et al. 2001; Xu 2006; Kawasaki et al. 2010; Sue et al. 2011). Although the T-shaped mixer has a simple geometry, its orientation allows for three different configurations as displayed in Figure 2.8 and 2.9.

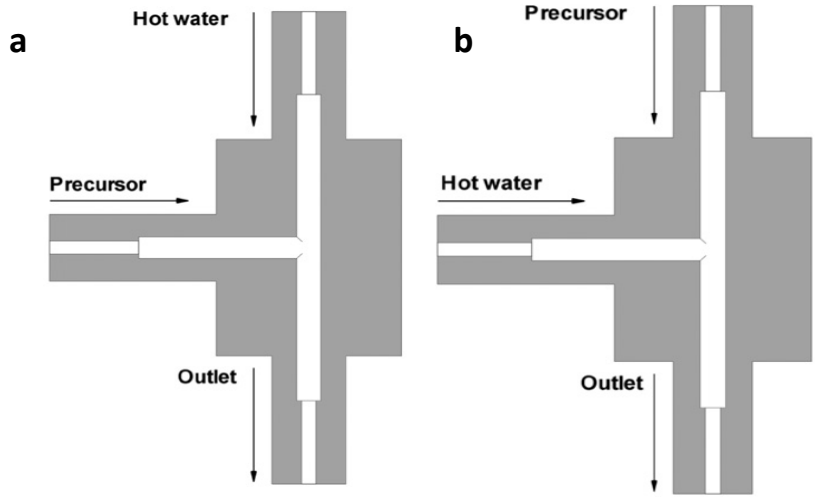

Figure 2. 8 - Vertical orientation of a T-shaped mixer where (a) has the hot water entering from the top and the precursor solution from the side and (b) where the precursor solution enters from the top and the hot water enters from the side - reported by Sierra-Pallares et al. (2011)

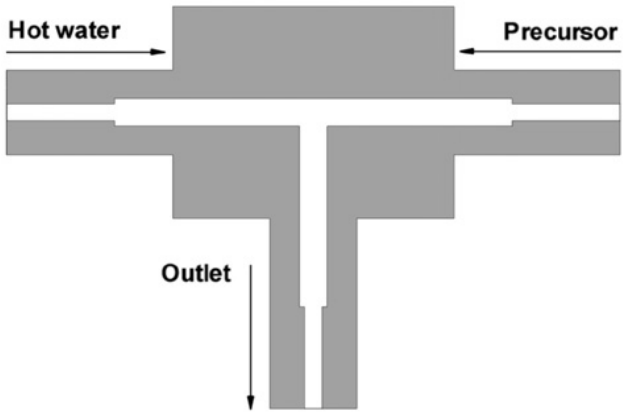

Figure 2. 9 - Horizontal orientation of T-shaped mixer where the hot water enters from the left, the precursor solution enters from the right and the particles in suspension exit through the outlet below - reported by Sierra-Pallares et al. (2011)

The quantification of mixing efficiency on flow direction and orientation of a T-shaped mixer has been investigated by a handful of researchers, using techniques such as light adsorption imaging (LAI) and computational fluid dynamics (CFD) (Blood et al. 2004; Lester et al. 2006; Sierra-Pallares et al.

2011). CFD uses computational software to solve complex calculations and predict flow patterns, whilst the LAI method utilizes a pseudo reactor. Two fluids with a comparable viscosity of those mixed at supercritical conditions are mixed at room temperature, where the 'pseudo' precursor was impregnated with a dye. This technique is therefore based on the adsorption of light through a dyed fluid, which produces an accurate and quantitative concertration map (Blood et al. 2004). Work by Sierra-Pallares et al. (2011) has shown that both techniques are effective for predicting flow patterns during mixing, when they compared the results of their flow modelling with the LAI results published by Blood et al. (2004), which is displayed in Figure 2.10.

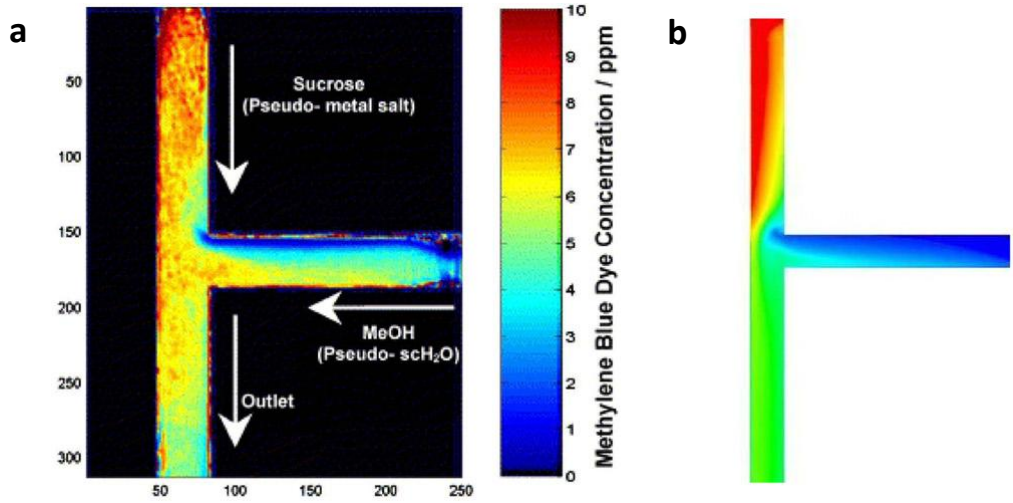

Figure 2. 10 - Comparison of flow patterns in a vertically orientated T-shaped mixer with the pseudo metal salt entering from the top and the pseudo supercritical water entering from the side between (a) LAI predicted mixing pattern reported Blood et al. (2004) and (b) modelling predicted pattern reported by Sierra-Pallares et al. (2011)

Blood et al. (2004) discovered that the mixing patterns in their pseudo reactor were driven by the density gradient of the two fluids. They further identified that the density is linked to the buoyancy forces during mixing, and as buoyancy is a factor the exact positions of the inlet and outlet streams become key parameters in the reactor's design. Similar findings were reported by Lester et al. (2006), who found that the two streams were highly laminar prior to mixing, yet as they converged towards the T-shaped mixer, highly turbulent mixing was clearly observed. As the two fluids interacted in the mixer, the relatively low density of the supercritical water (371 kg m^{-3}) and the higher density of the precursor solution (998 kg m^{-3}) lead to strong natural convection forces. The extent to which buoyancy forces dominate, was calculated through dimensional analysis using the Reynolds (Re) and Grashof (Gr) numbers. The Reynolds number and Grashof number are represented as: (Blood et al. 2004)

$$Re = \frac{\rho V d}{\mu} \quad \text{(Equation 2.3)}$$

Where Re is the Reynolds number (dimensionless); ρ is the fluid density (kg m^{-3}); d is the internal diameter (m); V is the fluid velocity (m s^{-1}); and μ is the dynamic fluid viscosity (kg m^{-1} s^{-1}).

$$Gr = \frac{g \Delta \rho \delta^3}{v^2} \quad \text{(Equation 2.4)}$$

where Gr is the Grashof number (dimensionless); g is the gravitational constant (m s^{-2}); δ is the characteristic dimension (m); and v is the kinematic viscosity (m^2 s^{-1}).

The Reynolds number is a measure of relative importance of dynamic (inertia) forces and viscous (shear) forces. At high Reynolds numbers, the inertial forces dominate and the fluid is said to be turbulent. The point at which the flow transforms from laminar to turbulent flow is known as the critical Reynolds number (Swarup 2009). It was stated by Blood et al. (2004) that the Grashof number is similar to the Reynolds number, except where as the Reynolds number is typically a measure of forced convection, the Grashof number is used for cases of natural convection. They further noted that both values are dimensionless ratios of convection to viscous forces. Therefore, similar to the Reynolds number, a high Grashof number suggests that the natural convection forces will overcome the fluid's viscous forces and induce turbulence (Blood et al. 2004). Another useful number is the Richardson number (Ri), which represents a relationship between the natural convection relative to the forced convection. It is taken as a ratio of the Re and Gr numbers and its value determines what type of convection will dominate the fluids motion. The Richardson number is represented as (Sierra-Pallares et al. 2011):

$$Ri = \frac{Gr}{Re^2} \quad \text{(Equation 2.5)}$$

if Ri > 1, natural convection dominates

if Ri = 1, neither force dominates

if Ri < 1, forced convection dominates

Lester et al. (2006) determined from the large Grashof number calculated that natural convection or buoyancy forces were sufficient to induce turbulent flow, and that they dominated over the inertial forces generated from the pumps ($Gr/Re^2>1$). They concluded that the use of a mixing tee is

inefficient for handling mixing in the CHS, and proposed their new "nozzle mixer" design, which is discussed in greater detail in section 2.6.3.2.

For mixing tees, Sierra-Pallares et al. (2011) stated that the orientation of the mixer is a key parameter in determining the limit at which natural convection dominates. Mixing improves when the two fluids mix in a perpendicular fashion, i.e. at right angles to one another. Although some contradiction occurs, as Sierra-Pallares et al. (2011) reported that mixing improves when the cold precursor solution enters from the side arm perpendicular to the main hot stream (Figure 2.8a). Yet Blood et al. (2004) found that Figure 2.8b was slightly more effective when compared to Figure 2.8a using their unique mixing quantification method. By contrast, both researchers agreed that when both jets are introduced horizontally in an impinging jet configuration (Figure 2.9), mixing is ineffective and extreme fluid partitioning was observed (Blood et al. 2004; Sierra-Pallares et al. 2011). However a study by Kawasaki et al. (2010) revealed that no significant trend in average particle size was observed at different flow directions of straight, bending and counter current streams in T-shaped mixers. In all cases, mixing was enhanced when forced convection was increased (i.e., higher Reynolds numbers), as high local Reynolds numbers results in and promotes faster mixing at all scales (Sierra-Pallares et al. 2011). No systematic study has been reported on the effect of Reynolds number on particle characteristics, although Kawasaki et al. (2010) found that as they reduced the inner diameter of the mixing tee from 1.3 to 0.3mm, which is known to increase the Reynolds number (Equation 2.3), the average size of nickel oxide (NiO) nanoparticles decreased from 47.2 to 26.8nm. However, Sierra-Pallares et al. (2011) also noted that the effect of mixer orientation tends to disappear as forced convection increased, because the effect of gravity is reduced. This can be visualized by CFD modelling performed by Sierra-Pallares et al. (2011) as depicted in Figure 2.11.

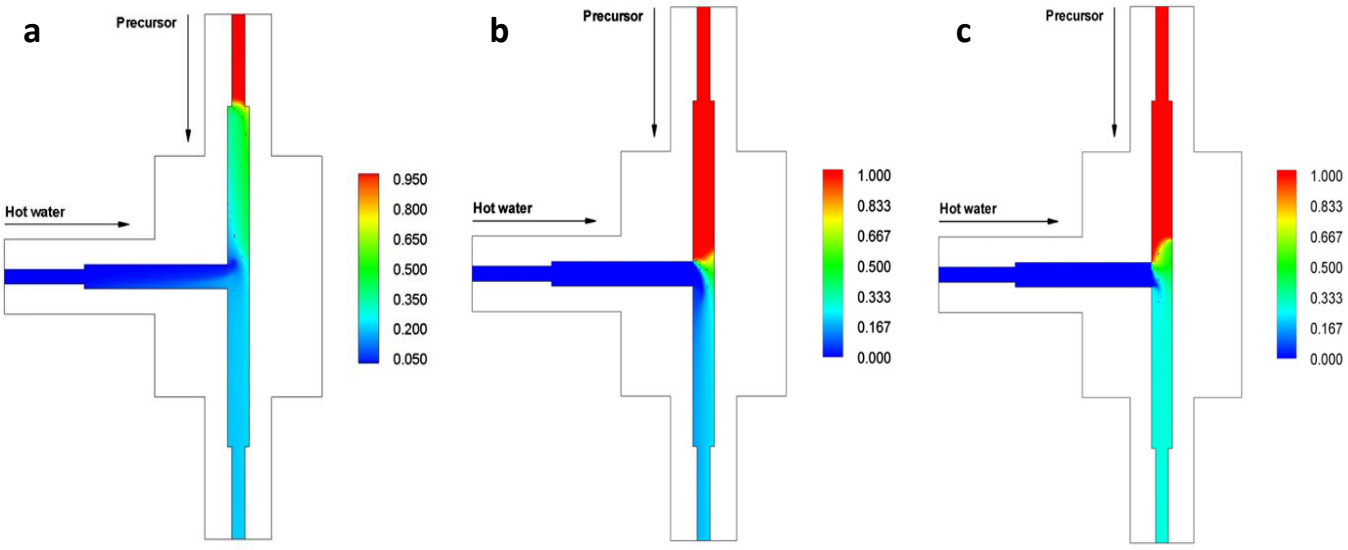

Figure 2. 11 - Comparison of the dominant mixing force on flow patterns for a vertically orientated tee mixer with the supercritical water entering from the side and the precursor solution entering from the top where (a) natural convection dominates (Ri = 80) (b) no dominating force (Ri = 1) (c) Forced convection dominates (Ri = 0.01) reported by Sierra-Pallares et al. (2011)

2.5.3.2) The nozzle reactor

Blood et al. (2004) studied the orientation and flow direction of a tee piece mixer through LAI modelling and concentration mapping, and they identified that this method was also useful at predicting areas which may be prone to particle accumulation leading to a potential blockage. In all the cases studied, it was found that certain undesirable mixing phenomena occurred. They were identified as (Blood et al. 2004):

- *Inlet mixing* - The large difference in density between the two fluids in the system readily induces macro-mixing in one/both of the inlets.
- *Stagnant zones* - With poor net flow, the mixing in these areas may, however, still be strong.
- *Flow partitioning* - When the two flow streams separate into two distinct channels with minimal mixing due to differences in their densities.

Lester et al. (2006) stated that the T-shaped mixer was continuously plagued by unreliability and particle accumulation. They identified that the key to optimal reactor design is to exploit the difference in densities between the two fluids. The CFD and LAI modelling enabled them to define optimal conditions for a mixer/reactor which were identified in Table 2.5 (Lester et al. 2006):

Table 2. 5 - Optimal mixing conditions in a CHS mixer

Optimal mixing conditions	Rationale
Instantaneous strong and uniform mixing of two reactant streams	To aid in the formation of many small metal oxide nuclei which promotes small particle formation
Short average residence time combined with a narrow residence time distribution	To minimise the subsequent particle growth and to promote a narrow particle size distribution
Minimal heating of the aqueous metal salt stream prior to the reactor	Followed by immediate and rapid heating of the salt solution within the reactor, to prevent premature precipitation/ deposition of metal salts in the pipes prior to the reactor
Strong net downstream flow/eddies for the rapid transport of product particles out of the reactor	to prevent particle accumulation within the reactor and to minimise subsequent particle growth.

The above design criteria led to the design of the nozzle reactor by Lester et al. (2006). The nozzle reactor has been patented and is currently in use by the Clean Technology Research Group at the University of Nottingham, as depicted in Figure 2.12.

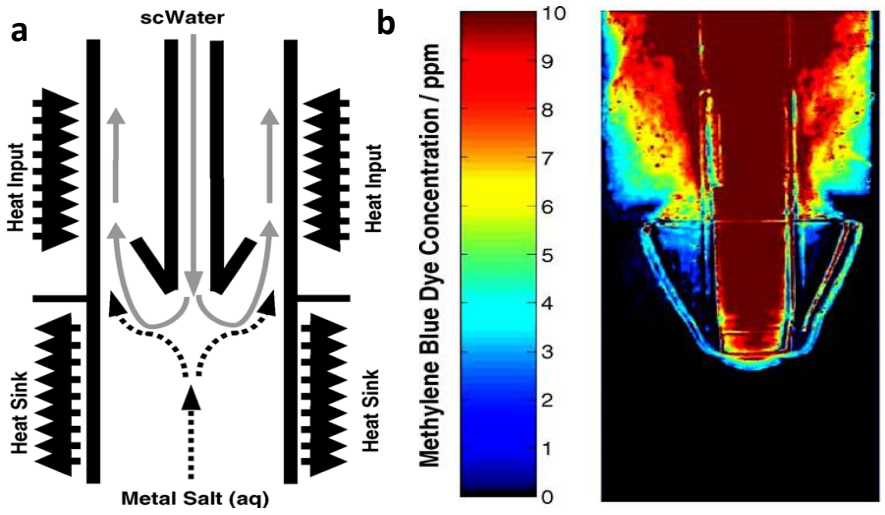

Figure 2. 12 - Nozzle reactor with (a) schematic diagram of ideal heating/cooling profile and (b) LAI modelling and flow pattern of mixing as reported by Lester et al. (2006)

The nozzle reactor has been shown to exploit the density differential between the reactant streams, as where the two fluids meet, mixing is instantaneous and strong. The resulting turbulent mixing eddies are forced downstream to the reactor outlet, which aid in effectively removing the particles from the reactor with a relatively uniform, high net flow rate. It was also found that there were no areas of low net flow (i.e. stagnant zones), which has been identified as the main source of particle

accumulation in tee mixers. Finally, no inlet mixing was observed, therefore the metal salt solution remained cold until it came into contact with the supercritical water (Lester et al. 2006).

An independent review of the counter-current nozzle reactor was conducted by Tighe et al. (2012), who expressed a few concerns. As the supercritical water exited the nozzle, the momentum of the jet was largely influenced by three forces (Figure 2.13): (i) drag force due to the difference in velocity between the downward moving superheated water and the upward moving mixture, (ii) buoyancy due to differences in density and (iii) the net pressure gradient ΔP/dz.

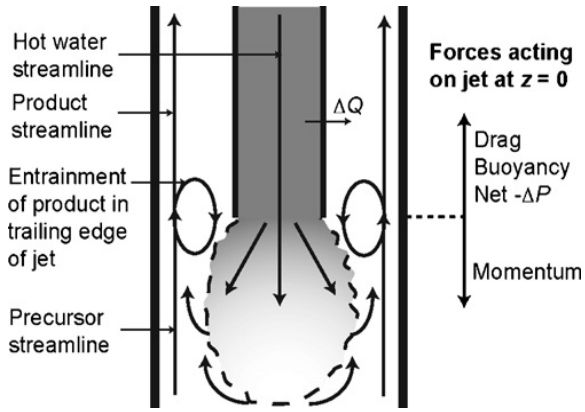

Figure 2. 13 - Representation of the momentum and heat transfer processes and the forces acting on the jet of superheated water at z = 0 in a counter-current nozzle reactor reported by Tighe et al. (2012)

At balanced flow rates of supercritical water to precursor solution (on a mass basis), it was found that the supercritical water did not penetrate far into the opposing precursor stream. However, when the flow was unbalanced (an excess of supercritical water), rapid fluctuations of temperature versus time were measured below the mixing point using in situ thermocouples. This suggests that the water jets or protrudes too far into the precursor stream which is undesired for the controlled synthesis of nanoparticles. Furthermore, they found that the temperature where the supercritical water and precursor solution meet, and where particles begin to form, was significantly lower than that predicted by an overall heat balance on the mixer. This maximum temperature was only achieved at the outlet of the mixer, due to heat transfer from the hot inner pipe to the surrounding slightly cooler mixture of particles in suspension (Tighe et al. 2012). This is troublesome, as it has been well documented that temperature plays a fundamental role in particle growth (Xu 2006). Yet Sierra-Pallares et al. (2011) concluded with their study of different mixer designs, geometries and configurations by stating that further research is needed to study turbulence–chemistry interactions in high pressure fluids, by showing that increasing turbulence can increase mixing efficiency. The

above authors, Tighe et al. (2012), are currently investigating alternative designs, such as a co-current 'confined jet' mixer.

2.6) Growth mechanisms of particles in solution

Zhuang et al. (2009) stressed that understanding the dynamics that affect crystal growth kinetics and the microstructure development in nanocrystals is fundamental to tailor new types of nanostructures and control material properties. Yet Xu (2006), identified that a complete understanding of the CHS process is not available and the mechanisms of particle formation in near- or supercritical water are still currently unknown. In this section, the general growth theory along with classical growths mechanisms for particles grown from solution will be briefly discussed followed by growth kinetics in CHS.

2.6.1) General growth theory

According to Yadong and Alivisatos (2005), nanoparticle growth takes place through several stages. After heating the reactants to the required high temperature, the precursors chemically transformed into monomers, and these monomers inherently formed nanocrystals. Although, the exact monomer addition is still not well understood, owing to the complexity of the crystal growth. The crystal formation involves two steps. Firstly, the nucleation of an initial 'seed', followed by further growth. Secondly, precursors decompose or react at high temperatures to form a supersaturation of monomers followed by nanocrystal nucleation. After which, these nuclei grow further by consuming additional monomers.

According to crystallization thermodynamics, a solid phase will only form out of solution when the molar Gibbs free energy is less than zero (Demopoulos 2009). The molar Gibbs free energy is given by Equation 2.6 (Demopoulos 2009).

$$\Delta G = -RT\ln(\alpha/\alpha_0) < 0 \qquad \text{(Equation 2.6)}$$

where ΔG is the molar Gibbs free energy; R is the universal gas constant; T is the absolute temperature; α is the activity of the solute in the initial solution; and α_0 is the activity of the solute in the final solution (i.e. in equilibrium with the solid phase).

The ratio of $\alpha/\ \alpha_0$ can be defined as the saturation ratio (SR) and in terms of gross simplification, this can be simplified relating activities to concentrations, and expressed as: (Demopoulos 2009)

$$SR = \alpha/\alpha_0 \approx C/C_{eq} \quad \text{(Equation 2.7)}$$

Where C_{eq} represents the equilibrium concentration.

When SR > 1 and ΔG < 0 then the solution is said to be supersaturated. The supersaturation ratio may be defined as (Demopoulos 2009).

$$(C\text{-}C_{eq})/\ C_{eq} = SR-1 \quad \text{(Equation 2.8)}$$

The level or degree of supersaturation is therefore the driving force for crystallization and results in the nucleation, growth and aggregation of particles (Demopoulos 2009). Yet Garside (1985) identified that depending on the nucleation site, three nucleation mechanisms may occur:

i) homogeneous, i.e. primary production of nuclei in the absence of a surface.
ii) heterogeneous, i.e. primary production of nuclei on a foreign surface
iii) surface, i.e. secondary production of nuclei on the surface of a solid of the same kind with the one which precipitates.

After nucleation has occurred, the particles begin to grow in solution. Yadong and Alivisatos (2005) noted that the size and shape of the particles also depends on the rate of crystal growth. At low growth rates, near spherical nanocrystals were formed, which exhibited a broad size distribution. As the growth rate increased, an incredible variety of highly anisotropic shapes were obtained. These began with simple rods and disks, but ultimately led to shapes exhibiting arrow-like and tetrapod orientation. The classical growth kinetics are discussed below.

2.6.2) Ostwald-ripening (OR) kinetics

Ostwald-ripening kinetics involve the growth of larger particles at the expense of smaller ones, where the driving force was a decrease in Gibbs free energy (Zhang et al. 2010). Hematite (α-Fe_2O_3) crystals were suggested by Liang et al. (2010) to grow in sub-critical water via dissolution and precipitation processes, as supercritical water has a rather low solvent power that suppressed crystal growth. Although, Gilbert et al. (2003) further identified that this dissolution–precipitation based mechanism for particle growth in solution is Ostwald-ripening. The kinetics of Ostwald-ripening crystal growth may be described by a power law function (Borg & Dienes 1992).

$$D(t) = D_0 + K_{OR}\, t^{1/n} \qquad \text{(Equation 2.9)}$$

where D_0 is defined as particle size, D(t) is the size at time t, K_{OR} is a rate constant for the limiting step, and the exponent, n, is determined by the nature of the rate limiting step. The rate of the growth may be controlled by diffusion in solution (n ≈ 1), diffusion at the particle surface (n ≈ 2), or the interface dissolution/precipitation step (n ≈ 3).

Furthermore, diffusion-based growth can occur without a solvent matrix, given particle contact, by atomic diffusion from smaller particles to bigger ones (Gilbert et al. 2003). A schematic representation of the OR kinetics was presented by Zhang et al. (2010) in Figure 2.14.

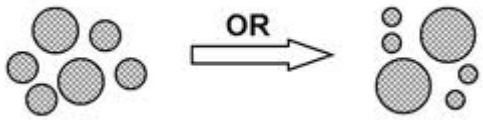

Figure 2. 14 - Schematic diagram of particle growth through OR kinetics adapted from Zhang et al. (2010)

2.6.3) Oriented attachment (OA) kinetics

It was specified by Gilbert et al. (2003), that when looking at systems containing nanoparticles, in addition to the OR kinetics, the particles themselves may act as "building blocks" for crystal growth. An oriented pair of particles may come into contact and attach to one another, thus eliminating the attaching free surfaces and releasing the surface energies associated with the free surfaces (Gilbert et al. 2003). This new mechanism for growth has been termed oriented attachment (OA). Imperfect OA growth can produce defects in the crystal structure leading to edge dislocations, stacking faults and twins are often marked by original boundaries between component nanocrystals growing via the OA pathway (Gilbert et al. 2003). Evidence of the OA growth mechanism may come from close inspection of the crystal structure, and may exhibit a distinct deviation from the classic OR growth kinetics. The OA kinetics do not follow OR kinetics, and can be expressed as follows (Gilbert et al. 2003):

$$D(t) = D_0\,(\sqrt[3]{2}\,kt + 1)/(Kt + 1) \qquad \text{(Equation 2.10)}$$

Where D is particle diameter, D_o is initial particle diameter, K_{OA} is the growth rate constant dependent on temperature, and t is the time. A schematic representation of the OA kinetics was presented by Zhang et al. (2010) as depicted in Figure 2.15.

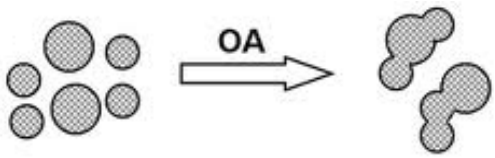

Figure 2. 15 - Schematic diagram of particle growth through OA kinetics adapted from Zhang et al. (2010)

2.6.4) Growth kinetics in CHS

A study was conducted by Chen et al. (2011) on precipitation kinetics in CHS. The authors mentioned that it is well believed that in CHS particles precipitate through a reaction crystallization process. This involved solution mixing, chemical reaction and crystallization processes, such as supersaturation generation, nucleation and crystal growth.

Inside the reactor, metal oxide particles form rapidly into suspension after metal salt precursor solutions are met with supercritical water. At the high reaction temperatures, the metal salt solubility is greatly reduced and the degree of solution supersaturation becomes the driving force for particle growth. This rapid nucleation leads to the formation of numerous nuclei, followed by these nuclei to go through a phase of growth and coalescence and result in the formation of fine particles and aggregates (Chen et al. 2011). A schematic representation of the growth kinetics can be seen in Figure 2.16.

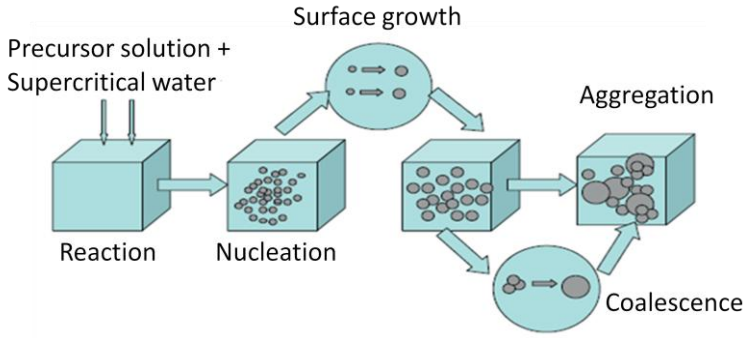

Figure 2. 16 - Schematic representation of growth kinetics in CHS illustrated in Chen et al. (2011)

As mentioned above in section 2.6.2, Liang et al. (2010) suggested that hematite particles grew in sub-critical water via dissolution and precipitation processes because supercritical water had a rather low solvent power which suppressed crystal growth. Gilbert et al. (2003) identified that this particle growth mechanism in solution was Ostwald-ripening. However, Xu (2006) identified that a complete understanding of the CHS process is not available and the mechanisms of particle formation in near or supercritical water are still currently unknown.

2.7) Effect of operating parameters on nanoparticle characteristics in CHS

A fundamental aspect of nanotechnology research is the development of reliable synthesis protocols for nano structured materials over a range of chemical compositions, shapes and sizes (Mandal & Muller 2008). As the physical and chemical properties of nanoscale materials are strongly dependent on their size, size distribution, structures and dimensions, it is essential to maintain control over particle characteristics (Zhu et al. 2011). It has been well documented throughout the literature that several operating parameters directly influence particle characteristics of nanomaterials synthesized via the CHS route. This includes reaction temperature, pressure, concentration, chemistry of raw materials, type of salt and pre-treatment of the starting solution, including pre-mixing, pre-heating and pre-aging (Hakuta et al. 2003; Xu 2006). Although high quality particles with a narrow size distribution have been produced via the CHS method, Xu (2006) stressed that the effects of operating parameters are not well understood, often citing conflicting reports in the literature. Hence this section will serve as an overview of the present knowledge basis, and highlight the effects of various operating parameters in CHS reported by numerous authors.

2.7.1) Effect of precursor concentration

Particle size and shape are highly dependent on the applied reactant concentrations (Li et al. 2011). It was reported by authors Li et al. (2011), that by altering the ratio of reactants ($NaOH/Zn(Ac)_2$) between 10 and 20 and by altering the $Zn(Ac)_2$ concentration (between 0.02M and 0.1M), it resulted in particles of varying morphology including flower-like and star-like particles being formed. The effects of high and low reactant concentrations were investigated by Hayashi et al. (2010) on the growth of $BaTiO_3$ particles. They identified that an increase in reactant concentration lead to a decrease in particle size along with a narrower size distribution. $CoFeO_4$ was synthesized by Cote et al. (2003) in the presence of NaOH as a strong base and found that reactant concentrations appeared to have little effect on particle size, size distribution or morphology.

Iron oxides have been successfully synthesized from an iron nitrate precursor salt. Especially, an oxi-hydroxide was prepared at a low reactive concentration whereas a mixture of two crystalline phases (α-Fe_2O_3 and γ-Fe_2O_3) was obtained with a high concentration of the reactive solution (Aimable et al. 2009). It was reported by Kawai-Nakamura et al. (2008) that as they increased the concentration of $Fe(NO_3)_3$ precursor salt from 0.01 to 0.05 mol/kg, the size of the Fe_2O_3 nanoparticles increased slightly from 3.4 to 4.9 nm. The overall conversion also dropped from 99% to 97%, which was attributed to the slight decrease in supersaturation, with degrees of supersaturation calculated at 10.5 and 9.4 for concentrations of 0.01 to 0.05 mol/kg respectively.

Xu (2006) performed solubility modelling using OLI software in order identify the solubility of ions in solution for a ferric nitrate solution, and looked at the effect of concentration on the solubility of such ions under reaction conditions. Out of numerous soluble ions, $Fe(OH)_2^+$; Fe^{3+}; Fe^{2+} and $Fe(OH)^{2+}$ were deemed the most significant at the reaction conditions of 300°C and 240atm.

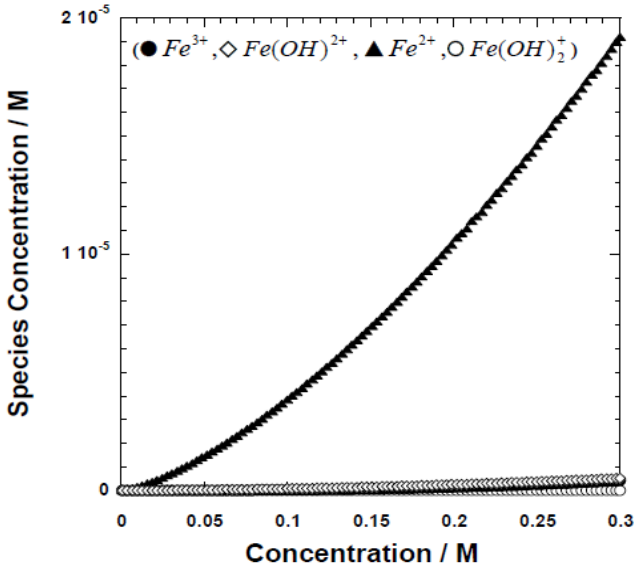

Figure 2. 17 - Effect of concentration on the solubility of individual species concentration in solution

Figure 2.17 shows that the most soluble ion in solution is Fe^{2+}, yet the Fe^{3+} ion, which is responsible for the formation of α-Fe_2O_3 (Hematite) also increased slightly as the concentration increased. This revealed that the level of supersaturation in CHS increases with increasing precursor concentration, although not as much as expected due to the accompanying increase in solubility.

Xu and Teja (2008) varied the concentration of ferric nitrate precursor between 0.03 and 0.06M, whilst keeping all other parameters constant. They found that the particle size increased from 15.6nm to 27.4nm, yet more interestingly, the particle morphology tended to change from spherical to rhombic.

2.7.2) Effect of temperature

A study performed by Aimable et al. (2008) on the significant parameters which effected the characteristics of $BaZrO_3$ particles, revealed that of the parameters studied (temperature, pressure, concentration and residence time), temperature had the greatest significance (>99%). It was found that higher temperatures lead to smaller particles sizes, with an average size of 129nm at 500°C compared to 174nm at 400°C. On the contrary, Shin et al. (2009) found that the average particle sizes

of Co_3O_4 synthesized at subcritical temperatures increased with increasing temperature, although, the particle sizes of the HT-$LiCoO_2$ obtained at supercritical temperatures did not seem to have a strong relation to reaction temperature. In further contradiction, Cote et al. (2003) found that temperature had little effect on particle size of $CoFeO_4$ particles in the temperature range studied. Temperature was also found to have negligible effect above supercritical conditions on the particle size distribution of TiO_2 nanoparticles synthesized by Chen et al. (2011), who proposed that this was due to rapid nucleation and short residence times.

Xu and Teja (2008) found that increasing the reaction temperature from 483K to 573K resulted in a size increase of hematite nanoparticles from 7.7nm to 10.1nm. Yet the particle size remained relatively constant as the reaction temperature exceeded 573K. The effect of temperature on the characteristics of hematite nanoparticles was studied by Liang et al. (2010), who found that at 200°C the powder obtained was amorphous. While the crystalline phase was obtained at 250°C, crystallinity was found to increased with increasing temperature. The particle size was also found to double in size when the reaction temperature was increased from 250°C to 350°C (20 - 40nm), while as the reaction temperature exceeded 350°C the particle size began to decrease in size. The trend of increasing particle size from 250°C to 350°C was explained by an increase in monomer concentration in the reactor. Nucleation occurred as the monomer concentration reached the saturation point. As a result, the crystal size tended to increase as the reaction temperature was raised from 250°C to 350°C (below the critical temperature), and the solubility of the hematite particles gradually decreased until it reached an extremely low level at the critical temperature. Yet the trend of a decrease in particle size as the temperature exceeded critical conditions (380°C and 420°C), was assumed to be related to the low solvent power of supercritical water and the high hydrolysis rate of ferric nitrate in supercritical water (Liang et al. 2010).

2.7.3) Effect of pressure

The effect of pressure on particle characteristics was evaluated by Noguchi et al. (2008) in increments between 25 and 35MPa. It was shown, interestingly, that the pressure had an influence on the selectivity of the products formed. γ-Al_2O_3 was formed between 25 - 30MPa, and mixed phases of γ-Al2O3 and γ-AlOOH were obtained at 32.5 and 35MPa. This was due to the changes in density of supercritical water that changed from 126 kg/m3 to 291kg/m3 over the pressure range of 25MPa to 35 MPa. No apparent trend was identified with the effect of pressure on particle size, it was found that the smallest particles were obtained at 25MPa which tended to increase linearly with increasing pressure, although the largest particles were formed at 30MPa. Another author, Xu (2006)

argued that the solvent properties of water do not change significantly with small changes in pressure in order to justify maintaining their system pressure between 24-25MPa.

2.7.4) Effect of residence time

It has been highlighted by Cote et al. (2003) that the residence time in CHS is closely related to other process variables, one such being temperature, which alters the density of the reactants and inturn affects the total residence time in the reactor. A study performed by Kawasaki et al. (2009) on the continuous hydrothermal synthesis of TiO_2 nanoparticles, found that the residence time could be altered at a constant reactor length by changing the reaction temperature. By increasing the temperature along the reactor from 400°C to 450°C and then 500°C, they adjusted the residence time to 1.7s, 0.7s and 0.6s respectively. The same concept was also used for a longer reactor (4.6m) which led to a maximum residence time of 5.5 seconds. It was determined that the residence time was reduced proportionately to the increased reactor temperature, therefore the size of the particles remained unchanged. On the contrary, Matsiu et al. (2008) found that extremely short residence times (7 milliseconds) allowed them to produce $BaTiO_3$ particles under 10nm using the CHS method. As the residence time increased to 2 seconds, the particles size increased, therefore the 7 milliseconds residence time stopped the reaction and prevented further growth, resulting in smaller particles being precipitated from solution.

A study by Sue et al. (2011) on three various metal oxide nanoparticles via CHS (CuO, NiO and α-Fe_2O_3) revealed that the hematite particles were least affected by changes in residence time. The residence time was varied between 0.002 and 2 seconds, and it was found that the conversion at 0.002 seconds was still greater than 95%, and only increased slightly with increasing residence time. Yet X-ray diffraction analysis (XRD) revealed that the α-Fe_2O_3 peak intensity increased greatly with an increase in residence time. The increase in residence time was also found to slightly increase particle size distribution with standard deviation increasing from 1.0 to 2.1nm, as well as average particle sizes increasing from 4.0 to 6.7nm at 0.002 and 2 seconds respectively. Similar findings were observed by Xu and Teja (2008), when they increased residence times from 2.6 to 5.2 to 10.4 seconds, the sizes of the hematite nanoparticles increased from 15.6 to 20.6 to 22.2 nm respectively. They also remarked on the XRD peak intensification with an increase in residence time, concluding that crystallinity increases with an increase in residence time. The residence time was reported to have a small effect on particle morphology, as rhombic particles were present at high concentrations and residence times (Xu & Teja 2008).

2.7.5) Effect of pH

Very few studies have discussed the effects of pH in CHS, although Kawasaki et al. (2009) reported that single crystal particles were formed under low pH conditions, while polycrystalline crystals were formed under high pH. This was attributed to the increased solubility at higher pH conditions, and hence lower degree of supersaturation. At lower supersaturation levels, nucleation was not homogenous when compared to that of lower pH conditions, and therefore the polycrystalline particles formed by secondary nucleation on the surfaces of the primary nucleation particles. Hayashi et al. (2010) also studied the effect of pH on the growth of $BaTiO_3$ nanoparticles, where they found that a pH greater than 11 lead to an increase in particle size from 6 to 14nm. The increased crystal growth rate was linked to an increase in $Ti(OH)_5^-$ solubility at a pH greater than 11, and stated that the growth of hydrothermal $BaTiO_3$ is generally enhanced in a strongly alkaline solution. It was reported by Noguchi et al. (2008) that a decrease in pH from 2 to 0.5 decreased the particle size of γ-Al_2O_3 particles, however, the drop in pH corresponded with an increase in precursor concentration ($Al(NO_3)_3{\cdot}9H_2O$). Therefore it was unclear whether the decrease in particle size was linked to the increase in precursor concentration or the pH itself.

2.7.6) Effect of precursor salt

An early study on the effect of precursor salt was conducted by Adschiri et al. (1992) who used ten different precursor salts, with four of them being salts containing iron. The iron containing salts were namely ferric nitrate ($Fe(NO_3)_3$), ferric sulphate ($Fe(SO_4)_3$), ferrous chloride ($FeCl_2$) and ferrous ammonium citrate ($Fe(NH_4)_2H(C_6H_5O_7)_2$). The results showed that the ferric nitrate, ferric sulphate and ferrous chloride all produced spherical hematite particles with an average particle size of approximately 50nm. While the ferrous ammonium nitrate yielded a different product, spherical magnetite (Fe_3O_4), which also had an average particle size of approximately 50nm. The formation of magnetite was linked to the reduction of Fe^{3+} to Fe^{2+}, with the reducing environment created by the formation of carbon monoxide which was formed in the thermal decomposition of ammonium citrate (Adschiri et al. 2000).

2.8) One dimensional nanoparticles and morphology control

Structures such as nanocubes, nanorods/wires, nanotubes, nanoflakes, urchin-like, flower-like, nanopropellers and nanodisks has been reported by various research groups (Liu et al. 2006; Yang et al. 2006; Mandal & Muller 2008; Jiang et al. 2010; Zhu et al. 2011). Non-spherical nanoparticles have also become attractive due to their anisotropic behavior (Jiang et al. 2010). Nanowires, nanotubes, and nanorods represent a class of one dimensional (1D) nano structured materials, in which carrier motion is restricted in two directions so that they are expected essentially to improve

photochemical, photophysical, and electron-transport properties (Zhu et al. 2011). Therefore essentially, one dimensional nanomaterials can be defined as particles where the dimensions of their cross section is in the nanometer range, whilst their length may range up to a few micrometers, such as nanorods/wires (Schubert & Husing 2012). Nanorods and nanowires only differ by their aspect ratio (the ratio of width to length), that is between 5 and 25, whilst particles are deemed as nanowires if their aspect ratio exceeds 25. Examples of different uniquely shaped nanomaterials have been displayed in Figure 2.18, with only A,B and F falling under one dimensional.

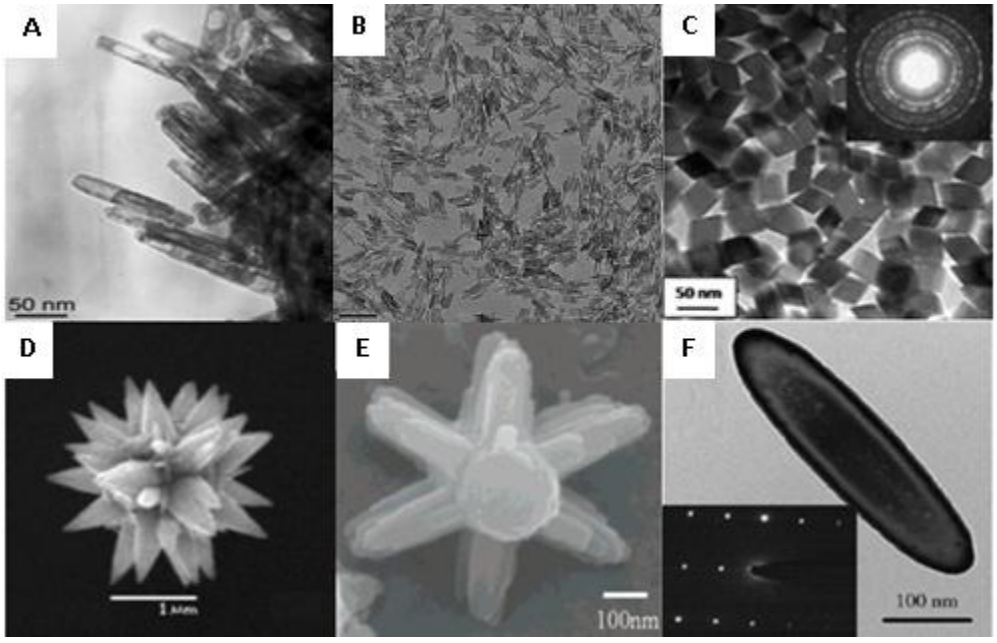

Figure 2. 18 - Examples of non-spherical particles reported in the literature, such as (A) nanotubes reported by Liu et al. (2006); (B) nanorods reported by Chowdhury et al. (2014); (C) nanocubes reported by Jiang et al. (2010); (D) flower shaped particles reported by Li et al. (2011); (E) nanopropellars reported by Yang et al. (2006) and (F) Shuttle-like particles produced by Zhu et al. (2011)

2.8.1) Conventional morphology control of nanoparticles in batch processes

In the past few years, great progress has been made in the chemical growth of uniform α-Fe_2O_3 nanocrystals with a variety of specific shapes and morphologies using batch synthesis techniques (Chen et al. 2010). Aimable et al. (2010) noted that the range of particle shapes can be extended by using surfactants, polymer additives or different water/solvent mixtures. The growth of iron oxide nano ribbons were described by Wei & Nan (2011), using sodium dodecyl sulfate (SDS), an anionic surfactant. He et al. (2005) reported on the synthesis of zinc oxide nanowires in the presence of polyvinyl alcohol. While hexagonal hematite nanoplates were prepared by Chen and co-authors (2010) in the presence of different alcohols.

2.8.2) The use of and effect of surface modifiers for morphology control in CHS

The literature regarding morphology control of particles in continuous synthesis techniques is almost non-existent, with few authors claiming the fabrication of non spherical particles or even utilizing polymers, surfactants or organic alcohols for morphology control. However, it is extremely difficult to predict the morphology of particles, as this is influenced by a large number of parameters which includes properties of the crystalline solid, properties of the solution, and operating conditions (Mersmann 1995). Li et al. (2011) postulated that different solvent mixtures may affect the particle shape in continuous systems. They studied the effects of the addition of different solvents on the particle morphology of ZnO particles in continuous synthesis. The list of solvent/water mixtures included the addition of polyacrylamide, triethanolamine, dimethyl sulfoxide, and a 1:1 water/isopropanol mixture. The resulting particle morphology was either spherical or cylinder-like, which differed greatly from the star or flower shaped particles fabricated in pure water systems. Thus proving that the addition of solvents may alter the particle morphology, although it is clear that more research is required for a better understanding of the mechanisms causing the change in morphology.

Polymer/surfactant additives in CHS have shown little effect on particle morphology. A study by Hayashi et al. (2010) studied the effect of several chemical modifiers on the continuous production of $BaTiO_3$ fine particles. The list of modifiers included n-hexylamine, n-octylamine, methoxyethanol (ethyleneglycol monomethylether), ethylenedia- mine, acetylacetone), polyvinyl pyrolidone, polyoxyethylene (20) sorbitan monooleate (Tween 80) and poly acrylic acid. The surface modifiers were injected into the reactor after the mixer, yet prior to cooling, and surface modification was deemed ineffective. Thus, the authors concluded that the presence of surface modifiers does not affect the nucleation and crystal growth of BaTiO3 particles. Although the surface modifiers had little effect on the particle surface or morphology, Hayashi et al. (2010) did report on the reduction of their particle size distribution. Similar findings were observed by Xu and Teja (2008), who used polyvinyl alcohol (PVA) as a growth inhibitor for α-Fe_2O_3 nanoparticles. They hypothesised, that the Fe^{3+} ions became sterically entrapped in an entangled polymer chain network, which is supported by a lack of colour change over time, as the Fe^{3+} ions are normally oxidised by ambient surrounding oxygen over time. When these polymer chains come into contact with supercritical water, very small α-Fe_2O_3 particles are formed inside the network limiting particle growth. Nano sized particles also tend to aggregate due to their high surface energy, and this can be counteracted by creating repulsive forces between particles using either electrostatic or steric interactions (Xu 2006).

Therefore the PVA acts as a polymer barrier, hindering particle aggregation and resulting in a narrow PSD (Xu & Teja 2008).

2.8.3) Critical process parameters for growth control in CHS

Numerous authors have reported the synthesis of non spherical particles in CHS, without the addition of surface modifiers. Although different metal oxides tend to naturally take on different crystal habits or morphology (i.e. hematite particles are commonly spherical or rhombohedral, whilst akaganeite tends to form spinel-like rods), it is the change in and control of morphology with a change in process parameters that is of particular interest in this study. For example, Chaudhry (2008) synthesized hydroxyapatite ($Ca_{10}(PO_4)_6(OH)_2$) nanorods using a CHS flow system, however as hydroxyapatite tends to naturally take on a hexagonal structure no change in morphology was attained. Therefore rod-like particles were expected.

By examining previous studies, it may be possible to identify the critical process parameters which are more influential on the resulting particle morphology. Adschiri et al. (1992) conducted a study on the effect of operating parameters on Boehmite (AlOOH) particles, and discovered that the particle morphology was highly dependent on the operating parameters. While operating in the temperature range of 523-763 K, pressure range of 25-40 MPa, and $Al(NO_3)_3$ concentration range of 0.0059-0.05 mol/L, rhombic particles were obtained at low temperatures and low concentrations, while hexagonal crystals were found at high temperatures or concentrations. As the temperature was increased to 523K, the particle shapes became football-like with some plate-like particles being present. As the critical temperature was exceeded, needle-like particles were observed. These findings were in agreement with later work performed by Hakuta et al. (2005), who also found that the particle morphology varied with feed concentration, with reports of rhombic and hexagonal γ-AlO(OH) plates being formed. As shown in section 2.5.4.1, Li et al. (2011) showed that by altering the ratio of their reactants NaOH/$Zn(Ac)_2$ between 10 and 20 and altering the $Zn(Ac)_2$ concentration (0.02M and 0.1M), it resulted in particles of varying morphology including flower-like and star-like particles being formed. Another study by Sue et al. (2004) found that the order of preheating and mixing is very important and may lead to different morphologies. Without the use of organics, they were able to grow spherical or rod-like ZnO particles by changing the order of mixing. Preheated water and the $Zn(NO_3)_2$ precursor were initially mixed, followed immediately by the introduction of a KOH solution, resulting in rod-like particles. However, when the preheated water and KOH solution were mixed prior to mixing with the $Zn(NO_3)_2$ precursor, spherical particles were obtained. The authors hypothesised that as the KOH solution was introduced, supersaturation increased rapidly,

allowing the rest of the precursor in solution to precipitate out onto the already formed particles resulting in a rod-like morphology via a secondary growth mechanism.

From the literature examined, the only mention of a change in iron oxide particle morphology in CHS has been reported by Xu (2006). He identified that temperature had no effect on the particle shape of hematite nanoparticles. Unlike the effect of precursor concentration and to some extent residence time, where increasing concentration led to increasing amounts of rhombic shaped particles in contrast to the spheres being reported at lower concentrations. This morphology change was more pronounced at higher residence times. Therefore it is apparent from the literature that the concentration may be a critical process parameter for changing particle growth kinetics. However, as the current evaluation of operating parameters through isolation has yielded little promise for particle characteristic and growth control, a more thorough approach may be necessary. One such approach is the evaluation of operating parameters through a factorial trial analysis, which uses a statistical method for evaluating a set of parameters as a whole, and can identify possible correlations and interactions between parameters. Identifying and analysing possible parameter interactions may also be a further step in aiding particle characteristic control.

2.9) Factorial designs

A factorial design is a screening experiment, with a simple strategy. Factors are selected and investigated by running experiments for all the possible combinations of the chosen factors. For example if there are 3 factors, at two levels, the number of combinations are 2^3, hence 8 experiments in total (Joglekar 2010). Most factorial experiments are conducted using two-levels, as they are easy to design, efficient to run, relatively simple to analyze and full of information (Mee 2009). Although many useful experiments can be conducted by evaluating single parameters, often research questions are more complicated. An example was given by Mee (2009) who stated, rather than asking "How does temperature affect strength?" we are more interested in understanding how a host of parameters jointly affect the output.

The main advantage of factorial trials is that it is revealed whether or not the effect of each factor is dependent on the levels of the other factors of the experiment. The is an advantage of multifactor experiments, as the interactions between parameters are not shown when a single parameter is isolated and evaluated (Mee 2009). It is well known that not all interactions will produce similar effects, with some effects being larger than others. A principle known as the Pareto principle is often applied, "the law of the vital few and the trivial many." It is the purpose of screening experiments

and is used to identify the vital few significant effects (Joglekar 2010). The significance of these interactions can also be categorized into statistical or practical interactions. Statistical significance is determined by prediction probability and practical significance is dependent if the interaction is large enough to be of practical utility. Most critical interactions are of statistical and practical significance (Joglekar 2010).

2.9.1) Three-level factorial designs

Three-level factorial designs are simple extensions of their 2-level counterparts, except the factors are varied at 3 levels instead of 2. The geometry of a 3-level, 3 factor design takes on a cube-like structure as depicted in Figure 2.19 resulting in 27 experiments (Eriksson et al. 2008). The pitfall of a 3-level factorial is the exponential growth of experiments as the factors increase, with 4 factors requiring (3^4) 81 experiments and a 5 factor resulting in (3^5) 243 experiments. Due to the increasing number of experiments by the addition of factors, 3-level factorials benefit greatly from replicated centre points (Eriksson et al. 2008).

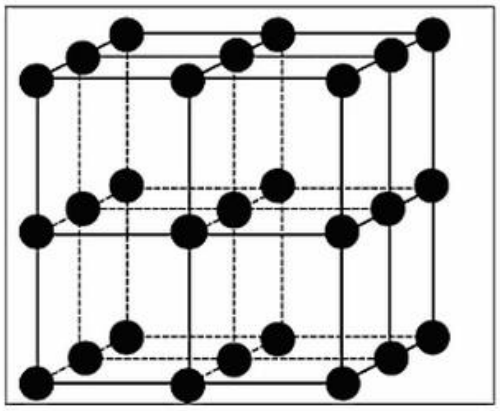

Figure 2. 19 - Cube-like structure of a 3-level, 3 factor full factorial trial as depicted by Eriksson et al. (2008)

2.9.2) Box-Behnken factorial design

Box-Behnken factorial designs use 3-levels, namely -1, 0 and +1, and these designs are either rotatable or "near rotatable" (Vining & Kowalski 2011). They are constructed by first combining two-level factorial designs with incomplete block designs, followed by the addition of a specific number of replicated central points (Anderson & Whitcomb 2005). The Box-Behnken design is very economical in terms of experimental runs and often requires less runs when compared with similar factorial designs, such as central composite designs (Lawson 2010). As shown in Figure 2.20, the experiments are located at the mid-point of each edge of the cube. The red dot in the centre of Figure 2.20 represents an optional number of centre-points. A two-factor Box-Behnken factorial trial does not exist, and hence the most commonly used are the 3 and 4 factor designs (Eriksson et al. 2008). Box-

Behnken designs allow for the estimation of a general quadratic model and are also useful when experimental conditions at the corners are undesirable or impossible (Lawson 2010; Eriksson et al. 2008).

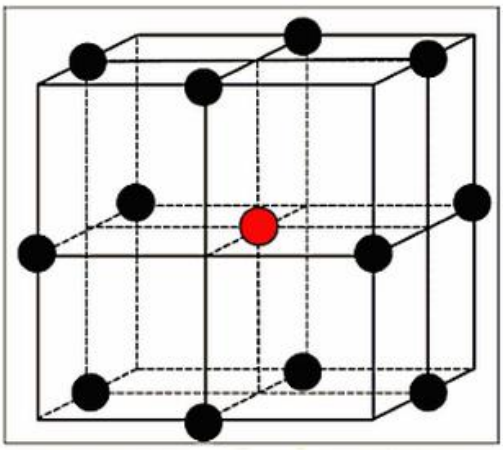

Figure 2. 20 - Cube-like structure of a Box-Behnken factorial design as depicted by Eriksson et al. (2008)

2.9.3) Factorial designs in CHS

A factorial trial was performed by Aimable et al. (2008) using the Taguchi method, as displayed in Table 2.6. This method used statistical calculations in order to determine significant parameters on the resulting APS of $BaZrO_3$ particles. The design consisted of a 2-levels and 5 factors resulting in 32 experimental runs, which evaluated the temperature, pressure, concentration, NaOH addition and residence time.

Table 2. 6 - Varying parameters in the Taguchi method experimental design for BaZrO3 synthesis adapted from Aimable et al. (2008)

	Low value (-1)	High value (+1)
Temperature (°C)	400	500
pressure (bar)	250	350
concentrations (mol/L)	Zr = 0.025	Zr = 0.075
	Ba = 0.1	Ba = 0.3
NaOH (mol/L)	1	2
Residence time (sec)	10	17

In the Taguchi method, a parameter is only considered significant if its significance is greater than 95%. In their study, they identified that the temperature and NaOH addition both had significance levels of over 95%. It was found that higher temperatures lead to smaller particles sizes, with an average size of 129nm at 500°C compared to 174nm at 400°C. When looking at the addition NaOH,

the grain size was found to increase from 127nm to 175nm as the NaoH concentration was increased from 1M to 2M (Aimable et al. 2008). The factorial trial performed by Aimable et al. (2008) on $BaZrO_3$ was focused on determining influential parameters, and no attempt was made at identifying or analysing parameter interactions.

2.10) Common nanomaterial characterization techniques

Numerous methods exist for the characterisation of fine, nanoscale particles, however a brief description of the common characterization techniques for nanomaterials have been discussed below. A general description of each process and the reason or rationale for each test has been reviewed in this chapter.

2.10.1) X-ray diffraction (XRD)

X-ray diffraction is commonly used for the determination of bulk crystallographic structures and for identifying the grain size of nanostructured materials. When a monochromatic beam is aimed upon a crystalline material, the incident X-ray photons interact with the electrons that surround the atoms, therefore the approaching X-rays are then scattered in all directions by the electron clouds. However, at certain angles (θ) the distance travelled by the incident and scattered X-rays differ by a complete number (n) of wavelengths, as illustrated by Figure 2.21. Consequently, the scattered X-rays remain in phase, known as constructive interference (Cullity & Stock 2001).

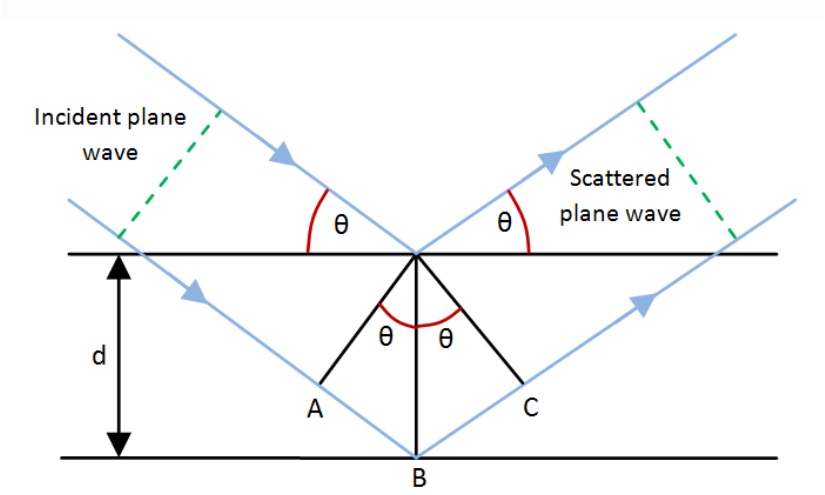

Figure 2. 21 - The Bragg description of diffraction in terms of reflection of an incident wave redrawn from Williams and Carter (1996)

The spatial variation of the scattered X-rays is then measured. As the wave length of the X-rays are in the order of interatomic-plane distance, crystalline material or any material with some order in its

atomic arrangement, will diffract the X-ray beam. The key conditions for constructive interference of the reflected beam is known as Bragg's law (Ramsden 2009):

$$d_{LS} \sin \theta = n\lambda \qquad \text{Equation 2.11}$$

where d_{LS} is the lattice spacing, n is the number of reflected wavelengths, λ is the X-ray wavelength and θ is the angle of diffraction. This technique was developed shortly after the discovery of X-rays by Rontgen in 1895, well before the era of nanotechnology (Ramsden 2011).

2.10.2) Electron microscopy

Electron microscopy can be defined as a unique field of science which utilizes an electron microscope as a tool, by using a beam of electrons to form an image of a desired specimen (Bozzola & Russell 1992). Electron microscopes take advantage of the extremely short wavelength of the electron (λ = 0.005nm at an accelerating voltage of 50) compared to the visible wavelength of light (λ = 400-700nm). Electron microscopy is operated under a vacuum, and focuses the electron beam and magnifies images with the help of electromagnetic lenses. As the voltage is increased, the wavelength of the electrons decrease along with the resolution i.e. higher voltage leads to higher resolving power (Flegler et al. 1993). Research and development into electron microscopes began in the 1920s, with 2 techniques existing at present, namely transmission electron microscopy (TEM) and scanning electron microscopy (SEM) (Stadtländer 2007).

2.10.2.1) Transmission electron microscopy (TEM)

A beam of electrons is transmitted through a specimen in order to form an image, which displays its structure. More specifically, the atomic planes of a crystalline core can be differentiated from the irregular network of the amorphous layer (Sepeur 2008). Electrons interact very strongly with atoms by elastic and inelastic scattering. The specimen must therefore be extremely thin, usually in the range of 5-100nm for 100 keV of electrons. However this is dependent on the density and composition of the object, as well as the desired resolution.

A conventional TEM consists of a number of electron-optical components, as illustrated in Figure 2.22. Electrons are emitted from an electron gun via thermionic emission or field emission and are accelerated toward the anode at high energy. A series of condenser lenses, typically 3 or 4, are responsible for focusing the electrons onto a probe and for varying the spot size. Whilst a condenser aperture filters out any electrons which stray too far from the optic axis and controls the number of

electrons passing through the specimen. After the electrons have passed through the specimen, the electron intensity distribution is imaged with a lens system, typically consisting of 3 to 8 lenses, with an objective aperture blocking any transmitted electrons which have scattered too far, enhancing the contrast of the projected image. The image is then projected onto a electron sensitive florescent screen or a charged couple device (CCD) camera by the projector lens (Reimer & Kohl 2008; Almeida 2010).

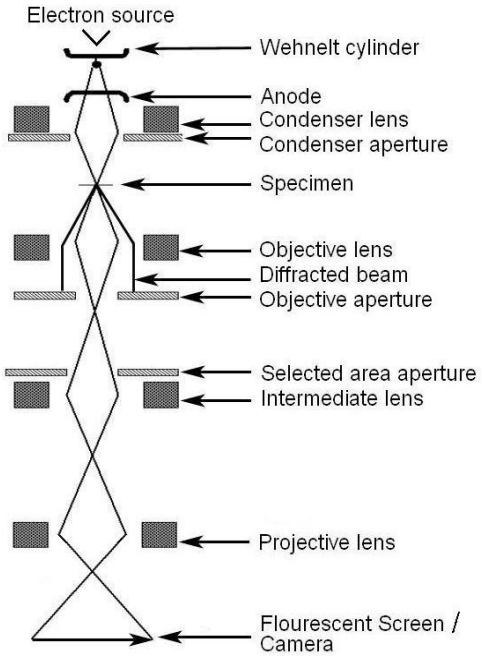

Figure 2. 22 - Schematic diagram of the basic electron-optical components of a TEM illustrated in Almeida (2010)

2.10.2.2) Scanning electron microscopy (SEM)

Scanning electron microscopy is a powerful method for the evaluation of surface structures (Stadtländer 2007). Not only can it display an image of the morphology of nanostructured materials, but it can also provide detailed information about the chemical composition and distribution (Wang & Cao 2011). This technique also offers a wide depth of field, which means that a relatively large portion of the specimen can be kept in focus at the same time. Another advantage is the range of magnification is quite high, allowing the operator to focus in on an area of interest scanned at a lower magnification. The three dimensional images may also be more appealing and easier to interpret when compared to the two dimensional images produced through TEM (Stadtländer 2007).

As depicted in Figure 2.23, a typical SEM consists of an electron gun, two condenser lenses, an objective lens, an electron detection system, and a set of deflectors, all operating in a vacuum. The

electron gun provides a source of electrons, which accelerate through and are demagnified by a three stage electron lens system, so that a probe of diameter 1-10nm is formed at the specimen surface. The electron beam interacts with the near surface region of the specimen at a depth of approximately 1 micron, generating signal electrons used to form an image. A deflection system in front of the final lens scans the electron probe across the specimen and operates in synchronism with a computer display monitor (Khursheed 2011).

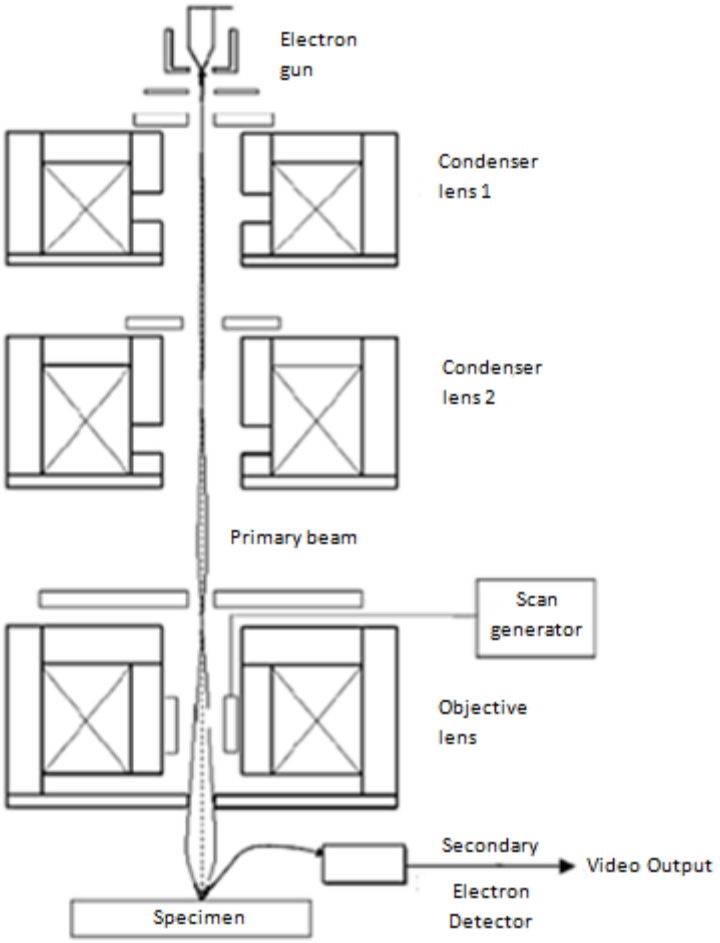

Figure 2. 23 - Schematic diagram of the basic electron-optical components of a SEM depicted in Kursheed (2011)

Electron detectors are used to collect various kinds of signals generated from the electron beam/specimen interaction. As the electrons penetrate the specimen surface, electrons are scattered from a range of different depths, some of which escape from the surface. Electrons which escape from near the surface are known as secondary electrons, and are created through inelastic collisions. While electrons scattered back from deeper levels are known as backscattered electrons,

which are generated through multiple elastic collisions. Secondary and backscattered electrons make up the two most common signals used to form a SEM image (Khursheed 2011).

2.10.3) Energy-Dispersive X-ray spectroscopy (EDX)

Energy-dispersive X-ray spectroscopy (EDX) is a standard method for the local identification of elements within a sample, while using SEM or TEM (Almeida 2010). A material is bombarded with high energy radiation, which in turn emits x-rays (Holloway & Vaidyanathan 2010). An incident electron can supply enough energy to a bound electron that it is able to leave the atom completely. This process, known as ionization, now leaves the charged atom or ion in an excited state (Garrett-Reed & Bell 2003). As a result, an electron from an outer orbiting shell jumps into the core level to fill the vacancy, and energy is emitted in the form of an X-ray photon. The energy of the emitted X-rays arises from the difference in energy between the shells, and is unique and characteristic to an atoms atomic number (Almeida 2010). The x-rays emitted are characteristic of the atoms present, allowing for an atomic breakdown of the sample (Holloway & Vaidyanathan 2010).

The relationship between atomic number and energy for a given X-ray is given by Moseley's Law: (Almeida 2010).

$$\sqrt{E} = C_1(Z - C_2) \qquad \text{Equation 2.12}$$

Where E is the energy of the emission line for a given X-ray series (e.g. Kα, Kβ, Lα, Mα, etc.), Z is the atomic number and C1 and C2 are constants.

2.10.4) Brunauer, Emmett and Teller (BET) surface area

The surface area of a solid material is important as it provides information on the available void spaces on the surfaces of a powdered solid (Ahuja & Scypinski 2001). The Brunauer, Emmett and Teller (BET) is a method of surface are measurement. Their method utilizes isotherms describing low temperature sorption of nitrogen or argon onto the particle surface, although any inert, compressible gas can be used. This method takes into account microscopic irregularities on the external surface, including internal porosity of mineral grains unlike other geometrical surface area measurements (Drever 2005). The unit of measurement is square meters per gram (m^2/g), while nitrogen is commonly used for samples exhibiting surface areas of $2m^2/g$ or more (Ahuja & Scypinski 2001).

2.11) Overview and conclusion

This chapter provided an introduction to nanotechnology and the various types of iron oxides and their respective properties, the numerous synthesis routes for nanomaterials were explored. It was shown from the numerous techniques that wet synthesis methods offer better control over particle characteristics and more effective scalability when compared with gas phase methods. Research suggested that of the wet phase techniques evaluated, a novel synthesis route known as the continuous hydrothermal synthesis offered the most promise. This was attributed to low residence times, lack of solvents and the lack of calcination or post treatment steps required to form crystalline products. The principle of CHS was identified along with a description of the process, which included all relevant information discussed in detail, including the properties of supercritical water, CHS design considerations, particle growth mechanisms, and the effect of operating parameters on particle characteristics.

The unique properties of one dimensional nanomaterials were also discussed, and it was shown the morphology of these particles, such as nanorods and nanowires, have a significant effect on their respective properties and hence their potential applications. Numerous uniquely shaped particles have been grown in batch systems while unique shapes in continuous systems are more scarce. This has been associated with a lack of understanding of the particle growth mechanism in CHS. Although a few authors have reported the use of surfactants, polymers and organic alcohols in CHS, little progress has been made in terms of controlling particle growth. Operating parameters such as concentration have shown some promise for manipulating particle characteristics. However, the interactions between parameters are not well understood and therefore the critical parameters for particle characteristic control have yet to be identified. In order to do this, a CHS plant will be constructed and through the use of a 3 level Box-Behnken factorial trial, the significance of key parameters will be evaluated and the corresponding parameters interactions will be identified and analysed.

Chapter 3 – Design, construction and commissioning of the CHS pilot plant and experimental methods.

3.1) Introduction

The first part of this chapter provides an overview of the design, construction, commissioning and operation of a continuous hydrothermal synthesis (CHS) pilot plant for the evaluation of critical process conditions and interactions on the resulting characteristics and morphology of iron oxide nanoparticles. It will include previous CHS designs and studies reported by various research groups, a full description of the CHS pilot plant constructed in this research along with an individual component breakdown, followed by the commissioning process.

The second section will focus on the experimental factorial trial designed to identify the critical process parameters and parameter interactions. It includes preliminary testing, experimental procedures and precursor makeup, a sample matrix of experimental runs and process conditions, a list of chemicals used in this study and will conclude with the characterization techniques used for particle analysis. The safe operation of the CHS pilot plant (start up and shutdown procedure) and various safety aspects and concerns (HAZOP Analysis) are provided in Appendix D.

Section 1

3.2) Experimental methodology and previous work

3.2.1) CHS Previous work

The use of continuous hydrothermal synthesis for the fabrication of metal oxide particles is not novel in the literature, with several authors describing their experimental setup and synthesis procedures. Xu (2006), compiled a list of all single phase and doped metal oxide particles reported in the literature which were prepared using the CHS route using supercritical or near-supercritical water as a reaction medium. His findings are depicted in Table 3.1.

Table 3. 1 - List of metal oxides prepared by various authors using CHS in the literature adapted from Xu (2006)

products	Precursor	particle size (nm)	References
AlOOH	$Al(NO_3)_3$	~100-600	Adshiri et al. 1992; Hakuta et al. 2005
$BaO{\cdot}6Fe_2O_3$	$Ba(NO_3)_2$, $Fe(NO_3)_3{\cdot}9H_2O$,KOH	~100-200	Hakuta et al. 1998
CeO_2	$Ce(NO_3)_4$	~300	Hakuta et al. 1998
Co_3O_4	$Co(NO_3)_2{\cdot}6H_2O$, NaOH	~50	Adschiri et al. 1992; Cote et al. 2003; Hao & Teja 2003
α-Fe_2O_3	$Fe(NO_3)_3{\cdot}9H_2O$, $FeCl_2$, or $Fe(SO_4)_3$	~50	Adschiri et al. 1992; Cote et al. 2003; Hao & Teja 2003
Fe_3O_4	$Fe(NH_4)_2H(C_6H_5O_7)_2$	~50	Adshiri et al. 1992
$LiCoO_2$+Co_3O_4	LiOH and $Co(NO_3)_2{\cdot}6H_2O$	~1000	Kanamura et al. 2000
NiO	$Ni(NO_3)_2$	~100	Adshiri et al. 1992
TiO_2	$TiSO_4$ or $TiCl_4$	~20	Adshiri et al. 1992
ZrO_2	$ZrOCl_2$	~10	Adshiri et al. 1992; Galkin, et al. 2001
YAG:TB	$Al(NO_3)_3{\cdot}9H_2O$, $Y(NO_3)_3{\cdot}6H_2O$, $TbCl_3{\cdot}nH_2O$	~100	Hakuta et al. 1999
$CoFe_2O_4$	$Co(NO_3)_2{\cdot}6H_2O$, $Fe(NO_3)_3{\cdot}9H_2O$, NaOH	~10	Cote et al. 2003; Millot et al. 2005
$BaZrO_3$	$ZrO(NO_3)_2$, $Ba(NO_3)_2$, NaOH	~74	Millot et al. 2005
ZnO	$Zn(NO_3)_2$, $Zn(CH_3COO)_2$, $ZnSO_4$, KOH	~120-320; ~10-80	Viswanathan et al. 2003; Sue et al. 2004
$BaTiO_3$	TiO_2, $Ba(OH)_2$	~10-60	Hakuta et al. 2005

Although a vast amount of metal oxides have been synthesized, very little research has focused on any specific metal oxide, including hematite (α-Fe_2O_3). The trend in the literature is to identify and produce new and novel metal oxides, including doped metal oxides, as opposed to performing in-depth research on one specific metal oxide in order to fully understand the effect of operating parameters and reaction conditions on the resulting particle characteristics. This lack of understanding of operating parameters can be highlighted using an example of the effect of temperature on particle size. Hao and Teja (2003) reported that temperature has no evident effect on the size of iron oxide nanoparticles, while Matson et al. (1995) and Xu and Teja (2008) identified that particle size increased with increasing temperature. On the contrary, it was shown by Hakuta et al. (1998) that ceria particles decreased in size along with an increase in temperature. It is therefore

essential that the effects of operating parameters need to be understood in CHS as particles with highly specific characteristics are required for a growing number of unique applications.

3.2.2) Previous experimental methodologies and procedures used to synthesize hematite (α-Fe_2O_3) nanoparticles via CHS.

For simplicity, the previous experimental methodologies below have been broken up into each individual research group as their experimental procedures and methodologies are generally identical, although slight variations do occur. Evans (2006), identified that outside of his research group, the Green Energy Institute in Nottingham, England, 4 other research groups have reported synthesizing iron oxide and ferrite compounds in flow reactors. The groups are listed below in chronological order as follows (including the Green Energy Institute):

- Matson, Linehan and Bean at the Pacific Northwest Laboratory, USA, 1992
- The group of Adschiri and Arai at Tohoku University, Japan, 1992
- The Green Energy Institute in Nottingham, England, 2000
- Cote and Teja from the Georgia Institute of Technology, USA, 2002
- Rho and Park from the Korea Institute of Energy Research, 2002.

As the Barium hexaferrite synthesized by Rho and Park from the Korea Institute of Energy Research are dissimilar to the iron oxides studied in this research, the plant description has been omitted below. Yet another research group reported after the work of Evans (2006) has been added below which is the research conducted by Liang et al. (2010) from the I-Shou University, Taiwan.

3.2.2.1) The Pacific Northwest Laboratory (USA)

It is believed that the Pacific Northwest Laboratory (USA) were the first to attempt the hydrothermal flow synthesis of Fe_2O_3 around the same time as the Adschiri and Arai group in 1992. Although it should be noted that the flow reactor design used by the Pacific Northwest Laboratory differs greatly from the designs used by all other research groups. They gave this process a title of rapid thermal decomposition of precursors in solution (RTSD). In their early research, they used 0.1M aqueous solutions of ferric nitrate and ammonium iron (III) sulphate as precursor solutions, which were pumped and heated under high temperature and pressure along a 1 meter long tube (Evans 2006). Their temperatures and pressures ranged from 100-400˚C and 4-8Kpsi (27.5-55 MPa) respectively. However hematite was only formed at temperatures exceeding 250˚C (Matson et al. 1995). Despite

the slow heating of their precursor feed, they still managed to produce particles in the range of 10-60nm which was confirmed using powder X-Ray diffraction (PXD) (Evans 2006).

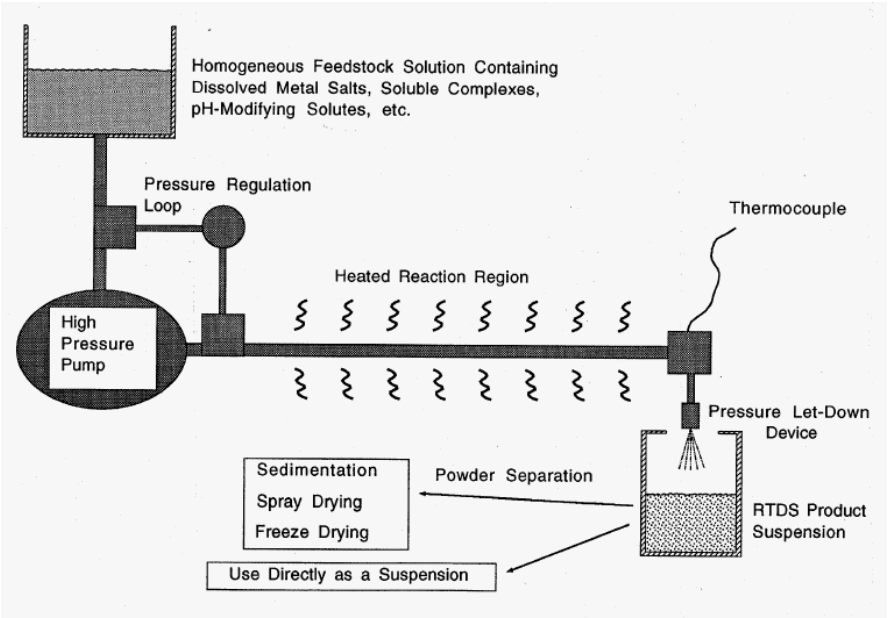

Figure 3. 1- Process flow diagram of the Rapid Thermal Decomposition of precursors in Solution (RTSD) method used by the Pacific Northwest Laboratory (USA) adapted from Matson et al. (1995)

As explained in Figure 3.1 by Matson et al. (1995), the feed solutions were initially prepared by mixing together a particle-forming precursor salt species along with a suitable solvent. In the formation of oxide and oxyhydroxide powders, the authors identified water as an ideal solvent. A premixed precursor solution was then pumped under high pressure by a reciprocating piston type pump (all wetted parts stainless steel 316) and pumped through a 1 meter long linear heated reaction vessel (1/8" OD). As a result, nucleation and solid particle formation occurred under the high temperature and pressure conditions. The residence times were generally kept short (1-30 seconds) and depend upon the reactor volume and flow rates. A thermocouple was used to measure the temperature at the end of the reactor tube and the particles in suspension are passed down through a pressure let-down device with a nozzle head and is collected as a suspension. If a dry powder was required, a centrifuge was used to aid sedimentation otherwise spray or freeze drying was utilized (Matson et al. 1995).

3.2.2.2) The group of Adschiri and Arai at Tohoku University, Japan

As early as 1992, the Arai and Adschiri group synthesized metal oxide particles in a supercritical flow system, which amongst other particles included the fabrication of hematite within the nanoscale

range (Fang 2010). Three different precursor salts were used to produce hematite, namely ferric nitrate ($Fe(NO_3)_3$), ferric sulphate ($Fe(SO_4)_3$) and ferrous chloride ($FeCl_2$). The salts were individually fed through a typical continuous hydrothermal process as outlined in Figure 3.2. The reaction conditions ranged between concentrations of 0.0066-0.16 mol/L, precursor feed rates of 0.8-2.2 ml/min, SCW feed rates of 2.5-6 ml/min, temperatures ranging from 673-763K and pressures ranging from 30-35 MPa (Fang 2010). It was concluded that spherical hematite nanoparticles of roughly 50nm were fabricated for all 3 precursor salts and there was negligible difference between the precursor salts used (Adschiri et al. 2000).

Further work by Sue et al. (2006) studied the effect of metal solubility and supersaturation on particle size by synthesizing various metal oxide compounds. This included the production of hematite nanoparticles at varied pressure (25-37.5MPa) and precursor salt concentrations (0.005-0.5 mol/kg). Their solutions were prepared by dissolving a precise amount of ferric nitrate nonahydrate ($Fe(NO_3)_3 \cdot 9H_2O$) in deionized and distilled water. The authors confirmed that there is a definite relationship between metal oxide solubility and particle size, and proposed that this trend shows promise for the production of various size-controlled particles.

More recent work by Sue et al. (2011) studied the effect of residence time on particle size and growth along the reactor. Once again ferric nitrate nonahydrate was used as a precursor salt to form small hematite nanoparticles at varied residence times (0.002 - 2.028 seconds). It was found that as the residence time increased, so did the average particle size. However along with the size increase came a slight increase in conversion and crystallinity.

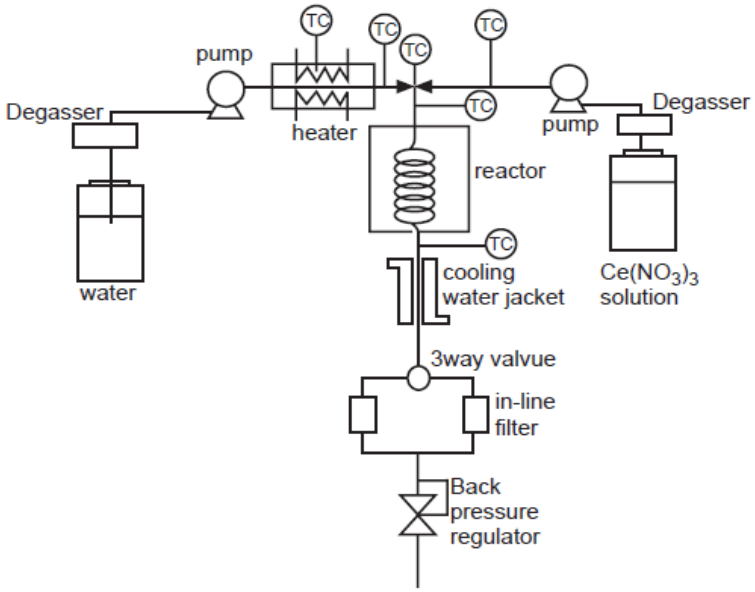

Figure 3. 2- Process flow diagram of the continuous hydrothermal synthesis plant used by the Adschiri and Arai group at Tohoku University (Japan) depicted in Hakuta et al. (1998)

This early design, described by Hakuta et al. (1998) in Figure 3.2, explained that after the precursor solution was prepared, it was pumped under high pressure by a Nihon Seimitsu Kagaku (NP-AX-15) high pressure pump at a flow rate of 2ml/min. The precursor solution was then met by a stream of pre-heated water (+- 450˚C) supplied through another line at a flow rate of 6ml/min. The precursor solution was heated rapidly to the desired reaction temperature during mixing, and was maintained at this temperature along the reactor using an external heater. After the reactor, the reacted solution then passed through a water cooling jacket and exited out of the system after passing through a back pressure regulator which maintained the pressure in the system at 30 MPa. The particle suspensions recovered were passed through a 0.1µm membrane filter and then dried in an oven at 60˚C for 24 hours.

3.2.2.3) The Georgia Institute of Technology, USA

In 2002, Cote and Teja (2002), reported on the synthesis of hematite nanoparticles using the continuous hydrothermal process. In their research, they studied the effect of temperature on particle characteristics in the presence of a sodium hydroxide base under hot and cold mixing conditions. Solutions of 0.03M ferric (III) nitrate nonahydrate ($Fe(NO_3)_3 \cdot 9H_2O$) and 0.08M sodium hydroxide were prepared by adding a known amount of substance to de-ionized water in order to make up 500ml of solution. In their research, they studied the effect of hot or cold mixing for the

addition of the NaOH solution into the system by altering the feed position at different reaction temperatures. The authors identified that the particles formed were smaller when the NaOH stream entered the hot water stream (hot mixing) prior to mixing when compared to the NaOH stream entering the cold precursor stream (cold mixing) prior to mixing. It was determined that the solubility of the cation plays a role in attaining the right product by comparing the relatively insoluble iron to more soluble cobalt. However iron precipitates rather easily and in all cases the thermodynamically stable hematite (α-Fe_2O_3) structure was formed.

Hao and Teja (2003) also studied the effect of various operating parameters on the production of hematite nanoparticles using the CHS method. Their samples were prepared in a similar fashion to that described by Cote and Teja (2002) and ferric nitrate was also used as a precursor salt. In their research they studied the effect of particle size by altering the precursor concentration, reaction temperature and residence time independently. They concluded that a clear trend was visible when the concentration was increased which showed an increase in particle size with an increase in concentration. While temperature was stated to have a negligible effect and residence time showed a slight decrease in particle size along with a decrease in residence time.

More recent work was performed by Xu and Teja (2008), who also produced hematite particles in the same method described by Cote and Teja (2002), however experiments were conducted in the presence and absence of polyvinyl alcohol (PVA) at varied operating parameters in order to highlight the effect of added PVA in reducing particle aggregation. The authors showed that the particle size and size distribution tended to decrease with an increase in PVA concentration. Therefore it was concluded that the addition of PVA was effective method of reducing particle aggregation which was backed up by a proposed mechanism.

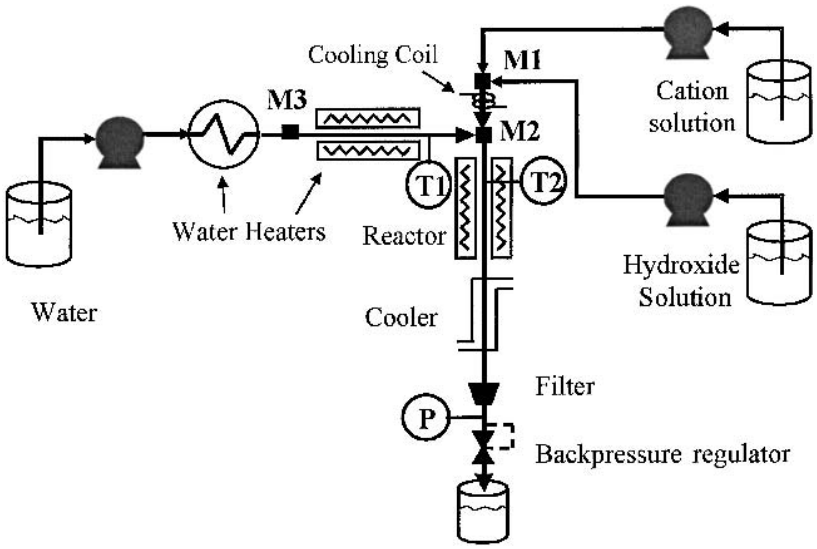

Figure 3. 3- Process flow diagram of the continuous hydrothermal synthesis plant used at the Georgia Institute of Technology (USA) illustrated in Cote & Teja (2002)

The experimental apparatus in Figure 3.3 was described in detail by Xu and Teja (2008). After each precursor solution was prepared, a Milton Roy micro metering pump was used to deliver the salt solution to the mixer where it was met with hot, compressed water. The water was then heated by pumping it through two stainless steel coils (1/8" O.D.) and was delivered to the mixing tee by two Isco high-pressure syringe pumps (Model 260D and Model 100DX), which maintained a water to precursor ratio of 3:2. The 2 coils were heated with cartridge heaters controlled by variable transformers, and additionally by heating tape controlled by a feedback controller linked to a thermocouple. The temperature in the mixer was also controlled by using an inline thermocouple linked to heating tape wrapped around the reactor/crystallizer. The particles in suspension were then passed through a tubular condenser, an inline filter and through a back pressure regulator (Tescom) which was used to maintain the system pressure between 24-25MPa. The particles were collected in a vessel and allowed to settle, afterwards the solution was filtered to remove the solid product. The particles were then dried in an oven at 52°C overnight.

3.2.2.4) The Green energy institute in Nottingham, England

Early work by Cabanas in 2000 at the Green energy institute used metal acetate solutions, including ferric acetate, in rig 1 of their CHS pilot plant for the production of iron containing nanomaterials. Ferric acetate was reacted under mixing temperatures ranging from 200-345°C and at a constant pressure of 25MPa. The resulting product formed was magnetite (Fe_3O_4), which was attributed to the degassing of the deionized water. The deionized water was degassed using nitrogen which was

bubbled through the water in order to remove most of the dissolved oxygen. The lack of oxygen in the water lead to only partial oxidation of Fe^{2+} to Fe^{3+} ions hence the formation of magnetite which contains both ions (Evans 2006).

While research conducted by Evans (2006), reported that when deionized water was not degassed, the product formed was hematite (Fe_2O_3) which was owed presumably to the oxidising effect of the dissolved oxygen. The effect of temperature was evaluated on particle size, reaction conversion and crystallinity. Ferric nitrate solutions were prepared at a constant 0.05mol/dm^3 concentration and the flow rate of the water and precursor streams were set to 10ml/min and 5ml/min at a constant 250 bar pressure. The temperature was varied from 100°C to 400°C in 25°C increments and the conversion and particle size increased with an apparent irregular linear trend. Amorphous particles were reported at low temperatures, while the critical temperature where the amorphous hematite particles changed to crystalline particles was found to be 250°C.

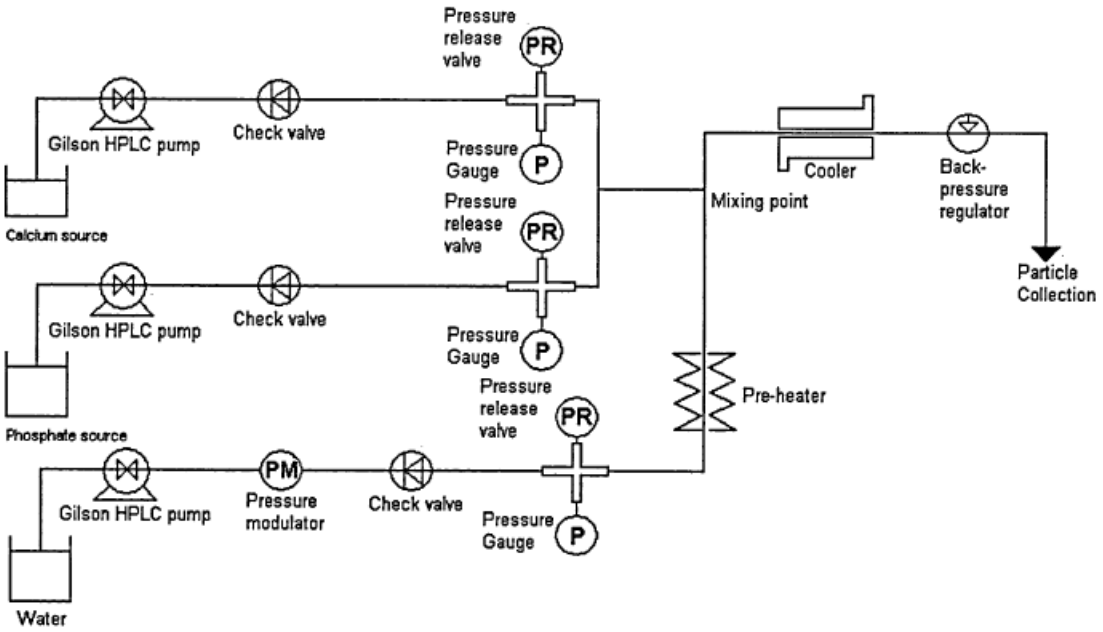

Figure 3. 4- Process flow diagram of the continuous hydrothermal synthesis plant used at the Green Energy Institute in Nottingham (England) illustrated in Chaudhry (2008)

The experimental apparatus in Figure 3.4 was described by Chaudhry (2008), which was set up in a 3 pump configuration. All 3 pumps were Gilson HPLC type pumps, with the water line fitted with a 10SC pump head and set to deliver 10ml/min. The precursor and alternate feed line were fitted with 5SC pump heads and set to deliver 5 ml/min. All feed lines were fitted with a one-way valve, a

pressure gauge and a pressure release valve which was set to vent/burst at 31MPa. The feed line tubing used was 1/8" (3.175 mm OD) stainless steel 316 (Swagelok) with a 0.028" (0.71mm) wall thickness. Cold water was passed through a custom built electrically powered heater which consisted of 6 meters of 1/4" (6.35 mm OD) stainless steel (Swagelok) tubing wrapped around an aluminium 6082 cylindrical core. The inside of the core was fitted with a Watlow 1000 W cartridge heater and the outside was fitted with two Watlow 750 W band heaters. Two J-type thermocouples were used to monitor the inlet and outlet temperature which was linked to a controller which controlled the heaters to maintain the set point temperature. The mixer used was a nozzle type which has been described in great detail in section 2.5.3.2, which allowed the supercritical water and precursor stream to meet in a counter current configuration and the particles precipitated from solution. After the reaction, the particles in suspension were passed through a pipe in pipe cooling column, through a 15µm filter and out through a back pressure regulator (Tescom) and collected in a collection vessel. The back pressure regulator was used to maintain the system pressure at 24MPa. After collection, 50 ml of solution was centrifuged at 4500 RPM for 3 minutes. Afterwards 45ml of liquid was extracted and 45ml of deionized water was added and the particles were redispersed and centrifuged again for 3 minutes at 4500 RPM. The removed particles were then frozen using liquid nitrogen and freeze dried for 18 hours.

3.2.2.5) Liang et al. (2010) from the I-Shou University, Taiwan

Recent work by Liang et al. (2010) reported on the synthesis of fine hematite nanoparticles in their CHS system. Using ferric nitrate as a precursor, 0.1 mol/dm^3 solutions were prepared and the effect of temperature was evaluated by varying the reaction temperature between 250-420°C at a constant 30 MPa pressure. The precursor solution was fed at a flow rate of 3ml/min which was met in the mixer with a supercritical water flow rate of 30ml/min and it was shown that the average particle size increased with reaction temperature. The average particle size tended to increase until the supercritical temperature of water was reached (373°C), following which, the particle size tended to decrease with an increase in temperature. The authors proposed that the decrease in particle size after the supercritical temperature was probably due to the low solvent power of supercritical water. The authors also concluded that crystallinity increased with an increase in temperature.

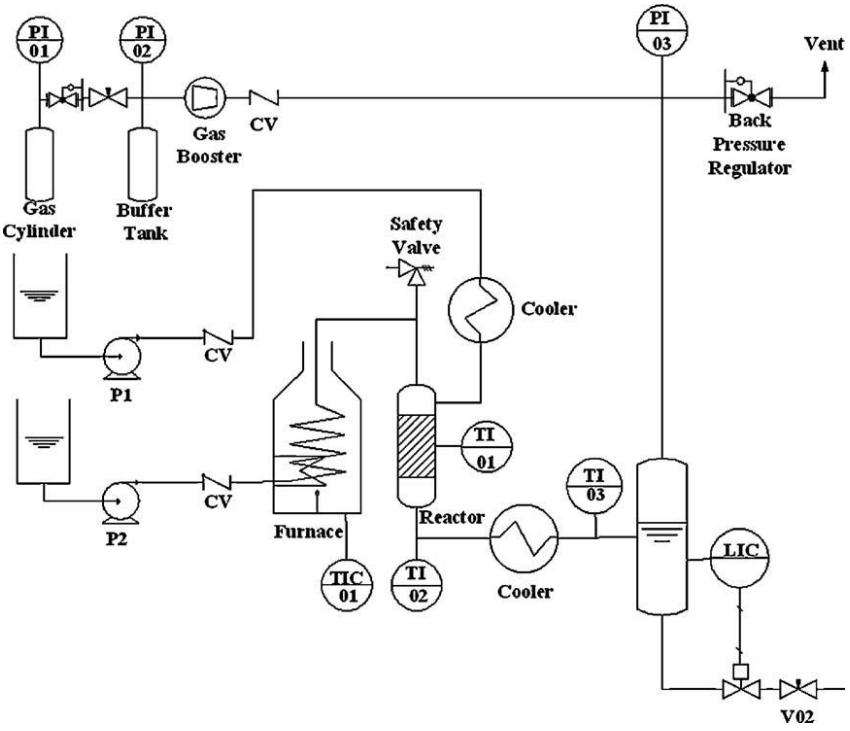

Figure 3. 5- Process flow diagram of the continuous hydrothermal synthesis plant used by Liang and colleagues at the I-Shou University (Taiwan) depicted in Liang et al. (2010)

The continuous hydrothermal process in Figure 3.5 was briefly described by Liang et al. (2010), where deionized water was pumped through a furnace and heated to set point temperature at a flow rate of 30ml/min. After the system had reached steady state, a 0.1M solution of 99% ferric nitrate was fed through the other line to the mixing point at a flow rate of 3ml/min. A buffer tank containing nitrogen was used to stabilize the pressure surge as a result of the inputs and a back pressure regulator was used to control the pressure. After the reaction, the particle suspension was then passed through a cooler and cooled down to room temperature. The particles were then dried and collected.

3.2.2.6) Summary

Taking into account all the different CHS pilot plant designs, an optimal design was drafted, drawing influences from previous work. The CHS pilot plant design used in this study was majorly influenced by the plant utilized by the Georgia Institute of Technology. However, the design used in this study differed in many ways and was designed specifically to operate within our space limitations and desired operating parameter range. Various modifications were also implemented in order to avoid possible shortcomings such as blockages reported by Lester et al. (2006).

Table 3. 2 - Summary of previous conditions used by other researchers for the fabrication of hematite nanoparticles via the CHS route. (NS = not stated)

Author/s	Precursor type	Precursor concentration (Mol/dm3)	Reaction temperature (°C)	Pressure (MPa)	Water flow rate (ml/min)	Precursor flow rate (ml/min)	Total flow rate (ml/min)	pH	Reactor length (m)	Residence time (sec)	Additives	Particle size range (nm)
Matson et al. (1995)	ferric nitrate & ammonium iron sulphate	0.1	100-400	27.5-55	N/A	N/A	50-75	NS	1	2	N/A	10-60
Adschiri, et al. (2000)	ferric nitrate; ferric sulphate & ferrous chloride	0.0066-0.16	400-490	30-35	2.5-6	0.8-2.2	3.3-8.2	NS	NS	NS	N/A	50
Sue et al. (2006)	ferric nitrate nonahydrate	0.005-0.5	400	25-37.5	80	20	100	NS	NS	NS	N/A	5.1-8.2
Sue et al. (2011)	ferric nitrate nonahydrate	0.05	400	30	80	20	100	NS	0-4	0.002 to 2.028	N/A	4.0-6.7
Cote & Teja (2002)	ferric nitrate nonahydrate	0.03	200-385	25	3	1	5	NS	NS	9 to 20	NaOH (1ml/min)	33-97
Hao & Teja (2003)	ferric nitrate nonahydrate	0.01-0.5	247-300	24	NS	NS	NS	NS	NS	10 to 20	N/A	12.3-32.4

Author/s	Precursor type	Precursor concentration (Mol/dm3)	Reaction temperature (°C)	Pressure (MPa)	Water flow rate (ml/min)	Precursor flow rate (ml/min)	Total flow rate (ml/min)	pH	Reactor length (m)	Residence time (sec)	Additives	Particle size range (nm)
Xu & Teja (2008)	ferric nitrate nonahydrate	0.03-0.06	214-375	22	NS	NS	Ns	NS	0.05-0.2	2.6 to 10.4	PVA	7.2-27.4
Evans (2006)	ferric (III) nitrate	0.05	100-400	26	10	5	15	NS	NS	NS	N/A	6.5-39.9
Liang et al. (2010)	ferric nitrate	0.1	250-420	30	30	3	33	NS	NS	NS	N/A	20-40

3.3) Experimental apparatus - overview and design of the CHS pilot plant

The CHS pilot plant design was designed to operate under a wide range of operating conditions, in order to manipulate process conditions such as temperature, pressure and flow rate. By manipulating certain variables, it was possible to control parameters such as the reactor residence time and the mixing conditions in the reactor.

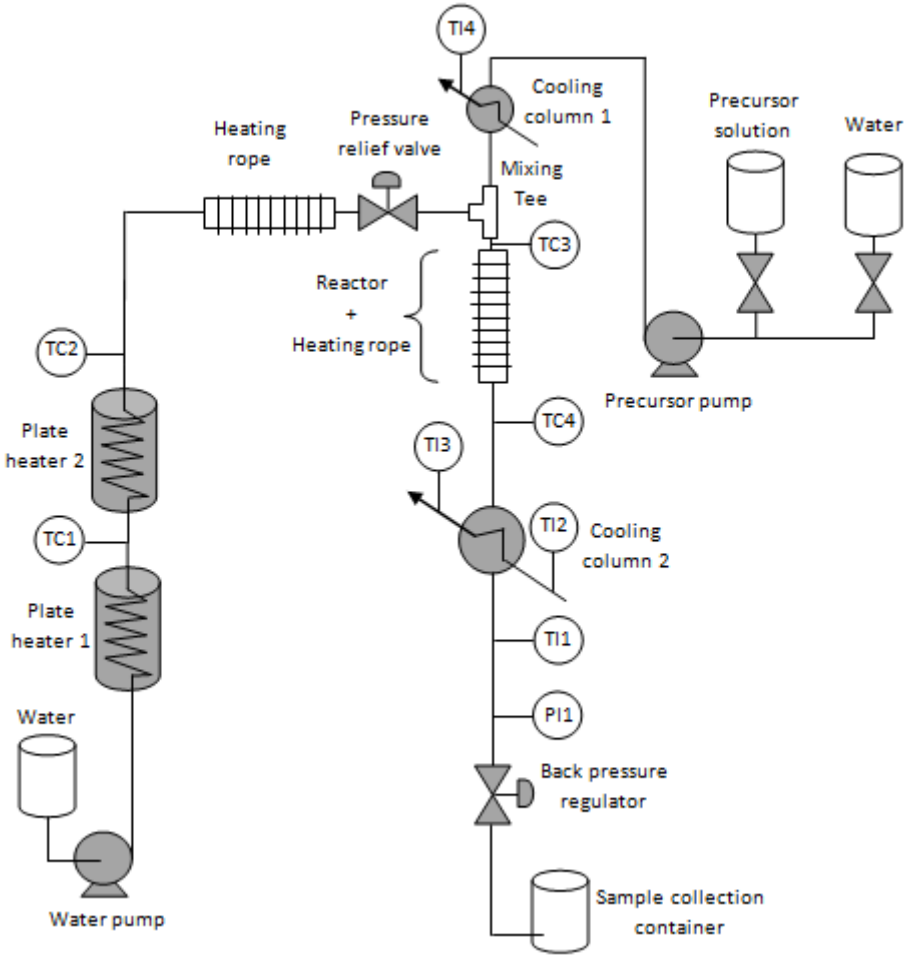

Figure 3. 6- Process flow design of CHS pilot plant used in this study, CPUT, Cape Town, South Africa

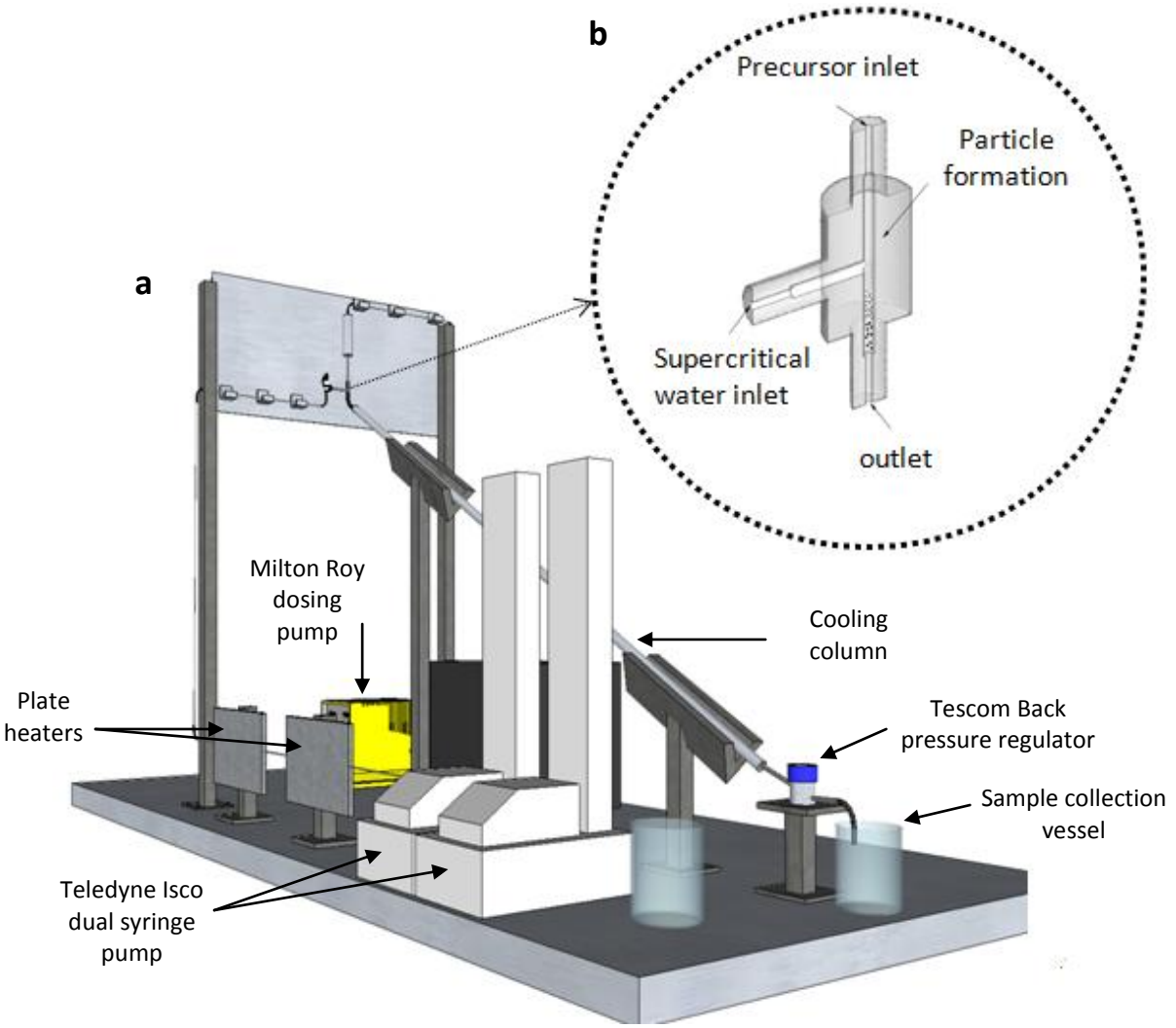

Figure 3. 7- (a) 3D design of CHS pilot plant and (b) close-up of mixer adapted from Sierra-Pallares et al. 2011

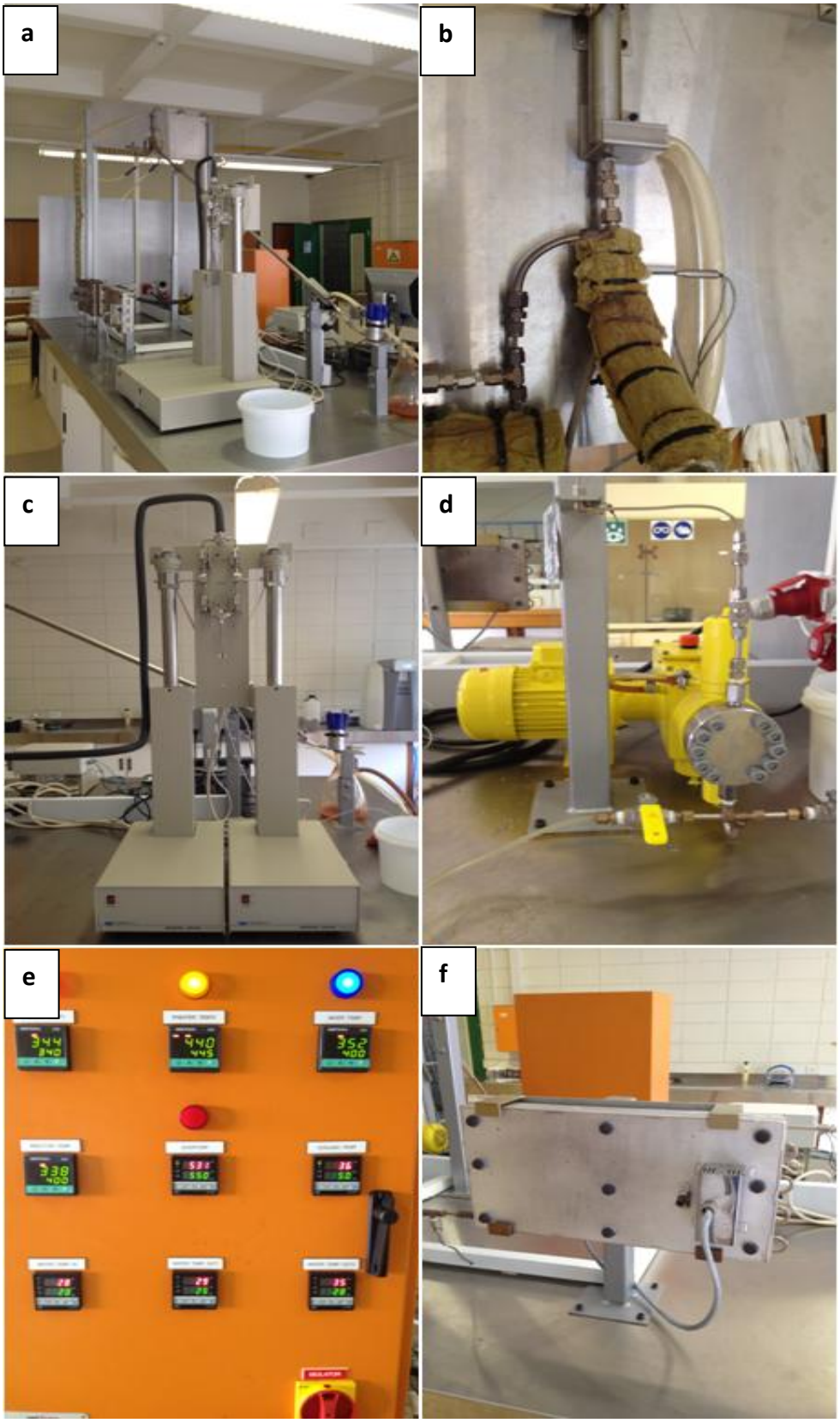

Figure 3. 8- Actual images taken from CHS pilot plant with (a) overall CHS plant (b) mixer and reactor (c) Teledyne Isco dual syringe pump (d) Milton Roy metallic diaphragm dosing pump (e) temperature control enclosure (f) plate heater

The pilot plant depicted in Figure 3.6, 3.7 and 3.8, consisted of two Isco Teledyne 260D high pressure syringe pump (water pump in Figure 3.8c) set up in a duel system, for the constant delivery of supercritical water of up to 80ml/min. A Milton Roy metallic diaphragm dosing pump (precursor pump in Figure 3.8d) was used for pumping the precursor solution, which was capable of pumping corrosive fluids at up to 96.6ml/min. Two plate heaters in series were used for heating the water feed, followed by a mixing tee, a reactor/crystallizer, a pipe in pipe cooling column and a back pressure regulator supplied by Tescom, leading to a sample collection vessel.

All tubing was supplied by Swagelok, where 3.175mm O.D (1/8") stainless steel 316 was used up to the mixing tee (except 6.35 mm OD tubing used in the plate heaters), afterwards 6.35 mm OD (1/4") stainless steel 316 tubing was used up to the collection vessel.

For process control, 4 temperature feedback controllers and 5 temperature indicators along with 9 thermocouples (5 inline and 3 clamp type) were supplied by Unitemp, R.S.A, for temperature monitoring and control. A pressure gauge (Model: PGI-63B-PG200-LAOX) was supplied by Swagelok, a pressure transducer was supplied from WIKA for pressure logging and a back pressure regulator was supplied by Tescom in order to monitor and control the pressure in the system. For safety purposes, a check valve was placed after each pump to prevent reverse flow, and a pressure release valve (set to fail at 320 atm) was installed in case of a pressure build up due to failure of the back pressure regulator.

3.4) Individual component breakdown

3.4.1) Teledyne Isco 260D high pressure syringe pump duel system

Two Teledyne Isco 260D high pressure syringe pumps (Figure 3.8c) were used for the constant delivery of deionized water under high pressure. The pumps were set up in a dual system, as one syringe pump is pumping the water, the other is refilling. The system is controlled by electric valves, which allows for continuous delivery of water under pulseless flow. Each syringe has a volume of 266ml and the duel system has a continuous flow range of 0.001-80 ml/min with a flow accuracy of 0.5% of its set point. The working temperature and pressure ranges are 5-40˚C and 0.7-510 atm (516 bar). The dimensions of each pump are: height: 108 cm, width: 27 cm, depth: 47 cm. The pumps were locally supplied through Elemental analytics, RSA; however they were shipped from Teledyne Isco which is based in Lincoln Nebraska, USA (Teledyne Isco n.d.).

3.4.2) Milton Roy metallic diaphragm dosing pump

A Milton Roy metallic diaphragm dosing pump (Figure 3.8d) was used for pumping the corrosive ferric nitrate based precursor solution. The dosing pump has a flow capacity of 96.6 ml/min, and can operate accurately within 10-100% of its capacity, i.e. its flow range is 9.7-96.6 ml/min. The pump has a pressure rating of 296 atm (300 bar), with a maximum rating of 385 atm (390 bar) and it has a 0.37kW motor which operates at 380 volts. It was supplied locally by Ecochem (PTY) LTD, RSA; and was shipped down from Milton Roy Europe based in Sunderland, UK.

3.4.3) Aluminium and copper plate heaters

Two plate heaters (Figure 3.8f) in series were used to heat the deionized water from ambient temperature to a maximum temperature of 450˚C, dependent on the required mixing temperature. The two plate heaters are identical in dimensions, although the first heater was constructed with aluminium grade 6082, while the second hotter plate heater required copper plates as it operated under higher temperatures. Each heater comprised of two metal plates bolted together, with dimensions of 8mm thick, 500 mm long and 250 mm wide. Each plate had 3.175 mm deep grooves cut in, with 6.35 mm O.D tubing running through, so that when the plates are bolted together the tubing running through fits flush with the plate to allow for optimal heat transfer. Each plate has 9 loops of 0.5m, which allowed for 4.5 meters of tubing per plate. Two 3kW ceramic plate heaters were attached to each of the two aluminium plates (one on top and one at the bottom) making 12kW of energy in total for heating the water from ambient to 450˚C. The system has been overdesigned to account for varying flow rates and temperature requirements. At the exit of each

plate heater, a tee piece with a thermocouple placed inside was used to measure the temperature, which is linked to a feedback temperature controller. The set point temperature after the first plate heater (aluminium) was 300˚C, with the second (copper) being up to 450˚C. As the water temperature rises above 300˚C, the specific heat capacity of the water increases drastically. This meant that the amount of energy required to heat up the water increased exponentially as the water temperature increased, with a specific heat capacity of 13.27 J. $g^{-1}K^{-1}$ at 400°C and 25MPa (Brunner 2014). For safety purposes, a thermocouple was used to monitor the temperature of the aluminium plates, linked to a cut-off switch, if the aluminium temperature exceeded 400˚C. Although the melting point of aluminium grade 6082 is rated to roughly 650°C, it was found to lose its structural integrity at far lower temperatures. The aluminium plates had to be replaced for one of the plate heaters due to partial melting between 450-500°C.

3.4.4) Tee piece mixer design

The mixer (Figure 3.8b) is arguably the most important section of the CHS pilot plant, as effective mixing is required in order to yield high quality particles. Mixer designs have also evolved over the years, and alternative designs are explored in chapter 2. The mixer used in this study was a Swagelok 6.35 mm (1/4") tee piece with the precursor solution entering from the top, the supercritical water from the side, and both steams exiting through the bottom. The supercritical water enters from the side as it has a low density, when compared to that of the precursor solution. This leads to a buoyancy driven updraft which promotes turbulent flow due to semi counter current mixing (Blood et al. 2004; Lester et al. 2006). Work by Lester et al. (2006) revealed that the high temperature of the tee piece mixer may tend to heat up the surrounding tubing through conduction heat transfer. They further stated that premature heating of the precursor solution may lead to premature particle formation and hence a greater deviation of particle characteristics. To combat this problem, a 20mm O.D tube with a length of 150mm was placed just above the mixer around the tube carrying the precursor solution, and cooling water was passed through to ensure that the tubing remained cool and no premature particles precipitated into the solution.

Several authors have reported the significance of reaction temperature during mixing and its varying effect on particle characteristics. A 20mm O.D aluminium rod was cut into 30mm lengths and 3.175mm holes were drilled down the centre. They were then slid onto the supercritical water tubing, making up a total length of 0.5m. One meter of 250W heat trace cable was then wrapped around the 0.5m of aluminium rod pieces. The rod had to be used as the heating cable had a minimum bend radius of 6mm. A pipe clamp thermocouple was attached to the mixer in order to

determine the mixing temperature, and a temperature feedback controller was linked to the heating cable in order to control and maintain a constant temperature in the mixer.

3.4.5) Reactor/crystallizer

After mixing, a specific length of tube was required to allow for particle grow and crystallization. The length of tubing is therefore referred to a reactor or crystallizer (Figure 3.8b). It serves two main functions: (1) to allow enough time to allow particles to grow to their desired size i.e. residence time and (2) to keep a constant temperature throughout in order to keep a constant growth and nucleation rate. The reactor or crystallizer consisted of a vertically orientated Swagelok 6.35mm O.D tube bent at a 60 degree angle from the vertical plane with a length of 0.2m long. The reactor length was chosen as it allowed for a low residence time under high flow and a higher high residence time at low flow rates. For more information on the effects of residence time on particle characteristics see chapter 2. Copper wire with a 1.5mm diameter was wrapped around the reactor in order to increase its outer diameter to 12mm. A 125W 0.5m heating cable was then wrapped around the reactor which had a minimum bend radius of 6mm. A pipe clamp thermocouple was attached near the end of the reactor, and a temperature feedback controller was linked to the heating cable in order to control and maintain a constant temperature along the reactor to ensure uniform particle growth.

3.4.6) Cooling column jacket

After the reactor, the solution needed to be cooled rapidly in order to cease particle growth. A pipe in pipe cooling column was utilized, where a 20mm OD tube with a length of 2.5 meters surrounded the 6.35mm OD tubing after the reactor. The cooling column rested at a 30 degree angle relative to the horizontal, as it was too long to orientate vertically, however the angle was required in order to avoid particle settling and build up, leading to a possible issue of clogging discussed by Lester et al. (2006) and Xu (2006). Cooling water was supplied from a nearby tap at ambient temperature and flowed up the column to allow for counter current cooling. The flow rate was measured using a rotameter and was adjusted manually by adjusting the tap valve. A pipe clamp thermocouple was placed after the cooling column in order to monitor the temperature of the reactant mixture and particles in suspension. The cooling water inlet and outlet temperatures were monitored with inline thermocouples which made it possible to easily determine the change in temperature of the cooling water and hence the rate of heat transfer. The flow rate was adjusted so that the temperature

change was 5˚C for the cooling water and the reactant mixture outlet was maintained at roughly 40˚C. The cooling water used ran to drain, which allowed for a constant feed temperature.

3.4.7) Back pressure regulator and pressure control

The pressure in the system was controlled via a back pressure regulator. The pressure regulator used was a Tescom (Part No. 26-1762-24-33) and was supplied by Air Liquide (PTY) LTD, RSA. Its pressure control ranged from 3.35 to 407.5 atm (3.4-413 bar), and It was used to regulate the overall system pressure by maintaining it at 250 atm. A pressure gauge (Model: PGI-63B-PG200-LAOX) was supplied by Swagelok and was installed just before the back pressure valve for visual confirmation of the pressure status in the pilot plant, while a pressure transducer supplied by WIKA was used for pressure logging.

3.4.8) Tubing and fittings

All tubing and fittings were supplied by Swagelok, RSA. The 3.175mm OD, 0.71mm thickness (1/8" OD) stainless steel 316 was used up to the mixing tee (except 6.35mm OD tubing used in the plate heaters), afterwards 6.35 mm OD, 1.65mm thickness (1/4" OD) stainless steel 316 was used up to the collection vessel. The maximum operational pressure rating of the 3175mm and 6.35 mm tubing was 578 atm and 694 atm respectively. Numerous fittings were used in the construction of the pilot plant, including straight fittings, 3.175mm to 6.35mm expansion fittings, 6.35mm to 3.175mm reducer fittings, 90˚ elbows, mixing tees, check valves and a pressure release valve. Some fittings were used to avoid pipe bending, such as the 90˚ elbows, whilst other fittings such as straight fittings were used only to separate plants sections allowing them to be easily removed if necessary. All fittings have a maximum operational pressure rating equal to the tubing with which they are attached.

3.5) Commissioning process

Before experimental runs could commence, the CHS plant had to be commissioned to ensure that all components were functioning properly and that the pilot plant was safe to operate. Table 3.3 comprises of all components that were tested during the commissioning process. A HAZOP and risk analysis were also performed and can be found in the Appendix D along with a start up and shutdown procedure in Appendix C.

Table 3. 3 - Summary of testing and commissioning process before the CHS plant could be operated

Component	Testing	Performance	Problems	Action
Overall pressure testing	The pressure testing was conducted externally by Fluval Marine. The pilot plant was taken up to 50MPa of pressure, twice that of the operating pressure.	The pressure was increased incrementally until the final pressure of 50MPa was achieved. This pressure was held for 10 minutes without any leaks.	A few small leaks.	All leaking fittings were tightened or the ferrules were replaced.
Teledyne Isco dual syringe pump	The pump was tested under pressure and the accuracy and range of flow was tested between 10-80 ml/min.	The pump performed extremely well, and delivered water accurately over the desired range of flow.	The pump occasionally stopped as the other syringe was still refilling while the running syringe ran dry.	Pump controller settings had to be reconfigured.
Milton Roy Diaphragm dosing pump	The pump was tested under pressure and the accuracy and range of flow was tested between 5-50 ml/min.	The pump performance was slightly lower than expected. A maximum flow rate of only 45 ml/min was achieved under pressure, lower than the rated 96.6ml/min	The pumping head in the system was too great for the pump to achieve maximum flow rate under pressure	None - the 45ml/min flow rate was more than sufficient as the flow rate capacity was over designed

Component	Testing	Performance	Problems	Action
The plate heaters	The plate heaters were tested by trying to reach the desired temperature set point in the system. With plate heater 1 set to 300°C and plate heater 2 set to 450°C	The plate heaters worked well and easily achieved the set point temperatures. Although the aluminium was not suitable for the high temperatures in the second plate heater.	The aluminium plates used in the second plate heater started to melt at 450°C.	The aluminium 6082 plates were changed for copper which has a much higher melting point
The cooling column	The cooling column was tested by passing water through it up to 350°C and observing the output temperature.	The cooler was extremely effective, working better than expected. The water exited the column just above ambient temperature	N/A	N/A
The heating rope	The heating rope was tested to see if the set points could be maintained in the system.	Once working, the heating ropes performed well. Although higher energy output heating rope is recommended for a future upgrade, as a slight temperature drop occurred along the reactor	The heating ropes were tripping through earth leakage.	Special Mica insulation was used to separate the heating rope and the surrounding metal.

Component	Testing	Performance	Problems	Action
The back pressure regulator	The back pressure regulator was tested by slowly increasing the pressure in the system	The back pressure regulator worked perfectly and maintained the pressure in the system effectively up to 30MPa.	After a few experimental runs, the back pressure regulator struggled to increase the pressure in the system.	The regulator was sent in to the supplier for repairs. It was replaced and has been working well.
The pressure release valve	The pressure release valve was set to a low blow off pressure to ensure it was venting. Once tested it was then set to a release pressure of 32MPa and retested.	The pressure release valve popped and re-seated as required. It was set to 32MPa and upon retesting it popped at 32MPa.	N/A	N/A
Insulation	The insulation was tested by observing the temperature drop between the inline thermocouples.	The glass insulation tape used had a relatively large temperature drop (30-40°C) over the 2-3 meters of tubing.	The large temperature drop was undesired and so a new insulation was obtained.	Rock wool insulation was used instead which gave a better performance and lower temperature drop.

Section 2

3.6) Chemicals used

The following Chemicals were used in this research

- Ferric nitrate nonahydrate $Fe_2(NO)_3 \cdot 9H_2O$ (>98%) was supplied by Sigma-Aldrich and was the main constituent of the precursor solution makeup. It is a water soluble salt with a molar mass of 404g/mol and was used a source of Fe^{3+} ions in solution.
- Deionized water was used, which was deionized in the Lab using a Lasec Purite deionizer.
- Lab grade 99.9% ethanol was used.
- Sorbitan Oleate (Span 80) surfactant was supplied by Lake International Technologies, South Africa (see Appendix A).
- Polyoxyethylenesorbitan monooleate (TWEEN 80) surfactant was supplied by Lake International Technologies, South Africa (see Appendix A).
- Poly(isobutylene) succinic anhydride (PIBSA-MEA) was supplied by Lake International Technologies, South Africa (see Appendix A).

3.7) Experimental procedure

A ferric nitrate nonahydrate solution was prepared by mixing a given mass of the salt with deionized water in order to achieve a desired concentration. The pH of the solution was then adjusted to 1.8 by adding a 7 molar solution of sodium hydroxide in a drop wise manner. A 100ml of precursor solution was prepared for each experimental run. Once the CHS plant was running at steady state, and at the desired parameters for the experimental run, the precursor solution was pumped through the system and reacted in a 3:2 ratio of water to precursor. A precise volume of 100 ml of product solution was collected at the end of the process and stored until separation. The particles were separated through centrifugation, with all experiments being centrifuged at 6000RPM for 5 minutes a minimum of 3 separate times, or until all particles were removed from suspension. The separated particles were then dispersed in deionized water and dried in an oven at 60°C for 24 hours. The yield of each experimental run was determined by weighing each empty Petri dish and full dish of particles after drying, using an electric balance accurate to 2 decimal places.

3.8) Preliminary testing and pH trial

A pH trial was conducted to evaluate the effect of pH on the particle characteristics, as information regarding the effect of pH in CHS on iron oxides is scarce. In experimental runs a, b and c shown Figure 3.9, the pH was altered in increasing increments through the addition of a concentrated NaOH solution, while other parameters were kept constant at 0.04M concentration, 300°C reaction temperature and a 50 ml/min flow rate. As the pH was increased from 1.79 to 5.26 to 9.79, particle aggregation occurred to such an extent that it was not possible to determine the crystallite size.

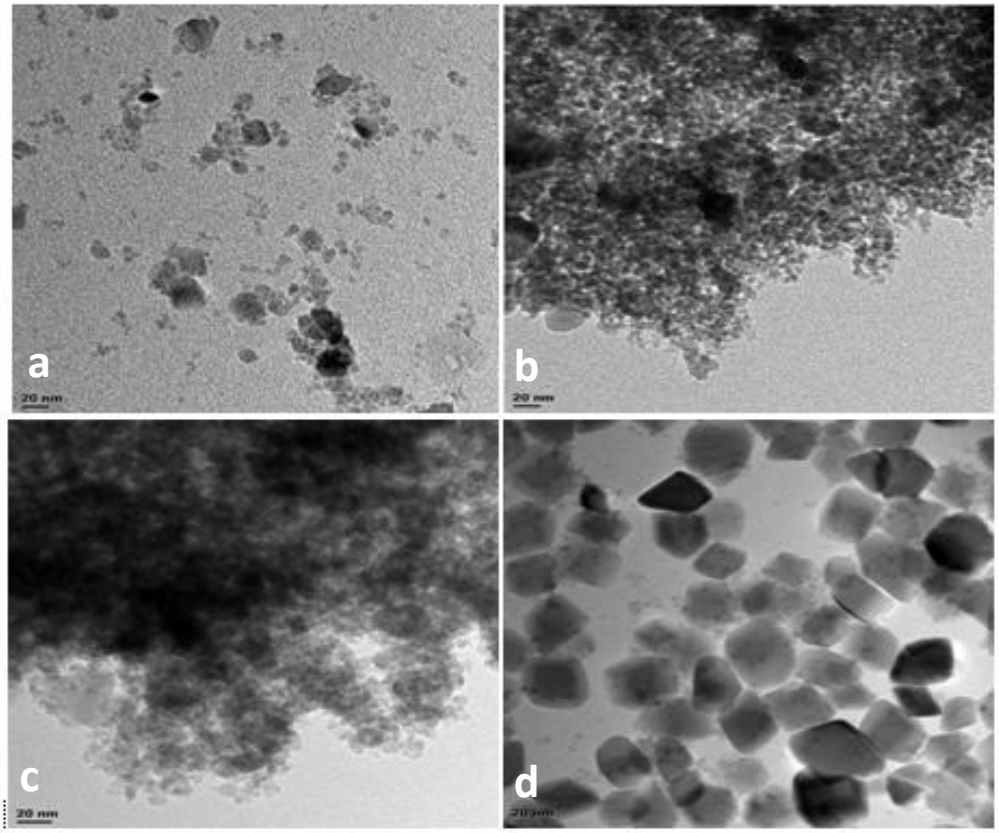

Figure 3. 9- TEM images of a pH trial where all experiments were conducted at a reaction temperature of 300°C and a flow rate of 50ml/min with a) 0.04M and 1.79 pH b) 0.04M and 5.26 pH c) 0.04M and 9.79 pH and d) 0.2M and 1.78 pH

Demopoulos (2009), touched on the effect of pH in aqueous crystallization systems and mentioned that hydrolysis is a pH dependent reaction and therefore affects the solubility and hence supersaturation rate. Yet the observed particle aggregation was linked to the change in zeta potential. The zeta potential has been defined as the electric potential in the double layer at the

interface between a particle which moves in an electric field and the surrounding liquid (Ohtsubo & Yoshimura 1991).

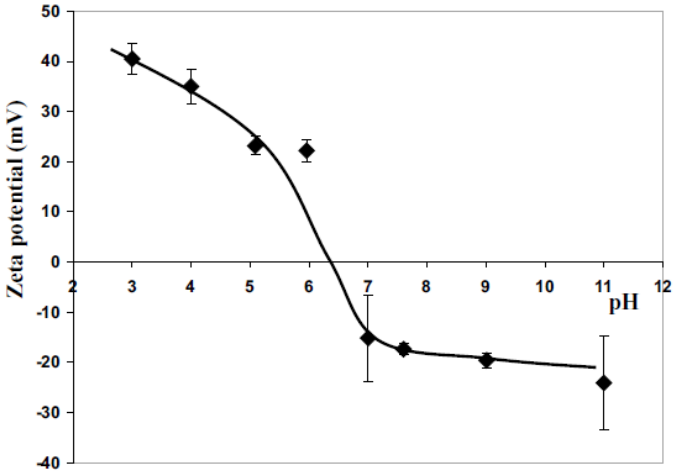

Figure 3. 10- Dependency of pH on the zeta potential of hematite phase iron oxide - adapted from Pan et al. (2004)

The stability of particles in suspension has been correlated to the zeta potential, and stability is increased as the zeta potential deviates from a zero charge either in the negative or positive domain. The zeta potential has been found to be highly influenced by the pH of the solution, and the effect of pH on the zeta potential of hematite particles in solution has been shown in Figure 3.10 (Pan et al. 2004). It can be seen in Figure 3.10 that as the pH of the solution exceeds 3, the zeta potential tends to zero. This zero charge is obtained around roughly a 6.4 pH, continuing the zeta potential tends to decrease slightly until pH 11. It can be concluded that particles are most stable below a pH of 3, and that the aggregation observed with an increase in pH in Figure 3.9 is associated with the decrease in zeta potential. As particle aggregation is undesired, the pH of all precursor solutions were adjusted to 1.8 using a 7 molar solution of NaOH.

3.9) Box-Behnken factorial design

A 3-level Box-Behnken factorial design was used to statistically analyse the interactions between operating parameters using Stat Ease Design Expert V 7.0.0. It has been identified by Mujtaba et al. (2014) as an effective method for exploration of quadratic response surfaces for the construction of second order polynomial models, aiding in process optimization. The selected parameters included precursor concentration, reaction temperature and flow rate (Table 3.4) and were evaluated by

studying their interactions and effect on particle size, size distribution, particle relative crystallinity and molar conversion or yield.

Table 3. 4 - Variables in Box-Behnken design

Formulation variables	Levels used		
	Low	medium	high
Concentration (mol/dm)	0.1 (-1)	0.25 (0)	0.4 (+1)
Temperature (°C)	250 (-1)	300 (0)	350 (+1)
Flow rate (ml/min)	50 (-1)	75 (0)	100 (+1)

The factorial trial also allowed for accurate point prediction within the range of operating parameters highlighted in Table 3.4. In some cases, accurate predictions were used to obtain values within the range of parameters in order to highlight specific trends. The summarized data and responses of the experimental runs are depicted in Table 3.5 and the full experimental conditions with variation are shown in Table 3.6.

Table 3. 5 - Factorial trial sample matrix - Operating parameters and their respective particle characteristics

Run	Concentration (mol/dm^3)	Temperature (°C)	Flow rate (ml/min)	Size (nm)	Coefficient of variation (%)	Relative Crystallinity (%)	Product yield (%)
1	0.1	300	100	31.3	20.1	60.0	17.2
2	0.25	350	100	47.6	18.3	84.5	62.0
3	0.4	300	100	58.3*	24.7*	55.8	55.6
4	0.25	300	75	42.9	22.1	78.2	44.5
5	0.1	300	50	33.8	14.8	98.9	31.3
6	0.1	350	75	35.1	20.5	98.5	34.4
7	0.25	250	50	42.8	15.7	100	36.3
8	0.4	250	75	50.4*	22.6*	48.1	25.0
9	0.1	250	75	43.2*	26.4*	78.2	14.1
10	0.25	300	75	46.2	16.7	81.5	43.8
11	0.25	350	50	45.9	16.8	98.7	33.8
12	0.25	250	100	39.5*	19.7*	72.2	24.4
13	0.4	350	75	51.8	19.7	60.0	48.5
14	0.4	300	50	57.2	15.9	83.0	39.1
15	0.25	300	75	42.9	17.5	96.3	30.7

* - only 100 particles counted

Table 3. 6 - pH and temperature variation during experimental runs

Run	Concentration (mol/dm^3)	Temperature (°C)	Flow rate (ml/min)	pH before	pH after	Start mixer temp (°C)	End mixer temp (°C)	Start reactor temp (°C)	End reactor temp (°C)
1	0.1	300	100	1.84	1.11	300	303	286	290
2	0.25	350	100	1.82	0.98	347	351	334	337
3	0.4	300	100	1.80	1.29	300	305	291	298
4	0.25	300	75	1.86	1.29	300	305	290	295
5	0.1	300	50	1.83	1.21	300	313	290	299
6	0.1	350	75	1.86	1.11	348	348	335	335
7	0.25	250	50	1.80	1.11	250	262	244	260
8	0.4	250	75	1.81	1.27	250	277	243	267
9	0.1	250	75	1.83	1.44	250	258	242	248
10	0.25	300	75	1.81	0.97	300	309	289	296
11	0.25	350	50	1.80	0.88	339	349	327	332
12	0.25	250	100	1.80	1.2	250	255	244	249
13	0.4	350	75	1.81	1.01	349	358	336	342
14	0.4	300	50	1.81	1.01	300	323	289	304
15	0.25	300	75	1.82	1.02	300	314	290	300

3.10) Particle characterisation

Common characterization techniques for nanoparticles were discussed previously in Chapter 2, however, the exact experimental conditions are provided in this section.

3.10.1) Transmission Electron Microscopy

High resolution Transmission Electron Microscopy or HRTEM was performed at the University of Cape Town. The iron oxide particles were dispersed in methanol and then sonicated for 20 minutes prior to being placed onto a copper-coated carbon grid. Once dried, the samples were placed inside the TEM and the surface morphology of the nanoscale crystals was studied using a Tecnai TF20 thermoionic TEM, equipped with a LaB6 filament and a Gatan GIF energy filter. The images were captured at 200keV in bright field mode. Using Image J version 1.47 software, 200 individual crystals were counted in order to determine the average particle size (APS) and particle size distribution (PSD). In some cases, only 100 particles were counted if the TEM images revealed large numbers of aggregates. The effect of operating parameters were analysed on the resulting average particle size as the process parameters were varied in the factorial trial.

3.10.2) Particle size distribution (PSD)

Using the data collected from counting 200 individual crystals, the mean particle size and standard deviation were calculated using Microsoft Excel 2010. The mean particle size and standard deviation were then used to calculate the coefficient of variation which is a more accurate representation of the particle size distribution. The coefficient of variation has been defined as the percentage expression of standard deviation by Jain and Sandhu (2009), and provided a quantitative method for analysing the PSD. The coefficient of variation can be calculated as follows:

$$CV = \frac{standard\ deviation}{mean\ particle\ size} \times 100 \qquad \text{(Equation 3.1)}$$

The effect of process parameters on the resulting particle size distribution were therefore analysed by evaluating the coefficient of variation under different process conditions.

3.10.3) X-Ray diffraction (XRD) and Relative Crystallinity

X-ray diffraction was conducted at the University of Cape Town. The as prepared samples were examined using XRD, by plotting the angular positions, 2θ, and their resulting intensities. The information from the diffraction patterns about the crystal structure of the synthesized particles was

determined from the peak position, intensity and profile. The characterization was performed using a Phillips PW 3830/40 generator with a PW 3710 mpd control X-ray diffraction system with Cu-Kα radiation (λ = 1.506 $\mathring{A}$) and the scan was conducted between 5 and 70 degrees with a 0.02 degree step width. The crystal phase was then identified and evaluated using X'PertHighscore (PANalytical. version 2.2c) software. All samples were found to be hematite (α-Fe_2O_3) phase iron oxide, with an example of the diffraction pattern of run 7 in Figure 3.11.

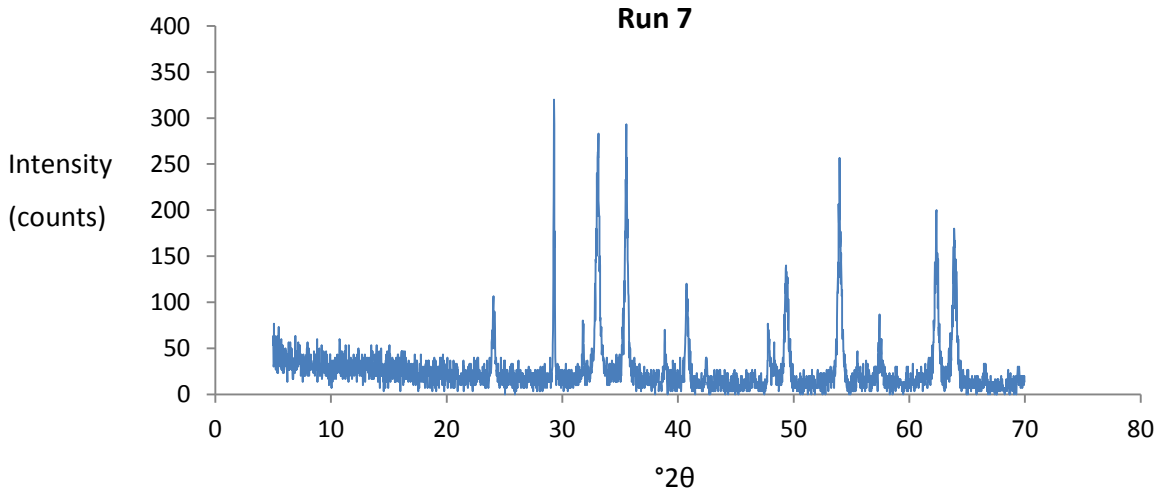

Figure 3. 11 - An example of the hematite diffraction patterns - using Run 7

The degree of crystallinity was determined using a method described by Mainganye (2012), where the sum of the peak intensities for were collected from the XRD data set and compared to the reference sample of the highest sum of peaks in this study. The major peaks were selected specifically as they are least influenced by factors such as the degree of hydration (Mainganye, 2012). Therefore a relative crystallinity percentage could be obtained, converting the qualitative diffraction patterns into a quantitative crystallinity percentage. The relative crystallinity can be represented as follows in Equation 3.2 (Gosh et al. 1994).

$$\text{Relative crystallinity} = \frac{Sum\ of\ area\ under\ the\ XRD\ peaks\ of\ the\ product}{Sum\ of\ area\ under\ the\ XRD\ peaks\ of\ the\ reference\ sample} \times 100 \qquad \text{(Equation 3.2)}$$

The relative crystallinity was therefore evaluated according to a change in process parameters, highlighting the effect of concentration, temperature and flow rate on the resulting RC.

3.11) Conclusion

The various CHS pilot plants reported by other research groups and their design aspects have been summarised and evaluated. Through the analysis of other pilot plants designs and by taking into

account potential problems highlighted by other researchers, an optimal design was conceptualised and a CHS pilot plant was constructed and commissioned at the Cape Peninsula University of Technology in Cape Town, South Africa. The pilot plant constructed and utilized in this study was mainly influenced by the experimental setup used by the Georgia Institute of Technology, however, numerous modifications were made in order to improve the CHS plant performance. The modifications included the use of two plate heaters in series for more effective, consistent heating of the water stream; The addition of a pipe in pipe cooler in the precursor stream prior to mixing, in order to prevent premature crystallization; and the cooling column was fastened at a 30 degree angle relative to the horizontal in order reduce particle settling, which may lead to potential blockages. A full design and individual component breakdown was provided, along with a description of the commissioning process.

Preliminary testing and a pH trial were conducted, firstly confirming that nanoscale particles were synthesized and secondly that the pH has a significant effect on particle characteristics. The pH was adjusted using a concentrated NaOH solution, and was found to promote particle aggregation at higher pH values. The pH was therefore adjusted to 1.8 for all further experiments. A 3-level, 3-factor Box-Behnken factorial trial was performed, which was used to evaluate the effect of concentration, temperature and flow rate on the resulting APS, PSD, PY and RC. All particles were characterized through TEM and XRD analysis. The results of the effect of operating parameters and their interactions on the resulting particle characteristics are discussed in Chapter 4 and 5. A brief study on particle morphology and the effect of solvents and surface modifiers is presented in Chapter 6.

Chapter 4 – Effect of operating parameters on the resulting average particle size (APS) and particle size distribution (PSD).

4.1) Introduction

In this chapter, the effect of concentration, reaction temperature and flow rate have also been evaluated individually and discussed with respect to their resulting effect on APS and PSD. The correlation factors between the operating parameters and the resulting average particle size (APS) and particle size distribution (PSD) are presented, and the interactions between parameters were identified and discussed.

The following topics below are presented in this chapter in the following order:

- Effect of individual operating parameters on APS
  - Effect of precursor salt concentration on APS
  - Effect of reaction temperature on APS
  - Effect of flow rate on APS
- Effect of operating parameter interactions on APS
- Effect of individual operating parameters on PSD
  - Effect of precursor salt concentration on PSD
  - Effect of reaction temperature on PSD
  - Effect of flow rate on PSD
- Effect of operating parameter interactions on PSD

4.2) Factors influencing average particle size

4.2.1) Effect of individual operating parameters on APS

The factors influencing the average particle size of iron oxide nanoparticles were evaluated through a 3-level Box-Behnken factorial trial analysis as discussed in Chapter 3. The particle size was found to be majorly influenced by the concentration of the precursor solution, with very slight albeit negligible effect of temperature and flow rate as shown in Table 4.1.

Table 4. 1 - Correlation factor of operating parameters on average particle size

Operating parameter	Correlation factor on APS
Concentration	0.893
Temperature	0.054
Flow rate	-0.036

4.2.2) Effect of precursor salt concentration on average particle size (APS)

The effect of concentration was evaluated by observing the effect on APS at high and low concentrations. The concentration of the precursor solutions were varied between 0.1M and 0.4M at a range of different operating conditions as shown in Table 4.2 and the representative HR TEM images in Figure 4.1.

Table 4. 2 - Comparison of high and low concentrations at varied operating parameters and the resulting effect on APS

Letter	Run	Concentration (mol/dm^3)	Temperature (°C)	Flow rate (ml/min)	Size (nm)
a	9	**0.1**	250	75	**43.2***
b	8	**0.4**	250	75	**50.4***
c	1	**0.1**	300	100	**31.3**
d	3	**0.4**	300	100	**58.3***
e	5	**0.1**	300	50	**33.8**
f	14	**0.4**	300	50	**57.2**
g	6	**0.1**	350	75	**35.1**
h	13	**0.4**	350	75	**51.8**

* - only 100 particles counted

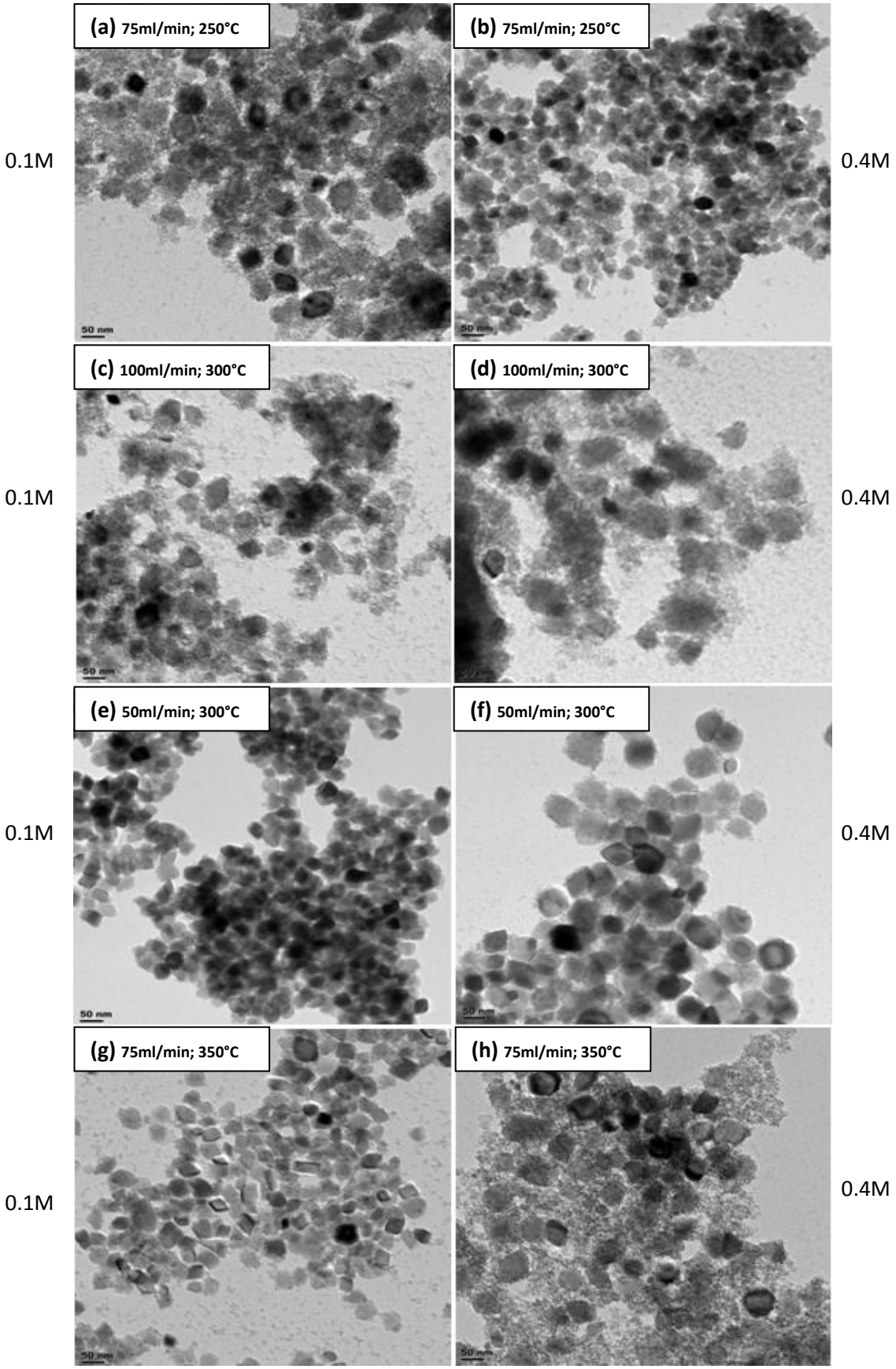

Figure 4. 1 - HR TEM images showing the effect of concentration at varied operating parameters

The correlation factor of 0.893, as depicted in Table 4.1, indicates that the concentration had a significant effect on the average particle size. The APS increased between 16% to 86%, as the concentration was increased from 0.1M to 0.4M at different combinations of temperature and flow. Similar findings were reported by Xu and Teja (2008), who found an increase in particle size from 15.6nm to 27.4nm as the precursor concentration was increased from 0.03M to 0.06M.

Hao and Teja (2003) also studied the effect of concentration on the size of iron oxide nanoparticles produced via CHS. The precursor solution varied at several increments from 0.01M to 0.5M at a constant reaction temperature of 573K (300°C), a constant pressure of 25MPa and a constant residence time of 12 seconds (flow rate not specified). Figure 4.2 shows a comparison of the results found by Hao and Teja (2003) and those found in this study at similar conditions (same temperature and pressure yet at a higher flow rate i.e. lower residence time - 1.27s). Hao and Teja (2003) used a logarithmic model (Equation 4.1) to describe the particle growth as a function of concentration, where D is representative of the average particle size (nm) and c is the concentration (mol/dm^3).

$$D = 4.938 \ln c + 35.15 \quad \text{(Equation 4.1)}$$

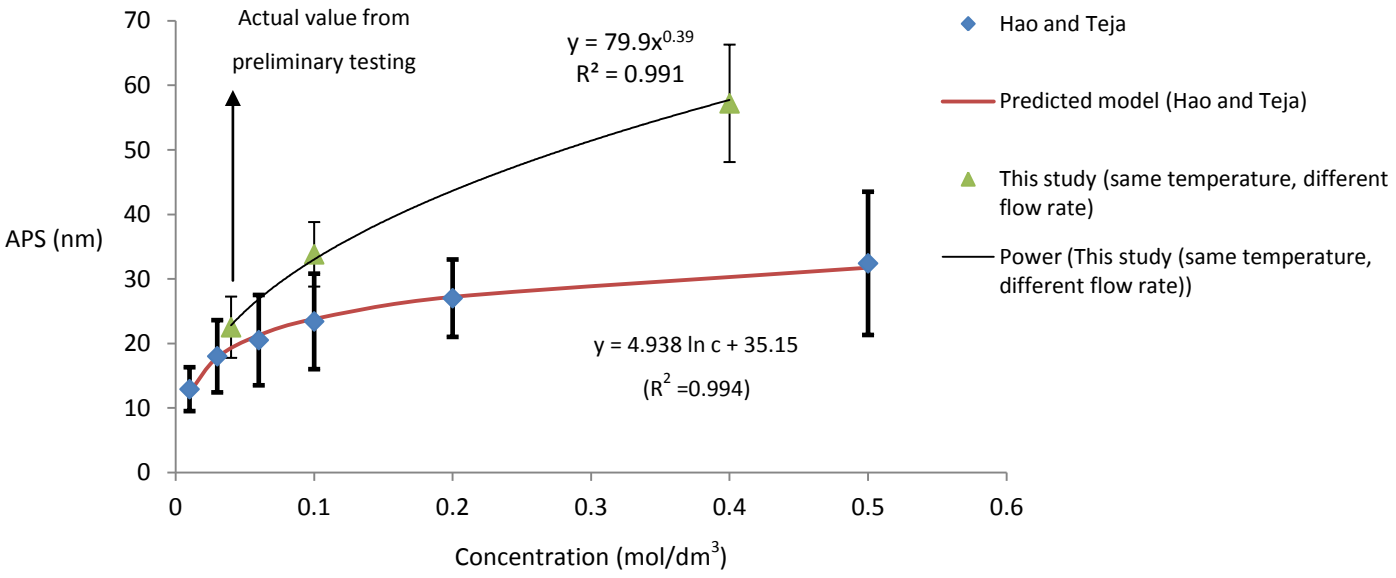

Figure 4. 2 - Comparison of average particle size (APS) versus concentration

When adding a data point from preliminary testing (0.04M), the APS increase with concentration in this research followed a power law trend (Equation 4.2) in comparison to Hao and Teja (2003), as depicted in Figure 4.2.

$$D = 79.9c^{0.39} \quad \text{(Equation 4.2)}$$

Xu (2006) performed solubility modelling using OLI software to evaluate the effect of concentration on the solubility of ferric nitrate ions under reaction conditions. Out of numerous soluble ions, $Fe(OH)_2^+$; Fe^{3+}; Fe^{2+} and $Fe(OH)^{2+}$ were deemed the most significant at the reaction conditions of 300°C and 240atm. As depicted in Figure 2.17, Xu (2006) identified that higher concentrations of metal salt solutions slightly increased the solubility of species in solution at the reaction conditions. Therefore the species solubility was found to be dependent on the precursor concentration. This showed that the level of supersaturation increases with increasing precursor concentration, although not as much as expected, due to the accompanying increase in solubility. According to particle growth theory, the critical size of monomer formation has been directly related to the degree of supersaturation (Demopoulos 2009). In practical terms, Demopoulos (2009) identified that a higher level of supersaturation would yield a greater number of fine particles. Although he further stated that particle aggregation is linked to the ionic strength of solutions, and aggregation was favoured as the precursor concentration increased.

The reason for larger particles reported in this study when compared to those of Hao and Teja (2003) are not clear, although it is assumed to be related to different residence times, mixing conditions and potentially the reactor dimensions. Numerous authors have reported an increase in APS with increased residence time due to particle aggregation (Hao & Teja 2003; Xu 2006; Sue et al. 2011). Although the lower residence times calculated in this study should result in a reduction in APS, other factors have also been identified to promote particle aggregation. When looking at the reactor dimensions, the diameter may play a larger role in nuclei "crowding" compared to the reactor length. Demopoulos (2009) documented that aggregation is also a function of colloid population density. Therefore the use of Swagelok's thickest $^1/_4$ inch tubing in this study (6.35mm OD; 3.05mm ID) and hence smallest ID is likely to have a smaller diameter than that used by Hao and Teja (2003). This is one possibility, as neither the diameter nor the length of the reactor were specified by Hao and Teja (2003). However the lack of comparison of mixing conditions is also of concern, as several studies have discussed how mixing conditions can affect the APS as identified in section 2.5.3.

Taking into account the solubility modelling and the growth comparison, the increase in APS with concentration was postulated as follows. At the high concentrations evaluated in this study, an abundance of monomers formed at the mixing point although not all Fe^{3+} ions nucleated instantaneously. Therefore the remaining ions in solution precipitated through secondary nucleation

onto the surface of the initially formed monomers along the length of the reactor, driven by the high concentration gradient. While concurrently, particle aggregation occurred during particle growth, supported by the high ionic strength of the solution and the small reactor diameter. This is in agreement with Xu (2006), who reported that an increase in APS with concentration must be due to particle growth, and that higher numbers of particles in solution favours aggregation due to increased probability of particle contact in solution. It is also noted that OR kinetics, or a dissolution-precipitation based mechanism may be present, as this mechanism would support particle growth of relatively spherical particles. The increased particle contact and growth due to high colloidal density may also be related to OR kinetics, as Gilbert et al. (2003) also advised that diffusion based growth can occur through particle contact. While Liang et al. (2010) proposed that OR kinetics were responsible for the growth of iron oxide particles in CHS, it is more likely that a combination of the above mentioned factors play a role on particle growth.

4.2.3) Effect of reaction temperature on average particle size (APS)

The effect of temperature was evaluated by observing the effect on APS at high and low reaction temperatures. As discussed in section 2.7.4, changing the temperature is well known to affect several other reaction conditions, including density, viscosity and residence time, and is therefore difficult if not impossible to isolate (Cote et al. 2003). The reaction temperature was increased from 250°C to 350°C at a range of different operating conditions as shown in Table 4.3 and the representative HR TEM images in Figure 4.3.

Table 4. 3 - Comparison of high and low concentration at varied operating parameters

Letter	Run	Concentration (mol/dm^3)	Temperature (°C)	Flow rate (ml/min)	Size (nm)
a	9	0.1	**250**	75	**43.2***
b	6	0.1	**350**	75	**35.1**
c	7	0.25	**250**	50	**42.8**
d	11	0.25	**350**	50	**45.9**
e	12	0.25	**250**	100	**39.5***
f	2	0.25	**350**	100	**47.6**
g	8	0.4	**250**	75	**50.4***
h	13	0.4	**350**	75	**51.8**

* - only 100 particles counted

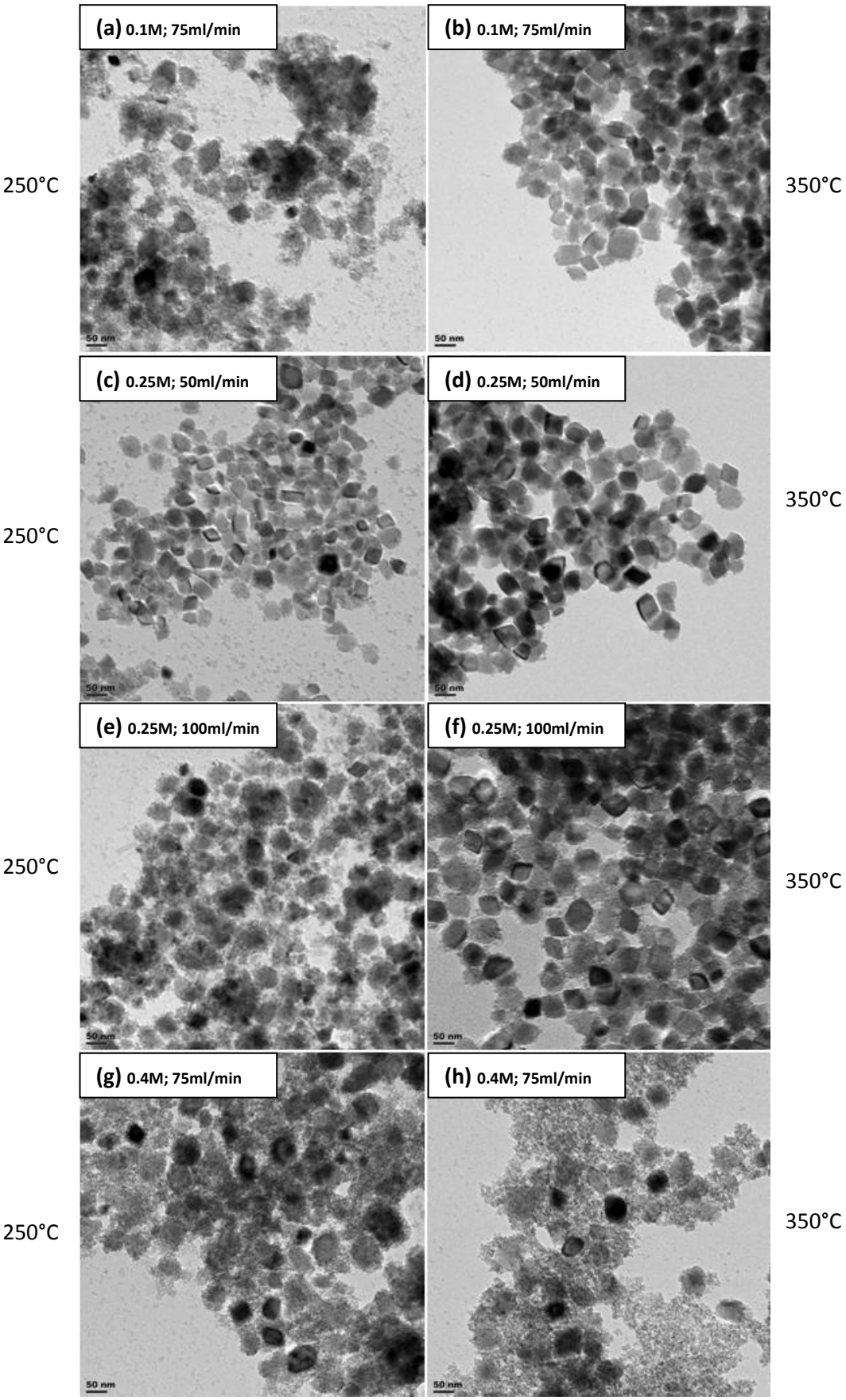

Figure 4. 3 - HR TEM images showing the effect of temperature at varied operating parameters

The effect of reaction temperature had very little effect on the APS and was found to fluctuate between -19% to +21%. A low correlation factor of 0.054 was also determined for the significance of temperature on APS as shown in Table 4.1. However, the effect of temperature on APS in CHS has been hotly debated since its origin in the early 1990's, with conflicting reports often cited (Xu 2006). Hao and Teja (2003) reported that temperature has no evident effect on the size of iron oxide nanoparticles, while Xu and Teja (2008) identified that particle size increased with increasing temperature. On the contrary, it was shown by Hakuta et al. (1998) that ceria particles decreased in size along with an increase in temperature.

Liang et al. (2010) studied the effect of reaction temperature on particle size. They synthesized hematite particles by mixing a 0.1M stream of aqueous ferric nitrate solution at 3ml/min with a stream of 30ml/min supercritical water at 30MPa. The effect of reaction temperature on APS was found to double in size from 20nm to 40nm when the temperature increased from 250°C to 350°C. It was noted by Xu (2006), that classic nucleation theory predicts that smaller particles will be formed at higher temperatures due to increased levels of supersaturation. However the increased temperature influences the diffusivity of the solute as it approaches the supercritical region. Therefore an increase in crystal size may be linked to an increase in the diffusivity coefficient at higher temperatures. The particle size has also been observed to decrease slightly around the supercritical temperature, which has been attributed to lesser particle aggregation due to a decrease in surface tension of water as it approaches the supercritical region (Hayashi et al. 2010; Liang et al. 2010). The evidence presented shows how the effect of temperature can have numerous consequences on the resulting APS.

It has been shown thus far that two researchers agree that there is negligible effect of temperature on APS for iron oxide particles synthesized via CHS, including Hao & Teja (2003) and this study. Another two authors agree that a substantial increase in APS occurs along with an increase in temperature for iron oxide particles produced using CHS (Xu & Teja 2008; Liang et al. 2010). Although these findings appear to contradict one another, they may be identifying different dominating growth mechanisms under different conditions.

4.2.4) Effect of flow rate on average particle size (APS)

The effect of flow rate was evaluated by observing the resulting effect on APS at high and low rates of flow. The flow rates were increased from 50ml/min to 100ml/min at a range of different operating conditions as shown in Table 4.4 and the representative HR TEM images in Figure 4.4.

Table 4. 4 - Comparison of high and low flow rates at varied operating parameters

Letter	Run	Concentration (mol/dm^3)	Temperature (°C)	Flow rate (ml/min)	Size (nm)
a	7	0.25	250	**50**	**42.8**
b	12	0.25	250	**100**	**39.5***
c	5	0.1	300	**50**	**33.8**
d	1	0.1	300	**100**	**31.3**
e	14	0.4	300	**50**	**57.2**
f	3	0.4	300	**100**	**58.3***
g	11	0.25	350	**50**	**45.9**
h	2	0.25	350	**100**	**47.6**

* - only 100 particles counted

The effect of flow rate had two fundamental influences on the system, namely the mixing conditions and the residence time in the reactor. The residence time decreased significantly as the flow rate increased, while an increase in flow rate was also expected to improve turbulence and mixing. The residence time, τ, can be determined using Equation 4.3, which has been reported by numerous authors (Adschiri et al. 2001; Hao & Teja 2003; Xu 2006),

$$\tau = \frac{V}{Q\left(\frac{\rho_{25°C}}{\rho_T}\right)} \qquad \text{(Equation 4.3)}$$

where τ is the residence time (seconds), V is the volume of the reactor (m^3), Q is the volumetric flow rate (m^3/s), $\rho_{25°C}$ is the density of water at 25°C (kg/m^3) and ρ_T is the density of water at the reaction conditions (kg/m^3). As the ferric nitrate concentrations are relatively low, the densities are assumed to be those of pure water. The residence time of all 15 experimental runs can be found in Table 4.5.

Table 4. 5 - Residence times of different experimental runs in the factorial trial

Run	Concentration (mol/dm^3)	Temperature (°C)	Density (kg/m^3)	Flow rate (ml/min)	Residence time (s)
1	0.1	300	720	100	**0.63**
2	0.25	350	620	100	**0.55**
3	0.4	300	720	100	**0.63**
4	0.25	300	720	75	**0.84**
5	0.1	300	720	50	**1.27**
6	0.1	350	620	75	**0.73**
7	0.25	250	805	50	**1.42**
8	0.4	250	805	75	**0.94**
9	0.1	250	805	75	**0.94**
10	0.25	300	720	75	**0.84**
11	0.25	350	620	50	**1.09**
12	0.25	250	805	100	**0.71**
13	0.4	350	620	75	**0.73**
14	0.4	300	720	50	**1.27**
15	0.25	300	720	75	**0.84**

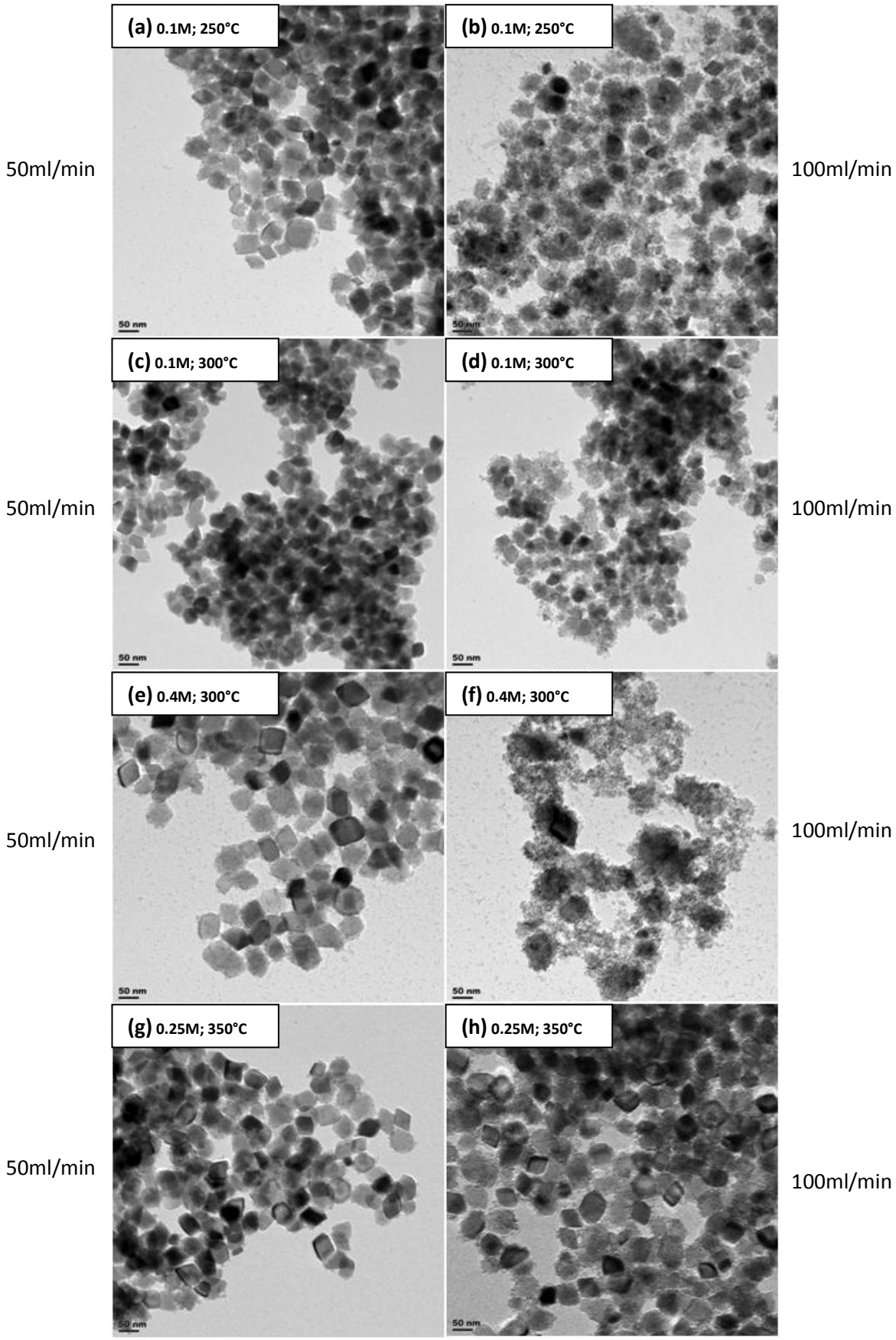

Figure 4. 4 - HR TEM images showing the effect of flow rate at varied operating parameters

The effect of flow rate on APS was found to be almost negligible, with a -0.036 correlation factor as depicted in Table 4.1. The APS tended to fluctuate between -8% to +4% as the flow rate was increased from 50ml/min to 100ml/min at different combinations of temperature and concentration. The effect of residence time on APS was studied by Hao and Teja (2003), Xu (2006), and Sue et al. (2011). Xu (2006) changed the length of their reactor (5cm, 10cm and 20cm) to ensure that the mixing conditions were not affected, and resulted in residence times in the range of 2.6-10.4s respectively. In contrary, Hao and Teja (2003) varied the flow rates (in some cases the flow ratios - but overall concentrations were constant) in order to achieve residence times in the range of 10-20s. While Sue et al. (2011) changed the length of their reactor between 1-4m and calculated the resulting residence times to a range of 0.13-2.03s. The resulting APS with residence time and the corresponding operating parameters has been replotted in Figure 4.5.

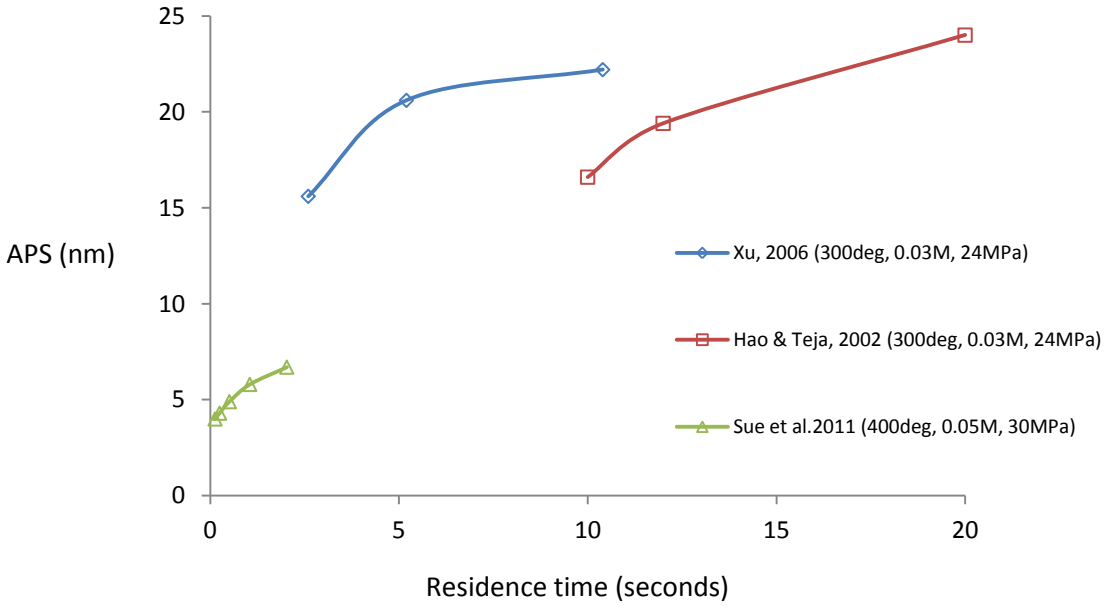

Figure 4. 5 - Effect of residence time on APS reported by different researchers at different operating parameters

As depicted in Figure 4.5, in all cases APS tended to increase with an increase in residence time. Xu (2006) made reference to the critical residence time at which particle growth stops due to dissolution and precipitation and particle aggregation becomes responsible for and increase in particle size with time. This critical residence time was found to be 5 seconds in his study. Although Hao and Teja (2003) didn't identify this critical residence time, a change in growth tends to occur around 12 seconds. Sue et al. (2011) studied the effect of residence time on APS within a similar

range of this research, where no critical residence time was observed which may indicate that the particle growth was still being dominated by OR kinetics.

The flow rates used in this study were relatively high, and due to the relatively short reactor length (20cm) and the small reactor ID (3.05mm), short residence times were achieved by changing the flow rates resulting in residence times from 0.55 - 1.42 seconds as shown in Table 4.5. Looking closely at the effect of flow rate on APS, when the flow rate is increased two different factors occur. Firstly, as the flow rate increases the residence time decreases allowing less time for particle growth and aggregation. Secondly, increased flow rates increases the Reynolds number as shown in Equation 2.3, which inturn increases flow turbulence. A study performed by Kawasaki et al. (2010) was found to reduce the APS as turbulence was increased.

When looking at Figure 4.5, work by Xu (2006) and Hao and Teja (2003) were both conducted at the same operating parameters. The difference being that Xu (2006) changed their reactor length in order to isolate residence time, while Hao & Teja (2003) just changed the flow rate to vary the residence time (in some cases the flow ratios - but overall concentrations were constant). Although the trends were similar, the APS was found to be different at the same residence time of roughly 10 seconds. This shows how the flow rate, and hence mixing conditions, play a role on APS. Therefore the small, although almost negligible decrease in APS with an increase in flow rate identified in this study was attributed to an increase in mixing turbulence, as the residence time range studied was very small.

4.3) Effect of operating parameter interactions on APS

4.3.1) Effect of operating parameter interactions on APS

The true effectiveness of the factorial trial method comes from the unique ability to evaluate the interactions between operating parameters on specific particle characteristics. Figure 4.6 depicts the percentage contribution of parameters and parameter combinations, hence revealing the influence of parameter interactions on the resulting APS. These interactions can also be observed by analysing Figure 4.7a and 4.7b.

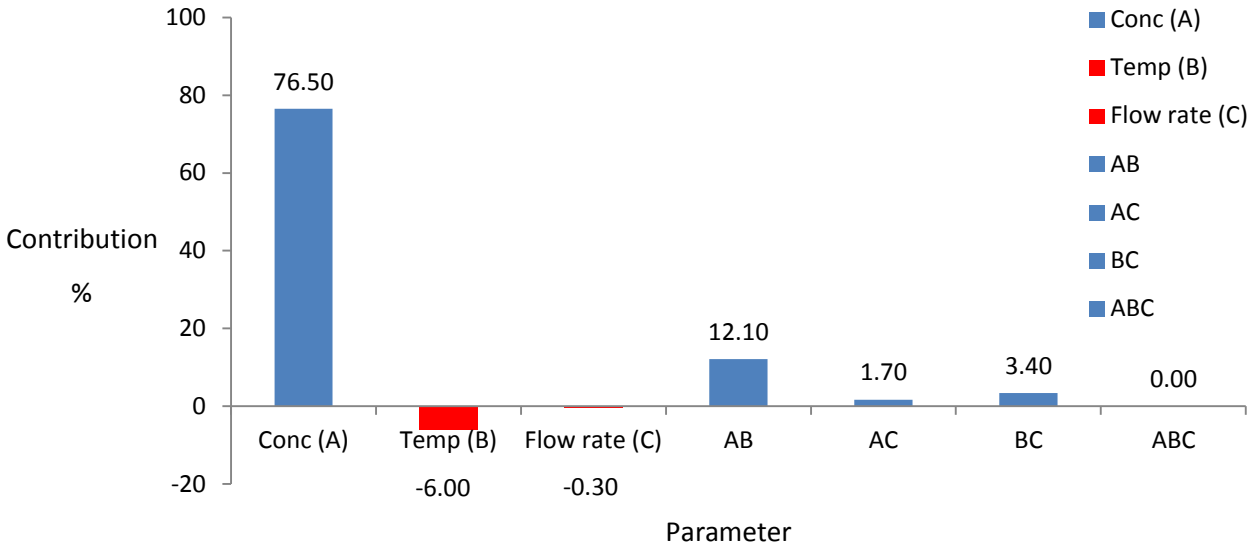

Figure 4. 6 - Contribution percentage and interaction of operating parameters on the resulting APS (Blue = positive effect; Red = negative effect)

A model to predict the APS was also derived through the factorial trial and is presented in Equation 4.4. This model can be used to predict the average particle size within the range of the factorial trial, by substituting the values of A,B and C within their -1 to 1 range as shown in Table 3.4.

$$APS = 44.00 + (9.29*A) + (0.56*B) + (-0.37*C) + (2.38*AB) + (0.90*AC) + (1.25*BC) + (1.16*A^2) + (-0.037*B^2) + (-0.013*C^2) \quad \text{(Equation 4.4)}$$

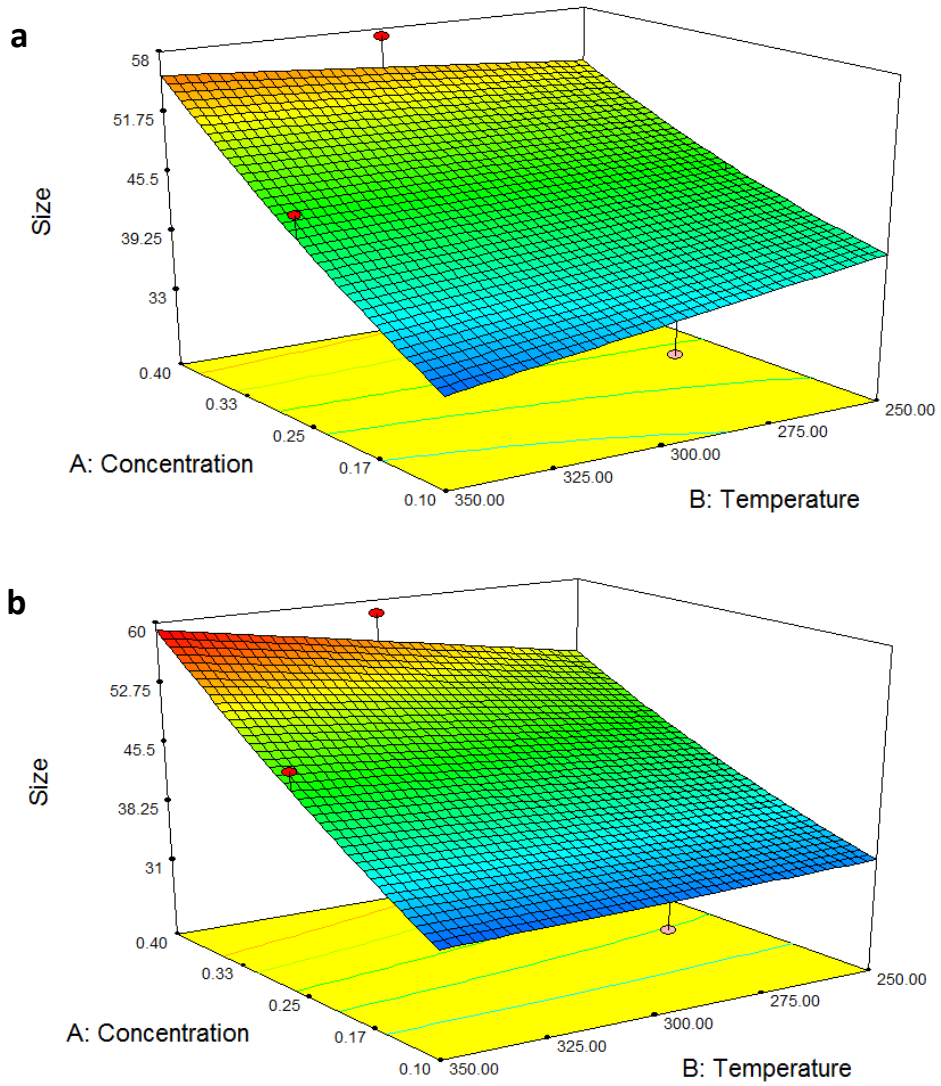

Figure 4. 7 - 3D quadratic plot of concentration versus temperature on the effect on particle size at (a) low flow rate - 50ml/min and (b) high flow rate - 100ml/min

4.3.2) Effect of the interaction between concentration and temperature on APS

The interaction between concentration and the reaction temperature, parameter AB, was found to have the largest interaction effect on particle size, with a 12.1% contribution factor as depicted in Figure 4.6. Interactions between these two operating parameters has led to conflicting reports in the literature, and in this study was found to have the second largest contribution percentage effect on APS. This contribution was higher than temperature alone, thus highlighting the ineffectiveness of evaluating operating parameter through isolation. This interaction was related to both parameters having a large effect on the level of supersaturation and growth kinetics. As noted previously, solubility modelling performed by Xu (2006) identified that at higher concentrations the solubility of

species in solutions increases exponentially, although an overall increase in supersaturation levels is still achieved as the precursor solution increases within the range of this study. While an increase in temperature decreases solubility and hence increases the degree of supersaturation. Although these occurrences both increase the degree of supersaturation, the key lies in the diffusion coefficient. Xu (2006) further stated that the diffusion coefficient was found to increase as the reaction temperature approached the supercritical region. An increased diffusion coefficient has also been linked to an increase in dominant crystal size (Cahn et al. 1991). Therefore it has been proposed that when the rate of diffusion and concentration are both high, rapid particle growth is promoted as shown in Figure 4.7a and 4.7b.

Using the factorial trial model for APS (Equation 4.4), accurate APS predictions were made at various combinations of concentration and temperature at constant flow. It can be shown from Figure 4.8 that the effect of temperature is highly dependent on the concentration of the precursor solution. At a 0.1M concentration, the APS was found to decrease linearly from 40.2nm down to 34nm as the temperature increased from 250°C to 350°C. Yet at a 0.25M concentration, the effect of temperature on APS was found to have little effect. The particle size was found to gradually decrease from 45nm to 43.6nm at 0.25M. While at the highest concentration of 0.4M used in this study, the APS was found to increase in a linear fashion from 52nm to 55.6nm. Therefore it can be deduced that under different concentrations, an increase in temperature may appear to show an increase in APS (0.4M), it may be shown to have negligible effect on average particle size (0.25M) or it may take on a downward trend or show a decrease in APS (0.1M).

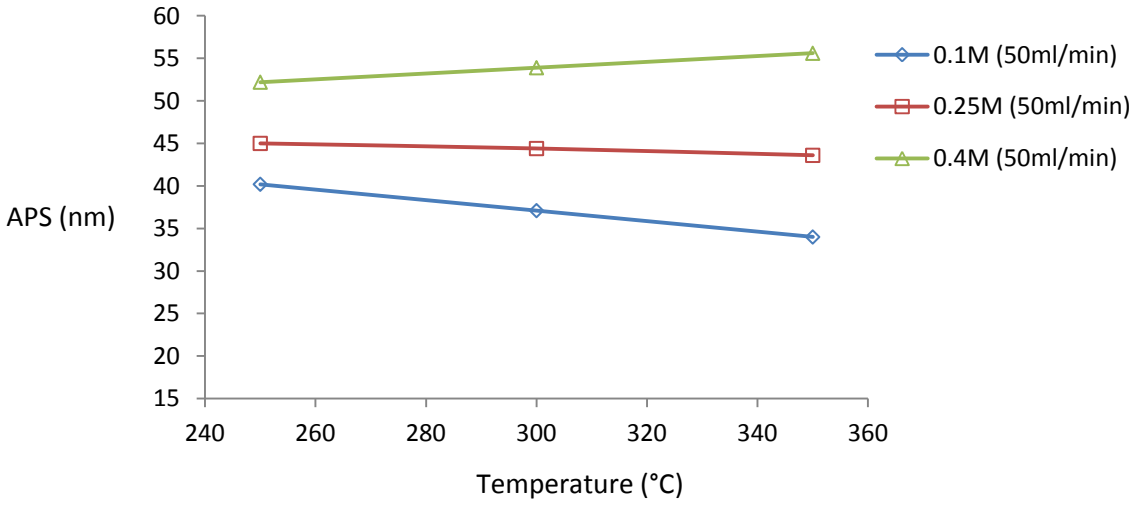

Figure 4. 8 - Prediction of the effect of temperature on APS at varied concentrations and 50ml/min flow rate

When comparing the effect of temperature on APS reported by different authors, it is important to keep in mind the sensitivity of temperature with concentration. Hao and Teja (2003) studied the effect of temperature at a concentration of 0.01M and 0.03M concluding a negligible effect of temperature on APS. Xu (2006) studied the effect of temperature also at 0.03M, yet their reaction was carried out in the presence of poly vinyl alcohol (PVA), which is known to affect the reaction kinetics and hence particle size, although an increase in temperature resulted in an increase of APS in their study. While Liang et al. (2010) used a constant concentration of 0.1M, yet they used a flow rate ratio of 1:10 precursor to water. When converting the concentration to a conventional 2:3 ratio (precursor: water) as used in this study and by other authors (Hao & Teja 2003; Xu 2006), it is comparable of 0.023M. Although this concentration is in the range of range of that studied by Hao and Teja (2003) (0.01M-0.03M), where an increase in temperature should have little effect on APS, an increase in APS was found with increasing temperature. This increase in APS was linked to poor mixing conditions, as the low flow rate of the precursor solution (3ml/min) would not have enough momentum to penetrate far enough into the water stream to promote efficient mixing and flow partitioning would more than likely occur (Blood et al. 2004).

This study has revealed that even when keeping all other parameters constant and evaluating the effect of temperature on APS at different concentrations, three different trends occurred. It was therefore proposed that the sensitivity of temperature to concentration may be responsible for the apparent conflicting reports and confusion in the literature. These trends also remained the same even when the flow rate and hence residence time was varied showing that the effect of temperature on APS was highly specific to the concentration of the precursor solution in this study.

4.3.3) Effect of the interaction between concentration and flow rate on APS

The interaction between the concentration and flow rate, parameter AC, was found to have an insignificant effect on APS with a contribution percentage of 1.7% as depicted in Figure 4.6. Although the concentration was a strong driving force for particle growth, when combined with the effect of flow rate a cancellation effect on APS occurred. At high flow rates, better mixing conditions are linked to a smaller particle size through rapid nucleation (Kawasaki et al. 2010), yet high concentrations are affiliated with increased particle aggregation and hence increased APS (Demopoulos 2009). While at lower rates of flow, less efficient mixing and an increase in residence time allowed for increased surface growth resulting in a slight increase in APS although surface growth has been reported to have a lesser influence during short residence times (Chen et al. 2011).

4.3.4) Effect of the interaction between temperature and flow rate on APS

Although the flow rate and temperature had almost zero effect on particle size by themselves, they were found to interact and have a minor 3.4% contribution on APS. The mild interaction between operating parameters BC, were identified to both favour rapid particle growth when they were both at their highest conditions. Figure 4.9 depicts the predicted values of APS at different residence times and reaction temperatures and a constant precursor concentration of 0.25M using the factorial trial model equation 4.4.

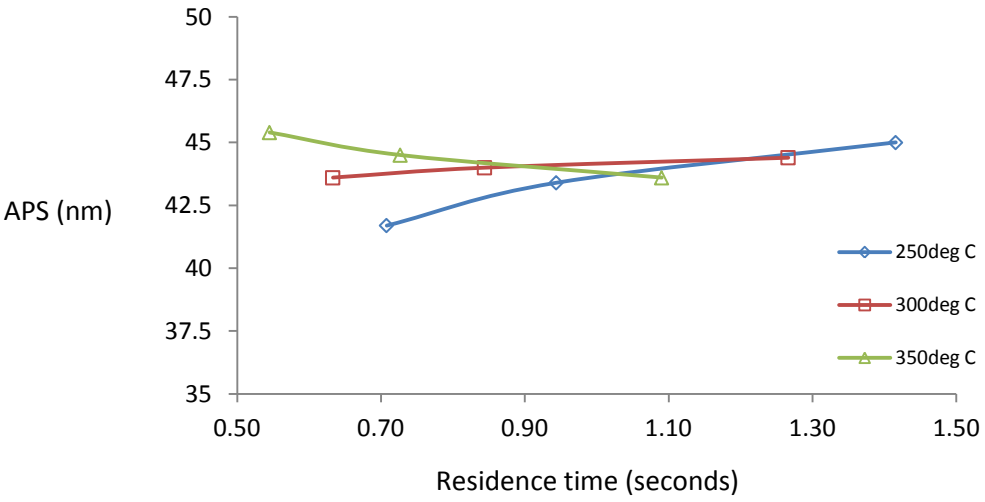

Figure 4. 9 - Predicted effect of residence time on APS at different reaction temperatures and at a 0.25M concentration

It was revealed in Figure 4.9 that the effect of residence time on particle APS was found to be mildly sensitive to temperature. As the temperature increased, the rate of change of the APS with residence time decreased until at the highest temperature (350°C), the particle size was found to decrease with time. At low (250°C) and moderate (300°C) temperatures the effect of residence time was found correspond well with results published by Sue et al. (2011) (Figure 4.5) at similar residence times, although the particle sizes were much greater in this study due to the higher precursor concentration of 0.25M compared to 0.05M.

However, at higher temperatures (350°C), the particle size was found to decrease with an increase in residence time. Although this may appear to be an error or false prediction, a decrease in APS with residence time was also observed between run 14 and 3 as shown in Table 4.4.e and 4.4f. Therefore the only other variable to consider was the mixing conditions. The importance of mixing conditions and the effect of changing the flow rate at a constant residence time have been discussed in section 4.2.4, revealing how mixing conditions may also have an effect on APS. As shown is Chapter 2

(section 2.5.3.1), numerous authors have conducted studies evaluating mixer orientation, geometry and performance (Blood et al. 2004; Lester et al. 2006; Kawasaki et al. 2010; Sierra-Pallares et al. 2011). As noted previously, mixing flaws have been identified in tee mixers, such as flow partitioning, stagnant zones and inlet mixing (Blood et al. 2004). It is plausible that this interaction between temperature and flow rate exploits these mixing flaws and enhances their effects. As water approaches the supercritical region, its density has been known to decrease exponentially as depicted in Figure 2.4, and therefore small changes in temperature have a large effect on density (Pioro & Mokry 2011). Therefore high temperature water had an extremely low density, and combined with high flow rates, allowed the water to protrude further into the precursor solution in the mixer. This can be visualised in Figure 2.10, where the large difference in density between the two fluids led to flow partitioning, causing the precursor solution to effectively be forced up the water stream (Blood et al. 2004; Sierra-Pallares et al. 2011). At the highest temperature and flow, the precursor solution travelled the furthest up the water line, increasing the exposure time between the metal salt and supercritical water. This resulted in theoretically increasing the residence time, allowing more time for particle growth. However it was hypothesised that if the reactor length and hence residence time was further increased, the decreasing trend of APS at 350°C as shown in Figure 4.9 would begin to increase with time due to aggregation and surface growth.

4.3.5) Effect of the interaction between all parameters on APS

The interaction between all three parameters, parameter ABC as depicted in Figure 4.6 was shown to have absolutely no contribution percentage on the APS. This was most likely due to the fact that the flow rate was found to have a negligible correlation factor, and to have no significant interaction with neither the temperature nor concentration on the resulting APS. As the flow rate also had negligible effect on APS in terms of correlation factor, it was determined that the flow rate had very little interaction with other parameters and therefore had minimal effect on the resulting APS.

4.4) Factors influencing particle size distribution (PSD)

4.4.1) Effect of individual operating parameters on PSD

The size distribution is most effectively analysed through the coefficient of variation (CV) as shown in Chapter 3 (section 3.8.2) and is a relationship between the standard deviation and the average particle size. As depicted in Table 4.6, the particle size distribution (PSD) was found to be majorly influenced by the flow rate, where increased flow rates increased the CV. Temperature was also found to have a small yet significant effect on reducing CV, while the concentration was evident to have negligible effect on CV.

Table 4. 6 - Correlation factor of operating parameters on size distribution (CV)

Operating parameter	Correlation factor on particle size distribution (CV)
Concentration	0.030
Temperature	-0.235
Flow rate	0.545

4.4.2) Effect of precursor salt concentration on particle size distribution

The effect of concentration was evaluated by observing the effect on PSD at high and low concentrations. The concentration of the precursor solutions were varied between 0.1M and 0.4M at a range of different operating conditions as shown in Table 4.7 and the representative PSD plots in Figure 4.10.

Table 4. 7 - Effect of high and low concentration on particle size distribution

Letter	Run	Concentration (mol/dm^3)	Temperature (°C)	Flow rate (ml/min)	Coefficient of variation (%)
a	9	**0.1**	250	75	**26.4***
b	8	**0.4**	250	75	**22.6***
c	1	**0.1**	300	100	**20.1**
d	3	**0.4**	300	100	**24.7***
e	5	**0.1**	300	50	**14.8**
f	14	**0.4**	300	50	**15.9**
g	6	**0.1**	350	75	**20.5**
h	13	**0.4**	350	75	**19.7**

* - only 100 particles counted

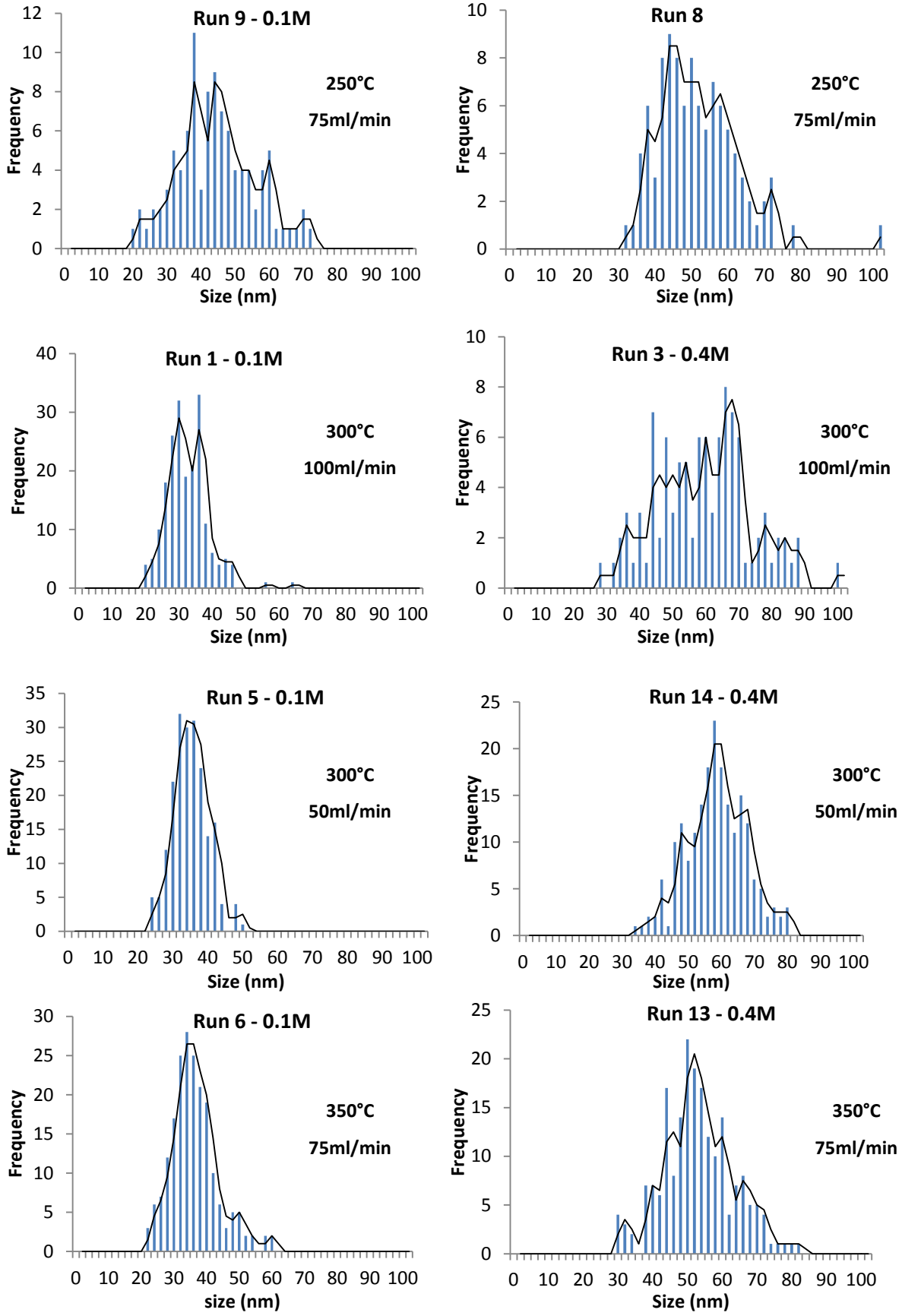

Figure 4. 10 - PSD plots showing the effect of concentration at varied operating parameters

The PSD was largely unaffected by a change in concentration as accompanied by a low correlation factor of 0.030 as depicted in Table 4.6. The CV percentage was found to increase and decrease between -14% to +23% as the concentration was increased from 0.1M to 0.4M under at different combinations of temperature and flow. Very few, if any researchers have reported on the effect of concentration on PSD, although the deviation between a negative and positive CV percentage may identify that the concentration is dependent on and may interact with other operating parameters.

4.4.3) Effect of reaction temperature on particle size distribution

The effect of temperature was evaluated by observing the effect on PSD at low and high reaction temperatures. The reaction temperature was increased from 250°C to 350°C at a range of different operating conditions as shown in Table 4.8 and the representative PSD plots in Figure 4.11.

Table 4. 8 - Effect of high and low temperature on particle size distribution

Letter	Run	Concentration (mol/dm^3)	Temperature (°C)	Flow rate (ml/min)	Coefficient of variation (%)
a	9	0.1	**250**	75	**26.4***
b	6	0.1	**350**	75	**20.5**
c	7	0.25	**250**	50	**15.7**
d	11	0.25	**350**	50	**16.8**
e	12	0.25	**250**	100	**19.7***
f	2	0.25	**350**	100	**18.3**
g	8	0.4	**250**	75	**22.6***
h	13	0.4	**350**	75	**19.7**

* - only 100 particles counted

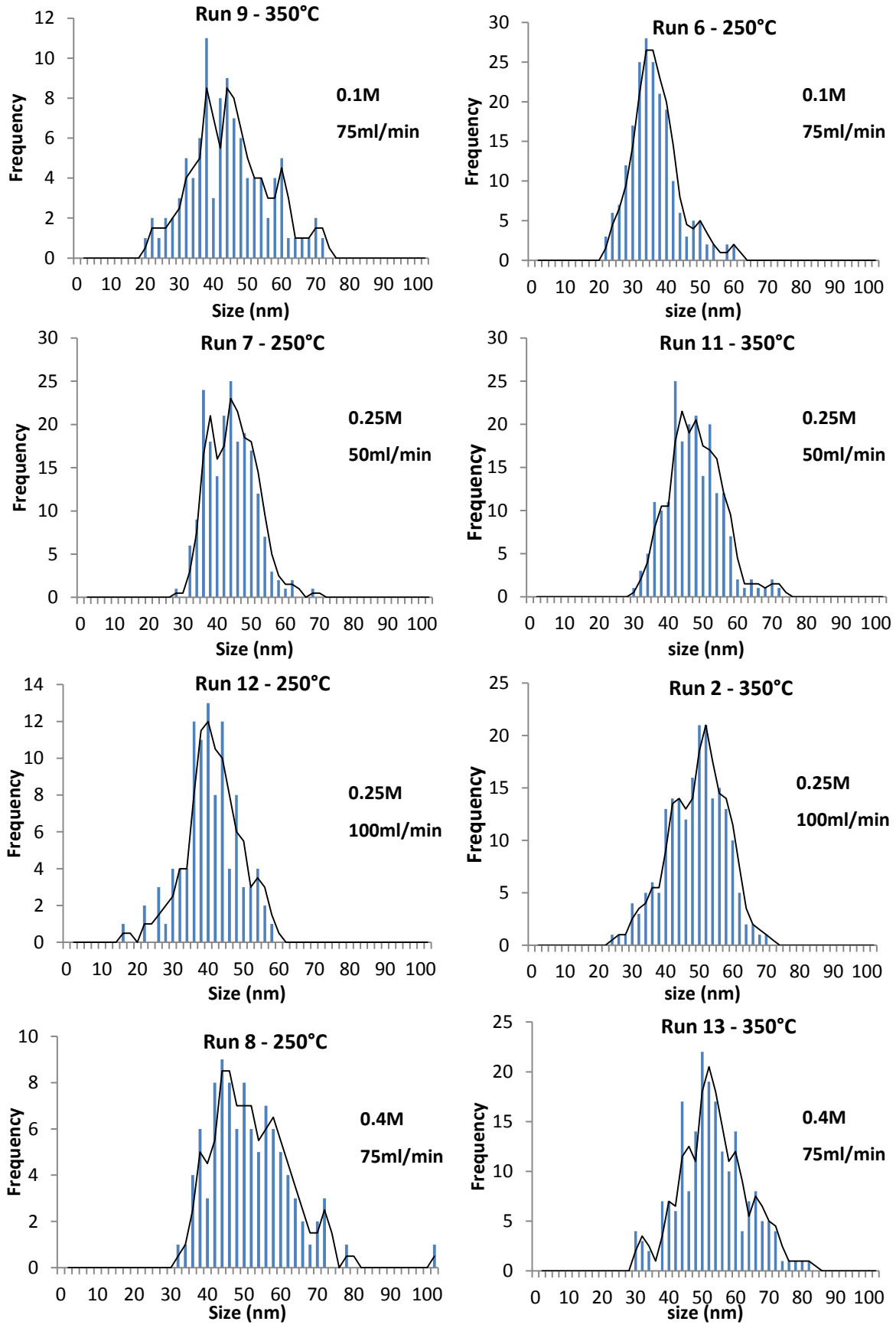

Figure 4. 11 - PSD plots showing the effect of temperature at varied operating parameters

The effect of temperature on was found to play a slight role in reducing the particle size distribution, as identified by a correlation factor of -0.235 as shown in Table 4.6. It was found that by increasing the temperature from 250°C to 350°C, the coefficient of variation was found to vary between -22% to +7%. Similar findings were reported by Evans (2006), who found that the CV decreased with an increase in temperature for iron oxide particles synthesized at 0.05M and 260 bar. The CV was found to be very small at low temperatures (200°C - 16.6%), was found to increase drastically at 300°C (42.8%), yet steadily decreased at 350°C (18.8%) and then further decreased at 415°C (14.3%). As the temperature increases it has several effects on the system, as discussed previously (Cote et al. 2003). The increased reaction rates at higher temperatures were able to promote increased growth rates, shown by particle shape refinement, and leading to a decrease in the CV percentage. Liang et al. (2010) proposed that particle growth in CHS is driven by dissolution and precipitation kinetics in sub-critical water, while the extremely low solvent ability of supercritical water suppressed crystal growth. Sato et al. (2008) also showed how the solubility of Fe_2O_3 decreased with an increase in temperature as depicted in Figure 4.12.

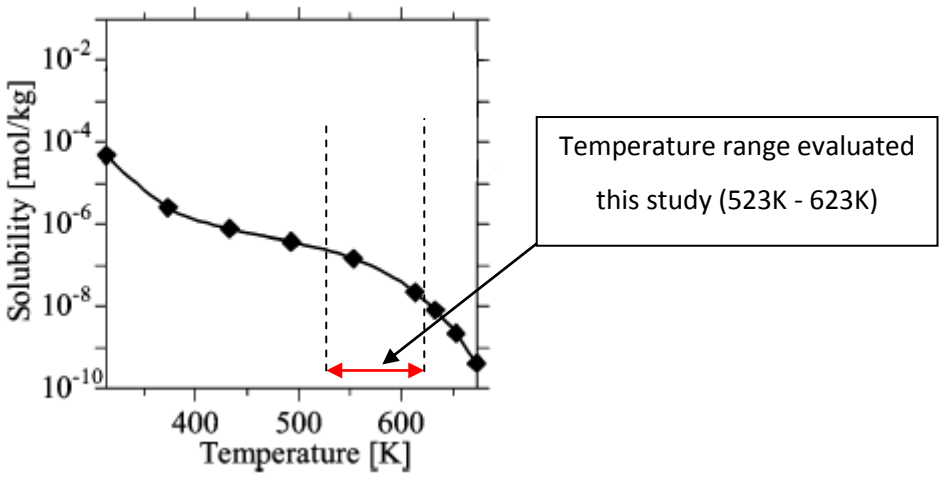

Figure 4. 12 - The effect of solubility of Fe_2O_3 as a function of temperature at 30MPa adapted from Sato et al. (2008)

Figure 4.12 shows that the solubility of Fe_2O_3 in solution takes an exponential drop as the temperature approaches the supercritical region of water at 646K (373°C). Therefore the decrease in solubility leads to an increase in supersaturation rates. At lower feed temperatures, it was predicted by Chen et al. (2011) that the heat transfer was not rapid enough, leading to a broad particle size distribution. While at higher temperatures, the low density of the water feed led to increased mixing turbulence due to buoyancy forces (Blood 2004; Lester 2006). Therefore efficient mixing and high levels of saturation experienced at higher temperatures are responsible for a narrower particle size

distribution. It should also be noted that the temperature is a function of residence time, and as an increase in temperature decreases the density of the water, the residence time is reduced. Therefore if it wasn't for a reduction in residence time caused by an increase in temperature, the effect of temperature on the PSD was predicted to be much more pronounced.

4.4.4) Effect of flow rate on particle size distribution

The effect of flow rate was evaluated by observing the effect of PSD at low and high rates of flow. The flow rates were increased from 50ml/min to 100ml/min at a range of different operating conditions as shown in Table 4.9 and the representative PSD plots in Figure 4.13.

Table 4. 9 - Comparison of high and low flow rates at varied operating parameters

Letter	Run	Concentration (mol/dm^3)	Temperature (°C)	Flow rate (ml/min)	Coefficient of variation (%)
a	7	0.25	250	**50**	**15.7**
b	12	0.25	250	**100**	**19.7***
c	5	0.1	300	**50**	**14.8**
d	1	0.1	300	**100**	**20.1**
e	14	0.4	300	**50**	**15.9**
f	3	0.4	300	**100**	**24.7***
g	11	0.25	350	**50**	**16.8**
h	2	0.25	350	**100**	**18.3**

* - only 100 particles counted

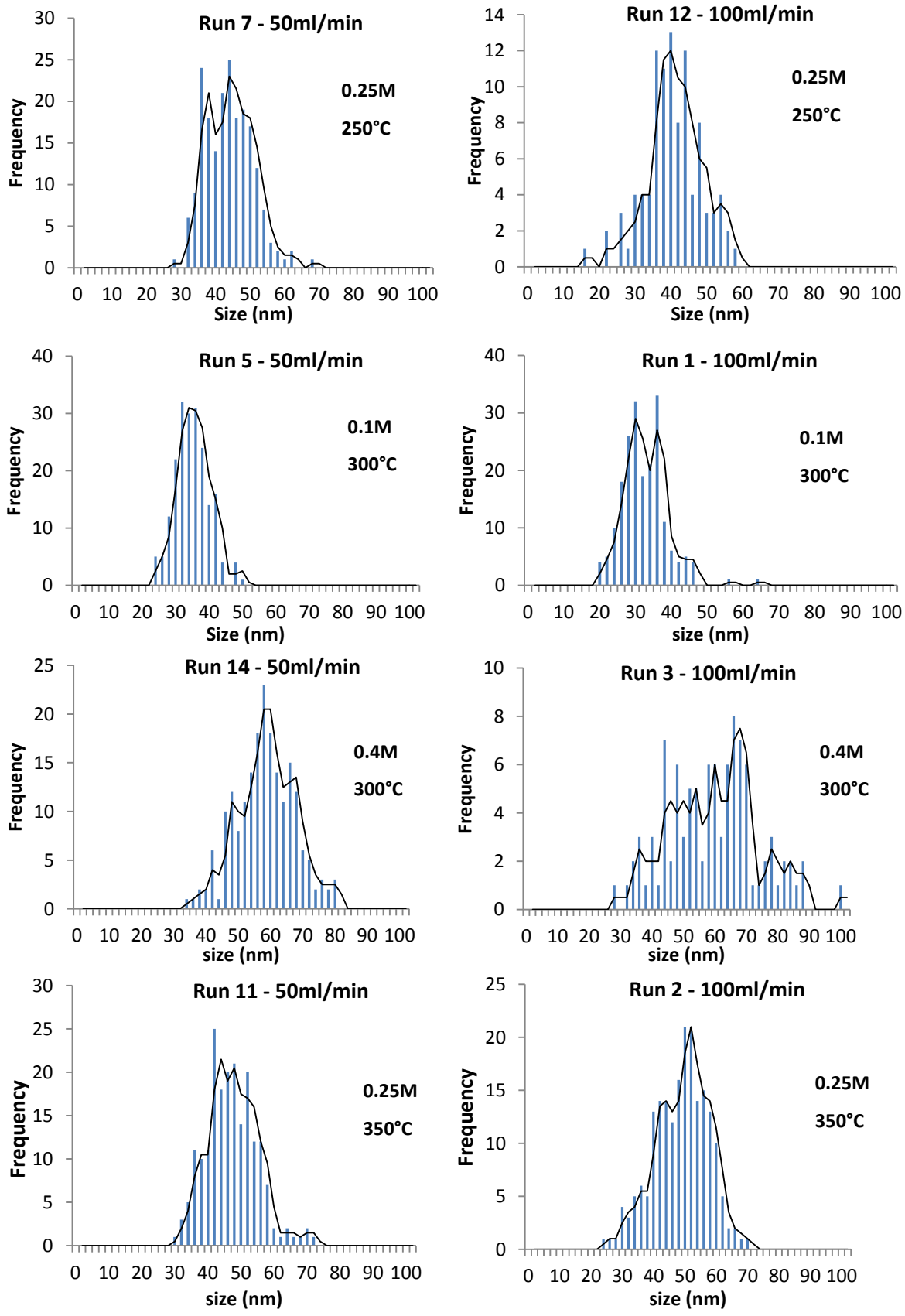

Figure 4. 13 - PSD plots showing the effect of flow rate at varied operating parameters

The particle size distribution was found to be heavily dependent on flow rate, with a high correlation factor of 0.545, as depicted in Table 4.6. As mentioned previously, the PSD has been evaluated by looking at the coefficient of variation. The CV was found to increase and fluctuate between 9% and 55%, which meant that in all cases the size distribution decreased along with a decrease in flow rate. Figure 4.14 shows the reduction in the PSD between experimental Run 1 and Run 5 at high and low flow rates and at a constant 0.1M concentration and 300°C reaction temperature. As the flow rate increased, the residence time decreased dramatically. In Run 1, the flow rate was high (100ml/min) and therefore the low residence time shows two distinct peaks which may reveal irregular growth and a broader PSD. Whereas the lower flow rate in Run 5, led to an increase in residence time which allowed for increased growth time to form more uniform particle sizes and hence a uniform distribution curve.

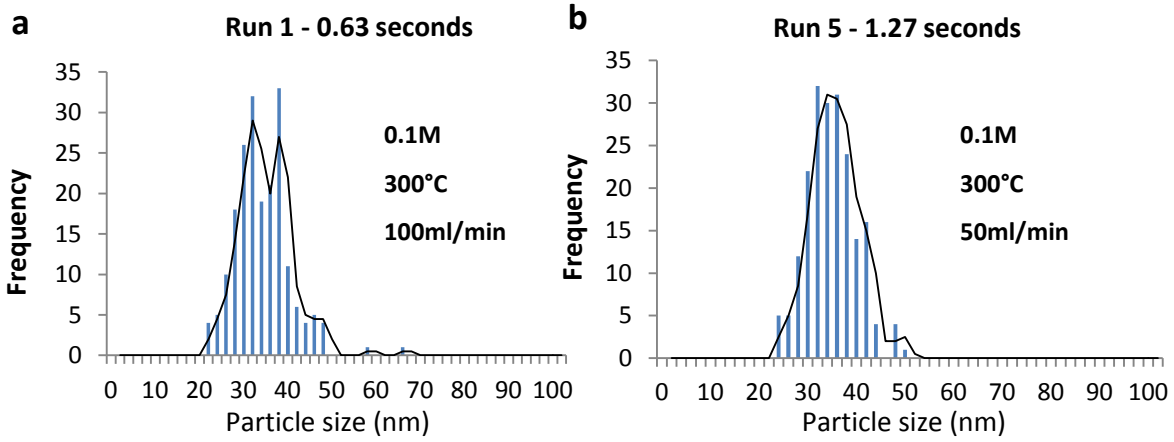

Figure 4. 14 - Effect of residence time on the size distribution curve at a constant 0.1M and 300°C (a) Run1 - 0.63s and (b) Run 5 - 1.27s

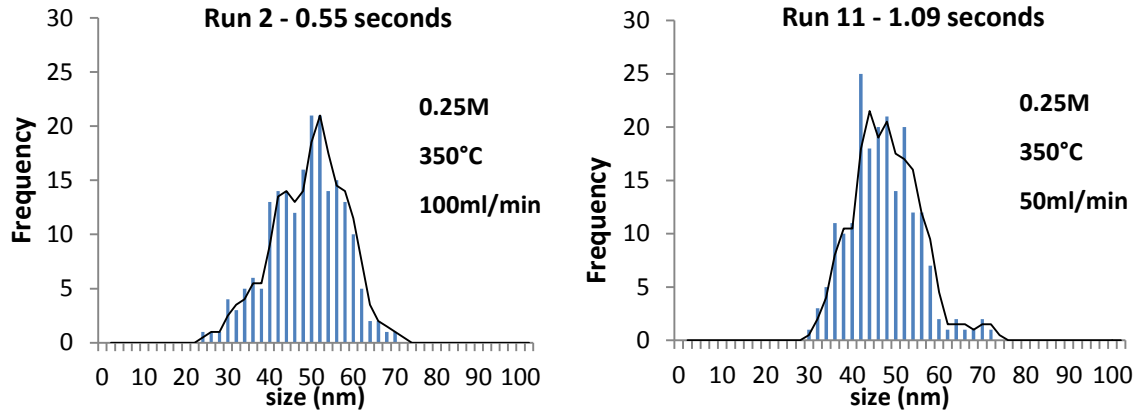

Figure 4. 15 - Effect of residence time on the size distribution curve at a constant 0.25M and 350°C (a) Run2 - 0.55s and (b) Run 11 - 1.09s

The double peak as shown in Figure 4.14a (Run 1) was not observed at all low residence times, as verified in Figure 4.15. However in all cases, an increase in residence time led to a decrease in CV value and hence a narrower PSD. Hao and Teja (2003) and Xu (2006) reported that no significant trend was observed when comparing the effect of flow rate or residence time on the resulting PSD. Yet Sue et al. (2011) plotted the CV versus residence time and found the CV to increase from 24% at 0.13s to around 30% after 1 second, where it remained constant between 1-2 seconds. This lack of growth after 1 second was linked to the high supersaturation rates. It was declared that after 1 second, no Fe^{3+} ions remained in solution and therefore no further growth took place (Sue et al. 2011). The growth was suggested to be caused by aggregation, as the only other growth possible while no Fe^{3+} ions were in solution were OR kinetics, yet this was not possible, as OR kinetics would result in a decrease in CV with an increase in residence time (Sue et al. 2011). Through the observations made by Sue et al. (2011), it was suggested that the decrease in CV along with an increase in residence time as found in this study, was likely due to OR kinetics and growth. Smaller particles are consumed and precipitate onto larger particles, this decreases the Gibbs free energy in the system and also decreases the PSD (Zhang et al. 2010). As shown in Figure 4.16, it was possible to visually witness the consumption of nuclei, supporting the presence OR kinetics.

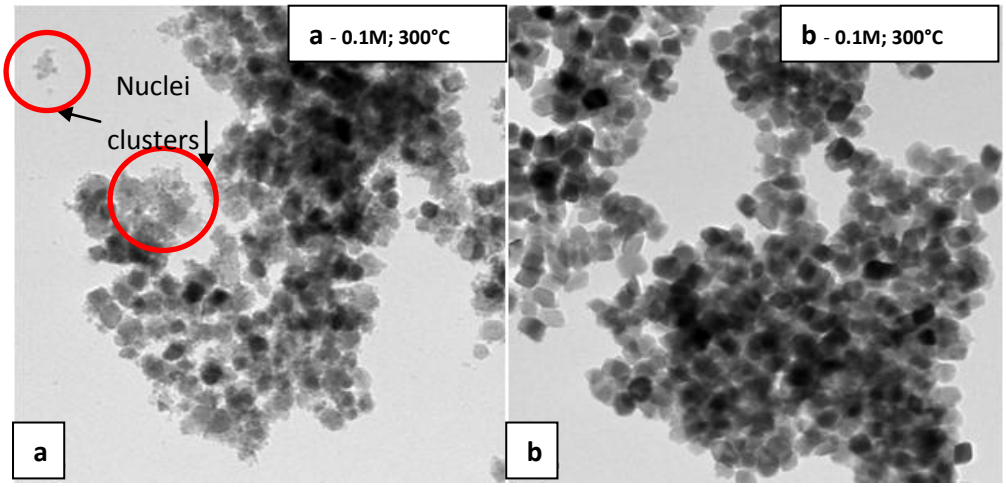

100 ml/min
0.63 seconds

50 ml/min
1.27 seconds

Figure 4. 16 - Consumption of nuclei through OR kinetics at low and high residence times at a constant 0.1M and 300°C (a) Run1 - 0.63s and (b) Run 5 - 1.27s

In Figure 4.16a, the nuclei clusters observed at a residence time of 0.63 seconds are non existent when looking at Figure 4.16b. Not all nuclei clusters disappeared when the residence time increased, but in all cases the number of nuclei decreased along with the nuclei apparent size, strengthening the hypothesis of OR kinetics .

It is most likely that the low concentration (0.05M) and high temperature (400°C) studied by Sue et al. (2011) led to rapid and instantaneous nucleation of all Fe^{3+} ions in solution. While the higher concentration range in this study (0.1-0.4M) and slightly lower temperature range (250-350°C) led to rapid nucleation, but did not consume all Fe^{3+} ions in solution instantaneously. The Fe^{3+} ions in solution continued to form nuclei and the particles continued to grow through OR kinetics. Therefore the effect of flow rate on the size distribution has shown to be of vital importance not only in reducing the CV, but also ensuring complete growth and particle refinement, especially when operating under high precursor concentration.

4.5) Effect of operating parameter interactions on PSD

4.5.1) Effect of operating parameter interaction on PSD

Figure 4.17 depicts the percentage contribution and hence interactions between operating parameters, showing which combinations of parameters play which role on the resulting PSD. These interactions can also be observed by analysing Figure 4.18a and 4.18b.

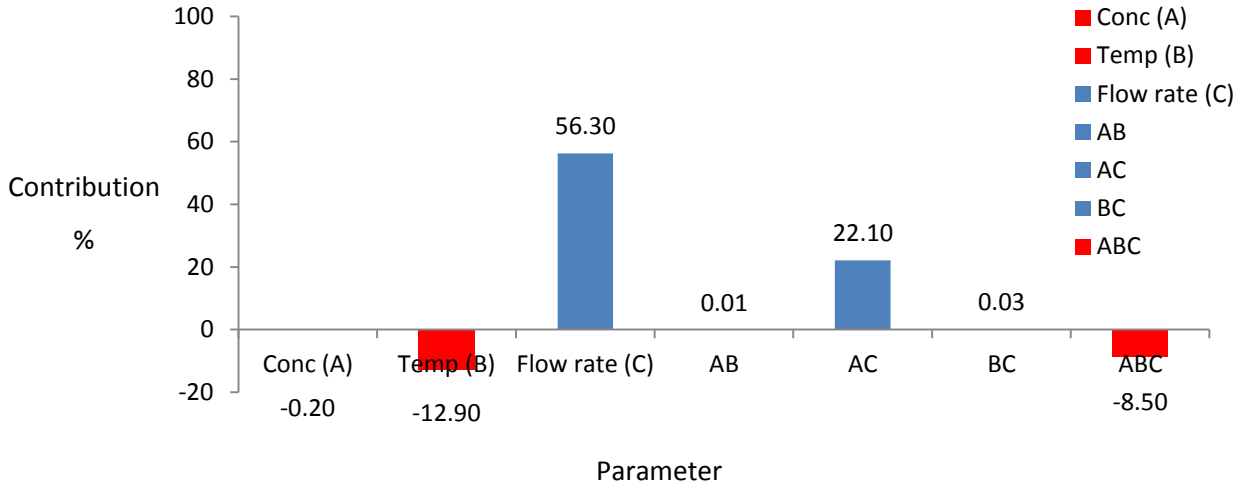

Figure 4. 17 - Contribution percentage and interaction of operating parameters on the resulting PSD (Blue = positive effect; Red = negative effect)

A model to predict the PSD was also derived through the factorial trial and has been depicted in Equation 4.5. This model can be used to predict the CV value within the range of the factorial trial, by substituting the values of A,B and C within their -1 to 1 range as shown in Table 3.4.

$$CV = 18.77 + (0.14*A) + (-1.14*B) + (2.45*C) + (0.75*AB) + (0.87*AC) + (-0.63*BC) + (2.39*A^2) + (1.14*B^2) + (-2.28*C^2) \quad \text{(Equation 4.5)}$$

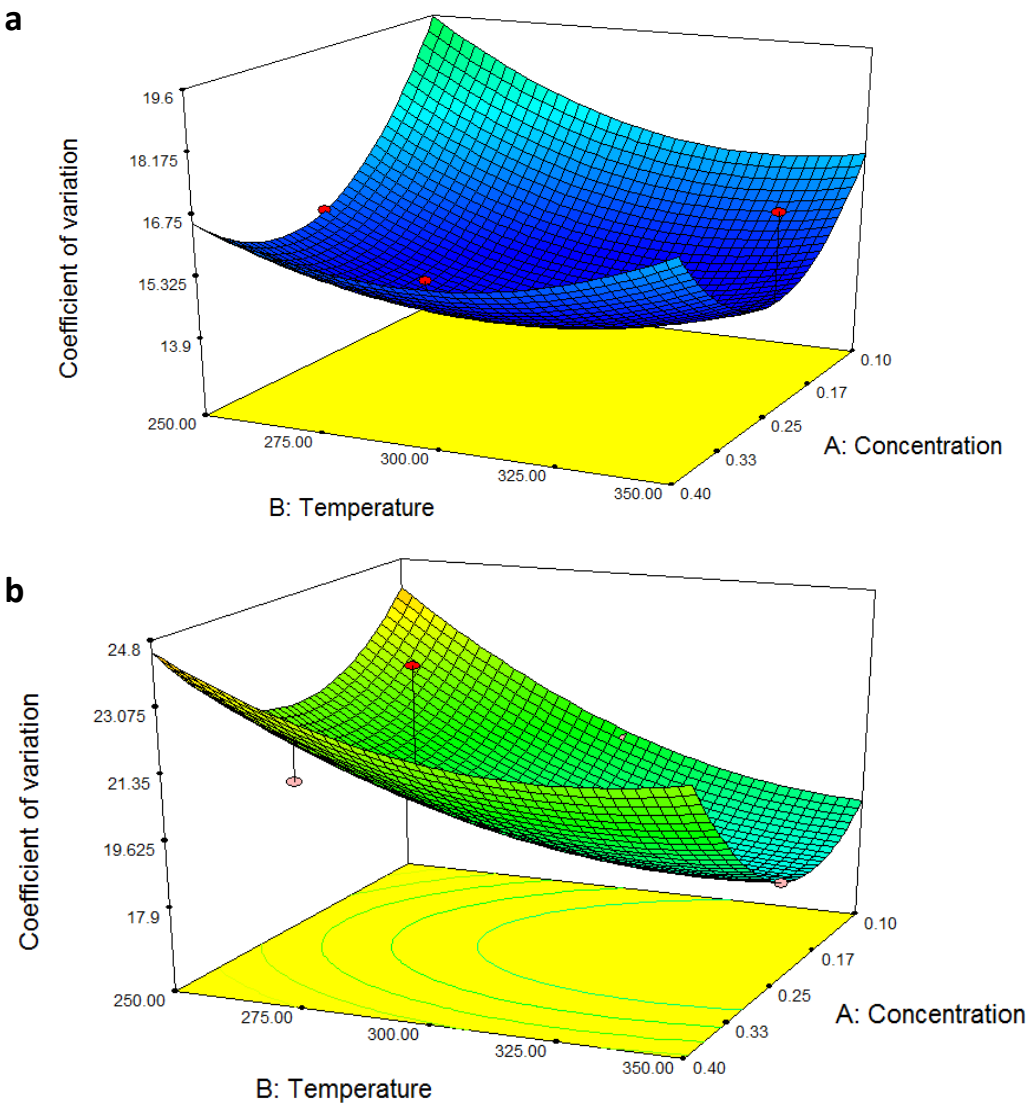

Figure 4. 18 - 3D quadratic plot of concentration versus temperature on the effect on PSD at (a) low flow rate - 50ml/min and (b) high flow rate - 100ml/min

4.5.2) Effect of the interaction between concentration and temperature on PSD

The contribution percentage and interaction between the concentration and temperature (parameter AB) were found to have almost zero effect on the contribution percentage, with a 0.01% contribution. It is likely that this interaction was negligible when the third parameter was kept constant. This is supported by the strong negative interaction between all three parameters shown in Figure 4.17. While the concentration and temperature were found to interact and strongly affect the APS, it was proposed that the increase in particle growth occurs in a uniform manner having little effect on PSD.

4.5.3) Effect of the interaction between concentration and flow rate on PSD

Although the effect of concentration by itself was insignificant, when coupled with flow rate it largely influenced the PSD, with a contribution factor of 22.1%. Figure 4.17 revealed a strong interaction between the concentration and flow rate. Using the factorial trial model predictions (Equation 4.5), the CV percentage was predicted and plotted versus flow rate at different concentrations, as depicted in Figure 4.19.

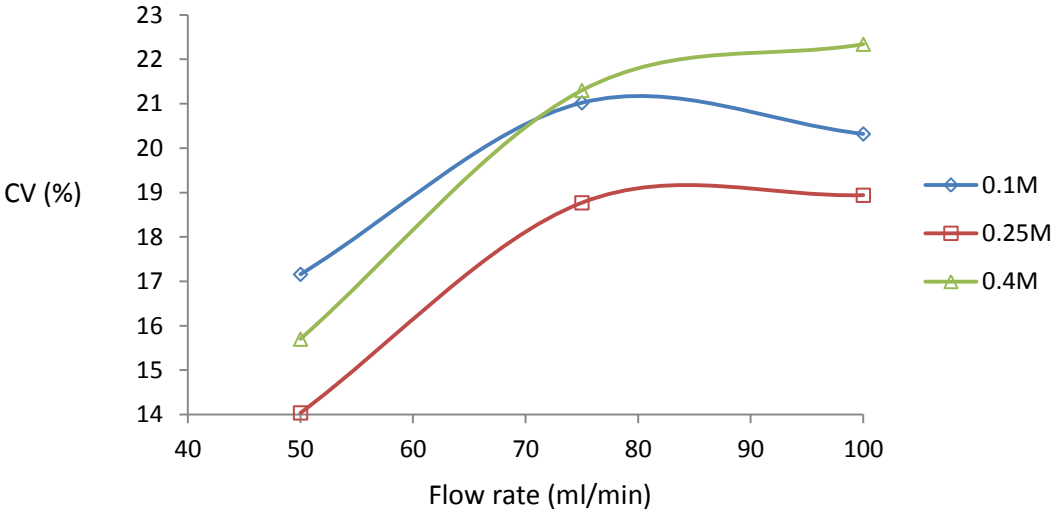

Figure 4. 19 - Effect of CV versus flow rate at different concentrations and at a constant temperature of 300°C

Figure 4.19 shows how different trends occur as the flow rate and concentration were varied at a constant reaction temperature of 300°C. When comparing the high concentration (green line) and low concentration (blue line), at high rates of flow (short residence times), the high concentration (0.4M) did not allow sufficient time for the reaction of all Fe^{3+} ions in solution - resulting in a higher CV value. While at the same high flow rates and at a low concentration (0.1M), the short reaction time was able to convert a higher percentage of Fe^{3+} ions to form particles, leading to a lower CV value. While as the flow rate was decreased, the increase in residence time allowed more time for particle growth. As it has been proposed that particle growth occurs via OR kinetics in CHS (Liang et al. 2010), higher residence times allowed for a narrower PSD at all concentrations. While at higher concentrations, as the monomers decomposed in solution, the remaining Fe^{3+} ions in solution were able to attach onto the newly formed particles through surface nucleation. Therefore as shown in Figure 4.19, as the residence time increased, higher concentrations favoured a decrease in CV value through secondary growth or surface nucleation. This was justified by calculating the gradient of CV decrease between 50 and 75ml/min in Figure 4.19, where it was determined that 0.4M had the steepest gradient (0.224), which decreased as the concentration dropped to 0.25M (0.189) and 0.1M

(0.154). The middle concentration, 0.25M, was also found to have the lowest CV value at all flow rates tested in this study, including at 100ml/min, lower than that of 0.1M. Although this was unexpected, it was noted that the slightly higher concentration had a stronger driving force for particle nucleation and growth, as mentioned previously (Sue et al. 2006). Therefore it was determined that 0.25M was the optimal concentration for obtaining a narrow PSD in the flow rate range studied, which was attributed to supersaturation rates high enough to induce rapid nucleation but a concentration low enough for sufficient Fe^{3+} ions to react and nucleate uniformly in the relatively short residence times calculated for this study.

4.5.4) Effect of the interaction between temperature and flow rate on PSD

The contribution percentage and interaction between the temperature and the flow rate (parameter BC) were found to have almost zero effect on the contribution percentage. It is likely that this interaction was negligible when the third parameter was kept constant, as supported by the strong negative interaction between all three parameters shown in Figure 4.17. As shown in Figure 4.17, an increase in temperature results in the reduction of the PSD, while an increase in flow rate led to an increase in the PSD. While it is unclear as to why no interaction exists between these two parameters, perhaps a cancellation effect occurs.

4.5.5) Effect of the interaction between all operating parameters on PSD

As displayed in Figure 4.17, the temperature was also found to interact with parameter AC, indicating that all three parameters interacted resulting in a reduction of the PSD, with a negative 8.5% contribution factor. The interaction between all three parameters revealed how important all parameters are on the resulting PSD, and that when try to adjust or minimize the PSD, all parameters need to be taken into account.

4.6) Conclusion

The effects of various operating parameters such as concentration, temperature and flow rate, and the interactions between these parameters were evaluated for their resulting effect on APS and PSD in this chapter.

The APS was found to be largely influenced by the concentration, and in all cases the APS was found to increase with an increase in concentration. While the effect of temperature and flow rate were found to have little effect on APS, an interaction between the concentration and temperature was identified through the factorial trial. This interaction was found to have a positive influence of 12.1%, and that this interaction may be responsible for the conflicting reports on the effect of temperature on APS in the literature. The flow rate was found to have the smallest effect on APS, apart from minor interactions with the concentration and temperature.

On the contrary, the PSD was found to be affected the least by concentration. A strong positive influence of the flow rate and a small negative affect of temperature were observed. Although concentration alone had little to no effect on PSD, a strong interaction between the concentration and flow rate was observed through the factorial trial, resulting in a 22.1% positive effect on PSD.

It may therefore be concluded that while some operating parameters may appear irrelevant individually, the interactions between parameters may be noteworthy, and understanding these interactions may be key to controlling particle characteristics in CHS.

Chapter 5 – Effect of operating parameters on the resulting product yield (PY) and relative crystallinity (RC).

5.1) Introduction

In this chapter, the effect of operating parameters (concentration, reaction temperature and flow rate) have also been evaluated individually and discussed with respect to their resulting effect on RC and PY . The correlation factors between the operating parameters and the resulting relative crystallinity (RC) and product yield (PY) are presented, and the interactions between parameters were identified and discussed.

The following topics below are presented in this chapter in the following order:

- Effect of individual operating parameters on PY
    - Effect of precursor salt concentration on PY
    - Effect of reaction temperature on PY
    - Effect of flow rate on PY
- Effect of operating parameter interactions on PY
- Effect of individual operating parameters on RC
    - Effect of precursor salt concentration on RC
    - Effect of reaction temperature on RC
    - Effect of flow rate on RC
- Effect of operating parameter interactions on RC

5.2) Factors influencing product yield (PY)

5.2.1) Effect of individual parameters on product yield

As depicted in Table 5.1, the product yield was found to be majorly influenced by the concentration and the temperature and an increase in each parameter led to increase in PY. The flow rate was also found to have a small yet significant effect on increasing PY.

Table 5. 1 - Correlation factor of operating parameters on product yield

Operating parameter	Correlation factor on product yield
Concentration	0.504
Temperature	0.557
Flow rate	0.132

5.2.2) Effect of precursor salt concentration on product yield.

The effect of concentration was evaluated by observing the effect on PY at high and low concentrations. The concentration of the precursor solutions were varied between 0.1M and 0.4M at a range of different operating conditions as shown in Table 5.2 and the representative iron oxide sample images in Figure 5.1.

Table 5. 2 - Comparison of high and low concentration at varied operating parameters

Letter	Run	Concentration (mol/dm^3)	Temperature (°C)	Flow rate (ml/min)	Yield (%)
a	9	**0.1**	250	75	**14.1**
b	8	**0.4**	250	75	**25.0**
c	1	**0.1**	300	100	**17.2**
d	3	**0.4**	300	100	**55.6**
e	5	**0.1**	300	50	**31.3**
f	14	**0.4**	300	50	**39.1**
g	6	**0.1**	350	75	**34.4**
h	13	**0.4**	350	75	**48.5**

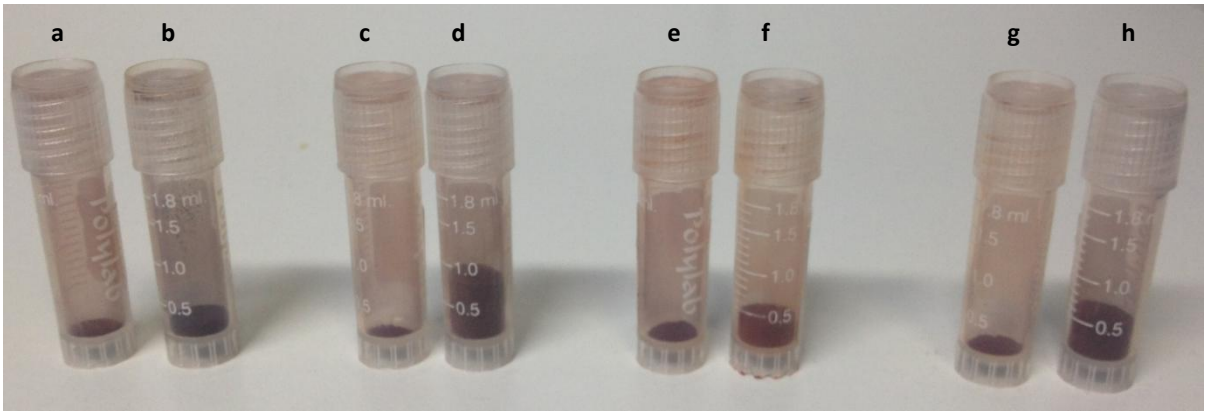

Figure 5. 1 - Images of iron oxide nanopowders in sample containers - effect of concentration on product yield

The product yield was found to be strongly dependent on concentration, as indicated by the correlation factor of 0.504 depicted in Table 5.1. Looking at Table 5.2, the PY increased between 41% to 223% as the concentration increased from 0.1M to 0.4M. The yield was percentage based and not mass based, therefore eliminating the change in concentration as a variable for increased yield on a mass basis. This indicated that the yield was actually increasing not only due to an increase in precursor solution concentration. As mentioned previously, an increase in concentration increases the saturation rate which is the driving force for particle nucleation. Sue et al. (2006) studied the effect of solubility and supersaturation rates on the effect of particle yield, where the supersaturation levels were calculated according to Equation 5.1.

$$\sigma = \frac{S_0 - S}{S} \qquad \text{Equation 5.1}$$

The rate of supersaturation is depicted by (σ), where S and S_0 represent the estimated metal oxide solubilities at the reaction temperature and starting precursor solution concentrations respectively.

Therefore the level of supersaturation increased as the concentration was increased from 0.1M to 0.4M. This promoted an increase in the nucleation rate, allowing for a greater number of nuclei to precipitate out during the relatively short reaction or residence times found in this study (0.545s to 1.416s). It was however predicted that at much longer residence or reaction times, the effect of concentration on molar conversion may be less significant or less pronounced.

5.2.3) Effect of reaction temperature on product yield

The effect of temperature was evaluated by observing the effect on PY at high and low reaction temperatures. The reaction temperature was increased from 250°C to 350°C at a range of different operating conditions as shown in Table 5.3 and the representative iron oxide sample images in Figure 5.2.

Table 5. 3 - Comparison of high and low temperature at varied operating parameters

Letter	Run	Concentration (mol/dm^3)	Temperature (°C)	Flow rate (ml/min)	Yield (%)
a	9	0.1	**250**	75	**14.1**
b	6	0.1	**350**	75	**34.4**
c	7	0.25	**250**	50	**36.3**
d	11	0.25	**350**	50	**33.8**
e	12	0.25	**250**	100	**24.4**
f	2	0.25	**350**	100	**62.0**
g	8	0.4	**250**	75	**25.0**
h	13	0.4	**350**	75	**48.5**

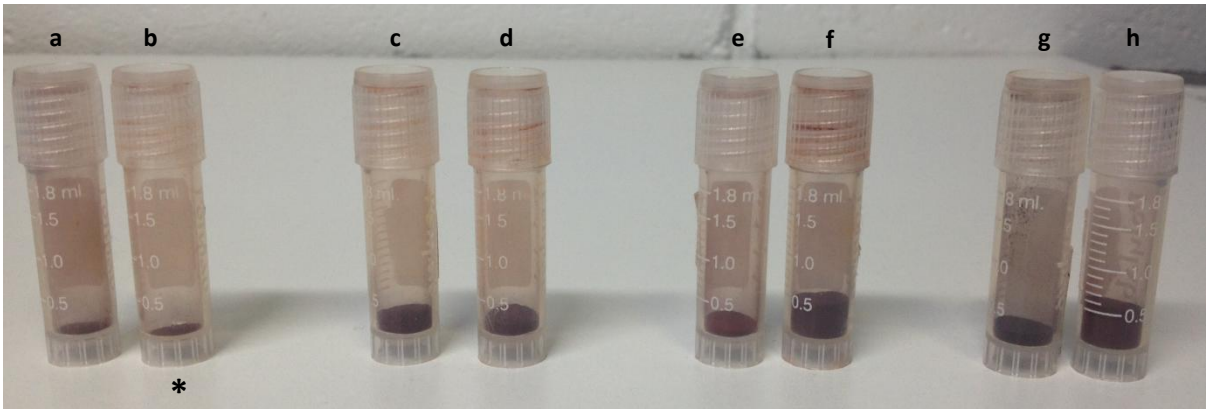

* - some sample was lost during XRD characterisation

Figure 5. 2 - Images of iron oxide nanopowders in sample containers - effect of temperature on product yield

The temperature was found to be the main contributor for increasing product yield percentage in CHS, with the highest correlation factor of 0.557 as depicted in Table 5.1. The PY percentage was found deviate between -7% and 154% as the temperature was varied. Despite the strange decrease

of 7%, as shown in Table 5.3c and 5.3d, in all other cases strong increases in PY were observed with an increase in temperature. The increase in PY with an increasing temperature is closely related to the effect of concentration on PY, as both are related to the level of supersaturation. As discussed previously, and depicted in Figure 4.12, the solubility of Fe_2O_3 in solution drops with an increase in temperature. As the temperature increases, so does the level of supersaturation, promoting increased particle nucleation (Demopoulos 2009). Higher temperatures have also been linked to increased reaction rates by favouring the dehydration step (Demopoulos 2009). Together, the above two factors allowed more particles to nucleate out within the short residence times calculated in this study, even though shortened residence times are experienced at higher temperatures.

Very few authors have reported on the effect of temperature on the product yield of iron oxide nanoparticles. A study on the effect of temperature on PY in CHS was conducted by Evans (2006), by varying the temperature in a range between 150-400°C. At low temperatures, extremely low conversions were obtained, while the opposite was found at higher temperatures, as shown in Figure 5.3.

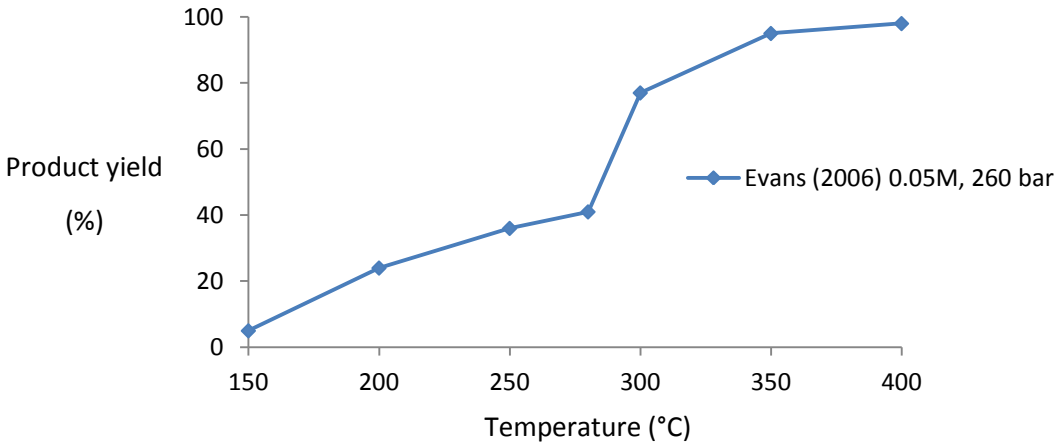

Figure 5. 3 - Effect of temperature on the resulting PY at varied flow rates and 0.1M

A steep increase was also observed by Evans (2006) between 280°C and 300°C, with the PY percentage doubling from 40% to just below 80%, yet no reason for the steep increase in conversion was proposed. While no critical temperature has been observed thus far in this study, an interesting occurrence was observed in the PY data in Table 5.3. When the flow rate was at its lowest, a small decrease in PY percentage occurred. While at the highest flow rate, a massive increase in PY percentage occurred, accompanied with two moderate increases in PY percentage at the middle flow rate studied. This suggests that the flow rate may play a role on the resulting PY percentage, and may possibly interact with the temperature.

5.2.4) Effect of flow rate on product yield (PY)

The effect of flow rate was evaluated by observing the resulting effect on PY at high and low rates of flow. The flow rates were increased from 50ml/min to 100ml/min at a range of different operating conditions as shown in Table 5.4 and the representative iron oxide samples in Figure 5.4.

Table 5. 4 - Comparison of high and low Flow rates at varied operating parameters

Letter	Run	Concentration (mol/dm^3)	Temperature (°C)	Flow rate (ml/min)	Yield (%)
a	7	0.25	250	**50**	**36.3**
b	12	0.25	250	**100**	**24.4**
c	5	0.1	300	**50**	**31.3**
d	1	0.1	300	**100**	**17.2**
e	14	0.4	300	**50**	**39.1**
f	3	0.4	300	**100**	**55.6**
g	11	0.25	350	**50**	**33.8**
h	2	0.25	350	**100**	**62.0**

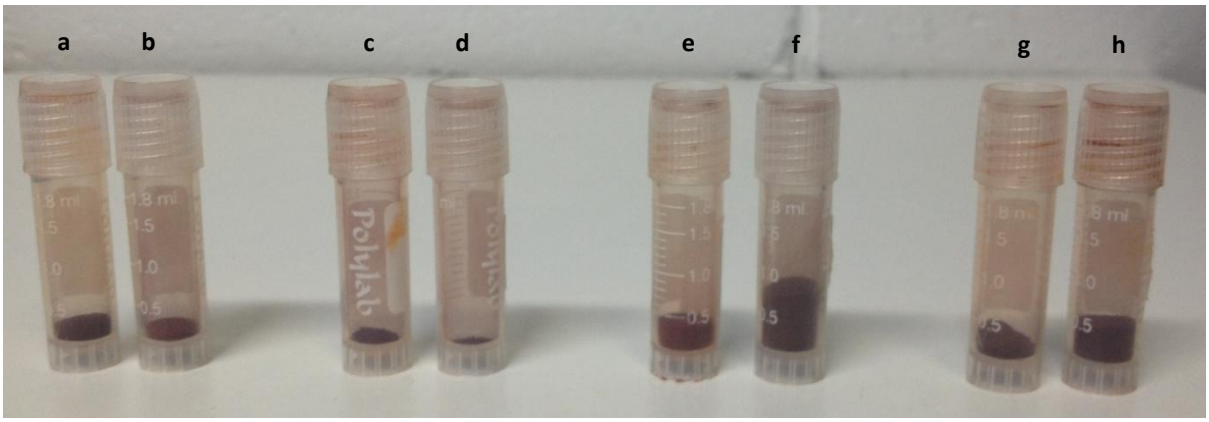

Figure 5. 4 - Images of iron oxide nanopowders in sample containers - effect of temperature on product yield

The effect of flow rate on PY was found to have a conflicting effect, with large fluctuations occurring. Of the four combinations evaluated in Table 5.4, two were found to have large increases with increased flow rates while the other two were found to have large decreases. A correlation factor of 0.132 provided little aid in determining the significance of the effect of flow rate on PY.

While very few researchers have reported on the effects of residence time on product yield, Sue et al. (2011) studied the effect of residence time on conversion, and found extremely high yields (>95%) at extremely low residence times (0.002s). The conversion was however still found to increase slightly with an increase in residence time. While the extremely high conversions found in their study were most likely associated with high reaction temperatures (400°C) and the use of their micro mixer which had an ID of 0.3mm, resulting in highly turbulent mixing.

As mentioned previously, the effect of flow rate has two influences on the system, namely influencing the mixing conditions (Blood et al. 2004; Lester et al. 2006; Kawasaki et al. 2010; Sierra-Pallares et al. 2011) and changing the residence time (Hao & Teja 2003; Xu 2006; Sue et al. 2011). Yet it appears that these two variables have opposing effects on the PY. As the flow rate increases, the turbulence and mixing efficiency is increased through forced induction (Sierra-Pallares et al. 2011), with improved mixing leading to an increase in the number of precipitated crystals. On the other hand, the increased flow rates decrease the residence time in the reactor, allowing less time for Fe^{3+} ions to precipitate from solution. While these opposing effects may result in a low correlation factor for the effect of flow rate on PY, it was found to deviate between -45% and 83% as depicted in Table 5.3 as the flow rate increased, which suggested a significant dependence on other operating parameters.

5.3) Effect of operating parameter interactions on PY

5.3.1) Effect of operating parameter interactions on product yield

Figure 5.5 depicts the percentage contribution of interactions between operating parameters on the resulting PSD. These interactions can also be observed by analysing Figure 5.6a and 5.6b.

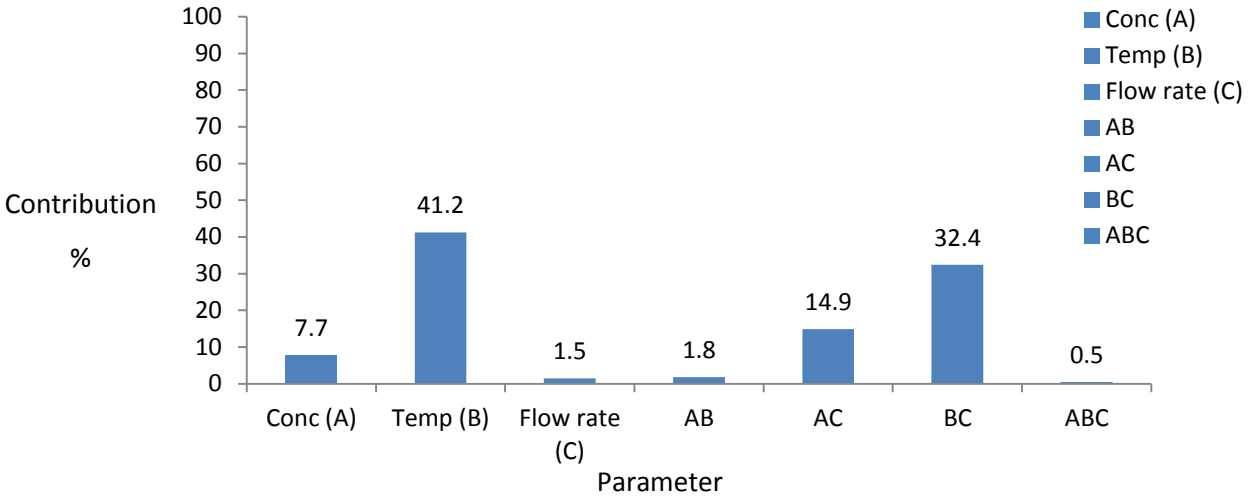

Figure 5. 5 - Contribution percentage and interaction of operating parameters on the resulting PY (Blue = positive effect; Red = negative effect)

A model to predict the product yield was also derived through the factorial trial and is given in Equation 5.2. This model can be used to predict the product yield percentage within the range of the factorial trial, by substituting the values of A,B and C within their -1 to 1 range as shown in Table 3.4.

$$PY = 39.67 + (8.91*A) + (9.85*B) + (2.34*C) + (0.78*AB) + (7.65*AC) + (10.02*BC) + (-6.23*A^2) + (-2.91*B^2) + (2.37*C^2) \quad \text{(Equation 5.2)}$$

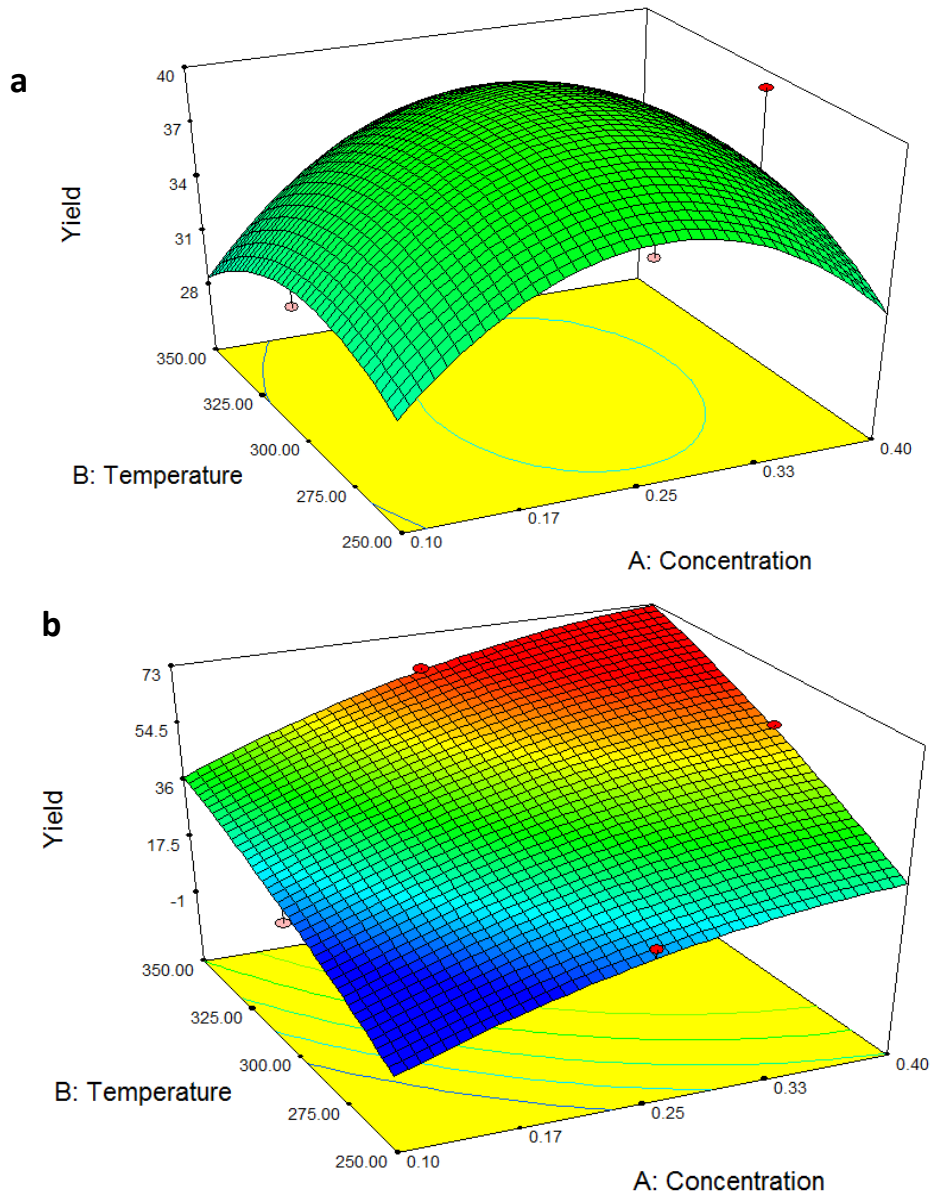

Figure 5. 6 - 3D quadratic plot of concentration versus temperature on the effect on product yield at (a) low flow rate - 50ml/min and (b) high flow rate - 100ml/min

5.3.2) Effect of the interaction between concentration and temperature on PY

Although the temperature and concentration were both found to have a significant effect on product yield independently, little interaction was observed between the two parameters, with a contribution of 1.8% as depicted in Figure 5.5. It was proposed that although the temperature and the concentration are both linked to increasing the supersaturation levels (Xu 2006; Demopoulos 2009), the effect of increased supersaturation had little effect on PY when not combined with an increased flow rate and hence turbulent mixing (Sierra-Pallares et al. 2011). Therefore the lack of interaction may be attributed to the unusual dome-like trend observed at low flow rates, as shown

in Figure 5.6a. This dome-like trend revealed that at low rates of flow, the highest PY were obtained at intermediate temperatures and concentrations. This contradicts the strong positive influence of concentration and temperature at high flow rates, as depicted in Figure 5.6b. While this contradiction led to the low contribution factor on PY, it does highlight the importance of flow rate on the product yield.

5.3.3) Effect of the interaction between concentration and flow rate on PY

The combination of high levels of supersaturation and efficient mixing also hold true for the interaction between the concentration and the flow rate, parameter AC, with a strong 14.9% contribution factor. The increased supersaturation levels associated with a higher concentration (Demopoulos 2009) and efficient mixing at higher flow rates (Sierra-Pallares et al. 2011) led to rapid nucleation. Although the residence time decreased drastically with an increase in flow rate, it was proposed that more particles precipitated at high concentrations due to the increased mixing turbulence when compared with the increased residence times associated with lower flow rates. Therefore the high degree of supersaturation and turbulence led to almost instantaneous nucleation of almost all Fe^{3+} ions in solution, and therefore the effect of increased residence time yielded little secondary nucleation. The relationship between the concentration and flow rate at a constant 300°C temperature is represented by Figure 5.7, which uses PY predictions from the PY factorial trial model (Equation 5.2).

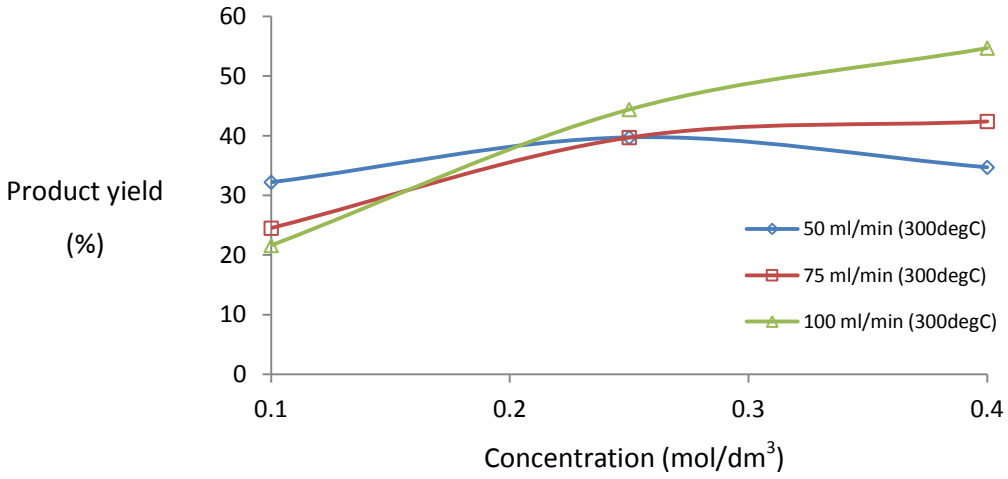

Figure 5. 7 - Effect of product yield versus concentration at varied flow rate and constant temperature

Figure 5.7 conveys how at low concentrations, lower rates of flow (higher residence times) are required to maximise the PY. While at higher concentrations, increased flow rates (turbulent mixing) become more effective at inducing rapid nucleation and hence increased product yield.

5.3.4) Effect of the interaction between temperature and flow rate on PY

When analysing the parameter interactions which effect PY, the strongest interaction was found to be that of temperature and flow rate, parameters BC, with a critical contribution factor of 32.4%. Although the effect of flow rate alone was minimal, when combined with temperature it had a massive effect on the resulting PY. Using the factorial trial model for PY (Equation 5.2), Figure 5.8 represents PY predictions versus flow rate at varied temperature and at a constant 0.25M concentration.

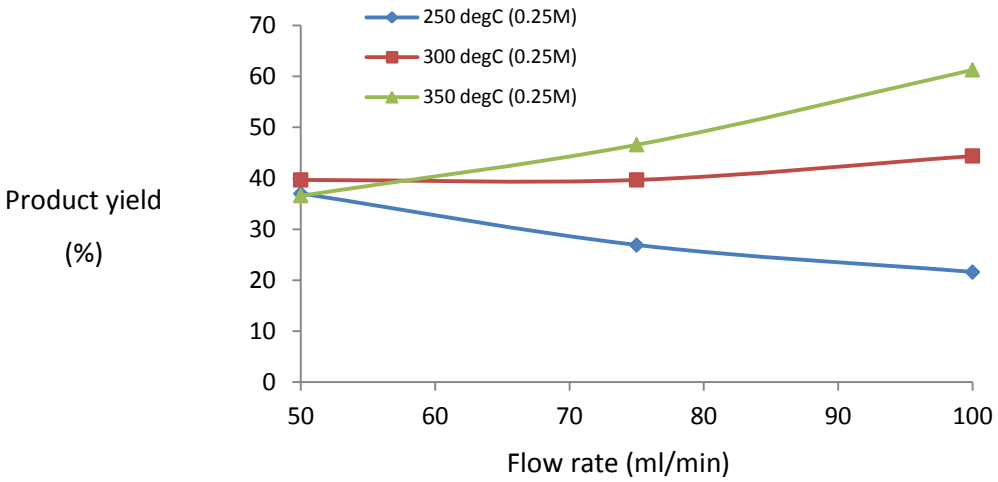

Figure 5. 8 - Effect of product yield versus flow rate at varied temperature and constant 0.25M concentration

As shown in Figure 5.8, the PY percentage was relatively constant at the lowest flow rate of 50ml/min and across all temperatures, while as the flow rate increased 3 different trends were observed. At low temperatures (250°), the PY decreased as the flow rate increased, unlike at moderate temperatures (300°C) where the PY increased gradually with increased flow. While at the highest temperature studied (350°C), the PY was found to greatly increase with flow rate.

The interaction between flow rate and temperature on PY is closely related to the same interaction discussed previously in section 4.3.4, on the effect of APS. It was identified that at high temperatures and flow rates, the precursor solution tends to migrate higher up into the water line due to the excessive difference in density of the two streams (Blood 2004). This small interaction in section 4.3.4 led to an increase in APS even at low residence times, as depicted in Figure 4.9. Therefore the combination of high flow rate and high temperature effectively enhanced flow partitioning, channelling the precursor solution higher up the water line, theoretically increasing the reactor residence time. Mixing studies in T-mixers have also shown increased turbulence as the flow rate

and the difference in densities between the two streams increases (Lester 2006), thus more effective mixing is also promoted in turbulent zones during this interaction. Taking all factors into consideration, high temperatures and high flow rates provide an optimal environment for a high PY across all concentrations, by increasing the theoretical residence time, increasing mixing turbulence and promoting high nucleation and growth rates.

5.3.5) Effect of the interaction between all operating parameters on PY

The interaction between all three parameters, parameter ABC, as depicted in Figure 5.5 was shown to have negligible effect of 0.5% contribution on the product yield. It was expected that a strong interaction would occur, as the highest product yield was found at the highest concentration, temperature and flow rate in Figure 5.6b. However, the dome-like trend in Figure 5.6a revealed that the highest PY was obtained at intermediate temperatures and concentrations at low rates of flow. The contradiction between the trends in Figure 5.6a and 5.6b are most likely responsible for the net low contribution percentage.

5.4) Factors influencing relative crystallinity (RC)

5.4.1) Effect of operating parameter correlations on relative crystallinity

As represented in Table 5.5, the degree of relative crystallinity was found to be heavily dependent on the concentration and the rate of flow, while a slightly lower dependence on temperature was observed. A negative correlation factor represents a negative influence on the RC.

Table 5. 5 - Correlation factor of operating parameters on relative crystallinity

Operating parameter	Correlation factor on Relative Crystallinity
Concentration	-0.483
Temperature	0.235
Flow rate	-0.589

5.4.2) Effect of precursor salt concentration on relative crystallinity (RC)

The effect of concentration was evaluated by observing the effect on RC at high and low concentrations. The concentration of the precursor solutions were varied between 0.1M and 0.4M at a range of different operating conditions as shown in Table 5.6 and the representative hematite reference peak plots as depicted in Figure 5.9.

Table 5. 6 - Comparison of high and low concentration at varied operating parameters

Letter	Run	Concentration (mol/dm^3)	Temperature (°C)	Flow rate (ml/min)	Relative crystallinity (%)
a	9	**0.1**	250	75	**78.2**
b	8	**0.4**	250	75	**48.1**
c	1	**0.1**	300	100	**60.0**
d	3	**0.4**	300	100	**55.8**
e	5	**0.1**	300	50	**98.9**
f	14	**0.4**	300	50	**83.0**
g	6	**0.1**	350	75	**98.5**
h	13	**0.4**	350	75	**60.0**

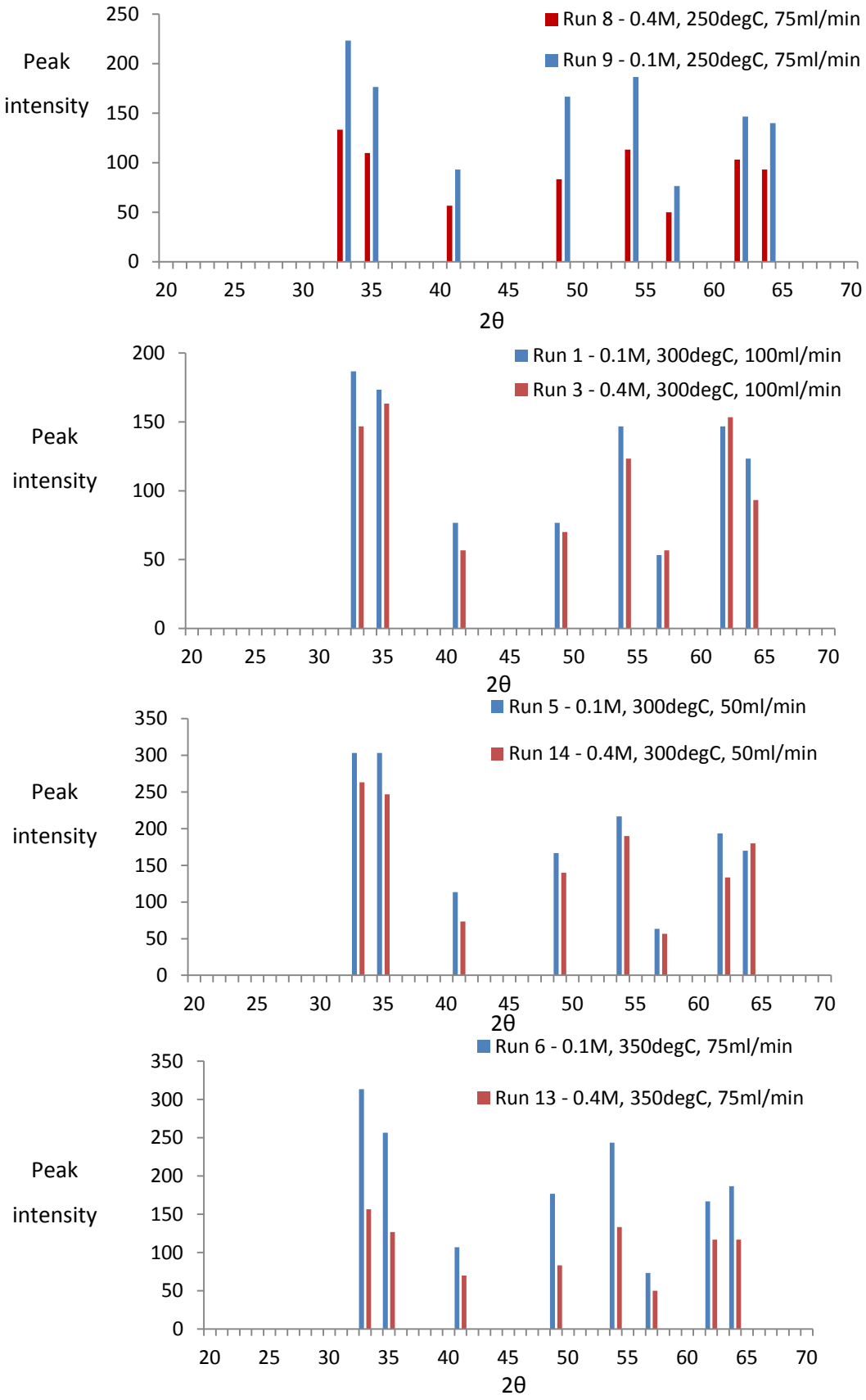

Figure 5. 9 - Hematite reference peak height plots - effect of concentration on RC

The concentration was found to strongly effect the relative crystallinity, which tended to decrease as the concentration increased, as determined from the strong negative correlation factor of -0.483 in Table 5.5. It was found to deviate between -7% and -31% as the concentration was increased from 0.1M to 0.4M. The decrease in RC along with an increased concentration has been compared in Figure 5.9 using the main hematite reference peak heights, with the peak reference positions found in Appendix B. Very few authors have reported on the effect of concentration on crystallinity in CHS, yet Lester et al. (2012) found that as they increased the concentration of the cobalt (II) acetate tetrahydrate precursor solution from 0.01M to 0.05M (415°C, 240 bars), the relative peaks tended to remain constant yet the scatter greatly increased. It was not conclusive whether the crystallinity of the cobalt oxide particles increased with concentration. Similar findings were reported by Noguchi et al. (2008) on the production of α-Al_2O_3 particles. As the concentration was increased from 0.3M, to 0.5M and then to 1.0M (425°C, 30MPa), the diffraction patterns were identical. In this study however, the crystallinity was found to decrease with an increase in concentration as depicted in Figure 5.9, which compared the peak heights of the main hematite reference pattern as shown in Appendix B.

5.4.3) Effect of reaction temperature on relative crystallinity (RC)

The effect of reaction temperature was evaluated by observing the effect on RC at high and low temperatures. The temperature was varied between 250°C and 350°C at a range of different operating conditions as shown in Table 5.7 and the representative hematite reference peak plots as depicted in Figure 5.10.

Table 5. 7 - Comparison of high and low concentration at varied operating parameters

Letter	Run	Concentration (mol/dm^3)	Temperature (°C)	Flow rate (ml/min)	Relative crystallinity (%)
a	9	0.1	**250**	75	**78.2**
b	6	0.1	**350**	75	**98.5**
c	7	0.25	**250**	50	**100**
d	11	0.25	**350**	50	**98.7**
e	12	0.25	**250**	100	**72.2**
f	2	0.25	**350**	100	**84.5**
g	8	0.4	**250**	75	**48.1**
h	13	0.4	**350**	75	**60.0**

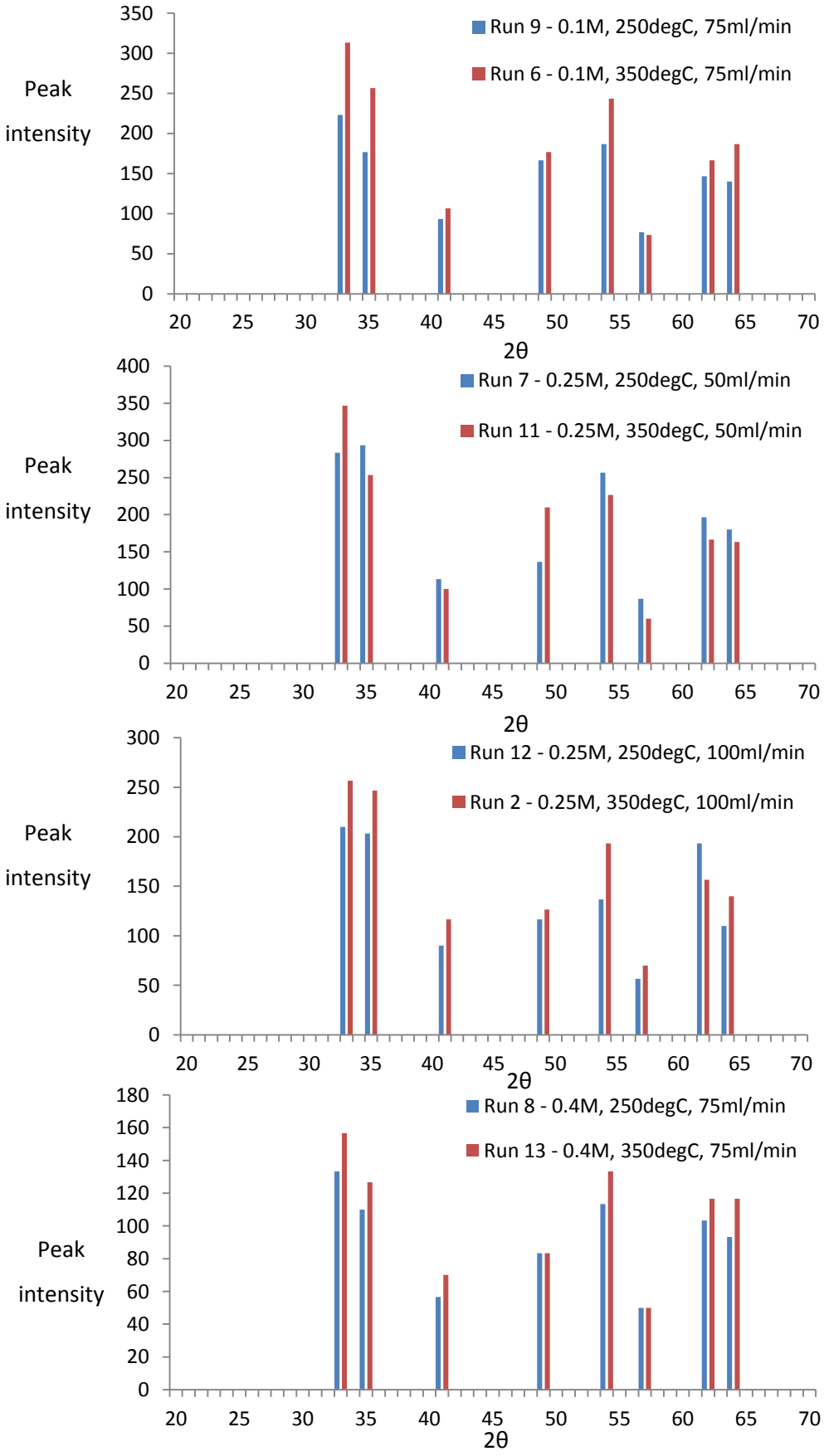

Figure 5. 10 - Hematite reference peak height plots - effect of temperature on RC

The reaction temperature was found to have the least effect the relative crystallinity, when compared to the other operating parameters evaluated, with a correlation factor of 0.235 as depicted in Table 5.5. The RC was found to deviate between -1% and 26% as the temperature was increased from 250°C to 350°C. The increase in RC with an increase in temperature has been represented by Figure 5.10, which compares the reference peak heights of crystalline hematite at high and low temperatures.

It has been well documented in the literature that an increase in temperature favours crystallinity (Evans 2006; Noguchi et al. 2008; Aimable et al. 2009; Liang et al. 2010; Lester et al. 2012). Not only did temperature increase crystallinity, but a critical temperature for crystalline materials was identified. Liang et al. (2010) and Evans (2006) both discovered that at reaction temperatures below 250°C, amorphous particles were obtained. Higher reaction temperatures have been identified to increase the rate of the dehydration step, increase the surface diffusion, and therefore the crystalline growth rate is accelerated (Demopoulos 2009). As noted previously, the temperature is a function of residence time. However, although higher temperatures favour an increase in crystallinity, it also decreases the residence time. Thus a slight cancelation effect occurs, but the net result was still an increase in the rate of crystallinity as the temperature increased. It was proposed if an increase in temperature did not also decrease the flow rate, a higher correlation factor would be obtained for the effect of temperature on RC.

5.4.4) Effect of flow rate on relative crystallinity (RC)

The effect of flow rate was evaluated by observing the effect on RC at high and low rates of flow. The flow rate was varied between 50ml/min and 100ml/min at a range of different operating conditions as shown in Table 5.8 and the representative hematite reference peak plots as depicted in Figure 5.11.

Table 5. 8 - Comparison of high and low concentration at varied operating parameters

Letter	Run	Concentration (mol/dm^3)	Temperature (°C)	Flow rate (ml/min)	Relative crystallinity (%)
a	7	0.25	250	**50**	**100**
b	12	0.25	250	**100**	**72.2**
c	5	0.1	300	**50**	**98.9**
d	1	0.1	300	**100**	**60.0**
e	14	0.4	300	**50**	**83.0**
f	3	0.4	300	**100**	**55.8**
g	11	0.25	350	**50**	**98.7**
h	2	0.25	350	**100**	**84.5**

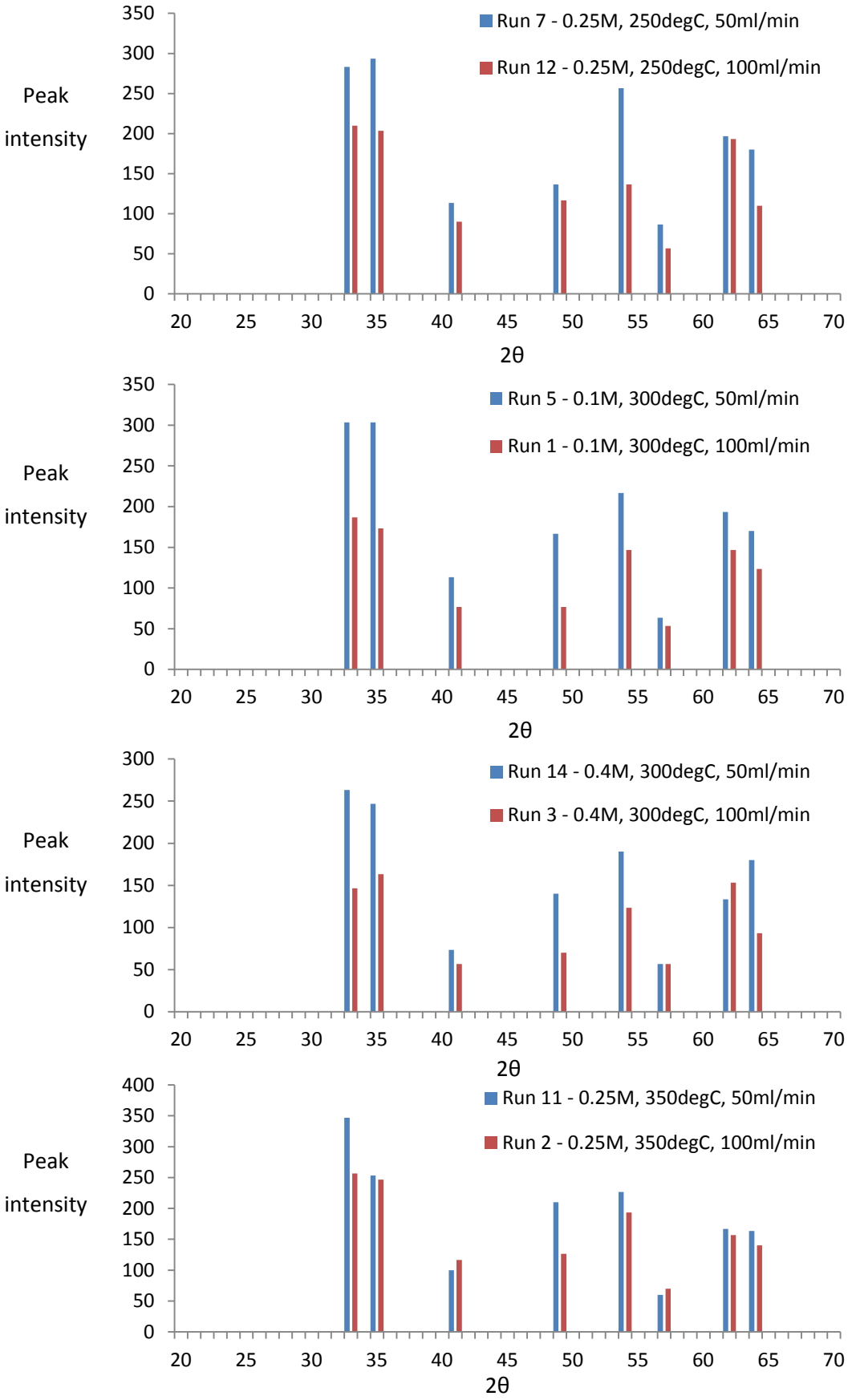

Figure 5. 11 - Hematite reference peak height plots - effect of flow rate on RC

The flow rate was found to have the largest effect on crystallinity, with a correlation factor of -0.589 as shown in Table 5.5, which was found to decrease as the flow rate increased. Therefore increased residence times were found to greatly favour the production of crystalline nanomaterials. An increase in flow rate led to a decrease in RC between -14% and -39% calculated from the changes in Table 5.8, as the flow rate was increased from 50ml/min to 100ml/min. The decrease in RC with an increase in flow rate has been represented by Figure 5.11, which compares the reference peak heights of crystalline hematite at high and low rates of flow.

An increase in crystallinity with an increase in residence time was in agreement with numerous authors (Matsui et al. 2008; Xu & Teja 2008; Sue et al. 2011), where Sue et al. (2011) even noticed a critical residence time for crystalline materials to be formed. When the residence time was below 0.254 seconds, a very low peak intensity was observed. Yet above this critical point, peak intensity became more pronounced, and began to increase with an increase in residence time. As illustrated in Figure 5.11, in all cases the RC decreased with an increase in flow rate.

5.5) Effect of operating parameter interactions on relative crystallinity

5.5.1) Effect of operating parameter interactions on relative crystallinity

Figure 5.12 depicts the percentage contribution and hence interactions between operating parameters, showing which combinations of parameters play which role on the resulting RC. These interactions can also be observed by analysing Figure 5.13a and 5.13b.

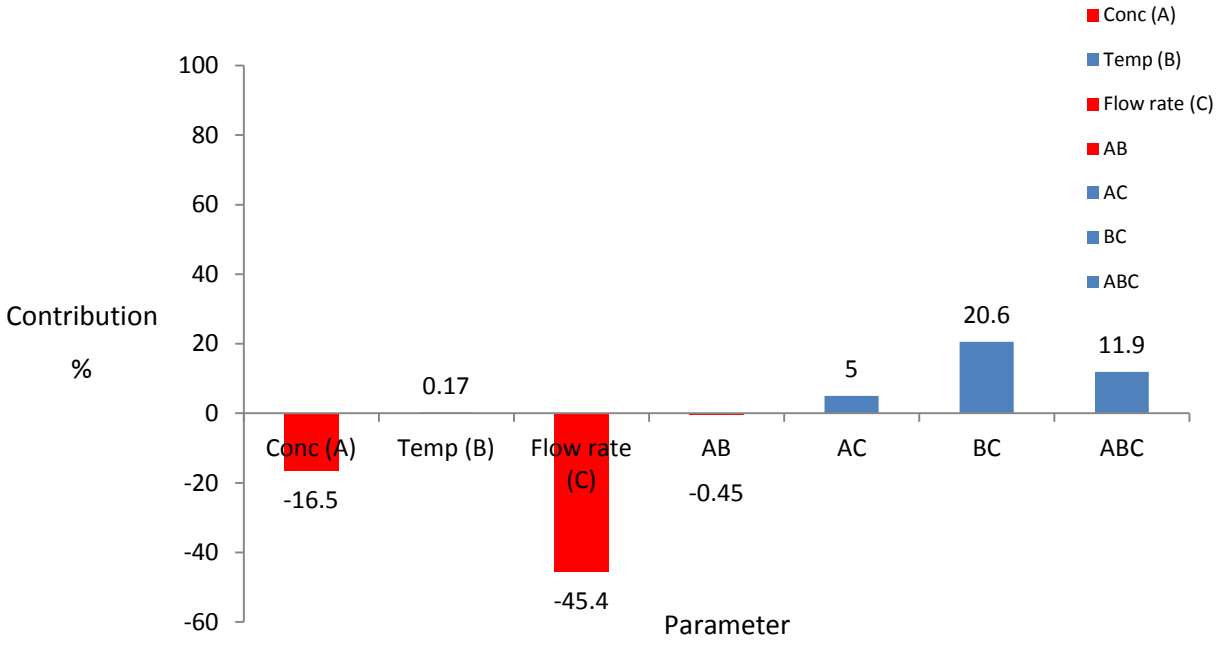

Figure 5. 12 - Contribution percentage of operating parameters on the resulting relative crystallinity (Blue = positive effect; Red = negative effect)

A model to predict the relative crystallinity was derived through the factorial trial and is depicted in Equation 5.3. This model can be used to predict the RC value within the range of the factorial trial, by substituting the values of A,B and C within their -1 to 1 range as shown in Table 3.4.

$$\text{Relative Crystallinity} = 85.33 + (-11.09*A) + (5.40*B) + (-13.51*C) + (-2.10*AB) + (2.93*AC) + (3.40*BC) + (-14.28*A^2) + (0.15*B^2) + (3.37*C^2) \quad \text{(Equation 5.3)}$$

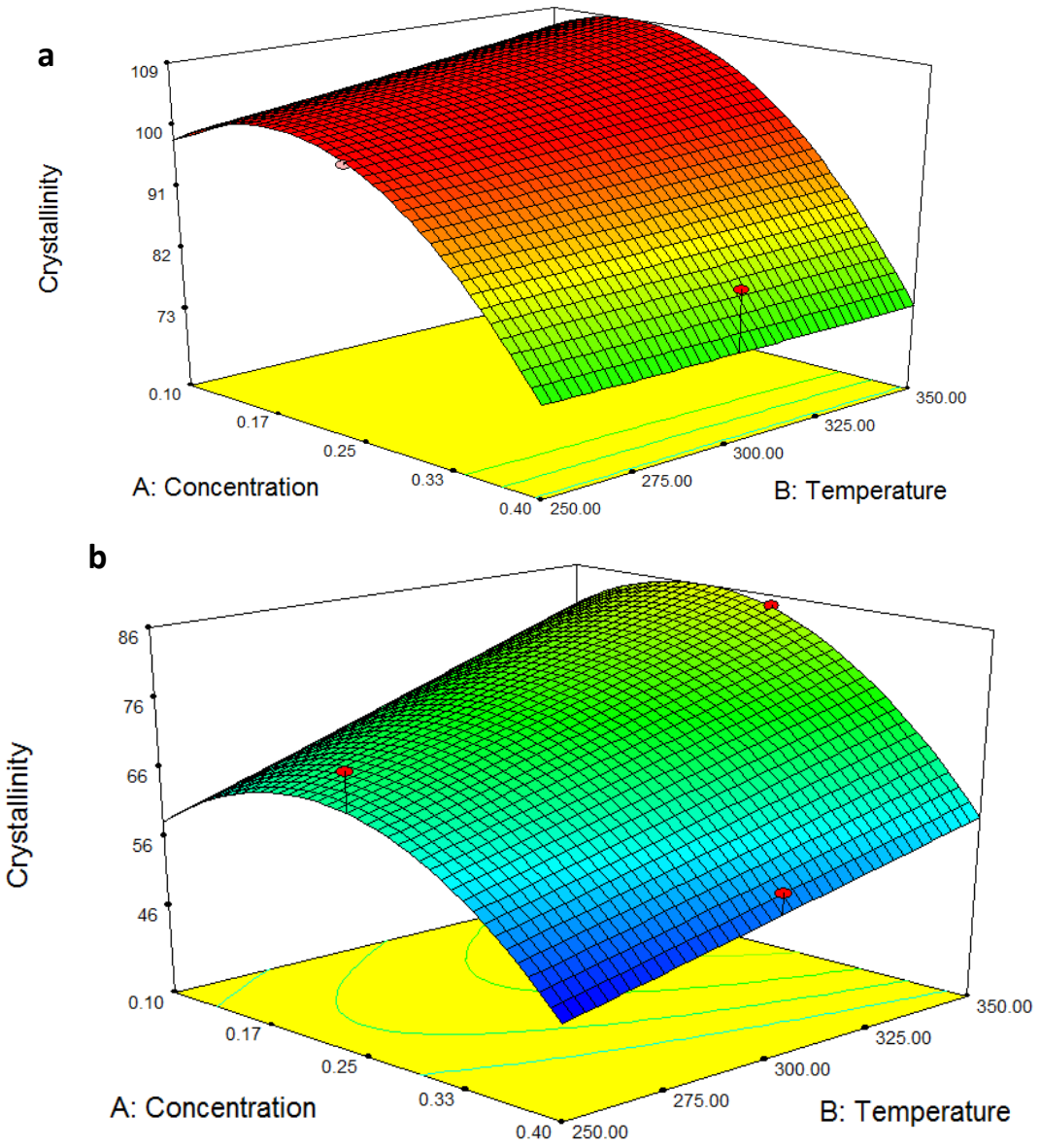

Figure 5. 13 - 3D quadratic plot of concentration versus temperature on the effect on relative crystallinity at (a) low flow rate - 50ml/min and (b) high flow rate - 100ml/min

5.5.2) Effect of the interaction between concentration and temperature on PY

Very little interaction between the concentration and the temperature, parameter AB, was observed with a negligible -0.45% contribution shown in Figure 5.12. It was proposed that a change in crystalline growth, associated within the temperature range evaluated in this study (250-350°C), was not significant enough to show a sizeable contribution percentage for the high concentrations evaluated in this research (0.1-0.4M).

5.5.3) Effect of the interaction between concentration and flow rate on PY

A small yet significant interaction was indicated between the concentration and flow rate, parameter AC, with a contribution factor of 5%. It was proposed that this interaction was associated with the number of nuclei in solution (concentration dependent) and the residence or reaction time (flow rate dependent). The factorial trial model for RC was used to plot the predicted RC values interaction versus concentration at different rates of flow and at a constant 300°C, as illustrated by Figure 5.14.

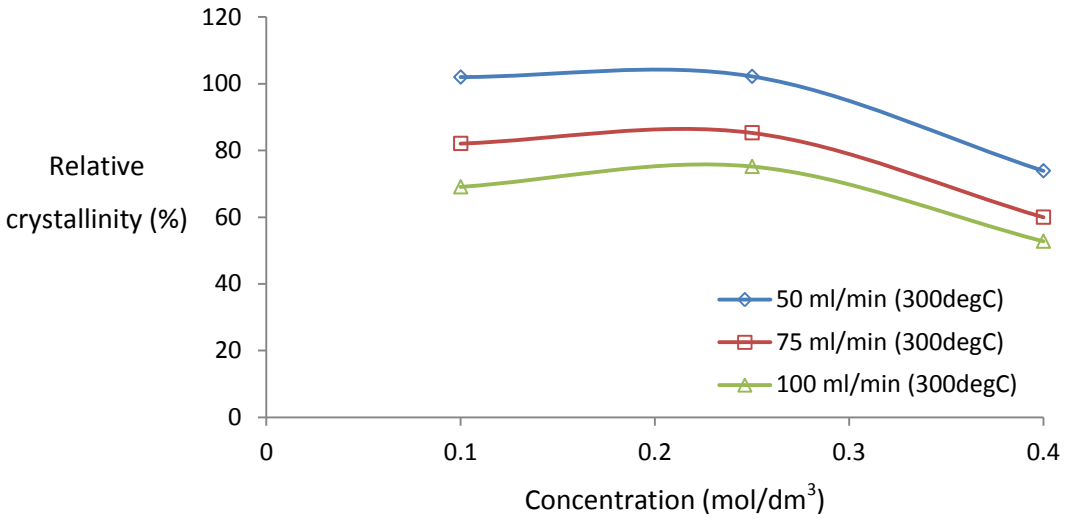

Figure 5. 14 - Effect of concentration on the resulting RC percentage at varied flow rates and 300°C

It was identified that even at relatively high temperatures (300°C), the short residence times observed in this study at higher flow rates were not sufficiently long enough to convert the higher number of nuclei in solution found at higher concentrations, to the same degree of crystallinity as the concentration exceeded 0.1M. Therefore to synthesize highly crystalline particles at higher concentrations, the residence time or flow rate needs to be adjusted accordingly.

5.5.4) Effect of the interaction between temperature and flow rate on PY

As indicated in Figure 5.12, a strong interaction between temperature and flow rate was identified, parameter BC, with a contribution factor of 20.6%. The factorial trial model for RC was used to plot the predicted RC percentage versus the flow rate at different temperatures and at a constant 0.4M concentration, as depicted Figure 5.15.

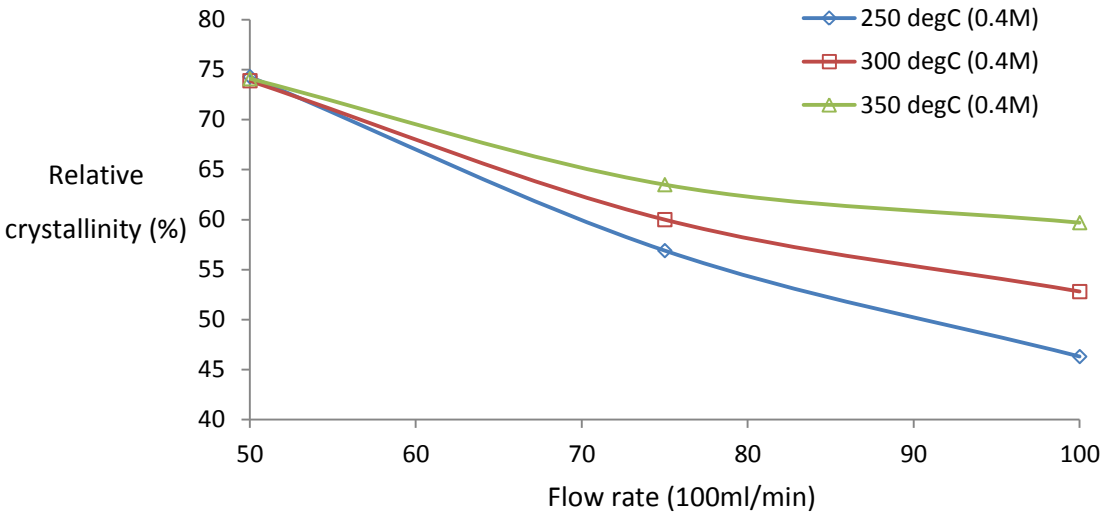

Figure 5. 15 - Effect of flow rate on the resulting RC percentage at varied temperature and 0.4M

It can be clearly observed from Figure 5.15, that at low flow rates (50ml/min) the RC is almost identical across the high and low temperature variations used in this study. However as the flow rate increased, the resulting RC was found to decrease proportionately with a decrease in temperature. As mentioned previously, the temperature is also a function of residence time, which decreases slightly as the temperature increases. Therefore a decrease in flow rate and hence increase in residence time allowed a longer reaction time for increased crystallographic arrangement under the high temperature conditions. Even though higher temperatures slightly decreased the residence time, they still favoured a higher relative crystallinity at higher at high flow rates (100ml/min) as depicted in Figure 5.15.

5.5.5) Effect of the interactions between all three parameters on PY

As mentioned previously, the rate of crystal grow is accelerated at higher temperatures (Demopoulos 2009), therefore it was expected that the interaction between concentration and flow rate was also dependent on temperature. As shown in Figure 5.12, an interaction between all three parameters, parameter ABC, did exist with a positive contribution factor of 11.9%. The crystallinity was therefore identified to be a function of all three operating parameters which interact, where the highest crystallinity found in this research was most favoured by low concentrations, low flow rates and high temperatures as showcased in Figure 5.13b.

5.6) Conclusion

The effects of various operating parameters such as concentration, temperature and flow rate, and the interactions between these parameters were evaluated for their resulting effect on product yield and relative crystallinity in this chapter.

The concentration and temperature were found to both play large roles on the resulting PY, with the flow rate having a lesser effect on PY - although the flow rate was in no way insignificant. Strong interactions between the flow rate and concentration, parameter AC, and the flow rate and temperature, parameter BC were identified. Parameter AC had a contribution percentage of 14.9% and parameter BC had a contribution percentage of 32.4%, which shows how prominent these interactions can be on the overall system, making up almost half of the contribution percentage.

The concentration and flow rate were established to have strong negative influence on the relative crystallinity. This implied that an increase in concentration and flow rate led to a large reduction in RC. The temperature was identified to have a positive effect on RC, although less significant. The temperature was found to interact strongly with the flow rate, parameter BC, with a 20.6% contribution percentage. More importantly, all 3 parameters were found to interact with one another. Parameter ABC was discovered to have a positive 11.9% contribution, which revealed that the RC is complex to control and was highly dependent on all 3 parameters.

Chapter 6 – Attempts at morphology control in the presence and absence of surface modifiers and solvents.

6.1) Introduction

In this chapter, attempts at morphology control are discussed and evaluated in the presence and absence of surface modifiers and solvents. The various additives were identified and their resulting effect on particle morphology and other characteristics were analysed and compared with the relevant literature.

The following topics are presented in this chapter in the following order:

- Factors influencing particle morphology
- Effect of surface modifiers and solvents on particle characteristics
- Effect Span 80 and PIBSA-MEA on particle characteristics
- Effect of Tween 80 on particle characteristics
- Effect of ethanol as a solvent on particle characteristics

6.2) Factors influencing particle morphology

The operating parameters were also evaluated on their resulting effect on particle morphology. As discussed in Chapter 2 (section 2.8.3), numerous authors have reported being able to change and control the shape of particles in CHS by varying critical process parameters (Adschiri et al. 1992; Sue et al. 2004; Hakuta et al. 2005). Yet little has been achieved on the growth of one dimensional iron oxide particles in CHS. However, it is extremely difficult to predict the morphology of particles, as this is influenced by a large number of parameters which includes properties of the crystalline solid, properties of the solution and the operating conditions (Mersmann 1995).

One such critical parameter for slight variation of iron oxide nanoparticle morphology in CHS has been the variation of concentration (Hao & Teja 2003; Xu 2006; Xu & Teja 2008). The particle morphology progression has been depicted in Figure 6.1, where at low concentrations (Fig 6.2a) (0.03M) particles were mostly spherical until the concentration was doubled (Fig 6.2b) (0.06M) resulting in some particles taking on a rhombic crystal habit (Xu 2006; Xu & Teja 2008). At considerably higher concentrations of 0.1M,0.25M and 0.4M used in this study (Fig 6.2c), some of the particles began to exhibit a bi-pyramidic morphology. While at the highest concentration of 0.5M (Fig 6.2d), the same bi-pyramidic shape was observed by Hao and Teja (2003).

The particle morphology found in this research did not appear to have any specific or obvious trend, as bi-pyramidic shaped particles were observed within the concentration range studied (0.1M, 0.25M and 0.4M). As bi-pyramidic particles were observed at all three concentration variations, the other parameters (temperature and flow rate) were also evaluated. It was proposed that a unique combination of the three parameters was required to form the bi-pyramidic shape. Depending on the concentration, the residence time and reaction temperature, there had to be sufficient time in order for particles to grow and reach their desired crystal habit. This was best visualized when comparing Figure 6.1a and b at a constant 0.25M concentration, where 6.1a is at a low temperature (250°C) and residence time (0.71s) and 6.1b is at a high temperature (350°C) and higher residence time (1.09s). Figure 6.1b clearly has a better refined morphology due to increased diffusion rates associated with higher temperatures (Demopoulos 2009) and the increased residence time allowed for an increased consumption of nuclei through proposed OR kinetics.

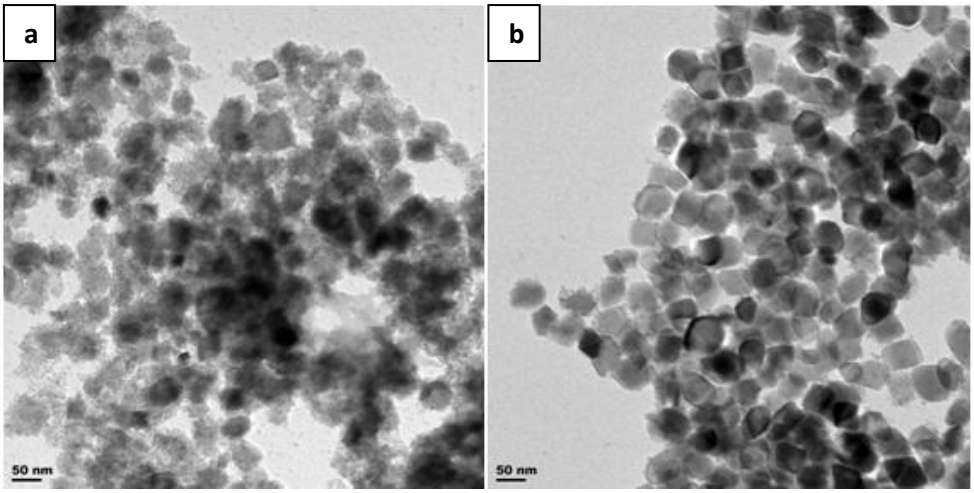

Figure 6. 1 - Comparison of particle morphology at a constant 0.25M concentration where (a) 250°C, 100ml/min. (b) 350°C, 50ml/min

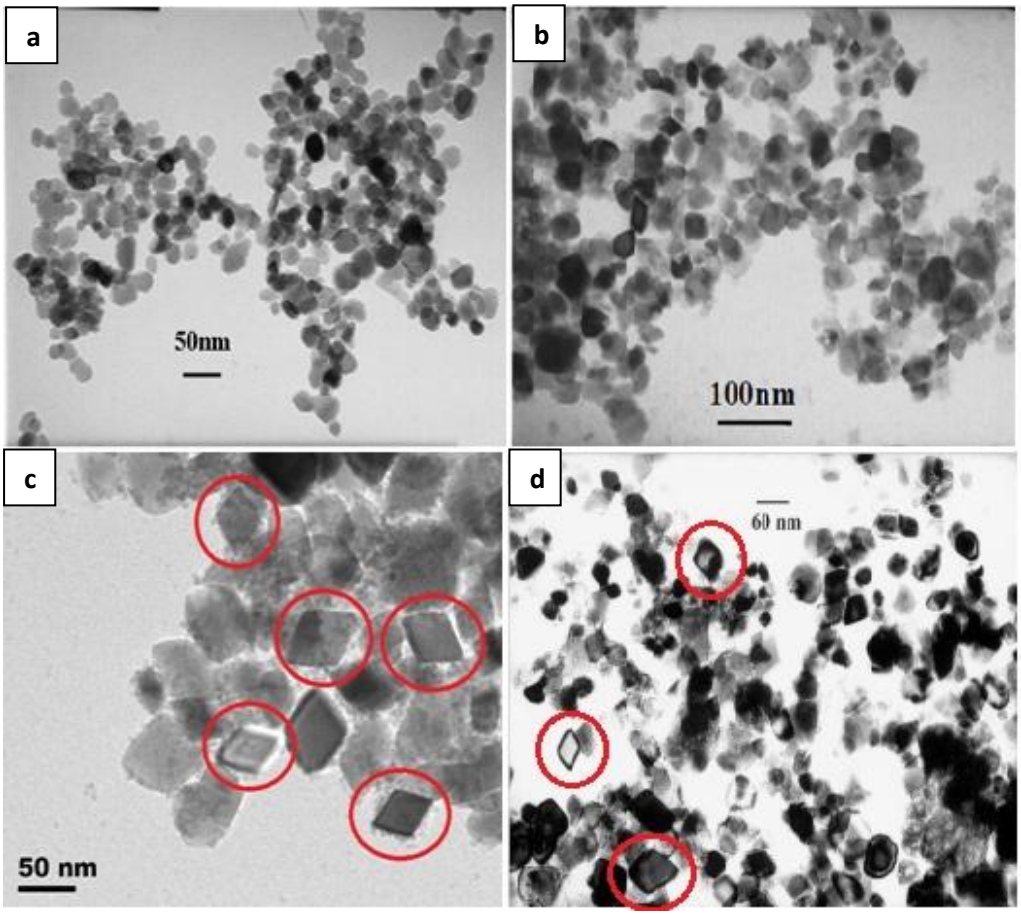

Figure 6. 2 - Progression of iron oxide particle morphology with increasing concentration with (a) 0.03M, 300°C, 10.4s residence time reported by Xu (2006) (b) 0.06M, 300°C, 2.6s residence time reported by Xu (2006) (c) 0.25M, 250°C, 1.42s residence time found in this study (d) 0.5M, 300°C, 12s residence time reported by Hao & Teja, (2003)

Early work by Hakuta (1999), who tried to explain the differing morphology of boehmite particles, attributed the change to selective ion absorption due to a change in ion species distribution. This was contested by Hao and Teja (2003) and Xu (2006) who both determined that the species distribution did not vary much for iron oxide particles with a change in operating parameters. Therefore it was stated that the change in morphology was most likely due to particle growth as all particles below 25nm in diameter were relatively spherical. The thermodynamic driving force for crystallization is the reduction of free energy, namely when the free energy of the initial solution phase is greater than the free energy of the crystalline phase plus the final solution phase (De Yoreo & Vekilov 2003). Therefore is was evident that at low concentrations, all Fe^{3+} ions in solutions nucleated almost instantly, resulting in spherical particles due to the lowest free energy. Yet as the concentration increased, some Fe^{3+} ions remained in solution after mixing and secondary nucleation allowed for deposition onto the spherical particles and hence particle growth, which led to a slight alteration in particle morphology or crystal habit.

It was also noted by Xu (2006) and Xu and Teja (2008) that increased residence times aided this minor change in morphology, as an increasing number of particles were found to have irregular shapes at higher residence times. This supports the theory of particle growth being linked to the change in morphology as increased residence time allows for increased time for particle growth and particle aggregation. Similar findings were identified in this study, with increasing numbers of bi-pyramidic shaped particles being formed at higher residence times.

6.3) Effect of Surface modifiers and solvents on particle characteristics

In the past few years, great progress has been made in the chemical growth of uniform α-Fe_2O_3 nanocrystals with a variety of specific shapes and morphologies, using batch synthesis techniques (Chen et al. 2010). However it has been stated by Aimable et al. (2009), that this spectrum of unique particle shapes can be further enlarged if surfactants, polymer additives and/or different water/solvent mixtures are applied. Only a handful of researchers have reported the addition of polymers (Xu 2006), alcohols or solvent mixtures (Li et al. 2011) or surfactants (Hayashi et al. 2010) in order to control particle characteristics in CHS. Although little if any progress for morphology control in CHS has been made through the addition of surface modifiers or solvents there is still a gap in the literature, and the effect of such additives is not well understood. While Xu (2006) investigated the effect of PVA addition on particle characteristics of iron oxide particles, work by Li et al. (2011) and Hayashi et al. (2010) were investigated on ZnO and $BaTiO_3$ respectively. As it has been proposed that the morphology of particles is dependent on the properties on the crystalline solid (Mersmann 1995), the effect of surfactants and solvent mixtures were investigated for their resulting effect on the particle characteristics of iron oxide particles in CHS.

Three different surfactants were chosen, namely Span 80, TWEEN 80 and PIBSA-MEA, where all the surfactant data can be found in Appendix A. One solvent mixture was evaluated with the use of ethanol instead of deionized water in the precursor makeup. Table 6.1 shows the different precursor makeup's and their respective additives. All experiments were conducted at a constant 0.1M ferric nitrate concentration, 300°C reaction temperature and 50ml/min flow rate. The precursors were made up on a mass basis, and 100 grams of each solution was prepared (4.04g of ferric nitrate salt per sample = 0.1M).

Table 6. 1 - Precursor solution additions and the resulting particle characteristics

Experiment number	Corresponding letter	Additive	Mass % of additive	Average particle size (nm)	Coefficient of variation (%)
1	A	Span 80	0.5	N/A	N/A
2	B	Tween 80	1	13.6	49.3
3	C	PIBSA-MEA	1	N/A	N/A
4	D	Ethanol as solvent	95.96 (no water)	11.2	37.1
5	e	none	None	33.8	14.8

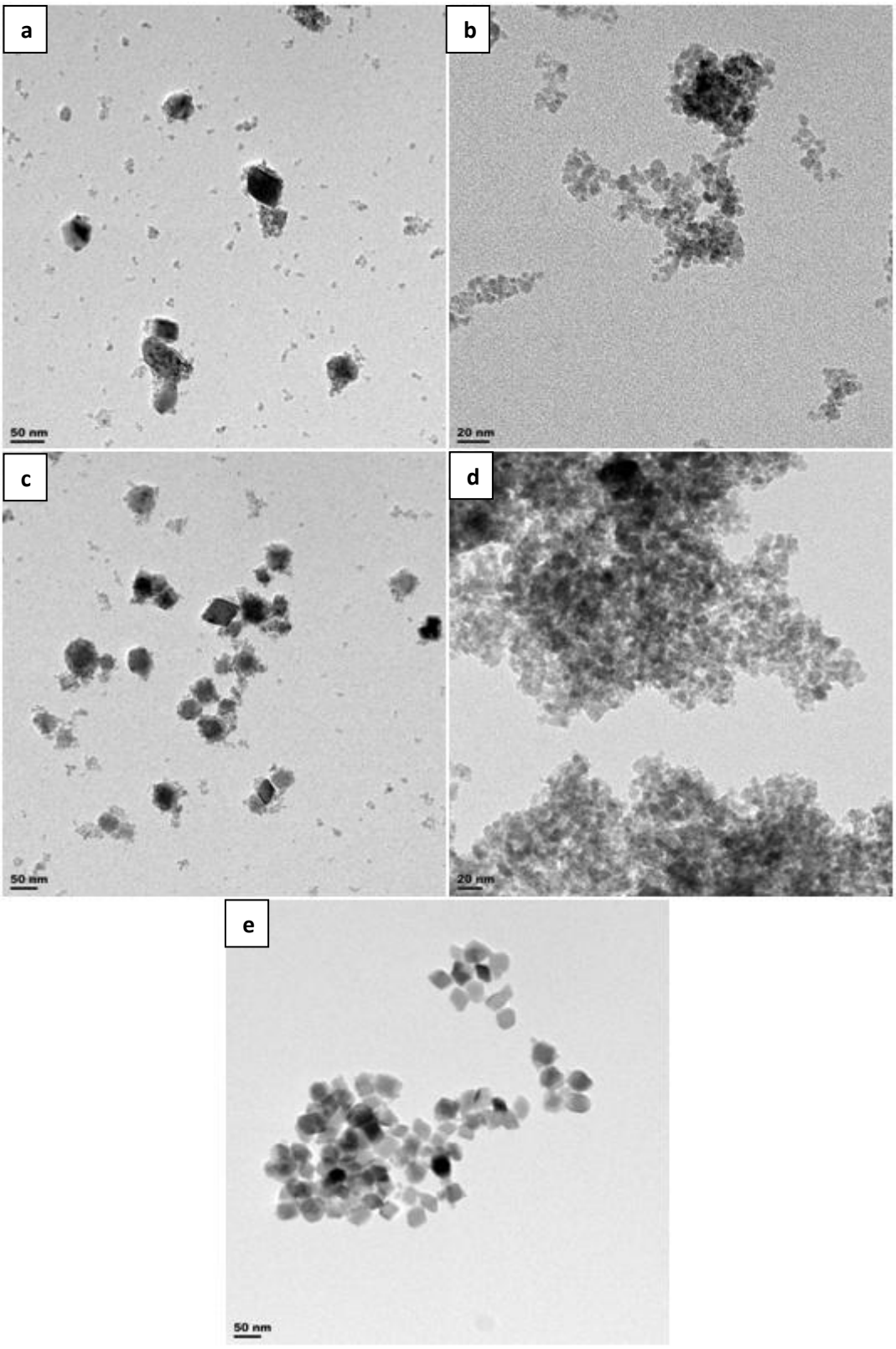

Figure 6. 3 - Comparison of particles synthesized at 0.1M, 300°C and 50ml/min using different surface modifiers and solvents with (a) 0.5% Span 80 (b) 1% Tween 80 (c) 1% PIBSA-MEA (d) 95.96% ethanol and (e) Reference sample - no additives

The operating parameters for the evaluation of surface modifiers and solvents were chosen as a concentration of 0.1M, a reaction temperature of 300°C and a flow rate of 50ml/min. These conditions have been proven to yield well dispersed particles with a well refined shape as shown in Figure 6.3e. Therefore the effects of the additives were compared to a reference sample which has previously produced high quality particles.

6.3.1) Effect Span 80 and PIBSA-MEA on Particle Characteristics

When looking at Figure 6.3a and 6.3c, it can be clearly observed that Span 80 and PIBSA-MEA surfactants had little effect on the system. The particle sizes appear to be identical to the reference sample (Fig 6.3e) and the small nuclei observed in the background indicate that particle growth was somewhat affected. Therefore both surfactants were found to have a negligible or even a negative impact on the system. It was identified that the minimal effects of Span 80 and PIBSA-MEA surfactants were linked to the hydrophile-lipophile balance (HLB) value as shown in Appendix A. The HLB ratio is the ratio between hydrophobicity and hydrophilicity of the head and tail groups respectively, and is not only responsible for surfactant performance but also determines if they are water soluble or water insoluble (Sjoblom 2001). The low HLB ratio of Span 80 (3.4) and PIBSA-MEA (<4) revealed that they were both relatively water insoluble even at low concentrations, and were therefore not able to compete and affect crystal growth at the crystal surface. Fester et al. (2008) and Liu et al. (2006) both reported on the growth of hematite nanorods and nanotubes respectively, in the presence of Span 80 and various alcohols in batch hydrothermal synthesis. Yet it was determined from this study that Span 80 was found to have little influence on particle characteristics in CHS when alcohols were absent. However the use of surfactant/solvent mixtures has yet to be studied in CHS.

6.3.2) Effect of Tween 80 on particle characteristics

Surfactant TWEEN 80 was found to be water soluble due to its high HLB ratio, and was therefore able to dissolve in the precursor solution and directly affect particle growth, as shown in Figure 6.3b. The addition of TWEEN 80 was found to significantly reduce the APS, from 33.8nm to 13.6nm. Similar findings were reported by Hayashi et al. (2010) on the addition of TWEEN 80 surfactant in the formation of $BaTiO_3$particles, where the addition of the surfactant hindered particle growth and reduced the PSD. In this study, the CV value was however found to increase from a low 14.8% to a high 49.3% giving rise to a wider PSD. It was presumed that the broad size distribution was a result of the low surfactant concentration not covering the entire crystal surface as some larger particles

were observed. It was thus proposed that higher surfactant concentrations will slightly drop the APS but significantly drop the CV due to increased surfactant coverage at the crystal/water interface. The morphology on the other hand was found to be of a spherical nature, which revealed a hindrance of surface growth.

The intended kinetic shape control mechanism or capping is through selective adhesion, where the organic surfactants attach to crystal facets during growth. As crystal facet growth is driven by free energy, higher energy facets will grow faster than facets at a lower energy. Therefore surfactants can attach themselves to selective facets, hindering growth in a certain direction (Yadong & Alivisatos 2005). The selective attachment of surfactants to produce unique particle morphologies has been termed templated growth, and Lui et al. (2006) revealed that this mechanism may be time dependent. They found that during longer reaction times, the hematite nanorods grew longer and were more pronounced in batch synthesis. Therefore the short residence times in CHS may not be favourable for templated growth and selective adhesion to occur successfully.

The binding strength of surfactants onto the crystal surface decreases with increasing temperature (Yadong & Alivisatos 2005). Therefore another possibility is that the rapid heating of the precursor solution and the high mixing temperatures in CHS may ultimately render surfactants useless for templated growth and morphology control in CHS. It has been mentioned previously that the change in morphology with an increase in concentration and residence time has been attributed to particle growth (Xu 2006; Xu & Teja 2008). The spherical nature of the particles precipitated in the presence of TWEEN 80 shows hindrance of particle growth. The surfactant is not attaching selectively in order to cap crystal growth. Instead, it is more likely that the surfactant attaches randomly at crystal facets, but the long surfactant tails intertwine causing a network shielding particles from growth and aggregation. A similar mechanism was first identified by Xu (2006) for the addition of PVA in CHS. Yet it is clear that research into the use of surfactants in CHS is lacking, and more experimental work is required for a better understanding of the effect of surfactants at the crystal surface. Surfactant concentration is also very likely to play a large role, as Lui et al. (2006) found that in their batch synthesis, the difference between 0.5ml and 1.5ml of the L113B surfactant changed the morphology from perfect spheres to perfect nanorods respectively.

6.3.3) Effect of ethanol as a solvent on particle characteristics

Ethanol (99.9% pure) was used as a solvent instead of deionized water for the precursor solution, and the resulting particles are expressed in Figure 6.3d. Although no water was used in the precursor make-up, the precursor solution was still reacted with the supercritical water stream at a ratio of 3:2, hence the overall solvent ratio in the product stream after mixing was 40% ethanol and 60% deionized water. From Table 6.1, it can be shown that the APS dropped significantly, from 33.8nm to 11.2nm in the presence of 40% ethanol/water mixture when compared to the reference sample. Little, if any literature exists on the addition of solvents or solvent mixtures in CHS for morphology control. Chen et al. (2010) used different ethanol mixtures to synthesize hematite nanoplates in a batch process, where different ethanol/water ratios could be used to tune plate thickness. They further stated that the addition of ethanol mixtures restricted vertical growth of hematite, which resulted from the inherent polar crystallographic structure of hematite and the organic solvent.

The particles obtained from the use of the 40% ethanol/water solvent were found to be spherical in nature, similar to those found with the addition of TWEEN 80 displayed in Figure 6.3b, thus no change to a unique morphology was observed. However, the decrease in APS can be explained through change in nucleation kinetics. According to De Yoreo and Vekilov (2004) the critical size of the nucleated particles is a function of the interfacial energy, where the lower the interfacial energy, the smaller the particle size and the more likely nucleation will occur at a given supersaturation rate. Shao et al. (2005) identified that the surface tension of water ($73x10^{-3}$ Nm^{-1}) is roughly 3 times higher than ethanol ($23x10^{-3}$ Nm^{-1}) at room temperature, and therefore ethanol/water mixtures reduce interfacial energy. The addition of ethanol therefore acts in a similar fashion to an increase in reaction temperature by increasing the likelihood for nucleation. Although the reaction temperature has more adverse effects on particles characteristics (Cote et al. 2003) which includes increasing the diffusion coefficient leading to a formation of larger particles (Xu 2006).

It should also be mentioned that when comparing the addition of TWEEN 80 and ethanol, the particles synthesized in the presence of ethanol appear to be more agglomerated as shown in Figure 6.3d. Although both experiments yielded a similar APS, the surfactant tail network as mentioned previously acted as a particle dispersant. While the lack of a dispersant in the ethanol/water mixture and the high surface area of the small particles promoted particle aggregation.

6.4) Conclusion

The morphology of most particles were relatively spherical in nature, although some bi-pyramidic particles were observed. Although these bi-pyramidic particles were observed at all concentrations studied (0.1M, 0.25M and 0.4M), the growth of these particles were promoted by an increase in concentration and were aided by lower flow rates, due to the increased reaction time allowing for the formation of these bi-pyramidic particles.

PIBSA-MEA and Span 80 were found to have little effect on the system, which was linked to their HLB value and hence water insolubility making them unable to compete at the crystal surface. In contrary, Tween 80 was water soluble, and significantly reduced the APS from 33.8nm to 13.6nm when compared to the absence of Tween 80. The particles were found to be relatively spherical and therefore the morphology remained unchanged.

When ethanol was used as the precursor solvent, the findings were similar to that of Tween 80, with a large reduction in APS from 33.8nm to 11.2nm and yielded particles of a spherical nature. The particles synthesized using the ethanol based precursor solution were also found to be highly aggregated, unlike the dispersed particles formed in the presence of Tween 80. It was proposed that the surfactant concentration and solvent percentage addition may have a large affect on the system, and requires further research.

Chapter 7 - Summary of Results and Conclusion

7.1) Introduction

This study investigated the critical process parameters required for the controlled growth of iron oxide nanoparticles using the continuous hydrothermal synthesis method. Numerous authors have reported the synthesis of high quality iron oxide particles using the CHS method (Adschiri et al. 2000; Cote & Teja 2002; Evans 2006; Sue et al. 2006; Xu 2006; Liang et al. 2010). However, Xu (2006) argued that the effects of operating parameters are still not well understood. Individual researchers had reported three completely different trends on the effect of temperature on APS in the literature. This necessitated action to resolve the apparent contradicting reports and to determine the critical process parameters required for controlled growth. It was proposed that a factorial design may be beneficial to not only to determine which parameters were significant, but also to identify interactions between parameters and to determine their influence on the CHS system. The objectives were therefore to construct and commission a fully functional CHS pilot plant, and to identify the critical process parameters and the critical process parameter interactions. A 3-level, 3-factor Box-Behnken factorial design was utilized and the concentration, temperature and flow rate were evaluated with their resulting affect of the APS, PSD, PY and RC. The addition of surface modifiers and solvents and their resulting affect on particle characteristics were also analysed.

7.2) Summary

The concentration had a critical influence on APS, drastically increasing the average particle size as determined from the high correlation factor. While the correlation factors for temperature and flow rate revealed negligible influence on APS. Looking at parameter interactions, it was discovered that a significant interaction between the temperature and concentration existed. This interaction led to three different trends on the resulting APS. It was highly probable, that this interaction between concentration and temperature and its effect on APS has been responsible for the conflicting reports on the effect of temperature in the literature.

The flow rate was the key parameter influencing the PSD, with the correlation factor identifying a major increasing effect. The temperature had a minor negative effect on PSD, while the effect of concentration was established to be negligible, as determined through the correlation factors. An interaction between the concentration and flow rate was found to have a major increasing effect on the PSD, and hence a negative effect. A moderate negative interaction between all three parameters was observed, which reduced the PSD.

The PY was equally dominated by concentration and temperature, with major positive correlation factors, while a minor positive correlation factor on the effect of flow rate was observed. A significant positive interaction was witnessed between the flow rate and concentration, while a critical positive interaction was observed between the flow rate and temperature. These two interactions combined made up almost half of the contribution percentage effect on PY, thus revealing the importance of flow rate.

As determined through the correlation factors, the RC was found to be dependent on all operating parameters, with a major negative effect of flow rate, a moderate negative influence of concentration, and a minor positive dependence on temperature. The temperature and flow rate were found to interact, having a major positive influence on the RC. While a significant positive interaction was observed between all three parameters on the resulting RC, further strengthening a dependence on all parameters.

The critical parameters identified are the interaction between temperature and flow rate. It had a critical increasing effect on PY and a major increasing effect on RC, with minimal increase in APS or PSD. This is a fundamental interaction, as maximising the yield and crystallinity will improve the efficiency of the CHS process and make it more appealing for upscale. The effects of all parameters and parameter interactions have been summarized in Table 7.1.

An investigation was also conducted on effects of parameters on particle morphology, which included the use of various additives in CHS. It was determined that the concentration was responsible for promoting a change in crystal habit from relatively spherical particles to a bi-pyramidic morphology. While these bi-pyramidic particles were observed at all concentrations, their growth appeared to be promoted by an increase in concentration and further aided by increased residence times. Further investigation led to the effect of additives, where surfactants and solvents (ethanol) were introduced. Water insoluble surfactants were found to have little effect, while water soluble surfactants and solvents drastically reduce the APS. A 1% addition of Tween 80 led to a 60% reduction in APS of dispersed particles, while using ethanol as a precursor solvent led to a 67% reduction in APS of aggregated particles. Yet no surface modification occurred and the particle morphologies remained in a relatively spherical nature.

Table 7.1 - Summary of process parameter and parameter interactions on particle characteristics

Parameter	Average particle size	Particle size distribution	Product yield	Relative crystallinity
Concentration	critical increase (0.893)	negligible (0.03)	major increase (0.504)	moderate decrease (-0.483)
Temperature	negligible (0.054)	minor decrease (-0.235)	major increase (0.557)	minor increase (0.235)
Flow rate	negligible (-0.036)	major increase (0.545)	minor increase (0.132)	major decrease (-0.589)
Interactions				
Conc and Temp	significant increase (12.1%)	negligible (0.01%)	very minor increase (1.8%)	negligible (-0.45%)
Conc and Flow	Very minor increase (1.7%)	major increase (22.1%)	significant increase (14.9%)	minor increase (5%)
Temp and Flow	minor increase (3.4%)	negligible (0.03%)	critical increase (32.4%)	major increase (20.6%)
All three parameters	negligible (0%)	moderate decrease (-8.5%)	negligible (0.5%)	significant increase (11.9%)

Correlation factor scale:

< 0.1 = negligible

0.1 - 0.3 = minor

0.3 - 0.5 = moderate

0.5 - 0.75 = major

> 0.75 = critical

Contribution factor scale:

< 1% = negligible

1 - 3% = very minor

3 - 5% = minor

5 - 10% = moderate

10 - 20% = significant

20 - 30% = major

> 30% = critical

7.3) Conclusion

A fully functional CHS pilot plant has been constructed and commissioned.

The critical parameters for particle control were identified as follows:

- For control of APS: concentration, and the interaction between concentration and temperature.
- For control of PSD: Flow rate, and the interaction between flow rate and concentration.
- For control of PY: Temperature; concentration; the interaction between concentration and flow rate, and the interaction between temperature and flow rate.
- For control of RC: Temperature; concentration; the interaction between flow rate and temperature, and the interaction between all three operating parameters.
- The RC was complex to control and is highly dependent on all three operating parameters.
- Certain operating parameters appeared to have little effect on a specific particle characteristic such as the effect of flow rate on PY, yet interacted strongly with other parameters.

It was shown that the interaction between concentration and temperature caused a significant increase in APS, thus providing a plausible explanation for the conflicting reports the effects of temperature on APS in CHS.

The critical process parameters for maximum product yield and high crystallinity with minimum effect on average particle size and size distribution was found to be the interaction between temperature and flow rate and could be the key for successful upscaling of the CHS process.

Surfactants and solvents showed little promise for changing the particle morphology, although influenced other particle characteristics such as a reduction in APS.

7.4) Contributions and recommendation for further research

This work contributed to understanding conflicting reports in the literature regarding the effect of process conditions, especially on the effect of temperature on the particle characteristics produced in CHS. The use of a factorial trial elaborated the importance on interactions between process conditions and that results obtained by changing one parameter at a time may not present a true reflection of that specific parameter under slightly different conditions. It therefore advocates the

use of factorial trials for evaluation and optimisation of process conditions for CHS due to the complex nature of the process. Although morphology control of iron oxides in CHS was not achieved, the operating parameter interactions identified will prove insightful for future researchers when designing and up scaling the CHS process for industrial use. Based on the results that interactions play a large role on particle characteristics, a factorial trial may also be suggested as to provide more promising results on the effect of surfactants and solvents in CHS. However it is clear that more research is required to gain a better knowledge and understanding into the growth mechanisms of particles in CHS. Some recommendations for future studies are as follows:

- The use of different solvent/water ratios for controlling particle characteristics
- The use of a factorial trial to evaluate the interactions between surfactants and solvents in the reaction system.
- Investigation of the synthesis of akaganeite (β-FeOOH) phase iron oxide at low reaction temperatures and in the presence of solvents to decrease interfacial energy and promote nucleation at lower temperatures.
- Investigation of the effect of reactor diameter would prove invaluable for up scale potential and industrialization of the CHS process.

References

Adschiri, T., Hakuta, Y. & Arai, K. 2000. Hydrothermal synthesis of metal oxide fine particles at supercritical conditions. *Industrial & Engineering Chemistry Research,* Volume 39, p. 4901-4907.

Adschiri, T., Hakuta, Y., Sue, K. & Arai, K. 2001. Hydrothermal synthesis of metal oxide nanoparticles at supercritical conditions. *Journal of Nanoparticle Research,* Volume 3, p. 227–235.

Adschiri, T., Kanazawa, K. & Arai, K. 1992. Rapid and continuous hydrothermal crystallization of metal oxide particles in supercritical water. *Journal of American Ceramics Society,* Volume 75, p. 1019-1023.

Adschiri, T., Mousavand, T., Takami, S. & Umtsu, M. et al. 2005. Supercritical Hydrothermal synthesis of advanced metal oxide nanoparticles. *Materials Chemistry in Supercritical Fluids.*

Ahuja, S. & Scypinski, S. 2001. *Handbook of Modern Pharmaceutical Analysis.* 2nd ed. USA: Elsevier inc.

Aimable, A., Aymes, D., Bernard, F. & Le Cras, F. 2009. Characteristics of $LiFePO_4$ obtained through a one step continuous hydrothermal synthesis process working in supercritical water. *Solid State Ionics,* Volume 180, p. 861–866.

Aimable, A., Buscaglia, M.T., Buscaglia, V. & Bowen, P. 2010. Polymer-assisted precipitation of ZnO nanoparticles with narrow particle size distribution. *Journal of the European Ceramic Society,* Volume 30, p. 591.

Aimable, A., Muhr, H., Gentric, C. & Bernard, F. et al. 2009. Continuous hydrothermal synthesis of inorganic nanopowders in supercritical water: Towards a better control of the process. *Powder Technology,* Volume 190, p. 99–106.

Aimable, A., Xin, B., Millot, N. & Aymes, D. 2008. Continuous hydrothermal synthesis of nanometric BaZrO3 in supercritical water. *Journal of Solid State Chemistry,* Volume 181, p. 183–189.

Almeida, T. 2010. *Hydrothermal Synthesis and Characterisation of α-Fe_2O_3 Nanorods.* Britain: Unpublished PhD thesis: University of Nottingham.

Anderson, M.J. & Whitcomb, P.J. 2005. *RSM simplified: Optimizing processes using response surface methods for design of experiments.* USA, New York: Productivity press.

Arai, Y., Sako, T. & Takebayashi, Y. 2002. *Supercritical Fluids: Molecular, Interactions,Physical Properties, and New Applications.* New York: Springer-Verlag Nerlin Heidelberg.

Averick, M. 2007. *Implications of Nanotechnology as percieved by Nano-Scientists.* USA, Providence: Unpublished Senior Honours Thesis.

Blood, P.J., Denyer, J.P., Azzopardi, B.J. & Poliakoff, M. et al. 2004. A versatile flow visualisation technique for quantifying mixing in a binary system: application to continuous supercritical water hydrothermal synthesis (SWHS). *Chemical Engineering Science,* Volume 59, p. 2853 – 2861.

Borg, R.J. & Dienes J.G. 1992. *The Physical Chemistry of Solids*. Boston: Academic press.

Bozzola, J.J. & Russell, L.D. 1992. *Electron Microscopy.* USA, Boston: Jones and Bartlett Publishers Inc.

Brunner, G. 2014. *Hydrothermal and Supercritical Water Processes.* 5th ed. United Kingdom: Elsevier B.V.

Cahn, R., Haasen, P. & Cremer, E. 1991. *Materials Science Technology: Phase Transformations in Materials.* 5th ed. Weiheim: WCH Press.

California Nanoscale Institute. 2002. *What is Nanoscience?.* [Online]

Available at: http://csep.cnsi.ucsb.edu/node/152

[Accessed 28th May 2012].

Cansell, F., Aymonier, C. & Loppinet-Serani, A. 2003. Review on materials science and supercritical fluids. *Current Opinion in Solid State and Materials Science,* Volume 7, p. 331-340.

Chaudhry, A.A. 2008. *Continuous Hydrothermal Flow Synthesis and Characterisation of Nano-Bioceramics and their Rapid Consolidation Using Spark Plasma Sintering.* UK, London: Unpublished Ph.D thesis submitted at Queen Mary, University of London.

Chen, L., Yang, X., Chen, J. & Liu, J. 2010. Continuous shape- and spectroscopy-tuning of hematite nanocrystals. *Inorganic Chemistry,* Volume 49, p. 8411–8420.

Chen, M., Ma, C.Y., Mahmud, T. & Darr, J.A. et al. 2011. Modelling and simulation of continuous hydrothermal flow synthesis process for nano-materials manufacture. *The Journal of Supercritical Fluids,* Volume 59, p. 131– 139.

Chowdhury, M.R, Fester, V., Kale, G. & Cespedes, O. 2014. Hydrothermal precipitation of b-FeOOH nanostructure(s) in mixed solvent: study of their morphological and structural evolution. *Journal of Nanoparticles Research,* Volume 16, p. 2412.

Cornell, R.M. & Schertmann, U. 2003. *The Iron Oxides: Structure, Properties, Reactions, Occurrences and Uses.* 2nd ed. Germany: Wiley-VCH.

Cote, L.J., Teja, A.S., Wilkinson, A.P. & Zhang, Z.J. 2002. Continuous hydrothermal synthesis and crystallization of magnetic oxide nanoparticles. *Journal of Materials Research.* Voulme 17, p.2140-2416.

Cote, L.J., Teja, A.S., Wilkinson, A.P. & Zhang, Z.J. 2003. Continuous hydrothermal synthesis of $CoFe_2O_4$ nanoparticles. *Fluid Phase Equilibria,* Volume 210, p. 307–317.

Cullity, B.D. & Stock, S.R. 2001. *Elements of X-ray Diffraction.* 3rd edition ed. USA, New Jersey: Prentice-Hall, Inc.

Cushing, B.L., Kolesnichenko, V.L. & O'Connor, C.J. 2004. Recent advances in the liquid-phase synthesis of inorganic nanoparticles. *Chemical Reviews.,* Volume 104, p. 3893-3946.

De Yoreo, J. & Vekilov, P. 2003. *Principles of Crystal Nucleation and Growth,* s.l.: Washington, DC: Mineralogical society of america.

Demopoulos, G. 2009. Aqueous precipitation and crystallization for the production of particulate solids with desired properties. *Hydrometallurgy,* Volume 96, p. 199–214.

Drever, J. 2005. *Water, Weathering and Soils.* 1st ed. UK, Oxford: Elsevier.

Edelstein, A.S. & Cammarata, R.S. 1996. *Nanomaterials: Synthesis, Properties and Applications.* UK, Bristol: Institute of physics publishing.

Eriksson, L., Johansson, E., Kettaneh-Wold, N. & Wikstrom, C. et al. 2008. Design of experiments: Principles and applications. 3rd ed. Sweden: Umetrics.

Evans, E. 2006. *Continuous Hydrothermal Synthesis of Inorganic Nanoparticles.* UK, Nottingham: Unpublished PhD thesis, University of Nottingham.

Fang, Z. 2010. *Rapid Production of Micro- and Nano- Particles using Supercritical Water.* China: Springer- verlag Berlin Heidelberg.

Fester, V., Slatter, P., Biggs, S. & Kale, G. 2008. *Significance of Alcohols in the Synthesis of Iron Oxide Nanorods.* New York, Albany, Green chemietry & engineering, process intensification & nanotechnology conference.

Flegler, S.L., Heckman Jr., J.W. & Klomparens, K.L. 1993. *Scanning and Transmission Electron Microscopy.* USA, New york: W.H. Freeman and Company.

Galkin, A.A., Kostyuk, B.G., Kuznetsova, N.N. & Turakulova, A.O. et al. 2001. Unusual approaches to the preparation of heterogeneous catalysts and supports using water in subcritical and supercritical states. *Kinetics and Catalysis*, Volume 42, p. 154-162.

Garrett-Reed, A. & Bell, D. 2003. *Energy Dispersive X-ray Analysis in the Electron Microscope.* UK, Oxford: BIOS Scientific publishers limited.

Garside, J. 1985. Industrial crystallization from solution. *Chemical Engineering Science,* Volume 40, p. 3-26.

Gilbert, B., Zhang, H., Huang, F. & Finnegan, M.P. et al. 2003. Special phase transformation and crystal growth pathways observed in nanoparticles. *Geochemical Transaction,* Volume 4, p. 20-27.

Gosh, B., Agrawal, D. & Bhatia, S. 1994. Synthesis of zeolite a from calcined diatomaceous clay: Optimization studies. *Industrial and Engineering Chemistry Research,* Volume 33, p. 2107-2110.

Grau-Crespo, R., Al-Baitai, A.Y., Saadoune, I. & De Leeuw, N.H. 2010. Vacancy ordering and electronic structure of gamma- Fe_2O_3 (maghemite): a theoretical investigation. *Journal of Physics: Condensed Matter,* Volume 22, p.255401-255408.

Gunn, J.W. 2008. *The Preparation and Characterization of Superparamagnetic Nanoparticles for Biomedical Imaging and Therapeutic Application.* USA, Washington: ProQuest LLC.

Guo, P., Wei, Z., Wang, B. & Ding, Y. et al. 2011. Controlled synthesis, magnetic and sensing properties of hematite nanorods and microcapsules. *Colloids and Surfaces A: Physicochemical and Engineering Aspects,* Volume 380, p. 234–240.

Hakuta, Y., Adschiri, T., Hirakoso, H. & Arai, K. 1999. Chemical equilibria and particle morphology of beomite (AlOOH) in sub and supercritical water. *Fluid Phase Equilibria,* Volume 158, p. 733-742.

Hakuta, Y., Hayashi, H. & Arai, K. 2003. Fine particle formation using supercritical fluids. *Current Opinion in Solid State and Materials Science,* Volume 7, p. 341–351.

Hakuta, Y., Onai, S., Terayama, H. & Adschiri, T. et al. 1998. Production of ultra-fine ceria particles by hydrothermal synthesis under supercritical conditions. *Journal of Material Science Letters,* Volume 17, p. 1211-1213.

Hakuta, Y., Seino, K., Ura, H. & Adschiri, T. et al. 1999. Production of phosphor (YAG:Tb) fine particles by hydrothermal synthesis in supercritical water. *Journal of Materials Chemistry,* Volume 9, p. 2671–2674.

Hakuta, Y., Ura, H., Hayashi, H. & Arai, K. 2005. Effects of hydrothermal synthetic conditions on the particle size of AlO(OH) in sub and supercritical water using a flow reaction system. *Material Chemistry and Physics*, Volume 93, p. 466-472.

Hao, Y. & Teja, A. 2003. Continuous hydrothermal crystallization of a-Fe_2O_3 and Co_3O_4 nanoparticles. *Journal of Materials Research,* Volume 18, p. 415-422.

Hayashi, H., Noguchi, T., Islam, N.M. & Hakuta, Y. et al. 2010. Hydrothermal synthesis of $BaTiO_3$ nanoparticles using a supercritical continuous flow reaction system. *Journal of Crystal Growth,* Volume 312, p. 1968–1972.

He, Y., Sang, W., Wang, J. & Wu, R. et al. 2005. Polymer-assisted complexing controlled orientation growth of ZnO nanorods. *Journal of Nanoparticles Research,* Volume 7, p. 307-310.

Holloway, P. & Vaidyanathan, P. 2010. *Characterization of Metals and Alloys.* USA, New York: Momentum press.

Hyatt, N. 2003. *Guidelines for Process Hazards Analysis, Hazards Identification and Risk Analysis.* 1st ed. Canada, Ontario: Dyadem Press.

Jain, T. & Sandhu, A. 2009. *Quantitative Methods.* New Delhi, India: V.K Publications.

Jessop, G.J. & Leitner, W. 1999. *Chemical Synthesis using Supercritical Fluids.* Germany: Wiley-VCH.

Jiang, X.C., Yu, A.B., Yang, W.R. & Ding, Y. et al. 2010. Synthesis and growth of hematite nanodiscs through a facile hydrothermal approach. *Journal of Nanoparticle Research,* Volume 12, p. 877–893.

Joglekar, A.M. 2010. *Industrial Statistics: Practical Methods and Guidance for Improved Performance*. USA, New Jersey: Wiley & Sons, inc.

Johnson, R.L. 2006. *Nanotechnology.* Minneapolis, USA: A division of lerner publishing group.

Kanamura, K., Umegaki, T., Toyoshima, K. & Okada, K. et al. 2000. Preparation and electrochemical characterization of $LiCoO_2$ single crystal particles prepared by supercritical water synthesis (SCWS). *Materials Research Society Symposium Proceedings*. Volume 575, p. 59-64.

Kawai-Nakamura, A., Sato, T., Sue, K. & Tanaka, S. et al. 2008. Rapid and continuous hydrothermal synthesis of metal and metal oxide nanoparticles with a microtube-reactor at 523 K and 30 MPa. *Materials Letters,* Volume 62, p. 3471–3473.

Kawasaki, S.I., Xiuyi, Y., Sue, K. & Hakuta, Y. et al. 2009. Continuous supercritical hydrothermal synthesis of controlled size and highly crystalline anatase TiO_2 nanoparticles. *The Journal of Supercritical Fluids,* Volume 50, p. 276–282.

Kawasaki, S.-I., Sue, K., Ookawara, R. & Wakashima, Y. et al. 2010. Engineering study of continuous supercritical hydrothermal method using a T-shaped mixer: Experimental synthesis of NiO nanoparticles and CFD simulation. *The Journal of Supercritical Fluids,* Volume 54, p. 96–102.

Khursheed, A. 2011. *Scanning electron microscope optics and spectrometers.* Singapore: World scientific publishing Co.

Kletz, T. 1999. *HAZOP and HAZAN.* 4th ed. UK, Warwickshire: Institution of Chemical Engineers.

Kohler, M. & Fritzsche, W. 2004. *Nanotechnology: An Introduction to Nanostructuring Techniques.* Weinheim, Germany: Wiley-VCH.

Kumar, C. 2009. *Magnetic Nanomaterials.* Germany, Weinheim: Wiley-VCH.

Lake International Technologies. 2012. *Material Safety Data Sheet - PIBSA-MEA ,* South Africa: Unpublished MSDS.

Lancaster, M. 2002. *Green chemistry - An introductory text.* UK, Cambridge: The royal society of chemistry.

Lawson, J. 2010. *Design and Analysis of Experiments with SAS*. USA: CRC Press.

Lester, E., Aksomaityte, G., Li, J. & Gomez, S. et al. 2012. Controlled continuous hydrothermal synthesis of cobalt oxide (Co_3O_4) nanoparticles. *Progress in Crystal Growth and Characterization of Materials,* Volume 58, p. 3-13.

Lester, E., Blood, P., Denyer, J. & Giddings, D. et al. 2006. Reaction engineering: The supercritical water hydrothermal synthesis of nano-particles. *Journal of Supercritical Fluids,* Volume 37, p. 209–214.

Liang, M.T., Wang, S.-H., Chang, Y.-L. & Hsiang, H.-I. et al. 2010. Iron oxide synthesis using a continuous hydrothermal and solvothermal system. *Ceramics International,* Volume 36, p. 1131–1135.

Li, S., Gross, G.A., Gunther, P.M. & Kohler, K.M. 2011. Hydrothermal micro continuous-flow synthesis of spherical, cylinder-, star- and flower-like ZnO microparticles. *Chemical Engineering Journal,* Volume 167, p. 681–687.

Liu, L., Kou, H.-Z., Mo, W. & Liu, H. et al. 2006. Surfactant-Assisted Synthesis of alpha-Fe_2O_3 Nanotubes and Nanorods with Shape-Dependent Magnetic Properties. *Journal of Physical Chemistry,* Volume 110, p. 15218-15223.

Mainganye, D. 2012. *Synthesis of Zeolites from South African coal fly ash: Investigation of Scale Pp Conditions.* South Africa, Cape Town: Unpublished MTech thesis, Cape Peninsula University of Technology.

Mandal, S. & Muller, A.H. 2008. Facile route to the synthesis of porous alpha-Fe_2O_3 nanorods. *Materials Chemistry and Physics,* Volume 111, p. 438–443.

Marcus, Y. 2012. *Supercritical Water - A Green Solvent: Properties and Uses.* USA, New Jersey: Wiley & Sons, inc.

Mata, J., Reynolds, P., Gilbert, E. & White, J. 2013. Extended Q-range small angle neutron scattering from inverse micellar solutions of PIBSA-micelle and molecular scattering. *Colloids and Surfaces A: Physicochemical Engineering Aspects,* Volume 418, p. 157-164.

Matsiu, K., Noguchi, T., Islam, N.M. & Hakuta, Y. et al. 2008. Rapid synthesis of BaTiO3 nanoparticles in supercritical water by continuous hydrothermal flow reaction system. *Journal of Crystal Growth,* Volume 310, p. 2584-2589.

Matson, D., Linehan, J.C., Darab, J.G. & Buehler, M.F. et al. 1995. *RTDS: A Continuous, Rapid, Thermal Synthesis Method.* USA, California, s.n.

Mee, R.W. 2009. *A Comprehensive Guide to Factorial Two-Level Experimentation.* USA, Knoxville: Springer.

Mersmann, A. 1995. *Crystallization Technology Handbook.* New York: Marcel Dekker, Inc.

Millot, N., Xin, B., Pighini, C. & Aymes, D. 2005. Hydrothermal synthesis of nanostructured inorganic powders by a continuous process under supercritical conditions. *Journal of the European Ceramic Society,* Volume 25, p. 2013-2016.

Mineral Data Publishing. 2001. *Maghemite,* USA, Arizona: Mineral Data Publishing.

Morimoto, M., Sato, S. & Takanohashi, T. 2012. Effect of water properties on the degradative extraction of asphaltene using supercritical water. *Journal of Supercritical Fluids,* Volume 68, p. 113-116.

Mujtaba, A., Ali, M. & Kohli, K. 2014. Statistical optimization and characterization of pH-independent extended release drug delivery of cefpodoxime proxetil using Box-Behnken design. *Chemical Engineering Research and Design,* Volume 92, p. 156-165.

Naskar, M., Patra, A. & Chatterjee, M. 2006. Understanding the role of surfactants on the preparation of ZnS nanocrystals. *Journal of Colloid and Interface Science,* Volume 297, p. 271-275.

Noguchi, T., Matsui, K., Islam, N.M. & Hakuta, Y. et al. 2008. Rapid synthesis of alpha-Al_2O_3 nanoparticles in supercritical water by continuous hydrothermal flow reaction system. *Journal of Supercritical Fluids,* Volume 46, p. 129–136.

Nolan, N. 2010. *Sol-gel Synthesis and Characterization of Novel Metal Oxide Nanomaterials for Photocatalytic Applications.* Dublin: unpublished PhD thesis, Dublin Institute of Technology.

Ohtsubo, M. & Yoshimura, A. 1991. Particle interaction and rheology of Illite-iron oxide complexes. *Clays and Clay Minerals,* Volume 39, p. 347-354.

Pan, Z., Somasundaran, P., Turro, N. & Jockusch, S. 2004. Interactions of cationic dendrimers with hematite mineral. *Colloids and Surfaces A: Physicochemical Engineering Aspects,* Volume 238, p. 123–126.

Phillips, M.J., Darr, J.A., Luklinska, Z.B. & Rehman, I. 2003. Synthesis and characterization of nano-biomaterials with potential osteological applications. *Journal of Material Science: Materials in Medicine,* Volume 14, p. 875-882.

Pioro, I. & Mokry, S. 2011. Thermophysical properties at critical and supercritical pressures. In: A. Belmiloudi, ed. *Heat Transfer - Theoretical Analysis Experimental Investigations and Industrial Systems.* s.l.: InTech.

Ramsden, J. 2009. *Applied Nanotechnology.* s.l.: Jeremy Ramsden & Ventus publishing ApS.

Ramsden, J. 2011. *Nanotechnology: An Introduction.* 1st ed. Oxford, UK: Elsevier inc.

Ratner, M. & Ratner, D. 2002. *Nanotechnology: A Gentle Introduction to the Next Big Idea.* USA, New Jersey: Pearson education, inc.

Reimer, L. & Kohl, H. 2008. *Transmission Electron Microscopy.* 5th ed. Germany: Springer.

Reza, F. & Masalova, I. 2011. Flow behaviour of highly concentrated emulsions of supersaturated aqueous solution in oil. *Rheologica Acta,* Volume 50, p. 897-907.

Sato, T., Sue, K., Suzuki, W. & Suzuki, M. et al. 2008. Rapid and Continuous Production of Ferrite Nanoparticles by Hydrothermal Synthesis at 673 K and 30 MPa. *Industrial & Engineering Chemistry Research,* Volume 47, p. 1855-1860.

Schiller, J. 2010. *Nanotechnology Development.* 1st ed. USA: Emilie M. Smyth.

Schubert, U. & Husing, N. 2012. *Synthesis of Inorganic Materials.* 3rd ed. Germany, Weinheim: VCH - Wiley.

Schwertmann, U. & Cornell, R.M. 2000. *Iron Oxides in the Laboratory.* 2nd ed. Germany: Wiley-VCH.

Sepeur, S. 2008. *Nanotechnology: Technical Basics and Applications.* Hannover: Vincentz network.

Shao, H.F., Xian, X.F., Yin, J. & Zhu, Z.K. 2005. Controlled morphology synthesis of β-FeOOH and the phase transition to Fe_2O_3. *Journal of Solid State Chemistry,* Volume 176, p. 3130-3136.

Shin, Y.H., Koo, S.-M., Kim, D.S. & Lee, Y.-H. et al. 2009. Continuous hydrothermal synthesis of HT-$LiCoO_2$ in supercritical water. *The Journal of Supercritical Fluids,* Volume 50, p. 250–256.

Sierra-Pallares, J., Marchisio, D.L., Alonso, E. & Parra-Santos, M.T. et al. 2011. Quantification of mixing efficiency in turbulent supercritical water hydrothermal reactors. *Chemical Engineering Science,* Volume 66, p. 1576–1589.

Sigma-Aldrich. 2014. *Span 80.* [Online]

Available at: www.sigmaaldrich.com/catalog/product/fluka/85548?lang=en&region=ZA

[Accessed 5 May 2014].

Sigma-Aldrich. n.d. *Tween 80 Product Information.* [Online]

Available at: www.sigmaaldrich.com/content/dam/sigma-aldrich/docs/Sigma-Aldrich/Product_Information_Sheet/p8074pis.pdf

[Accessed 5 May 2014].

Sjoblom, J. 2001. *Encyclopedic Handbook of Emulsion Technology.* USA, New York: Marcel Dekker, Inc.

Srivastava, M., Ojha, A.K., Chaubey, S. & Singh, J. et al. 2010. Investigation on magnetic properties of α-Fe_2O_3 nanoparticles synthesized under surfactant-free condition by hydrothermal process. *Journal of Alloys and Compounds,* Volume 500, p. 206–210.

Stadtländer, C.K.-H. 2007. Scanning Electron Microscopy and Transmission Electron Microscopy of Mollicutes: Challenges and Opportunities. In: A. Mendez-Vilas & J. Diaz, eds. *Modern Research and Educational Topics in Microscopy.* USA, Clemson: Formatex.

Suchanek, W.L. & Riman, R.E. 2006. Hydrothermal synthesis of advanced ceramic powders. *Advances in Science and Technology,* Volume 45, p. 184-193.

Sue, K., Kawasaki, S.-I., Suzuki, M. & Hakuta, Y. et al. 2011. Continuous hydrothermal synthesis of Fe_2O_3, NiO, and CuO nanoparticles by superrapid heating using a T-type micro mixer at 673K and 30MPa. *Chemical Engineering Journal,* Volume 166, p. 947–953.

Sue, K., Kimura, K., Yamamoto, M. & Arai, K. 2004. Rapid hydrothermal synthesis of ZnO nanorods without organics. *Material letters,* Volume 58, p. 3350-3352.

Sue, K., Kimura, K. & Arai, K. 2004. Hydrothermal synthesis of ZnO nanocrystals using microreactor. *Material letters,* Volume 58, p. 3229-3231.

Sue, K., Suzuki, M., Arai, K. & Ohashi, T. et al. 2006. Size-controlled synthesis of metal oxide nanoparticles with a flow-through supercritical water method. *Green Chemistry*, Volume 8, p. 634-638.

Swarup, S. 2009. *Fluid Dynamics.* 13th ed. India: Krishna Prakashan Media P Ltd.

Teja, A.S. & Koh, P.-Y. 2009. Synthesis, properties, and applications of magnetic iron oxide nanoparticles. *Progress in Crystal Growth and Characterization of Materials,* Volume 55, p. 22-45.

Teledyne Isco. n.d. *Precision Syringe Pumps,* USA, Lincoln Nebraska: Teledyne Isco.

Tighe, C.J., Gruar, R.I., Ma, C.Y. & Mahmud, T. et al. 2012. Investigation of counter-current mixing in a continuous hydrothermal flow reactor. *The Journal of Supercritical Fluids,* Volume 62, p. 165– 172.

Varadan, V.K., Sivathanu-Pillai, A., Mukherji, D. & Dwivedi, M. et al. 2010. *Nanoscience and Nanotechnology in Engineering.* Singapore: World Scientific Publishing Co.

Vining, G. & Kowalski, S.M. 2011. *Statistical Methods for Engineers*. 3rd ed. USA, Boston: Brooks/cole.

Virtual Museum Soils. 2005. *Magnetite.* [Online]

Available at: http://virtual-museum.soils.wisc.edu/magnetite/content.html

[Accessed 23rd September 2012].

Viswanathan, R. & Gupta, R.B. 2003. Formation of zinc oxide nanoparticles in supercritical water. *The Journal of Supercritical Fluids,* Volume 27, p. 187-193.

Wang, G., Gou, X., Horvat, J. & Park, J. 2008. Facile synthesis and characterization of iron oxide semiconductor nanowires for gas sensing application. *Journal of Physical Chemistry,* Volume 112, p. 15220-15225.

Wang, W.-W. & Yao, J.-L. 2010. Synthesis and magnetic property of silica/iron oxides nanorods. *Materials Letter,* Volume 64, p. 840–842.

Wang, Y. & Cao, G. 2011. *Nanostructures and nanomaterials: Synthesis, Properties and Applications.* UK, Covent garden: World scientific.

Wei, C. & Nan, Z. 2011. Effects of experimental conditions on one-dimensional single-crystal nanostructure of beta-FeOOH. *Materials Chemistry and Physics,* Volume 127, p. 220–226.

Weng, X., Zhang, J., Wu, Z. & Liu, Y. et al. 2011. Continuous syntheses of highly dispersed composite nanocatalysts via simultaneous co-precipitation in supercritical water. *Applied Catalysis B: Environmental,* Volume 103, p. 453–461.

Williams, B.D. & Carter, C.B. 1996. *Transmission Electron Microscopy: A Textbook for Materials Science*. 2nd ed. USA, Huntsville: Springer.

Xu, C. 2006. *Continuous and Batch Hydrothermal Synthesis of Metal Oxide Nanoparticles and Metal Oxide-Activated Carbon Nanocomposites.* USA, Georgia: Unpublished PhD thesis, Georgia Institute of Technology.

Xu, C. & Teja, A.S. 2008. Continuous hydrothermal synthesis of iron oxide and PVA-protected iron oxide nanoparticles. *Journal of Supercritical Fluids,* Volume 44, p. 85–91.

Yadong, Y. & Alivisatos, A. 2005. Colloidal nanocrystal synthesis and the organic-inorganic interface. *Nature,* Volume 437, p. 664-670.

Yang, G., Chen, Q., Li, X.-X. & Cao, X.-Y. 2010. Study on sorption behaviours of Tween 80 on marine sediments. *Chemosphere,* Volume 79, p. 1019-1025.

Yang, W.-H., Lee, C.-F., Tang, H.Y. & Shieh, D.-B. et al. 2006. Iron oxide nanopropellers prepared by a low-temperature solution approach. *Journal of Physical Chemistry B,* Volume 110, p. 14087-14091.

Yoshii, N., Miura, S. & Okazaki, S. 2001. A molecular dynamics study of dielectric constant of water from ambient to sub- and supercritical conditions using a fluctuating-charge potential model. *Chemical Physics Letters,* Volume 345, p. 195-200.

Zeng, S., Tang, K. & Li, T. 2007. Controlled synthesis of α-Fe_2O_3 nanorods and its size-dependent optical absorption, electrochemical, and magnetic properties. *Journal of Colloid and Interface Science,* Volume 312, p. 513–521.

Zhang, J., Huang, F. & Zhang, L. 2010. Progress of nanocrystalline growth kinetics based on oriented attachment. *Nanoscale,* Volume 18, p. 18-34.

Zhuang, Z., Zhang, J. & Huang, F. 2009. Pure multistep oriented attachment growth kinetics of surfactant-free SnO_2 nanocrystals. *Physical Chemistry Chemical Physics,* Volume 11, p. 8516-8521.

Zhu, L.-P., Liao, G.-H., Bing, N.-C. & Zhao, X. et al. 2011. Synthesis of monodisperse shuttle-like alpha-Fe_2O_3 nanorods via the EDA-assisted method. *Materials Letters,* Volume 65, p. 1287–1290.

Appendix A

Surfactant Data

Surfactant	SPAN 80	TWEEN 80	PIBSA-MEA
Full name	Sorbitan Oleate	Polyoxyethylenesorbitan monooleate	Poly(isobutylene) succinic anhydride - MEA
Description	non-ionic	non-ionic	N/A
Viscosity (mP.s)	1200-2000 at 20°C	4000-6200 at 25°C	400-1600 at 40°C
HLB value	4.3 +- 1	15	<4
density (g/ml)	0.99 at 20°C	1.07 at 25°C	0.85-0.92 at 20°C
Reference	Sigma-Aldrich 2014	Sigma-Aldrich n.d	Lake international technologies 2012; Reza & Masalova 2011

SPAN 80 structure (Naskar et al. 2006)

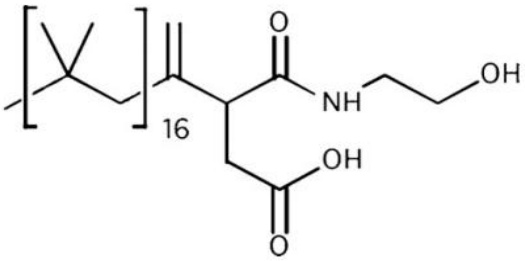

TWEEN 80 structure (Yang et al. 2010)

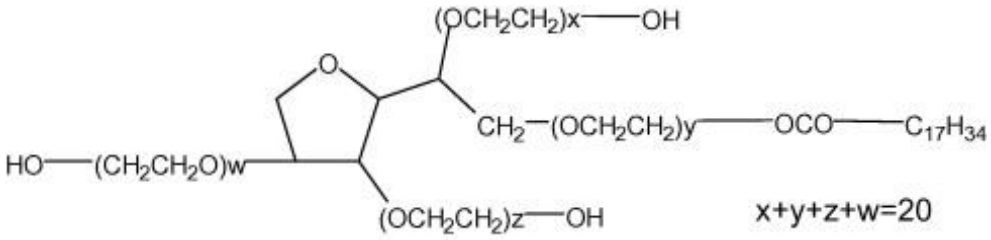

(a) PIBSA (Mata et al. 2013) Structure with (b) MEA functional head (Reza & Masalova 2011)

a

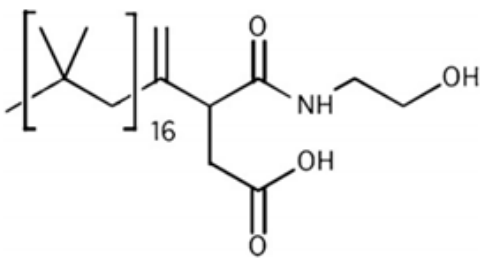

b

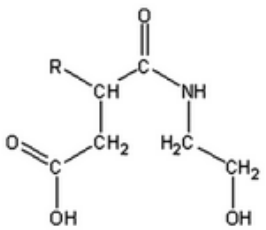

Appendix B

		Run 1	Run 2	Run 3	Run 4	Run 5	Run 6	Run 7	Run 8	Run 9	Run 10	Run 11	Run 12	Run 13	Run 14	Run 15
Peak Position (deg)	**Ref peak (Run 7)**	**Peak height**	**Peak height**	**Peak height**	**Peak height**	**Peak height**	**Peak height**	**Peak height**	**Peak height**	**Peak height**	**Peak height**	**Peak height**	**Peak height**	**Peak height**	**Peak height**	**Peak height**
33 °	283.33	186.67	256.67	146.67	213.33	303.33	313.33	283.33	133.33	223.33	236.67	346.67	210.00	156.67	263.33	276.67
35.5°	293.33	173.33	246.67	163.33	236.67	303.33	256.67	293.33	110.00	176.67	226.67	253.33	203.33	126.67	246.67	260.00
41°	113.33	76.67	116.67	56.67	86.67	113.33	106.67	113.33	56.67	93.33	100.00	100.00	90.00	70.00	73.33	110.00
49.5°	136.67	76.67	126.67	70.00	116.67	166.67	176.67	136.67	83.33	166.67	156.67	210.00	116.67	83.33	140.00	176.67
54°	256.67	146.67	193.33	123.33	166.67	216.67	243.33	256.67	113.33	186.67	176.67	226.67	136.67	133.33	190.00	233.33
57.5°	86.67	53.33	70.00	56.67	80.00	63.33	73.33	86.67	50.00	76.67	66.67	60.00	56.67	50.00	56.67	66.67
62.5°	196.67	146.67	156.67	153.33	166.67	193.33	166.67	196.67	103.33	146.67	143.33	166.67	193.33	116.67	133.33	186.67
64°	180.00	123.33	140.00	93.33	143.33	170.00	186.67	180.00	93.33	140.00	153.33	163.33	110.00	116.67	180.00	180.00
Sum of Peaks	**1546.67**	**983.33**	**1306.67**	**863.33**	**1210.00**	**1530.00**	**1523.33**	**1546.67**	**743.33**	**1210.00**	**1260.00**	**1526.67**	**1116.67**	**853.33**	**1283.33**	**1490.00**
	Relative Crystallinity %	**63.58**	**84.48**	**55.82**	**78.23**	**98.92**	**98.49**	**100.00**	**48.06**	**78.23**	**81.47**	**98.71**	**72.20**	**55.17**	**82.97**	**96.34**

Hematite stick reference pattern from Xpert HighScorePlus software

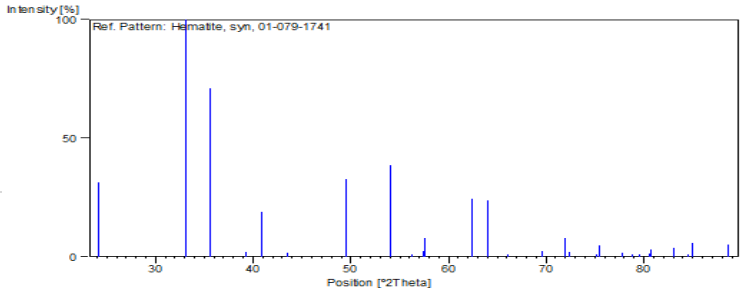

Appendix C

Start up Procedure

Before the CHP pilot plant is started, the following checks should be performed:

- Perform a visual inspection of the plant and pipelines for signs of damage/leaks.
- Check that nothing has tripped in the circuit breaker and that all power supplies are working.
- Ensure that there is enough deionized water to complete the experimental run and full the deionized water reservoir for both pumps .

Once the checks have been completed, the process may now be started.

1. Start the Milton Roy diaphragm pump on "full flow" and ensure the deionized water is flowing through the system.
2. Slowly close the inlet on valve A (waterline) while opening valve B (precursor line), and suck water through the precursor line in order to fill the precursor inlet line with deionized water, eradicating any inline air.
3. Once the precursor line is primed with water, quickly close valve B (precursor line) and reopen valve A (waterline). The precursor line is now primed and ready.
4. Set the flow rate of the Milton Roy pump to the desired set point using the pump calibration chart for 25 MPa of pressure.
5. After the desired flow rate is reached, refill each of the syringe pumps and then set the flow rate to the desired set point using the control panel. Ensure that the Teledyne Isco dual syringe pump is set up in continuous flow mode.
6. Once the water flow rate is steady, increase the system pressure by slowly adjusting the back pressure regulator. Increase the pressure incrementally and ensure that there are no leaks in the system.
7. Now open the tap for the cooling water and set the flow rate to the desired set point using the rotameter.
8. Turn on the control box, making sure that fuses are open (broken), and enter the desired set point temperature for each plate heater. Also set the desired mixer and reactor temperature.
9. Once all the set points have been entered, turn off the control box using the isolator and push in all the fuses.Turn the control box back on, the plate heaters and heating rope should start heating up.
10. Once the system has reached steady state, the precursor solution may now be pumped through the system. Place the water primed precursor inlet tube in the precursor solution.

Rapidly close the valve A and simultaneously open valve B. The precursor solution should now be pumping through the system.

Shutdown Procedure

After the experiments are complete, the plant needs to be shutdown correctly to ensure the safety to all operators and/or personal.

1. Once the desired amount of precursor solution has been fed through the system, close valve B and open up valve A to allow water to run through the Milton Roy diaphragm pump once again.
2. Shut off the isolator on the temperature control box. After this is done, open the box and break fuses 1-8. This will ensure the no heat is being supplied to the system.
3. Turn the temperature control panel back on. Now keep an eye on the temperatures on the control box, they should begin to drop slowly with time.
4. Continue pumping water through the system until all temperatures drop below 90°C, then slowly begin reducing the pressure by adjusting the back pressure regulator until finally reaching ambient pressure.
5. Once the pressure is ambient, take a pH reading of the water flowing out of the system. Continue pumping water through the system until the pH of the inlet and outlet water are constant.
6. Once the pH is constant, the Milton Roy diaphragm pump may be switched off and the dual syringe pump must be changed to independent pump mode and each syringe pump must be run until empty.
7. The temperature control box may now be switched off and the entire system, especially the plate heaters, may be allowed to cool overnight.
8. Finally, close the cooling water valve to shut off the cooling water. The plant is now safely shot down.

Appendix D

Hazard analysis and risk assessment

Before a process plant may be operated safely, all hazards and their potential risks and consequences have to be taken into account. Hyatt (2003), described a hazardous event as the release of matter or energy which has the potential of causing harm to a plant operator, the surrounding community, or the environment. While the term risk was defined by Kletz (1999), as the likelihood that an accident or damage of a particular type and severity will occur in a specific time period as the result of a particular action or event.

As risk is a function of not only consequence but also time, it can be expressed in the following way (Hyatt 2003):

$$\text{Risk} = \text{Consequence} \times \text{Frequency} \qquad \text{(Equation 1)}$$

The consequence and frequency have been illustrated in Table 1 and 2.

Table 1 - Sample of severity ranking adapted from Hyatt (2003)

Rank	Description
1	No injury or health effects
2	Minor injury or minor health effects
3	Injury or moderate health effects
4	Death or severe health effects

Table 2 - Sample of frequency (likelihood) ranking adapted from Hyatt (2003)

Rank	Description
1	Not expected to occur during the facility lifetime
2	Expected to occur no more than once during facility lifetime
3	Expected to occur several times during the facility lifetime
4	Expected to occur more than once in a year

A semi quantitative approach to addressing risk has been adapted from Hyatt (2003), and has been depicted in Figure 1. This method is often used in conjunction with hazard identification tools and has been proven effective for prioritizing risk issues.

Probability				
4	A	N	U	U
3	A	C	N	U
2	A	A	C	N
1	A	A	A	C
	1	2	3	4

Consequence

Figure 1 - Typical risk matrix adapted from Hyatt (2003)

A: **Acceptable -** No risk control measures are needed

C: **Acceptable with control -** Risk control measures are in place

N: **Not acceptable -** Risk control measures should be introduced within a specified time period

U: **Unacceptable -** Risk control measures should be introduced at the earliest opportunity

Hazard and Operability (HAZOP) study

A hazard and operability (HAZOP) study was performed on the CHS pilot plant in order to identify all potential hazards and protect any plant operators. A HAZOP study is a method for identifying potential hazards and problems which prevent safe and efficient plant operation. The HAZOP method of hazard identification also allows for the imagination of the engineers run wild, yet is still performed in a systematic manner to ensure that no hazards are overlooked (Kletz 1999).

For an effective HAZOP study, the following methodology needs to be followed (Hyatt 2003):

1. The process under evaluation first needs to be broken down into manageable nodes to ensure a thorough evaluation.
2. A list of all parameters to be evaluated needs to be constructed

3. Apply guidewords to the parameters; namely "no" or "none", "more than" or "higher", "less than" or "lower", "as well as", "reverse" or "opposite to", and "other than".
4. For each node create deviations by joining the guidewords and the parameter for e.g. higher temperature.
5. List and record Causes for each Deviation.
6. List and record Consequences associated with each cause.
7. List and record Safeguards or Controls that may prevent the Cause and for the consequences.
8. List any future Actions or Recommendations you think should be implemented.
9. A risk matrix may be applied to the consequences. It is fundamental that the severity be evaluated as if no safe guards are in place, while the likelihood or frequency be evaluated as if existing safe guards are in place.

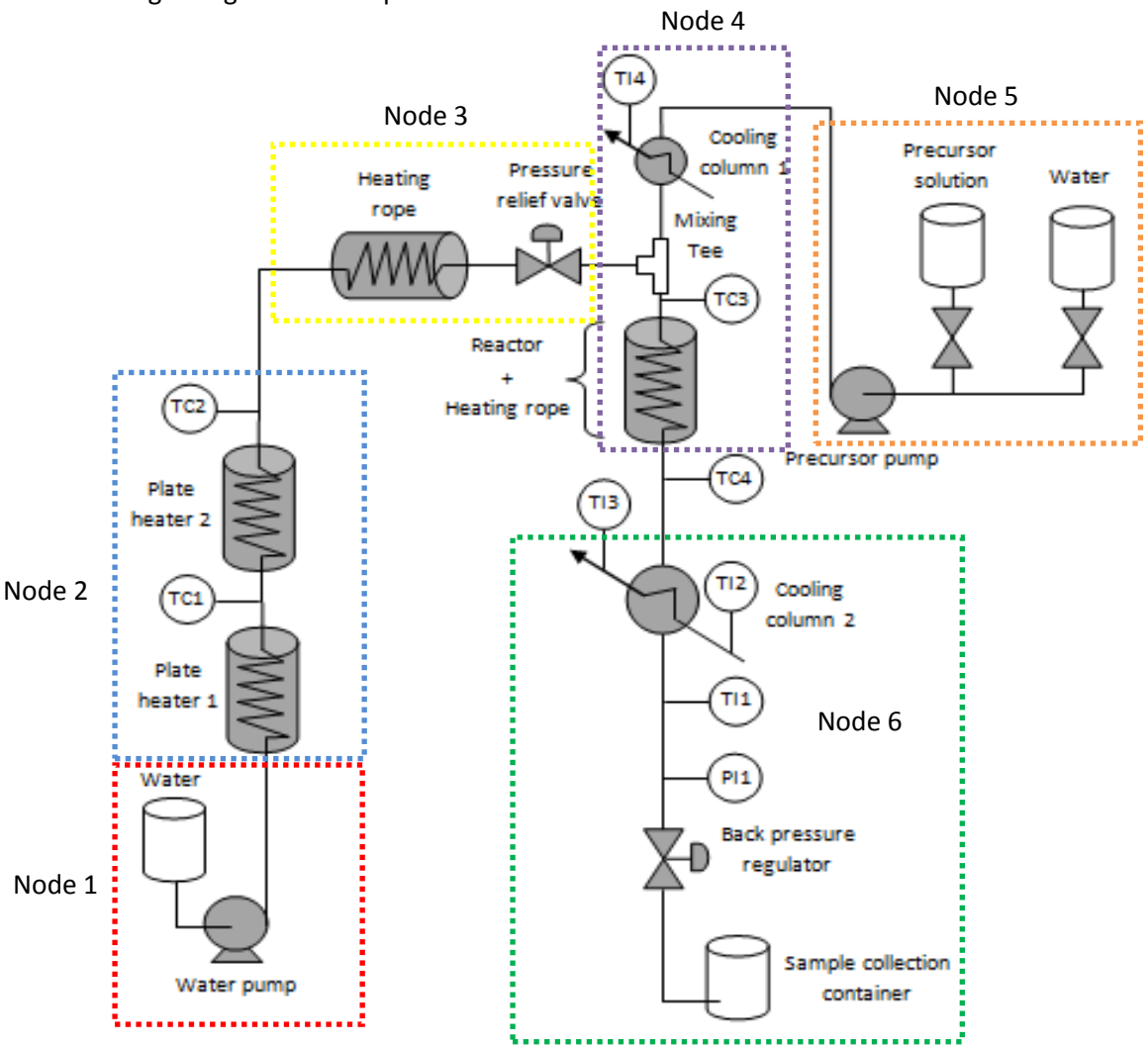

Figure 2 - Process flow diagram of CHS pilot plant broken up into workable nodes

HAZOP conclusion and recommendations

A hazard and operability study has been performed over the entire CHS pilot plant. It has been identified that there were many hazards present, although many of them are either minor or can be negated through simple safeguards. Initial hazards are related to the high temperatures and pressures which are present under standard operating conditions. However, the pressure in the system is controlled by a back pressure regulator and a pressure spike will be released by a pressure release valve. The temperature is controlled by 4 temperature controllers and therefore should remain steady during operation. Utilizing the HAZOP study and the risk rating system, it was possible to determine which risks were acceptable and which risks were not acceptable and required immediate safeguards. It has been identified that a major concern was that of air being pumped through the water line instead of deionized water. This would lead to the plate heaters shutting down, as they wouldn't be able to reach their desired set point and may also lead to particles settling inline. This can be caused by either the inlet beaker breaking and the pumps sucks up air, or the water level running low in the inlet beaker. This problem was overcome by using a large plastic inlet beaker, which will take longer to run low and will not break like a glass beaker. Another concern was loss of precursor pump flow. Without the precursor line flow the temperature in the mixer will spike rapidly and the cooler may not be able to cope with the increase in temperature and steam may exit from the system. It was recommended that a large, plastic beaker was also used to house the precursor pump feed solution. The final major concern was the loss of cooling water. If the cooling system fails, the exit stream temperature would begin to rise rapidly and if it exceeded 100°C, steam would exit the system and the back pressure regulator could be damaged. As the cooling water used was municipal water from the tap, the reliability of flow depends on the municipality. Although in order to avoid this risk all, hose connections were clamped on properly using hose clamps and the outlet temperature was monitored. Future safety improvements may include a flow measurement system in both lines and an alarm system linked to no flow, high temperature and high pressure readings.

It is strongly recommended that the above safety recommendations are implemented before the pilot plant is used for the manufacture of iron oxide nanoparticles, although it can be concluded that with all these safe guards in place, the plant may be operated safely.

HAZOP Analysis									
Node 1 (Red)									
Teledyne Isco dual syringe pump (water pump)									
Guidewords	**Deviation**	**Causes**	**Consequences**	**Risk matrix**				**Safe guards**	**Recommendations**
				P	S	R	RR		
None	No inlet flow	Inlet pipe blockage	Temperature spike; incorrect flow ratio of reactants; incomplete reaction. Particles will be affected	**2**	**2**	**4**	**A**	Blockage filter on inlet pipe	
	No outlet flow	Valve failure	Slight temperature increase; incorrect flow ratio of reactants; incomplete reaction. Particles will be affected	**1**	**2**	**2**	**A**		Regular pump servicing
Less	Lower flow rate	Pump Controller error/failure; Operator error	Temperature spike after heaters; incorrect flow ratio of reactants; incomplete reaction. Particles will be affected	**1**	**1**	**1**	**A**		Regular pump servicing
		Valve blockage	Temperature spike after heaters; incorrect flow ratio of reactants; incomplete reaction. Particles will be affected	**1**	**1**	**1**	**A**	Inlet filter to block incoming particles or impurities	Regular pump servicing
More	Higher flow rate	Controller error/failure	Mild pressure increase;	**1**	**1**	**1**	**A**	Pressure release valve and back	Regular pump

			temperature decrease; incorrect flow ratio of reactants. Particles will be affected					pressure regulator	servicing
		Valve fails while open	Pressure spike; temperature decrease; incorrect flow ratio of reactants. Particles will be affected	**1**	**1**	**1**	**A**	Pressure release valve and back pressure regulator	Regular pump servicing
Part of	Air along with water	Low level of inlet water	Temperature spike; plate heaters overheating; pressure spike; incorrect flow ratio of reactants; incomplete reaction. Particles will be greatly affected	**3**	**3**	**9**	**N**	Thermocouple on plate heater linked to a cut off switch; Keep a secondary water vessel linked via a valve for quick top ups of inlet beaker.	Use large inlet beaker
	Organic alcohols instead of water	Operator error	Minor temperature increase due to lower specific heat capacity when compared to water; incomplete reaction	**1**	**2**	**2**	**A**	Only use water straight from the de-ionizer; smell before use.	Correct labelling of all fluids and beakers
Reverse	Reverse flow	Leaking pump seal or loss of pressure in pump	Reverse flow may damage pump internals; particles may clog up pump.	**1**	**4**	**4**	**C**	A one way valve has been installed to prevent reverse flow	
Other than	Air instead of water	Empty inlet beaker	No water flow; plate heater overheat; no reaction; particle may settle inline. Particles will be	**2**	**4**	**8**	**N**	Thermocouple on plate heater linked to a cut off switch; Keep a secondary water vessel linked	Use large inlet beaker

			greatly affected					via a valve for quick top ups of inlet beaker	
		Broken inlet beaker	No water flow; plate heater overheat; no reaction; particle may settle inline. Particles will be greatly affected	**2**	**4**	**8**	**N**	Use plastic beaker instead of glass.	Use large inlet beaker
	Organic alcohols instead of water	Operator error	No reaction; may cause temperature spike due to lower specific heat capacity when compared to water	**1**	**2**	**2**	**A**	Only use water straight from the de-ionizer; smell before use.	Correct labelling of all fluids and beakers

HAZOP Analysis									
Node 2 (Blue)									
Plate Heaters									
Guidewords	**Deviation**	**Causes**	**Consequences**	**Risk matrix**				**Safe guards**	**Recommendations**
				P	S	R	RR		
None	No flow	Pump failure; upstream blockage.	Temperature spike; incorrect flow ratio of reactants; incomplete reaction. Particles will be affected	**2**	**2**	**4**	**A**		Regular pump servicing
	No heating	Power failure; thermocouple failure; controller failure; water short circuit.	Exponential temperature drop; exponential reaction rate decrease leading to no reaction. Particles will be affected	**3**	**2**	**6**	**C**	Insulate all exposed wires	Ensure all wiring is installed properly
Less	Lower flow rate	Pump controller error; operator error	Temperature spike after heaters; incorrect flow ratio of reactants; incomplete reaction. Particles will be affected	**1**	**2**	**2**	**A**		Regular pump servicing
	Lower output temperature	Thermocouple error; failure of 1 or more (1 of 4) plate heaters	Slower reaction rate; particles will be mildly affected	**2**	**1**	**2**	**A**	Heating rope; Thermocouples calibrated to ensure that they are reading accurately	
More	Higher flow rate	Pump controller error;	Pressure spike; temperature	**1**	**2**	**2**	**A**		Regular pump

		operator error	decrease; incorrect flow ratio of reactants. Particles will be affected						servicing
	Higher output temperature	Thermocouple under reading; lower flow rate	Higher reaction rates; pressure increase; Particles will be mildly affected	**2**	**1**	**2**	**A**	Thermocouples calibrated to ensure that they are reading accurately	
	Higher plate heater temperature	Thermocouple linked to cut-off switch failure	Massive temperature and pressure increase; increased reaction rates; cooler may not be able to cool down stream below 100°C i.e. steam will exit; aluminium plates may overheat and begin to melt. Particles will be greatly affected.	**1**	**4**	**4**	**C**	Remote manual cut-off switch to turn off plate heaters remotely in an emergency	Remote cut-off switch must be well labelled
Part of	Air along with water	Low level of inlet water	Temperature spike; plate heaters overheating; pressure spike; incorrect flow ratio of reactants; incomplete reaction. Particles will be greatly affected	**3**	**3**	**9**	**N**	Thermocouple on plate heater linked to a cut off switch; Keep a secondary water vessel linked via a valve for quick top ups of inlet beaker.	Use large inlet beaker
	Organic alcohols instead of water	Operator error	Minor temperature increase due to lower specific heat capacity when compared to water;	**1**	**1**	**1**	**A**	Only use water straight from the de-ionizer; smell before use.	Correct labelling of all fluids and beakers

			incomplete reaction						
Reverse	Reverse flow	Upstream leak	First plate heater will stop heating due to a higher temperature reading; particles may settle in plate heater coil.	**1**	**3**	**3**	**A**	Pilot plant pressure and leak testing	
Other than	Air instead of water	Empty inlet beaker	No water flow; plate heaters may overheat; no reaction; particle may settle inline. Particles will be greatly affected	**2**	**4**	**8**	**N**	Thermocouple on plate heater linked to a cut off switch; Keep a secondary water vessel linked via a valve for quick top ups of inlet beaker	Use large inlet beaker
	Organic alcohols instead of water	Operator error	No reaction; may cause temperature spike due to lower specific heat capacity when compared to water	**1**	**2**	**2**	**A**	Only use water straight from the de-ionizer; smell before use.	Correct labelling of all fluids and beakers

HAZOP Analysis									
Node 3 (Yellow)									
Heating rope and pressure release valve									
Guidewords	**Deviation**	**Causes**	**Consequences**	**Risk matrix**				**Safe guards**	**Recommendations**
				P	S	R	RR		
None	No flow	Pump failure; upstream blockage.	Temperature spike; incorrect flow ratio of reactants; incomplete reaction. Particles will be affected	**2**	**2**	**4**	**A**		Regular pump servicing
	No heating from heating rope	Power failure; thermocouple failure; controller failure; water short circuit.	Slight decrease in temperature; no control over reaction temperature set point	**3**	**1**	**3**	**A**	Insulate all exposed wires	
	No pressure release	Spring failure	Massive pressure spike; possible leakage; potential explosion	**1**	**4**	**4**	**A**	Back pressure regulator	A secondary manual release valve can be installed in case of primary release valve failure
Less	Lower flow rate	Pump controller error; operator error	Initial slight temperature increase which will stabilize; incorrect ratio of reactants.	**1**	**1**	**1**	**A**		Regular pump servicing
	Lower rate of heating	Thermocouple over	Slight decrease in temperature; no	**1**	**1**	**1**	**A**	Thermocouple calibration	

		reading; temperature controller error	control over reaction temperature set point						
	Pressure decrease	Inline leak; back pressure regulator failure	Change in properties of supercritical water; slight decrease in flow rate. Particles slightly affected	**1**	**2**	**2**	**A**	Pressure testing	Ensure all fittings are correctly tightened.
More	Higher flow rate	Pump controller error; operator error	Slight temperature increase - heating rope may not be able control the temperature at an increased flow rate; incorrect ratio of reactants	**1**	**1**	**1**	**A**		regular pump servicing.
	Higher rate of heating	Thermocouple under reading; controller error	Slight temperature increase; increased reaction rate; no control over reaction temperature set point	**1**	**1**	**1**	**A**	Thermocouple calibration	
	Pressure increase	Downstream blockage; particle build up; back pressure regulator failure	Change in properties of supercritical water; possible leakage; potential explosion	**2**	**3**	**6**	**C**	Pressure release valve	Ensure tubing is cleaned out regularly to prevent/avoid particle build ups
Part of	Air along with water	Low level of inlet water	Temperature spike; incorrect flow	**3**	**3**	**9**	**N**	Keep a secondary water	Use large inlet beaker

			ratio of reactants; incomplete reaction. Particles will be greatly affected					vessel linked via a valve for quick top ups of inlet beaker.	
	Organic alcohols instead of water	Operator error	Minor temperature increase due to lower specific heat capacity when compared to water; incomplete reaction	**1**	**2**	**2**	**A**	Only use water straight from the de-ionizer; smell before use.	Correct labelling of all fluids and beakers
Reverse	Reverse flow	Up stream leak	Particles may settle in water stream; acidic precursor may corrode inline thermocouples	**1**	**3**	**3**	**A**	Pressure testing	
	Reverse heat transfer	Controller failure; short circuit; thermocouple failure	If the heating rope controller fails it may end up drawing heat instead of providing it; slight temperature decrease; decrease in reaction temperature	**1**	**1**	**1**	**A**	Insulate all exposed wires	
Other than	Air instead of water	Empty inlet beaker	No water flow; heating rope may overheat as there is no cut off switch; no reaction; particles may settle inline. Particles will be greatly affected	**2**	**4**	**8**	**N**	Keep a secondary water vessel linked via a valve for quick top ups of inlet beaker	Use large inlet beaker

	Organic alcohols instead of water	Operator error	Incomplete reaction; possible undesired product; may cause temperature spike due to lower specific heat capacity when compared to water	**1**	**3**	**3**	**A**	Only use water straight from the de-ionizer; smell before use.	Correct labelling of all fluids and beakers

HAZOP Analysis									
Node 4									
Plate Heaters									
Guidewords	**Deviation**	**Causes**	**Consequences**	**Risk matrix**				**Safe guards**	**Recommendations**
				P	S	R	RR		
None	No flow	Double pump failure; blockage in mixing tee due to particle build up	Slight temperature increase; particles may settle inline. Particles will be affected.	**2**	**3**	**6**	**C**		Ensure tubing is cleaned out regularly to prevent/avoid particle build ups; regular pump servicing.
	No heating	Power failure; thermocouple failure; controller failure; water short circuit.	Temperature drop along the length of the reactor after mixing; particles will not grow at a uniform rate	**3**	**1**	**3**	**A**	Insulate all exposed wires	
	No cooling	Blockage in water pipe; municipal water issues	Particles may begin to form prematurely due to heating of the precursor stream. Particle size and size distribution will be affected	**1**	**1**	**1**	**A**		Inspect all cooling water hosing regularly
Less	Lower flow	Pump controller error; operator error	Slight temperature increase; increased reaction rate. Particles slightly affected	**1**	**1**	**1**	**A**		regular pump servicing.
	Lower heating	Thermocouple over reading;	Slight temperature drop along the	**1**	**1**	**1**	**A**	Thermocouple calibration	

		temperature controller error	length of the reactor after mixing; particles will not grow at a uniform rate						Inspect all cooling water hosing regularly
	Lower cooling	Partial blockage in water pipe; leak in water pipeline; drop of pressure of municipal water; increase in cooling water temperature (ground water) over reading rotameter	Particles may begin to form prematurely due to heating of the precursor stream. Particle size and size distribution will be affected	**1**	**1**	**1**	**A**		
More	Higher flow	Pump controller error; operator error	Temperature drop - Heating rope may not be able maintain the temperature set point at a higher flow rate; slower reaction rate. Particles slightly affected	**1**	**1**	**1**	**A**		regular pump servicing.
	Higher heating	Thermocouple under reading; controller error	Temperature increase; increased reaction rate. Particles slightly affected	**1**	**1**	**1**	**A**	Thermocouple calibration	
	Higher cooling	Pressure increase in municipal water; decrease in cooling water temperature (ground	Decrease in temperature of precursor stream. No negative consequences	**1**	**1**	**1**	**A**		Inspect all cooling water hosing regularly

		water); under reading rotameter.							
Part of	Air along with water	Low level of inlet water	Temperature spike; incorrect flow ratio of reactants; incomplete reaction. Particles will be greatly affected	**3**	**3**	**9**	**N**	Keep a secondary water vessel linked via a valve for quick top ups of inlet beaker.	Use large inlet beaker
	Organic alcohols instead of water	Operator error	Minor temperature increase due to lower specific heat capacity when compared to water; incomplete reaction	**1**	**2**	**2**	**A**	Only use water straight from the de-ionizer; smell before use.	Correct labelling of all fluids and beakers
Reverse	Reverse flow	Up stream leak	Particles may settle in water stream; acidic precursor may corrode inline thermocouples	**1**	**3**	**3**	**A**	Pressure testing	
	Reverse heat transfer	Controller failure; short circuit; thermocouple failure	If the heating rope controller fails it may end up drawing heat instead of providing it; slight temperature decrease; decrease in reaction temperature	**1**	**1**	**1**	**A**	Insulate all exposed wires	
Other than	Air instead of water	Empty inlet beaker	No water flow; heating rope may overheat as there is no cut off switch; no reaction; particles may	**2**	**4**	**8**	**N**	Keep a secondary water vessel linked via a valve for quick top ups of inlet beaker	Use large inlet beaker

			settle inline. Particles will be greatly affected						
	Organic alcohols instead of water	Operator error	Incomplete reaction; possible undesired product; may cause temperature spike due to lower specific heat capacity when compared to water	**1**	**3**	**3**	**A**	Only use water straight from the de-ionizer; smell before use.	Correct labelling of all fluids and beakers

HAZOP Analysis									
Node 5 (Precursor pump)									
Milton Roy metallic diaphragm dosing pump									
Guidewords	**Deviation**	**Causes**	**Consequences**	**Risk matrix**				**Safe guards**	**Recommendations**
				P	S	R	RR		
None	No inlet flow	Inlet pipe blockage	Temperature spike as supercritical water not cooled down by ambient precursor stream; Cooler may not be able to handle the temperature spike and water will exit system as steam; incorrect flow ratio of reactants; incomplete reaction. Particles will be greatly affected	**2**	**4**	**8**	**N**	Blockage filter on inlet pipe	
	No outlet flow	Valve failure	Temperature spike as supercritical water not cooled down by ambient precursor stream; Cooler may not be able to handle the temperature spike and water will exit system as steam; incorrect flow ratio of reactants; incomplete reaction. Particles will be affected	**1**	**4**	**4**	**C**		Regular pump servicing

Less	Lower flow rate	Pump Controller error/failure; Operator error; Valve blockage	Temperature spike due to incorrect flow rate ratios; incorrect ratio of reactants; incomplete reaction; increased reaction rate. Particles will be affected	**1**	**3**	**3**	**A**	Inlet filter to block incoming particles or impurities	Regular pump servicing
More	Higher flow rate	Controller error/failure; Valve fails while open	Mild pressure increase; temperature decrease due to incorrect flow rate ratios; incorrect ratio of reactants; incomplete reaction. Particles will be affected	**1**	**3**	**1**	**A**	Pressure release valve and back pressure regulator	Regular pump servicing
Part of	Air along with water	Low level of inlet water	Temperature spike due to lower precursor flow rate; incorrect flow ratio of reactants; incomplete reaction. Particles will be greatly affected	**3**	**3**	**9**	**N**	Keep a secondary water vessel linked via a valve for quick top ups of inlet beaker.	Use large inlet beaker
Reverse	Reverse flow	Leaking pump seal or loss of pressure in pump	Reverse flow may damage pump internals; particles may clog up pump.	**1**	**4**	**4**	**C**	A one way valve has been installed to prevent reverse flow	
Other than	Air instead of water	Empty inlet beaker	No water precursor flow; no reaction; Temperature spike as supercritical water not cooled down by ambient precursor	**3**	**4**	**12**	**U**	Keep a secondary water vessel linked via a valve for quick top ups of inlet beaker	Use large inlet beaker

			stream; Cooler may not be able to handle the temperature spike and water will exit system as steam. Particles will be greatly affected						

HAZOP Analysis									
Node 6 (Green)									
Main cooling column and back pressure regulator									
Guidewords	**Deviation**	**Causes**	**Consequences**	**Risk matrix**				**Safe guards**	**Recommendations**
				P	S	R	RR		
None	No flow	Double pump failure; upstream blockage.	Pressure spike	**1**	**2**	**2**	**A**	Pressure release valve	Regular pump servicing
	No cooling	Blockage in water pipe; municipal water issues; cooling water tubing connection comes loose	Product stream not cooled down from reaction temperature; the reaction will occur for longer than expected which will affect the particles; the product stream will pass through the back pressure regulator and exit as steam.	**2**	**4**	**8**	**N**	Thermocouples measuring inlet and outlet cooling water temperatures	Ensure all hosing is clamped on tightly
	No pressure control	Spring failure	May result in a rapid pressure increase or decrease; change in pressure will affect the properties of supercritical water; a massive pressure increase may lead to leaks or explosions	**1**	**4**	**4**	**C**	Pressure release valve	A secondary manual release valve can be installed in case of primary release valve failure

	Lower flow rate	Pump controller error; operator error	Slight temperature decrease of product stream temperature. Very little effect on particles	**1**	**1**	**1**	**A**		Regular pump servicing
Less	Lower rate of cooling	Partial blockage in water pipe; leak in water pipeline; drop of pressure of municipal water; increase in cooling water temperature (ground water); over reading rotameter	Slight increase in temperature of product stream; may affect particle size and size distribution	**1**	**1**	**1**	**A**		Monitor rotameter to ensure a consistent and accurate flow rate.
	Pressure decrease	Inline leak; back pressure regulator failure	Change in properties of supercritical water; slight decrease in flow rate. Particles slightly affected	**1**	**2**	**2**	**A**	Pressure testing	Ensure all fittings are correctly tightened.
	Higher flow rate	Pump controller error; operator error	Slight temperature increase - heating rope may not be able control the temperature at an increased flow rate; incorrect ratio of reactants	**1**	**1**	**1**	**A**		regular pump servicing.
More	Higher rate of	Pressure increase in	Slight temperature decrease of	**1**	**1**	**1**	**A**		Monitor rotameter to

	cooling	municipal water; decrease in cooling water temperature (ground water); under reading rotameter.	product stream temperature. Very little effect on particles						ensure a consistent and accurate flow rate.
	Pressure increase	Downstream blockage; particle build up; back pressure regulator failure	Change in properties of supercritical water; possible leakage; potential explosion	**2**	**3**	**6**	**C**	Pressure release valve	Ensure tubing is cleaned out regularly to prevent/avoid particle build ups
Part of	Air along with water	Low level of inlet water	Slight temperature decrease of product stream due to decreased flow rate. Decreased yield.	**3**	**1**	**3**	**A**	Keep a secondary water vessel linked via a valve for quick top ups of inlet beaker.	Use large inlet beaker
Reverse	Reverse flow	Up stream leak	Particles may settle in water stream; acidic precursor may corrode inline thermocouples	**1**	**3**	**3**	**A**	Pressure testing	
	Reverse heat transfer	Blockage in cooling column	Cooling water will begin to heat up rapidly; pressure will increase; water may change phase to steam and melt plastic hosing; leaks may occur	**1**	**3**	**3**	**A**	Thermocouples measuring inlet and outlet cooling water temperatures	

Other than	Air instead of water	Empty inlet beaker	No flow; particles may settle inline. Particles will be greatly affected	**2**	**3**	**6**	**C**	Keep a secondary water vessel linked via a valve for quick top ups of inlet beaker	Use large inlet beaker